Prifysgol Abertawe
Swansea University

Enabling Large Scale Manufacture and Processing of Perovskite Solar cells on Semiconducting Glass Substrates

Benjamin James Smith

Submitted to Swansea University in fulfilment
of the requirements for the degree of
Doctor of Engineering

Swansea University
Department of Materials Engineering

2022

DECLARATION

This work has not previously been accepted in substance for any degree and is not being concurrently submitted in candidature for any degree.

Signed: [redacted]

Date: 15/06/2022

STATEMENT 1

This thesis is the result of my own investigations, except where otherwise stated. Where correction services have been used, the extent and nature of the correction is clearly marked in a footnote(s). Other sources are acknowledged by footnotes giving explicit references. A bibliography is appended.

Signed: [redacted]

Date: 15/06/2022

STATEMENT 2

I hereby give consent for my thesis, if accepted, to be available for photocopying and for inter-library loan, and for the title and summary to be made available to outside organisations.

Signed: [redacted]

Date: 15/06/2022

"I have no doubt that we will be successful in harnessing the sun's energy. ... If sunbeams were weapons of war, we would have had solar energy centuries ago."

-George Porter
British Nobel Laureate

"We do not inherit the Earth from our ancestors; we borrow it from our children."

– *Native American Proverb*

"Only two things are infinite, the universe and human stupidity, and I'm not sure about the former."

-Albert Einstein
Physicist

Summary

It has been a decade since the initial breakthrough of perovskite solar cells in 2009 and their rise has been nothing short of extraordinary. Power conversion efficiencies have swollen to over 25 % for a single junctioned device. The multitude of different material sets, and applications seem almost limitless. Their relative low cost to manufacture complements an already existing array of PV technologies while offering an alternative route to decarbonising the earth. If the world is ever to meet a net zero emissions, we will need as many renewable sources of energy available as possible. However, perovskite solar cells are still in their relative infancy in terms of commercialisation when compared to more established PV technologies. There are still issues surrounding the large-scale manufacture of long-term stable perovskite solar cells for the commercial market and these issues will need to be addressed sooner rather than later.

In this body of work, we identify two existing semiconducting glass substrates from the sponsoring company NSG Pilkington that are currently mass produced for window applications. Remarkably, Eclipse Advantage™ and TEC15-D were fabricated into highly efficient and stable perovskite solar cells and displayed a remarkable suitability for use within a mass manufactured perovskite solar cell. With the long-term aim of the project to produce a semi-transparent solar window capable of generating its own electricity, the second phase of the project was to engineer perovskites, based on TiO_2 and SnO_2 respectively, that have the capability to absorb light bifacially or from every direction. We present 2 completely different systems engineered to potentially solve this problem. The first was a novel concept to combine silver nanowires and single walled carbon nanotubes to act as a highly transparent conductive top contact for perovskite solar cells. This composite adheres extremely well to smooth surfaces, something that conventional transparent conductive contacts using metal nanowires struggle with. The method involves no vacuum, is room temperature processed and deposited via a simple and scalable spray processing method that is able to generate power conversion efficiencies of over 11% compared to 16% for opaque evaporated metal contact control devices. The second system involves using a bilayer of IZO and MoOx to encapsulate SnO_2 based cells and enhance long term stability while maintaining a high optical transmission and low sheet resistance. By varying the amount of MoOx used to protect softer underlying layers from the sputtering damage of the IZO material we were able to produce cells that maintained and even improved upon initial efficiencies by over 70 % over the course of 700 + hours illumination. The MoOx also allows for the ability to tune

the perovskites overall colour, something that must be considered for commercial applications. With these developments a semi-transparent solar window capable of generating its own electricity isn't far away. In terms of commercialisation, TEC15-D and the bilayer of IZO and MoOx would be most advantageous of all the developments presented within this thesis owing to their ability to be produced at scale and displaying good long-term stability.

Acknowledgements

None of the work presented here would have been possible had it not been for the generous support of NSG Pilkington, Swansea University and the European Social Fund for their support during my research program.

I would like to take this time to say an enormous thankyou to my supervisor Prof. Trystan Watson. His guidance and encouragement have helped much over the years and I feel grateful to have been a part of his team for so long. I would also like to thank my secondary supervisor Dr. Justin Searle for always making sure making time to support me during my research and facilitating a lot of the relationships with the industrial partner. A special mention goes to my industrial supervisors Dr. Su Varma and Dr. Paul Warren of NSG Pilkington who help share a world of experience with someone so formative. I am a firm believer that more is achieved by the team than the individual, and I could not have asked for a better group of co-workers, the SPECIFIC PV team lead by Prof Watson. I would like to thank each personally for their input over the years especially Dr Adam Pockett, Dr Joel Troughton, Dr James McGettrick, Dr Katherine Hooper, Dr Jenny Baker, Dr Peter Greenwood, Dr David Beynon and my fellow PhD students Dave Richards, Tamara McFarlane and Amirah Way. I would also like to thank the administrative team looking after the M2A project: Beverly Williams, Rhian Nurse, Hayley McAuliffe, Becki Griffiths, Dave Penney and Ian Mabbett.

Without the support and love of my family I would not be here today so I big thankyou to mum Sarah, dad Michael and brother Andrew. Most of all I would like

to thank my beloved girlfriend Anwen Thomas who's love and support throughout the years has meant so much.

Contents

Abbreviations

AgNW	Silver nanowires
AS	Antisolvent
ASTM	American Society of the International Association for Testing and Materials
CdTe	Cadmium telluride
CIGS	Copper indium gallium selenide
CB	Chlorobenzene
CB*	Conduction band
CNT	Carbon nanotubes
CV	Cyclic voltammetry
CVD	Chemical vapour deposition
DAQ	Data acquisition board
DEE	Diethyl ether
DC	Direct current
DMF	Dimethylformamide
DMSO	Dimethyl sulfoxide
DSC	Dye-sensitised solar cell
DSLR	Digital single-lens reflex camera
EA	Eclipse Advantage (NSG Pilkington)
EA*	Ethyl acetate
EQE	External quantum efficiency
ETL	Electron transport layer
FTO	Fluorine-doped tin oxide
GBL	γ-butyrolactone
HOMO	Highest occupied molecular orbital
HTM	Hole-transport material
IPA	Isopropanol
IPCE	Incident photon-to-electron conversion efficiency
ITO	Indium tin oxide

IZO	Zinc indium oxide
LED	Light-emitting diode
LUMO	Lowest unoccupied molecular orbital
MAI	Methylammonium iodide
MAPI	$CH_3 NH_3 PbI_3$
MAPIC	$CH_3 NH_3 PbI_3$-x Cl_x
MAPBr	$CH_3 NH_3 PbBr_3$
MoOx	Molybdenum oxide
NIR	Near-infrared
OPV	Organic photovoltaics
PCE	Power-conversion efficiency
PET	Polyethylene terephthalate
PL	Photoluminescence
PTFE	Polytetrafluoroethylene
PVD	Physical vapour deposition
R2R	Roll-to-roll
RGB	Red-green-blue
RH	Relative humidity
RPM	Revolutions per minute
SSDSC	Solid-state dye-sensitised solar cell
SEM	Scanning electron microscope
SP	Spray pyrolysis
ST	Semi-transparent
TC	Triple cation-based perovskite
TCA	Transparent conducting adhesive
TPC	Transient photocurrent
TPV	Transient photovoltage
UV	Ultraviolet
VB	Valence band
WVTR	Water vapour transmission rate
XPS	X-ray photoelectron spectroscopy
XRD	X-ray diffraction

Chapter 1

1. Introduction

1.1 Rethinking Energy Production

The industrial revolution that began in Great Britain during the latter half of the 18th century marked a major turning point in human history, almost every aspect of daily life was influenced in some way and the demand for energy soared consequently. The energy demand further increased with the electrification of towns and cities later in the mid-19th century. 200 years of intensive fossil fuel use followed and the harm of which has only recently been realised. The consensus among the scientific community is that the earth is warming at an unprecedented rate, the cause of which is a result of human activity through the increased emissions of greenhouse gases generated from our demand for energy. Currents studies indicate even a relatively small increase in global temperatures could raise ocean levels by meters through melting in the polar regions and glaciers. With a large proportion of the human population living close to the coast this could have catastrophic impacts on low laying land. An increase in the occurrence of extreme weather patterns is predicted causing significant disruption to worldwide crop production and famine. Habitat disruption, coral bleaching, deforestation and the acidification of our oceans could lead to a mass extinction event not seen since the time of the dinosaurs as flora and fauna struggle to adapt to a rapidly changing climate. [1] [2].

The need for cheap, reliable and renewable sources of energy is apparent and this has been recognized in developed countries, especially by the G20 where large sums of money have been invested in developing renewable energy and nuclear energy sources. Renewable is defined as energy that comes from resources which are naturally replenished on a human timescale such as solar, hydropower, wind, tidal and geothermal heat.

Of the renewable sources of energy one of the most promising is solar. Solar energy can be harnessed using various technologies including photovoltaics, solar thermal energy and artificial photosynthesis. Photovoltaics are a very promising, ever evolving and very versatile technology. It actively harnesses the power of the sun by absorbing and converting sunlight and photons into electricity that can then be supplied directly into the grid or stored in battery technology. The amount of solar energy falling on the earth's surface is around 89,000 TW, this theoretical potential means that more energy falls on the earth's surface (480EJ) in one and a half hours than the world uses from all its combined sources in 2001 (430EJ). Photovoltaic cells of 10 per cent power conversion efficiency could theoretically generate 15 TW of electrical energy if solar cells covered just 0.17 per cent of the earth's surface. [3]. Advantageously, photovoltaics do not need significant additional infrastructure to connect it to the rest of the grid as photovoltaic systems can be fitted directly to roofing, and, in some cases, built into the fabric of the roof itself (building integrated photovoltaics or BIPV). Any excess energy can be stored on cite and accessed during times when light levels drop.

Crystalline silicon based solar cells originated in the 1950s [4]. The manufacturing routes for these thick film (typically 150-200 μm) devices are technically complex and sensitive to contamination, often requiring high precision vacuum processing and energy intensive procedures (process temperatures of > 1000 °C are required). This can lead to higher associated costs, but these are being lowered at a significant pace and the price per watt has dropped markedly in recent decades owing to economies of scale that allows for a greater uptake of the technology. More recently an emerging thin film PV

technology has the potential to rival as well as complement (tandems) established crystalline silicone. Organometal lead halide perovskite solar cells use earth abundant materials and aim to have a low cost to manufacture via various printing techniques on both rigid and flexible substrates. The high associated power conversion efficiencies as seen in figure 1.1 are offset by the two current draw backs to perovskite solar cells. Firstly, the scaling up of the various printing techniques from lab to factory scale and secondly the long-term stability. However rapid progress to address these known issues are well underway and it might not be long till factory scale devices in a variety of configurations are available on the market. [5]

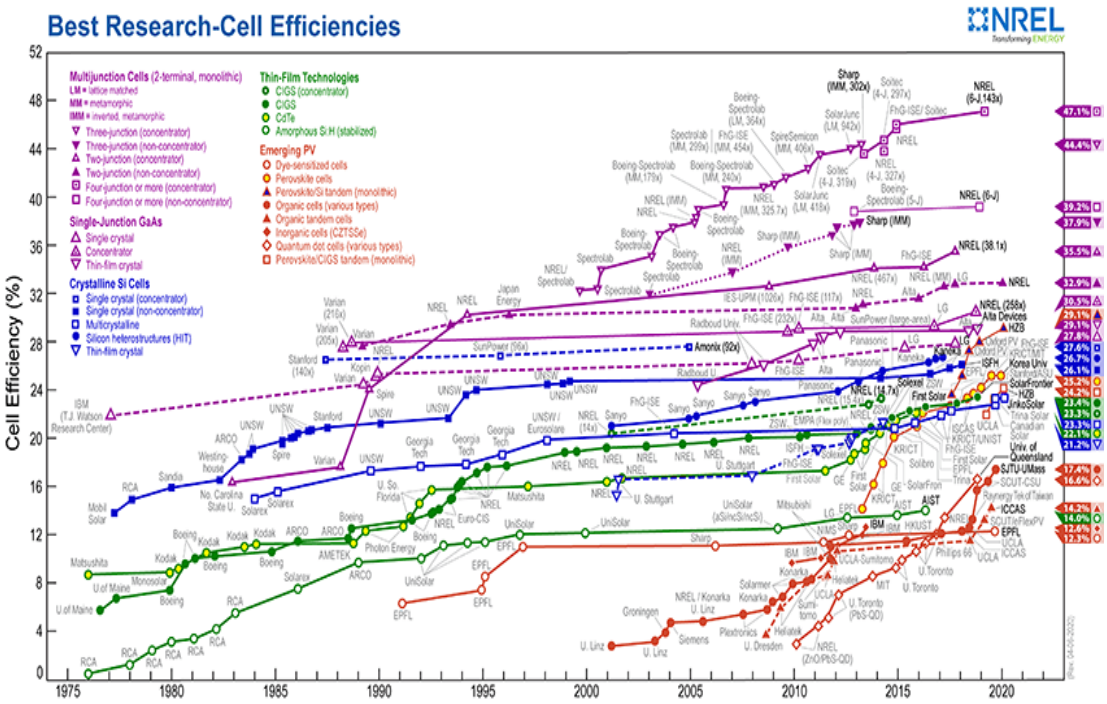

Figure 1.1: NREL chart showing various photovoltaic device efficiencies over time.

1.2 Third Generation Photovoltaics

To put the perovskite solar cell into context it is important to understand the so called “third generation photovoltaics”. First generation photovoltaics includes cells made from a range of semiconducting p-n junctions, second generation refers to what’s known as thin film cells and third generation are those that are

potentially able to over the Schokley-Queisser limit of 31-41% power conversion efficiency for single bandgap solar cells. Perovskite's are most commonly attributed to the development of solid-state dye sensitised solar cell which followed on from its predecessor, the liquid state dye sensitised solar cell (DSC) developed by Michael Gratzel and Brian O'Regan at the Ecole Polytechnique Fédérale de Lausanne in Switzerland in 1991 [6]. The following decades saw much attention from the scientific community and a now certified record for liquid state DSC achieved a PCE of 11.9% [7], at the time giving the technology an excellent market competitiveness as a cheaper alternative to crystalline silicon PV. A liquid state DSC is fabricated by sintering a thin layer of mesoporous nanocrystalline TiO_2 onto a conductive glass substrate to which a monolayer of sensitising dye is adsorbed. A redox electrolyte is added to connect the TiO_2 and the dye electrically and a platinum redox catalyst is coated onto a separate sheet of conductive glass and attached to the other remaining half of the cell. The liquid state DSC works via an oxidised dye molecule being reduced by the redox electrolyte couple ($I^-/I3^-$) on exposure to light which then automatically diffuses back to the counter electrode to receive an electron from an external circuit. A schematic diagram can be seen on the on the right of figure 1.2 with a direct comparison the technology next generation the solid state SDC.

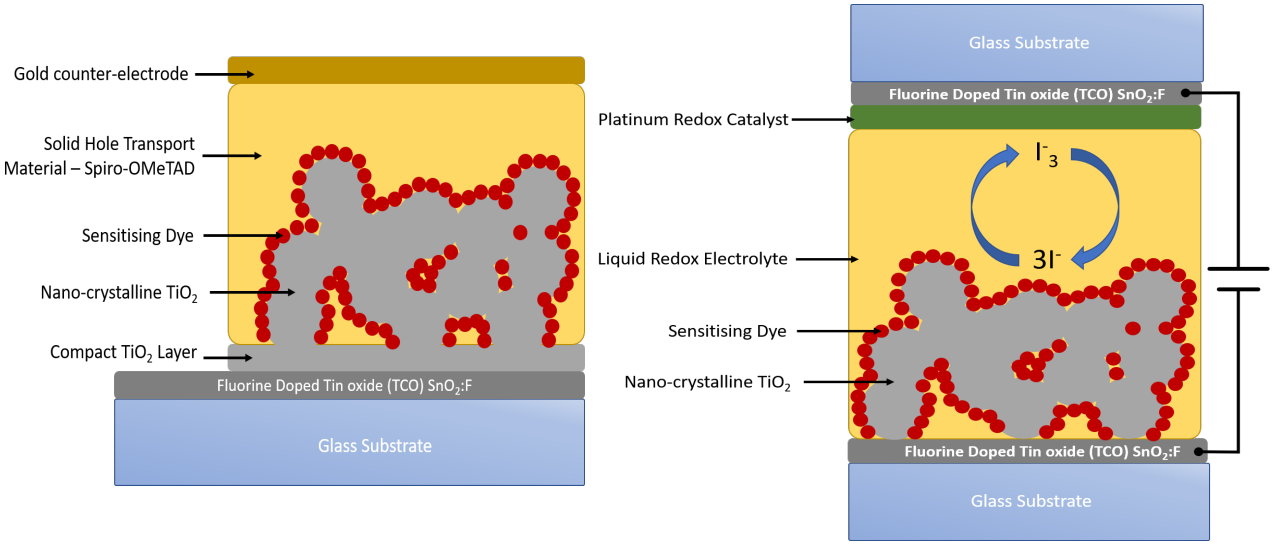

Figure 1.2: A simplified schematic diagram comparing a liquid state DSC on the right containing a liquid redox electrolyte and platinum redox catalyst, and a solid-state DSC on the left containing a solid hole transport material, Spiro-OMeTAD.

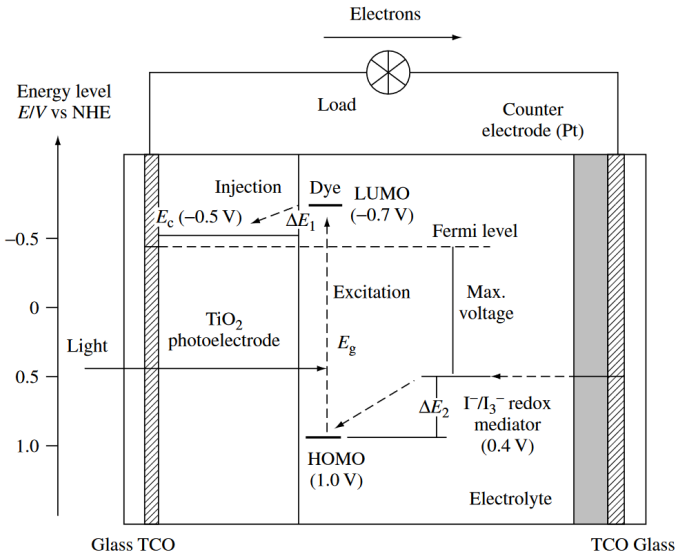

Figure 1.3: Schematic energy diagram and operating principle of DSC. [8]

Figure 1.3 shows a schematic energy diagram of a typical liquid state DSC. There are four energy levels associated to the performance of liquid state DSCS. First is the TiO_2 photoelectrode's Fermi level, or the theoretical level of potential energy for an electron to be excited. Second is the dye sensitizer's excited state, LUMO, or lowest unoccupied molecular orbital and third is the ground state, HOMO, or the highest occupied molecular orbital. Last is the redox potential of the intermediary within the electrolyte.

The evolution from the liquid to solid state DSC successfully came about in 1998, when Gratzel and co-workers reported a solid organic hole transporting material (HTM) ,2,7,7-tet-rakis (N,N-di-methoxy-phenyl amine)-9, 9-spirobifluorene (spiro-OMeTAD) that could replace the conventional liquid state redox electrolyte couple used previously. In this case, the dye is regenerated by a solid organic HTM. It has also been shown that inorganic HTMs can be used in place of the organic molecule such a Copper(I) thiocyanate[9]. Once charge injection occurs after exposure to light the hole transport material becomes mobile due to a hole movement that allows the hole to return to the counter electrode. A solid state-DSC also varies from the liquid-based DSC in that it often requires a solid or compact TiO_2 (ETL) in order to prevent the contact between the solid HTM (Spiro-OMeTAD) and the base FTO contact layer that would otherwise cause the

cell to short circuit. This owes to the fact that the Spiro-OMeTAD and FTO form a perfectly ohmic contact upon the slightest contact with one another, only a couple of nanometres of contact is needed to short circuit the cell. Another benefit of solid HTMs is that the platinum redox catalyst is no longer needed and a simple solid metal contact of appropriate work function like gold can be directly applied to the top of the cell to complete the circuit. A schematic diagram of a typical solid state-DSC can be seen in Figure 1.4.

The move from liquid to solid state promised to reduce the problems associated with liquid electrolytes such as electrolyte leakage, oxygen and water infiltration, substrate corrosion which would help to improve stability of devices. In addition is was hoped the switch would aid in the scaling up of the technology by removing the issues surrounding the liquid electrolyte redox couple. From 1998 to 2017 the PCE of solid state-DSC increased from 0.74% to over 11% using transition metal complexes such as copper (II/I) as hole transport material, thus rivalling liquid state DSC [10] [11]. Drawbacks to solid state-DSC include inadequate pore filling, stability and low conductivity, although some of these issues have been addressed with the use of dopants but these are not perfect solutions as will be discussed later.

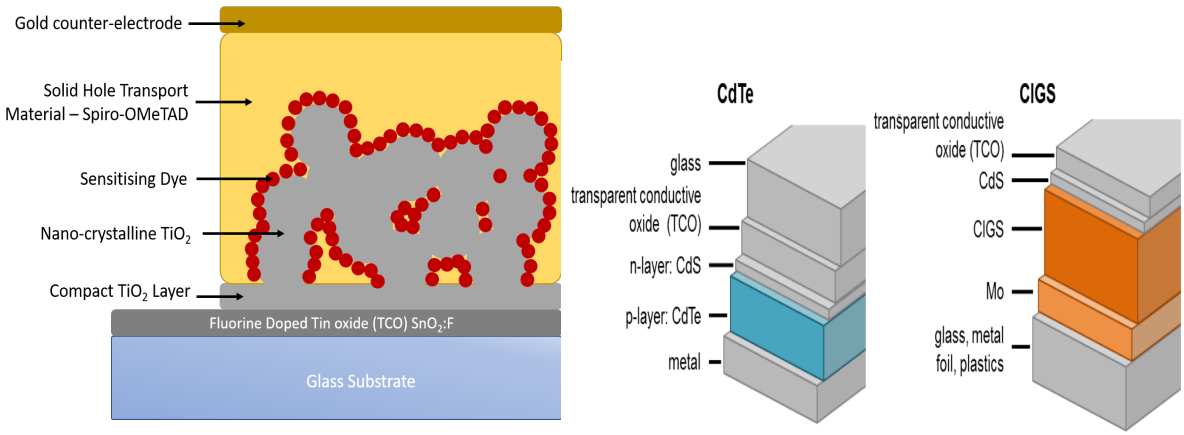

Figure 1.4: A simplified schematic diagram of a solid-state DSC to the left and to the right a schematic diagrams to the typical architectures shown in thin film CdTe (left) and CIGS (right) photovoltaics that rival perovskites [12].

While liquid and solid-state DSCs give us the basis from which perovskite solar originated, it is important not to underestimate the impact other thin film technologies had on the initial and continued development of perovskites. CdTe photovoltaics dominate the commercial thin film module market worldwide. The technology is based around creating a simple heterojunction between the p-type material CdTe and the n-type material CdS. The active layers of CdTe are typically a few microns thick (1 – 8 μm) whereas the CdS is typically of the order of 600 – 2000 Å. Finishing the cell requires sandwiching these layers between a top and bottom contact, usually a conductive metal such as copper and a transparent conducting oxide (TCO) such as SnO_2 or Cd_2SnO_4. The CdS also aids with the growth and electrical properties between said TCO and CdTe. The CdTe acts as the primary light harvesting layer and absorbs visible light within the first micron of material. Power conversion efficiencies for CdTe are now exceeding 22 % [13] thanks to its intrinsic band gap of 1.5 eV and an electron and hole mobility of at least 30 cm^2/ Vs^{-1} [11]. This all leads to a technology that has one of the lowest costs per KW_p [14].

CIGS solar cells employ a 2 - 4 μm thick, p-type, I-III-VI_2 compound semiconductor material comprising copper indium gallium selenide combined with a n-type buffer layer (most commonly CdS). A back contact, usually molybdenum is deposited via sputtering which reflects any unabsorbed light back into the cell. This buffer layer is then capped with a transparent conducting oxide. The buffer is often overlaid with a thin, intrinsic (i- ZnO) layer to protect it from the TCO sputtering process which is known to damage the CdS and CIGS absorber material. CIGS materials demonstrate a high optical absorption coefficient, direct bandgap and relatively high-power conversion efficiencies of over 22 % [13], this coupled with the ability to be deposited on flexible materials such a metal foils make them a promising thin film PV technology to rival perovskites while maintaining low costs to manufacture via their thin nature.

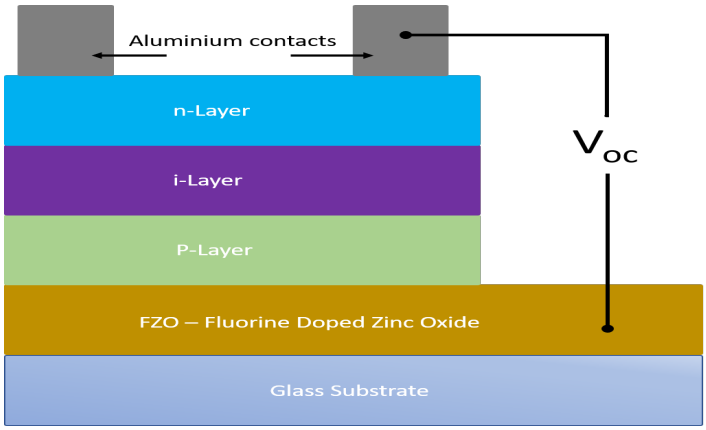

Figure 1.5: A schematic diagram to demonstrate a generalised structure configuration of the hydrogenated amorphous silicon thin film solar cell.

Amorphous silicon in contrast to crystalline silicon use a very thin layer of silicon as a light harvesting layer. The amorphous and thin film nature reduce power conversion efficiencies markedly and to date the record for an a-Si:H cell is only 14% at lab scale [13]. The thin nature of the Si is used primarily to save on costs and recent improvements mean they can now be deposited over large areas on flexible materials. The low efficiency is put down to the low hole mobility of the material [15]. The high defect density of a-Si that leads to poor photoconductivity and hinders semiconductor doping is overcome via a process that introduces hydrogen during the fabrication stage first described in 1969 by Chittick et al [16]. Most commonly it is used in low power applications such as pocket calculators, although higher efficiencies are possible by overlaying multiple cells. The big drawback to amorphous silicon (hydrogenated) is its propensity to degrade when exposed to sunlight known as the Staebler-Wronski effect (in the range of 15-35%).

1.3 Perovskite Solar Cells

The term Perovskite denotes a group of materials that share the same type of crystal structure as calcium titanium oxide. The mineral form of this material $CaTiO_3$ is called perovskite and was first discovered in the Ural Mountains of Russia by German scientist Gustav Rose in 1839 and named after the Russian mineralogist Lev Perovski.

One of the first reported uses of a perovskite material being used in photovoltaics was in 2007, when Kojima et al demonstrated that $CH_3NH_3PbI_3$ and $CH_3NH_3PbBr_3$ could be used as a replacement for the dye molecules in a liquid state DSC device. Initial power conversion efficiencies for the bromide-based device was recorded at 2.19 %, however the resulting photocurrent generated was low, owing to the narrow absorption band of 570 nm. It was postulated iodide based devices would fare better but initial PCEs were low (0.36 %) because of perceived problems associated with the corrosive liquid electrolyte and sub optimal preparation method of the photoelectrode [17]. Further work in 2009 by Kojima et al [18] reported improved efficiencies of 3.8 % of the same iodide-based architecture, this time employing a cell with a spectral sensitivity of up to 800 nm with a high photovoltage (V_{OC}) of 0.96 V and an external quantum efficiency of 65 %. The same concept was optimised by Park et al in 2011 [19] by spin coating a thin < 3nm nanocrystal quantum dot sensitised structured $CH_3NH_3PbI_3$ on top of a thinner TiO_2 film (< 4 μm). Power conversion efficiencies jumped to 6.5 % as the thinner layer of TiO_2 coupled with the $CH_3NH_3PbI_3$ with its higher absorption coefficient compared to that of the dye molecule used previously (N719) resulted in increased photocurrents. However, these cells were extremely short lived, lasting only 10 minutes under irradiation. This was again linked to the quantum dot perovskite being gradually dissolved by the redox electrolyte used.

It wasn't until late in 2012 that the electrolyte-perovskite dissolution problem was solved by Kim et al of the university of Sungkyunkwan, Korea in collaboration with the École Polytechnique Fédérale de Lausanne, Switzerland. By replacing the liquid electrolyte with a solid hole transport material Spiro-

OMeTAD and combining this with a sub-micron thick mesoscopic TiO_2 film, stable power conversion efficiencies of 9.7 % were achieved that previously couldn't be achieved using the sensitised liquid junction cells. A mechanism of hole injection from the excited $CH_3NH_3PbI_3$ to the Spiro-OMeTAD was followed by electron transfer to the mesoscopic TiO_2 [20]. At almost the same time Lee et al at Oxford university and the university of Yokohoma reported a similar increase in cell stability and performance by replacing the liquid electrolyte with the solid HTM Spiro-OMeTAD. Lee et al also demonstrated a mesostructured insulating scaffold of Al_2O_3 in place of the mesoporous TiO_2 structure used in similar devices. The scaffold is reported to structure the absorber material and force electrons to reside in and be transported through the perovskite, allowing for an increase in open circuit voltage and a PCE of 10.9 % [21].

The breakthrough has paved the way for rapid advancement in perovskite solar cell technology and PCEs are now in excess of 24.2 % [13]. A myriad of deposition methods, interfacial engineering techniques and architectures have been reported. From all slot dye coated materials [22], low temperature humidity controlled perovskite layer formation to reduce interfacial recombination [23] to a printed triple mesoscopic stack, incorporating a nearly 10 μm thick porous carbon material, that does away with the need for the costly hole transport material while still achieving PCEs of over 15 % with remarkable stability of over 700 hours [24]. Other notable advances include an antisolvent wash method developed by Jeon et al. [25] that removes the need for the single step annealing process producing excellent homogenous thin film perovskites with very few defects. Perovskite chemistries have seen much research and dual, triple, quadruple cation perovskites now exist that show excellent PCE and improved stability [26][27][28]. In part, the research into perovskite chemistries was motivated by the removal of Pb due to its environmental concerns[29]. Tandem applications that combine the benefits of both crystalline silicon and perovskites have set new world records that promise a genuine root to commercialisation [30][31].

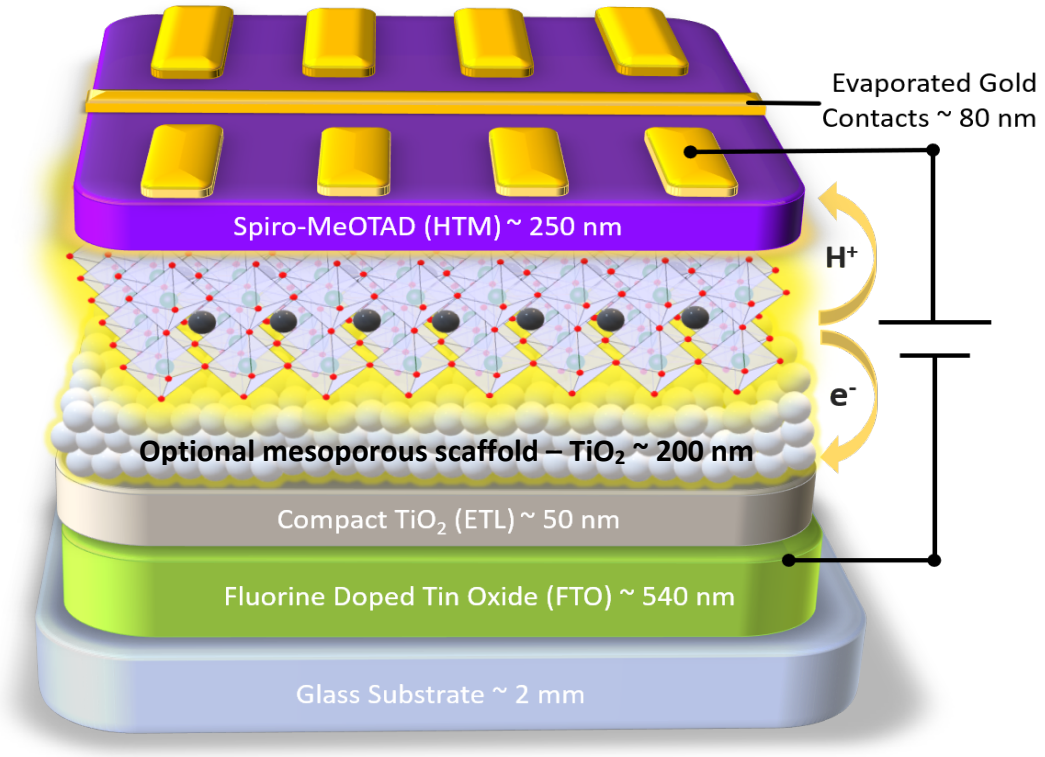

Figure 1.6: Schematic diagram of a typical mesoporous Perovskite Solar Cell (PSC). An inverted architecture swaps the ELT and HTL materials and appropriate work function contacts are chosen. In a planar device optional mesoporous scaffold material – in this case TiO_2 is removed.

A Perovskite solar cell is one that includes an intrinsic hybrid organic-inorganic lead trihalide based material that acts as the light-harvesting layer. A typical thin film Perovskite solar cell will have an architecture consisting of a thin layer of Perovskite sandwiched between two selective contacts known as an n and p type. In most cases the n-type contact (or electron transport layer, ETL) is a thin compact layer of sintered TiO_2 nanoparticles, and the p-type contact usually takes the form of a hole transport material, Spiro-OMeTAD. The p-type contact is connected to the cathode (usually gold) and the n-type connected to the anode complete the circuit. A common anode used in Perovskite manufacture is FTO glass (Indium doped Tin Oxide glass). A schematic of a general Perovskite solar cell architecture is shown above in figure 1.6 although a multitude of different material sets has been reported.

1.3.1 Conductive Substrates and N-type Electron Transport Layers (ETL)

In Perovskite solar cells, the base structure of most laboratory-fabricated devices consists of FTO glass. FTO glass consists of a thin sheet (or pane) of glass that has one side coated with an electrically conductive Fluorine Doped Tin Oxide layer. Thin coatings of FTO on glass were first developed in the 1940's as a solution to the problem of window fog in aircraft during World War 2. Subsequent developments made it suitable for use in a wide range of devices including opto-electronics, thin film photovoltaics, energy saving windows and insulating applications etc. Other applications include touch screen displays and RFI/EMI shielding (Radio Frequency interference/ electromagnetic interference). [32]

FTO glass is ideal for use in Perovskite based solar cells owing to its relatively high stability under atmospheric conditions, chemical inertia, mechanical strength, high temperature resistance and high tolerance to physical abrasion. These properties enable it to serve as the foundation of the cell as the properties allow it to withstand most if not all of the subsequent layer processing. High temperature resistance is a must as the curing of the electron transport layer (ETL) and Perovskite film occurs at temperatures exceeding 100 °C. Chemical inertia, mechanical strength and atmospheric stability allow the layers in Perovskite to be built up independently without the worries of inter layer degradation. FTO glass has an advantage over the alternative coating ITO (indium doped Tin Oxide) as fluorine is not a rare earth metal like indium which due to its relative scarcity and high demand make indium much more expensive and so less economically viable than fluorine.

When light interacts with the photoactive perovskite layer an electron is excited from the LUMO to HOMO and a hole is generated through the photovoltaic effect. To be of any practical use the holes and electrons must be extracted separately for the device to be used as a potential power source. This is done with electron and hole selective contacts that sandwich the perovskite solar cell as seen in figure 1.6. An efficient electron transport material needs to have a homogeneous

pinhole free morphology, high electron mobility for electron extraction, suitable energy level alignment with the perovskite and contact layers as well as a stable structure to help ensure long term stability. The device architecture and processing are also important factors to consider as it is possible to place the electron transport material on top of the perovskite photoactive material as well as beneath in what is termed n-i-p and p-i-n architecture. Without a properly functioning electron transport material, charge recombination can dominate and render the device useless. Defects in bulk materials and at interfaces can lead to trap states which hinder electron extraction and poor quality ETLs are known to cause current-voltage hysteresis [33]. Trap states, perovskite crystal morphology and interface kinetics are discussed further in chapter 1.3.4.

Various ETLs have been investigated but the most commonly used in the literature is titanium dioxide (TiO_2). TiO_2 is an extremely versatile and abundant material due to its high refractive index, high photo-catalytic ability in the visible light spectrum and low toxicity to humans. TiO_2 is such a versatile material is used in everything from pigments in paints to toothpaste to sunscreen and even food colouring. Its resistance to high temperatures, low reactivity, insolubility in water, organic solvents, alkalis and most inorganic acids means it's highly process able and very much suited to an integrated role in photovoltaic applications. It is however susceptible to degradation through ultraviolet radiation absorption as this breaks down the material and generates free radicals which leads to disintegration of the medium. The refractivity index in this case is however, minimal, because only a thin compact layer of about a few nanometres is needed to establish an effective ETL [34].

Titanium dioxide exists as atoms of Ti^{4+} attached to atoms of O^{2-}, in elemental form the titanium atoms are surrounded octahedrally by 6 oxygen atoms. TiO_2 in nature exists in three key distinct crystallographic forms: anatase, rutile, brookite. The atomic spacing and crystallographic arrangement of each is unique, giving each form of TiO_2 slightly different properties. Of the four forms both rutile and anatase are both susceptible to ultraviolet degradation. The properties of these 3 polymorphs vary considerably. Brookite is orthorhombic in crystal

structure meaning it has a larger cell volume than either anatase or rutile with 8 TiO_2 groups per unit cell compared to 4 for anatase and 2 for rutile. Arkansite is a variety of brookite found mainly in Arkansas, USA, it can also be found in parts of Siberia. [35]. Brookite and arkansite are relatively rare compounds compared to rutile and anatase which are much more abundant. It's this scarcity that forces the cost of brookite up meaning it not economically viable to scale it for mass production. If brookite is heated to temperatures above 750 °C it will revert to the rutile structure. For the purposes of photovoltaic applications we will focus on the other 2 forms; rutile and anatase.

Of the forms mentioned above rutile has the highest density and generally exhibits the highest temperature stability especially when compared to anatase. Rutile is stable up to temperatures around 1800 °C whereas anatase converts to rutile at temperatures above 915 °C, although this can be lower depending on crystal size and levels of impurities [35]. For PV applications anatase is preferred because of its ease of integration, exposed {101} facets within the cell, low cost, transparency, high bulk electron mobility, conductivity, greater stability at the nanometre scales required for PV even though rutile has a greater durability and higher refractive index than anatase.

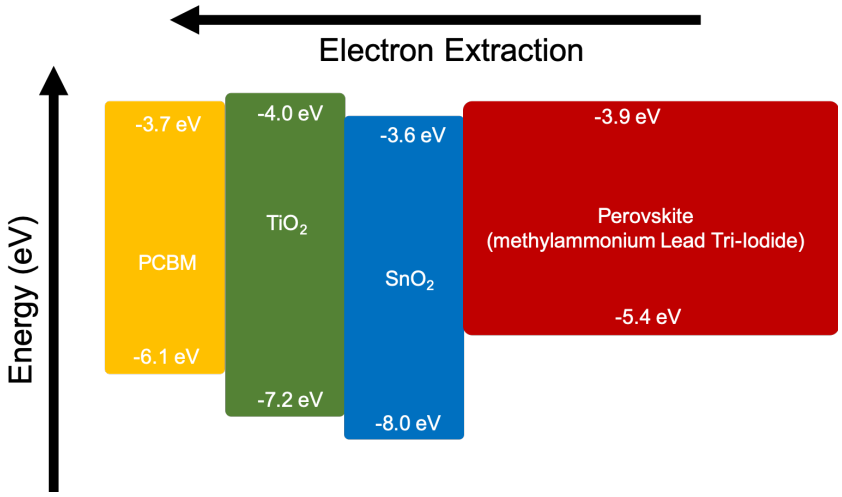

Figure 1.8: A figure to show the relative energy diagrams of common ETL materials and their association with the commonly used perovskite (MAPI), methylammonium lead triiodide.

The ideal thickness required for a thin film TiO_2 ETL was investigated by N.G Park et al [36] and results showed that a film between 50 nm and 140 nm was sufficient to adequately provide the desired blocking layer effect mentioned earlier depending on the solutions and additives used. However subsequent investigations by Aravind Kumar Chandiran et al. [8] demonstarted that an ultra thin nanometer conformal TiO_2 blocking with a thickness of around 2 nm was possible under the correct conditions. In their paper they report a 2 nm atomic layer deposied TiO_2 film with relatively high power conversion efficiencies of 11.5% when using a methylammonium lead triiodide-based Perovskite.

SnO_2 has been demonstrated as an effective alternative to the much used TiO_2 ETL [37] [38]. SnO_2 has several properties that make it suitable for use as an effective ETL material. It has a high bulk electron mobility of 240 $cm^2\ v^{-1}\ s^{-1}$ (TiO_2 is much lower at 4 to 20 $cm^2\ v^{-1}\ s^{-1}$) and a high conductivity with little to no doping. This can aid with electron transport and reduce recombination losses at the interface. Like TiO_2 (bandgap: -4.0 to -7.2 eV), SnO_2 is a wide bandgap material, between 3.6 – 4.5 eV as seen in figure 1.8. It has a high transparency over the visible spectra with a low refractive index, ensuring maximum light is absorbed by the photoactive perovskite. It also has a deep conduction band ensuring efficient electron extraction at the ETL/perovskite interface as well as hole blocking function to reduce recombination [39]. SnO_2 has also been processed using low temperature Nano-particle solution processing (<200 °C) that makes them suitable for use with flexible substrates and large-scale applications. The amorphous to crystalline transition temperature is similar to that of TiO_2 at around 550 degrees Celsius [40]. Devices using SnO_2 report extremely low or no J-V hysteresis in cells in addition to high power conversion efficiencies. This has been attributed to a high bulk electron mobility and fast quenching rate, that provides efficient electron transport and charge extraction at the interface of perovskite/SnO_2. This can help to prevent the accumulation of capacitive charge that leads to hysteresis [41].

The organic fullerene derivative, phenyl-C61-butyric acid methyl ester (PCBM) has received plenty of attention as an electron transport material owing to its low

temperature processing capabilities. This means it can also be used as a bilayer with SnO_2 to produce excellent ETL materials with PCE's over 19%. This is attributed to the ultrathin fullerene structure that can passivate surface defects and enhance charge extraction [42][41]. It has the advantage that it can be used in both n-i-p and p-i-n architectures, as it can be deposited both on top of the perovskite material or beneath it. This can be achieved as PCBM is solution processable in a wide variety of solvents such as chlorobenzene or toluene that are applicable and don't destroy the perovskite crystal structure.

Other ETL materials have been investigated from metal oxides like ZnO [43] to multilayer electron transport materials [44] and organic molecules derived from the OPV field (PCBM) [41][45]. Even graphene quantum dots composites have been looked at as effective electron transport materials. [46]. A summary table is provided below highlighting 3 ETLs that have demonstrated good PCEs in literature at the lab scale and their suitability's with respect to properties needed for the successful scale up perovskite solar cells.

Table 1.1 A summary table of key properties of selected ETL materials used in the fabrication of perovskite solar cells.

Material	Relative Hysteresis	Stability	Processing Temps/ methods	Cost	Appropriate bandgaps
TiO_2	Variable	UV stability issues	Low - various	low	Yes - tuneable
SnO_2	Low	Highly stable	Low - various	low	Yes - tuneable
PCBM	Low	UV stability issues	Low - various	High	Yes – tuneable

1.3.3. Fabrication of Metal Oxide n-type thin films

There are various lab scale methods employed to deposit metal oxide n-type thin films. Spray pyrolysis can be used to deposit a thin layer of TiO_2 via spraying a solution containing titanium nanoparticles onto a heated surface like FTO glass. The heat (550 degrees Celsius) from the surface of the substrate evaporates the solution (usually ethanol or isopropanol) and initiates crystallisation to anatase on contact that coalescence on annealing, leaving behind a thin film of TiO_2, the thickness of the layers can be accurately controlled by varying the number of passes and the pressure of the carrier gas. Drain coating uses a colloidal anatase aqueous solution deposited at low temperature. The solution consists of TiO_2 anatase nanoparticles of around 7nm in size that are stabilised with tetrabutylammonium (TBA^+) [48]. Atomic layer deposition (ALD) involves the sequential deposition of a gas phase chemical process. Two precursors are used that react with the surface of a target substrate one at a time in a sequential, self-limiting process. Through repeated exposures to the precursors a thin film is slowly built up. ALD is compatible for a broad range of materials, works with low vacuum and low temperature depositions and can build up large and small areas with acute atomic thickness precision and superior homogeneity. Sputtering involves a chemical reaction that occurs between the target material, such as Titanium, and a gas. Sputtering (RF magnetron and magnetron) allows thin metal oxides like TiO_2 to be deposited with a very high degree of accuracy through careful control of deposition rates. TiO_2 blocking layers can also be deposited using a hydrolysis reaction of an aqueous solution of $TiCl_4$ [49].

Scalable methods for depositing n-type thin film metal oxides like FTO, TiO_2 and SnO_2 is typically done via a float line using chemical vapour deposition (CVD). CVD has a multitude of processing options available, including metal oxide CVD (MOCVD), plasma enhanced CVD (PECVD), atmospheric pressure CVD (APCVD), low pressure CVD (LPCVD), ultrahigh vacuum CVD (UHVCVD) and sub atmospheric CVD (SACVD). CVD is discussed in further detail in chapter 1.3.4

below. Although FTO is a widely used transparent conductive metal oxide for perovskites, ITO is still an important substrate in certain types of photovoltaics, especially CIGS (Copper Indium Gallium Selenide). Here the ITO (indium doped tin oxide, In_2O_5Sn) is deposited at scale via physical or plasma vapour deposition (PVD), which consists of a vacuum, cathode assembly including the target material to be sputtered, a working gas (argon at low pressure) and a substrate to which is to be coated. The process involves the establishment of a glow discharge gas in the gas to create argon ions, Ar^+. A negative bias is then applied to the target to attract the argon ions. This is followed by ion bombardment of the target and ejection of the atoms at the target substrate. The yield of the coating depends on the energy and angle of the incidence of the ions, the mass of the ion and the target atoms as well as the binding energy of the surface atoms. To increase the yield or sputtering rate a tunnel of magnetic field lines can be formed over the target using permanent magnets in order to confine secondary electrons. This also has the effect of increasing plasma density and lowering the operating pressure. (AKA Magnetron sputtering). In addition to these commercially used methods, it is also possible to scale up technologies such as spray coating and ALD. Although the scaling up of ALD is prohibit ably expensive to smaller companies looking towards mass production unless large capital expenditure is available.

1.3.4 Chemical Vapour Deposition – Eclipse Advantage and TEC15-D

In most cases the FTO layer is made via a float line using chemical vapour deposition whereby precursors in the vapour form are decomposed into atoms or molecules. These chemically react with each other at the hot substrate surface to form a thin, non-volatile, homogeneous coating. The high temperature initiates the decomposition, which can also be initiated with light or plasma if equipped. The chemical equation for the process is as follows along with Figure 1.7 demonstrating the basic CVD process used by NSG Pilkington to produce the commercially available substrates Eclipse Advantage (25 nm TiO_2 on FTO) and TEC15-D (SnO_2 on FTO). Eclipse advantage is primarily used as a solar control

product allowing the control of heat and light into a building, primarily in warmer climates, where the aforementioned TiO_2 is used to control the optics in the system. TEC15-D is used in similar applications but instead the TiO_2 film is replaced with a 50 nm SnO_2 thin film. Tec15-D also acts as an excellent conductive contact, again highlighting the variations in potential applications.

$SnCl_4 + 2(H_2O) \rightarrow SnO_2 + 4(HCl)$

$TiCl_4 + 2(H_2O) \rightarrow TiO_2 + 4(HCl)$

(With doping materials like hydrofluoric acid, HF or organofluoride)

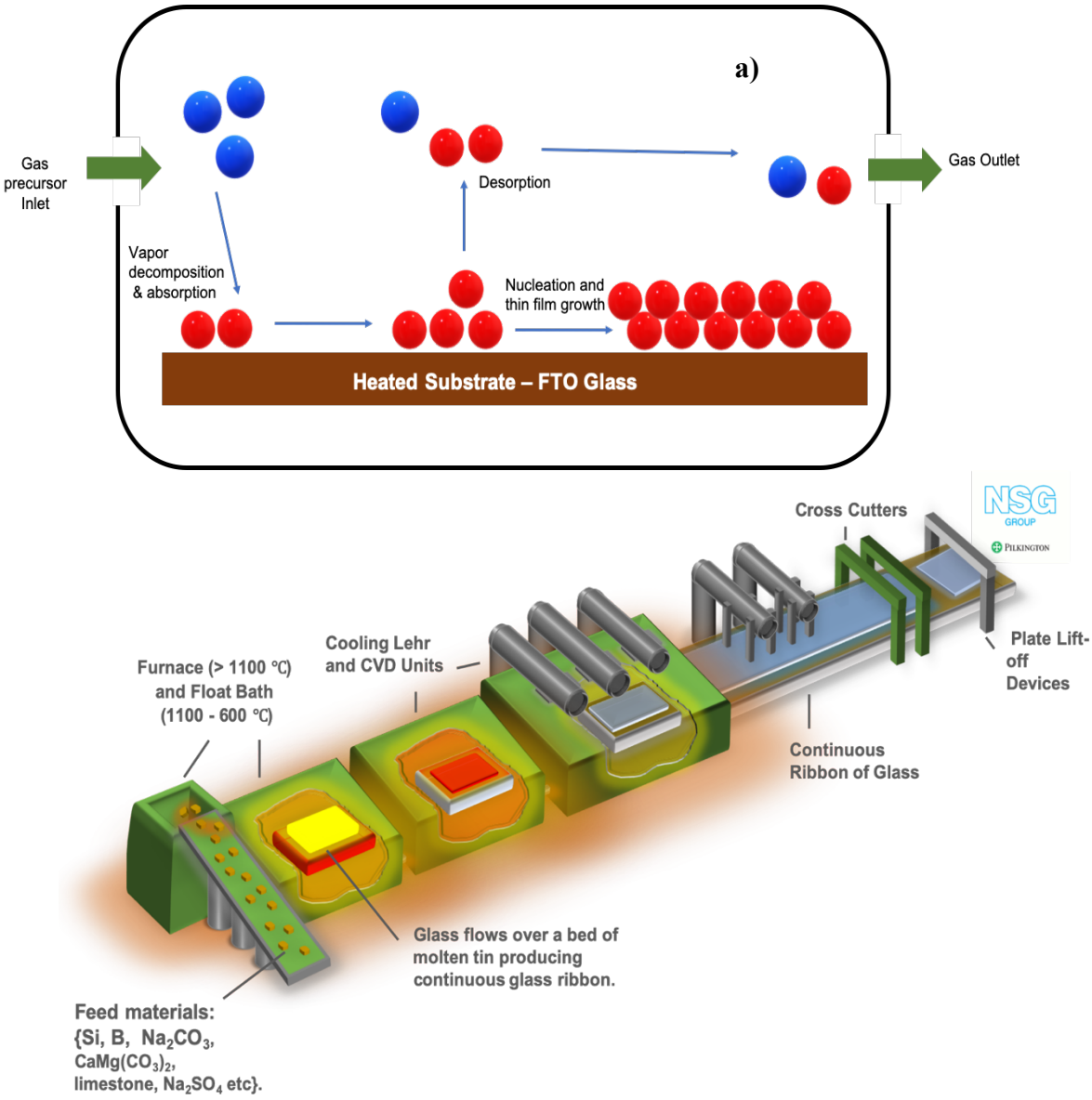

Figure 1.7: a) A basic schematic diagram to show the CVD process used to deposit thin films of TiO_2 and SnO_2. b) A simplified schematic diagram detailing the CVD production process used by NSG Pilkington to produce Eclipse Advantage.

The fabrication of TEC15-D and Eclipse advantage involves the production of glass where raw materials are fed into a furnace at temperatures in excess of 1100 °C the molten glass is deposited on bed of molten tin producing a continuous glass ribbon, cooling lehrs reduce the temperatures further as the glass moves down the line and CVD units are strategically placed at optimal temperature ranges where the TiO_2 and SnO_2 are deposited.

Process temperatures during CVD can reach upwards of 600 °C and this causes diffusion of ions from the soda lime glass (to which the FTO is being coated onto) into the FTO coating, this leads to degradation of the electrical properties of the SnO_2 so to combat this a barrier layer such as SiO_2 is deposited onto the glass before the SnO_2. The electrical sheet resistance varies depending on the thickness of the deposited layer, and common surface resistivities vary between 7Ω/sq. up to around 15Ω/sq. TEC glass manufactured by NSG Pilkington is widely regarded as a superior substrate with its excellent combination of cost and performance. FTO glass also avoids problems associated with ITO such as indium diffusion into the N-type TiO_2 or ZnO Nano-structured films [31]. FTO glass also has the added advantage of increased light transmittance while still optimizing electrical conductivity. Transparent conducting glass also has preferential illumination direction as it allows light to pass through onto the blocking layer then through onto the light absorbing Perovskite material, in the reverse direction photovoltaic performance is reduced because many hole transport materials (including Spiro-OMeTAD) act to screen/block light from reaching the Perovskite material. Metal-organic chemical vapour deposition (MOCVD) is a process that involves evaporating a organometallic (OM) precursor solution, for example Titanium isopropoxide, $[Ti\{OCH(CH_3)_2\}_4]$, via a hotplate and glass bubbler that condenses the layer onto a heated substrate such as glass/ FTO where high purity oxygen is used as the carrier gas and oxidant to transport the OM to the reactor where it's deposited [47].

1.3.5 Mesoporous Metal Oxide Scaffolds & Planar Heterojunction Architectures

Mesoporous scaffolds came about as a result of perovskites link with ss-DSC that incorporated mesoporous TiO_2 as a material for the dye molecule to anchor as discussed previously. TiO_2 is therefore the most commonly used scaffold for this reason, while ZnO_2 can be used as an alternative in place of TiO_2. Other materials used as scaffolds include alumina (Al_2O_3), silicon Dioxide (SiO_2) and Zirconium dioxide (ZiO_2), all of which act as inert insulators [50][51]. It has even been reported of metal oxide scaffolds incorporating graphene into the structure [52].

The mesoporous TiO_2 layer contains pores ranging from 2-50 nm and is typically combined in conjunction with $CH_3NH_3PbI_3$. The mesoporous nature allows for a larger surface area to volume ratio of interfacial interaction, providing more sites for efficient electron injection. In addition, the scaffold primarily provided a structure that could anchor the perovskite precursor material and aid with grain growth sites and nucleation, film homogeneity and improved crystallinity. The improved performances related to the presence of a mesoporous scaffold have been attributed to an increase in V_{OC} and J_{SC} resulting from improved band alignment and filling of the electron trap states at the ETL/perovskite interface via improved film homogeneity and reduced defects (pin holing) [53]. The presence of the TiO_2 scaffold hasn't been questioned as the long diffusion pathlengths for electrons and holes in the bulk material associated with perovskites is typically larger than the films thickness. Many planar architectures now achieve considerable PCE with no use of a mesoporous scaffold and the extra processing step and high temperatures often needed to obtain homogenous crystalline films is a barrier to commercialisation. Inert insulating scaffolds (Al_2O_3, ZrO_2 etc.) act in a slightly different way compared to the conductive scaffolds like TiO_2 and ZnO_2 because these inert metal oxide scaffolds are not injected with the photo generated electrons due to the very high band-gaps associated with alumina and zinc respectively. Instead of conducting the electrons generated upon excitation to the anode or ETL, they primarily act as a structural foundation for the Perovskite to sit on top of, helping to create of more

uniform, homogeneous layer of Perovskite. Using the scaffold helps to insure there aren't concentration build-ups of Perovskite in isolated regions. The long diffusion lengths (charge injection) associated with the perovskite's electron hole pair is sufficient to bypass a thin insulating scaffold and being conducted at their respective electrodes. Although there is debate on whether mesoporous scaffolds are necessary for perovskite solar cells to function, they still achieve near record efficiencies so their use cannot be ignored as they can act as reliable route for controlling the perovskite/ ETL interface. (19) [26] [54].

1.3.4 Perovskite Photo Active Layer

As discussed earlier the crystal structure of all perovskite materials follows the ABX_3 ($^{XII}A^{2+VI}B^{4+}X^{2-}{}_3$) chemical formula. Where "A" and "B" are two cations of vastly differing atomic radii with the "A" cation larger than that of "B". The "X" is a smaller anion that bonds to both. The overall cubic structure has the "A" cation situated in a cuboctahedra coordination with 12 "X" anions and the "B" cation in an octahedron shared with "X" anions of six-fold coordination. Stability of these materials is dictated by a strict ion size requirement which can lead to buckling and lower symmetry distortions where "A" and "B" cation numbers can be reduced. This gives rise to various orthorhombic, tetragonal and trigonal structures as well as many interesting properties for materials science that include magnetoresistance, ionic conductivity, superconductivity and various dielectric effects important to microelectronics etc. [55] [56][57] [58]. The perovskite unit cell is illustrated figure 1.9.

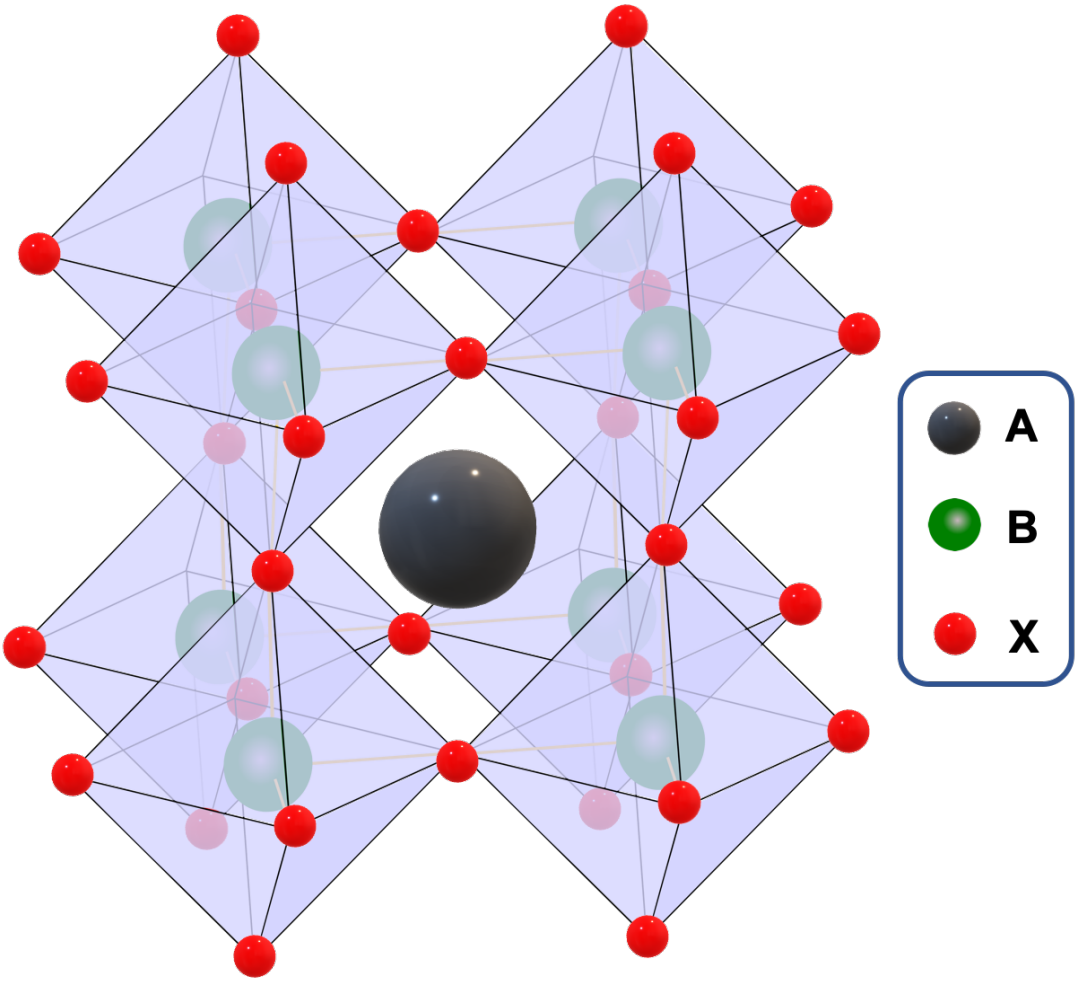

Figure 1.9: A schematic diagram of the perovskite unit cell structure, following the ABX_3 ($^{XII}A^{2+}{}^{VI}B^{4+}X^{2-}{}_3$) chemical formula.

The working principles of perovskite solar cells has been debated thoroughly since their breakthrough in 2012. Tradition PV technologies like crystalline silicon are indirect bandgap materials that require more energy to excite an electron from the valence to conduction band along with vibrational lattice energy (phonons) which leads to thicker films being required.

Thin film perovskite solar cell's fundamental working principles have been difficult to ascertain owing to the wide variety of materials used to synthesise the absorbing layer and the effects of the p and n contacts on perovskite film morphology and optoelectronic properties. This presents a problem when trying to compare perovskite solar cells using different contact materials as the nucleation and crystallisation growth processes of the perovskite are influenced

by the contact it is deposited onto. The top contact will also influence the upper regions of perovskite absorber layer and can produce significant changes depending on the contact and processing methods selected [59]. It is a great advantage of perovskites that similar photovoltaic effects can be engineered via a variety of chemistries. It was initially shown that perovskites utilising a mixed halide organo-lead structure had diffusion lengths of over 1 μm [60] [61]. These initial measurements can account for the fact that perovskite film thickness can be made into what is termed a bulk thin film material (ranging from 100 to several hundred nanometres in thickness) without suffering performance loss due to electron-hole recombination before extraction. The relatively high charge carrier mobility and charge carrier lifetimes of the triiodide semiconductor variant is also sufficient to ensure upon excitation energy isn't lost as thermal radiation within the cell. With perovskites emerging from a dye sensitised solar cell background it makes sense to assume the Pichot and Gregg mechanism.

In the photovoltaic process light absorption by the perovskite material occurs first, this produces a splitting of electrons and holes quasi fermi levels (E_{fn} and E_{fp}) with the difference between the two the termed the maximum free energy available. These must be separated in what is known as charge separation and this is done with the aid of selective p and n junctions with low and high work functions respectively as discussed previously and subsequently in section 1.3.2 and 1.3.5 and this governs the photovoltage limit. Ravishankar et al. [62] showed that despite a large variation in work functions of contact materials the perovskites V_{OC} remained near constant owing to a minor role of the built-in electric field. V_{OC} is generated by the fermi level splitting at the perovskite layer, where each selective contact follows the quasi fermi level of the respective carrier in the perovskite. Perovskites can be thought of as mostly flat band as the minor role of the electric field indicates with transport dominated by diffusion [63] this is illustrated in figure 1.10 and 1.11, and from the Pichot Gregg mechanism in

figure 1.12 we can see V_{OC} is controlled light absorption and carrier recombination.

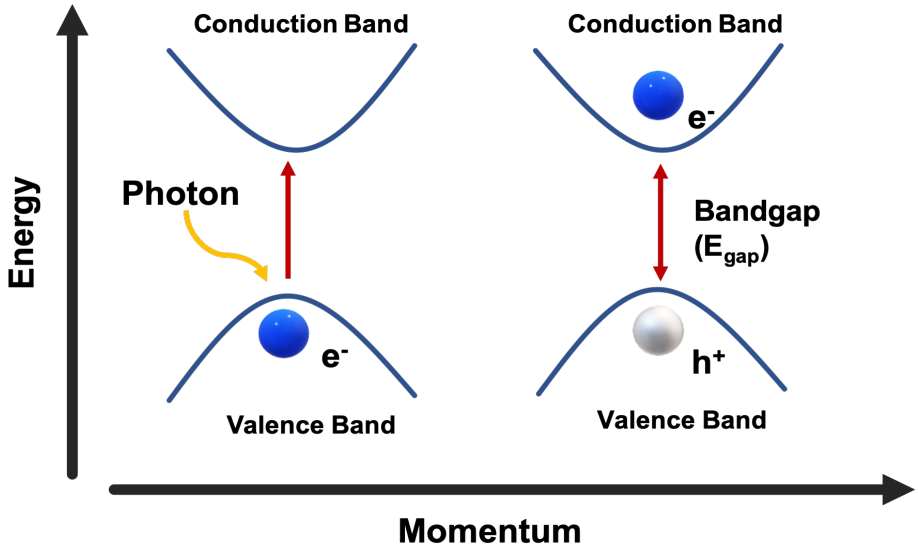

Figure 1.10: A schematic diagram to show the direct electron and hole transfer process in semiconductors

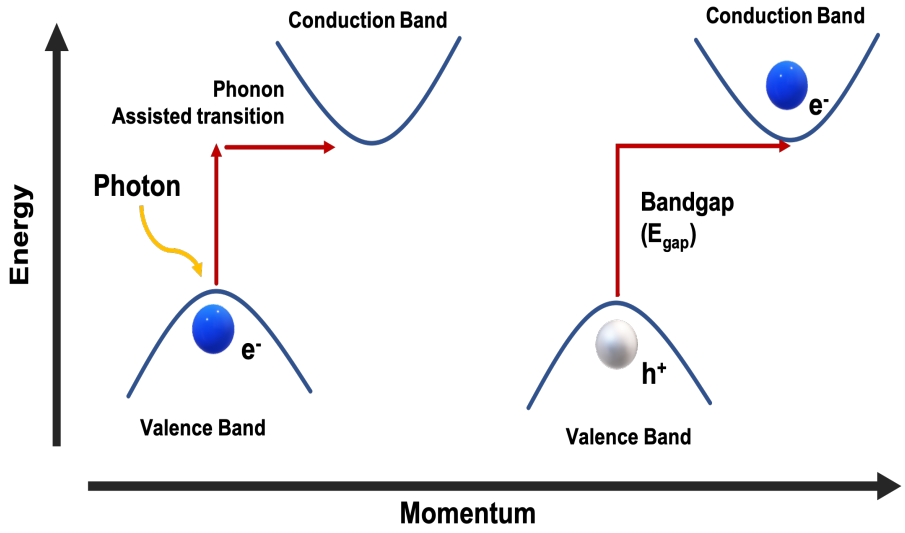

Figure 1.11: A schematic diagram to show the indirect electron and hole transfer process in semiconductors

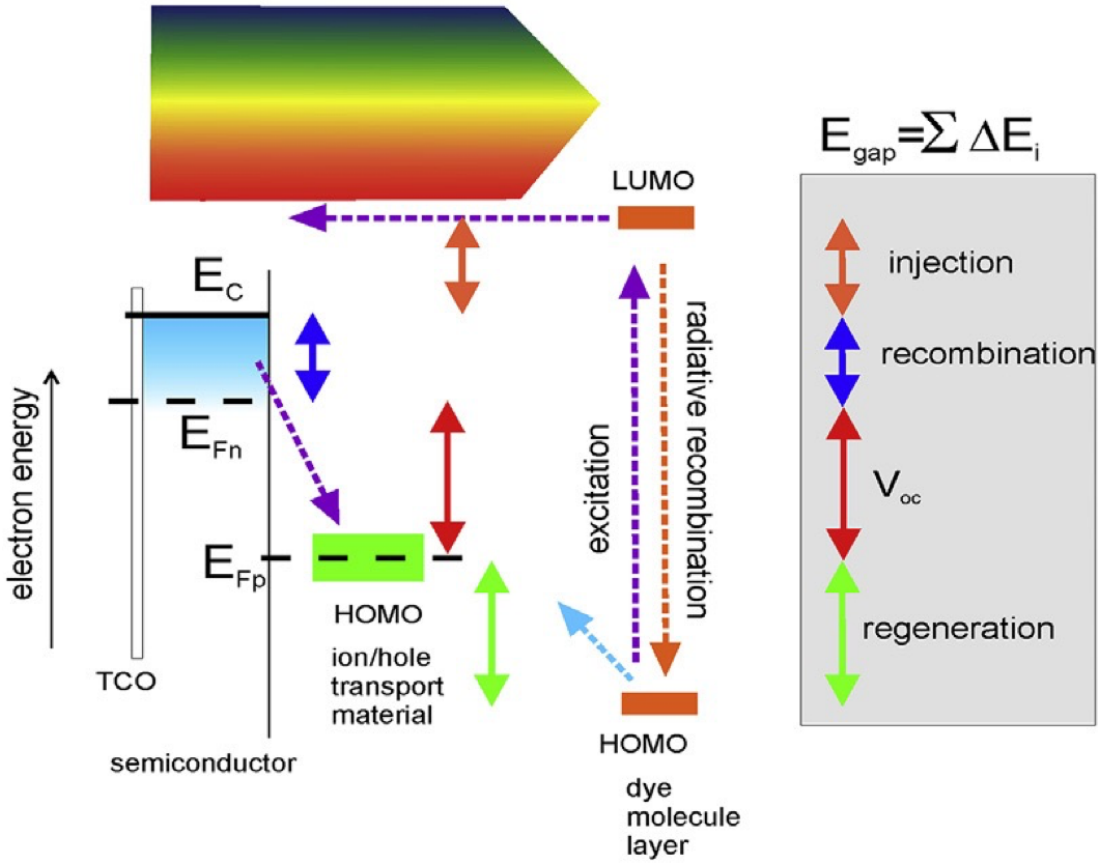

Figure 1.12: Energy diagram and working mechanisms of a dye sensitised solar cell also known as the Pichot and Gregg model [64].

The photocurrent is limited by the perovskites bandgap (E_{gap}), this is the minimum amount of energy required when an absorbed photon of light interacts with an electron in the perovskite semiconductor in order for it to jump from the valence band, or low energy state to the conduction band, or high energy state. The resulting space that is created by the movement of this electron is termed the hole and has the same charge as the electron although it is positive in nature as akin to the negatively charged electron. When perovskites undergo photoexcitation, the mechanism of charge transfer is referred to as a mix of "direct" electron and hole generation and Mott-Wannier excitation occurs. Mott-Wannier excitation are said to be weakly bound electron-hole pairs that attract coulombically over relatively large distances. Subsequently this weak force contributes to the long diffusion lengths observed in perovskites.

The first widely studied chemistry of the perovskite absorber layer focused around the organometal halide, methyl ammonium Lead Iodide ($CH_3NH_3PbI_3$). It exhibits excellent charge carrier mobility and charge carrier lifetime as well as excellent band-gap properties and devices of over 20% PCE are regularly reported in the literature. Its stability issues owing to a myriad of degradation mechanisms discussed in section 1.7 led to extensive research that culminated in an array of chemistries becoming widely used for the perovskite absorber layer. [65]

Mixed halide perovskites using methyl ammonium lead chloride ($CH_3NH_3PbCl_3$) and mixed $CH_3NH_3Pb(I_{x-1}Cl_x)_3$ are one such early example. In this instance chloride ions replace iodide ions (either completely or in small scale substitution) in order to improve certain optoelectronic, morphological properties such as absorption and conductivity or to aid fine tuning bandgaps. There is a drawback to using a mixed chloride Iodide halide system, the larger band gaps observed in $CH_3NH_3PbCl_3$ make the mixed halides less efficient light harvesters than $CH_3NH_3PbI_3$ alone. Although mixed halide (substitution) Perovskites are still a useful tool when controlling optoelectronic and morphological properties [60] [66] [67][68][69].

Perovskite materials that incorporate bromine into the structure have received significant attention. Both methyl ammonium lead bromide and the bromide-chloride mixture have significant advantages in that they are both able to generate high open circuit voltages due to band-gap modification [65], [70], [71]. It has been stipulated that a mixed chloride-bromide case could possibly achieve an open circuit voltage of over 1.5 V. Although these wide band gaps and high V_{OC} could limit performance as mismatching of the bandgaps can result in a loss of photocurrent through parasitic recombination and un-homogenous bromine rich regions [72].

Formamidinium (FA) has been cited as a potential replacement (total or partial) for the organic, methyl ammonium group that is known to be susceptible to both heat, moisture and oxygen degradation. The results have been very promising, with one group in Korea (The Korea Institute of Chemical Technology) reporting

device power conversions efficiencies (PCE) of over 20%. The group lead by Sang Il Soek placed a lead iodide – dimethyl sulfoxide (DMSO) film into a formamidinium iodide (FAI) solution. FAI has a greater affinity for lead iodide than DMSO meaning that the FAI substitutes for DMSO in the lattice to form a formamidinium lead iodide Perovskite structure. The devices exhibit such a high PCE because formamidinium based perovskites have the potential to absorb light from a broader solar spectrum than other conventional perovskites like that of methyl-ammonium lead Iodide. [73]. The formamidinium cation is slightly larger than that of methyl ammonium, which can aid the thermal stability of the by helping to reduce the loss of the organic cation upon heating. The understanding of the thermal and moisture driven degradation known to affect Perovskite absorbers will be very important in the future to enable commercialisation of the technology.

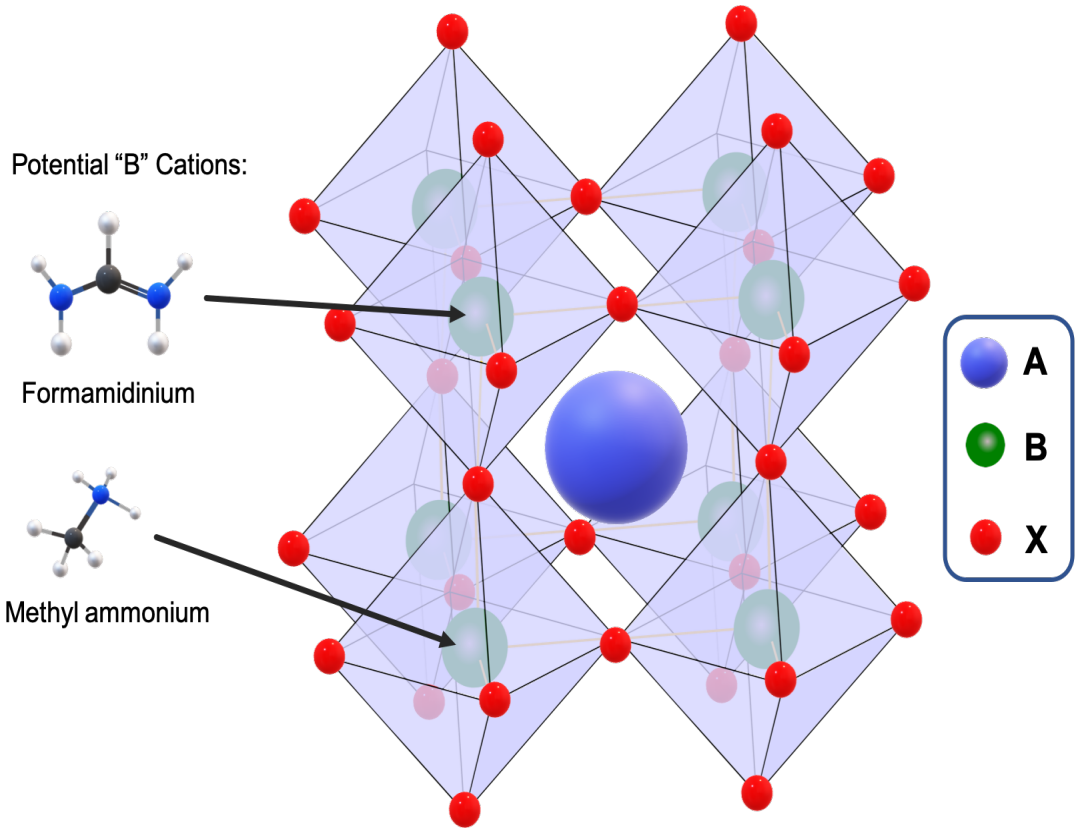

Figure 1.13: Diagram to show how FA (Formamidinium) molecule either partially or totally replaces the methyl ammonium (MA) molecule in a perovskite structure.

FA based perovskites also possess a tuneable band gap, even at the lower end of this band gap devices are well suited for single junction. Results published by Snaith and Eperon et al. show long range electron and hole diffusion lengths thus making them efficient PHJ devices. [74]. FA can also be combined with lead bromides as well as lead iodides as demonstrated by Pablo Decampo et al. [75]

Following on from the dual cation (FA and MA) approach, triple and even quadruple cation lead halide devices were found to show remarkable power conversions efficiencies with notable improvements in stability being reported at the same time. Saliba et al published work using a caesium-formamidinium-methylammonium based cation that dramatically improved reproducibility, stability and efficiency. The inorganic caesium was found help improve thermal stability, reduce phase impurities and improve the robustness of processing by reducing susceptibility of perovskites to external processing conditions. By doping the perovskite precursor solution with as little as 5 % CsI dissolved in non-toxic dimethyl sulfoxide, yellow phase impurities were supressed and highly uniform perovskite films with monolithic grains were recorded, it was postulated that caesium cations act as site for initial perovskite grain growth at room temperature that nucleate into larger equiaxed monolithic grains during crystallisation. The caesium-based films were noted to turn black at room temperature, indicating the photoactive phase of perovskite had already begun to form prior to annealing. This paved the wave for investigations into other alkali metals such as Li, Na, K, and Rb that have since shown beneficial stability effects as well as the ability to fine tune optoelectronic performances further [26] [27].

Lead halide-based perovskites have shown remarkable efficiencies with a wide range of chemistries and optoelectronic properties as demonstrated above. One ubiquitous problem with all these devices is their use of lead in fabricating effective light harvesting thin films. The issue is compounded by perovskite's high solubility in water which poses a threat to human health as well as environmental and ecological damage through run off. Ensuring good encapsulation is one method of preventing such dangers but eventualities like fire and other natural

disasters pose further problems when trying to contain the problem. The toxicity also hinders large scale manufacturing as workplace exposure limits for lead are relatively low given the high toxicity of the product and the solvents used to process perovskite solar cells. Alternatives such as Sn based halide perovskites show promising PCE performance with good direct band gaps of 1.20, 1.41 and 1.3 eV for the material's respective derivatives ($MASnI_3$, $FASnI_3$ and $CsSnI_3$). The decomposition products upon exposure to moisture are also relatively non-toxic and environmentally friendly [76][77][78]. Other non-toxic lead alternatives include germanium based halide perovskite, bismuth, copper and antimony absorbers have also been investigated and show promise[29][79][80].

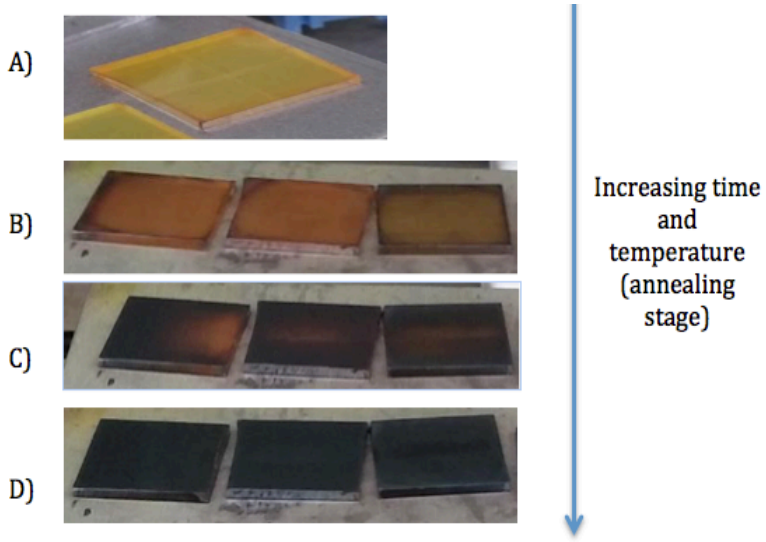

Figure 1.14: Illustration to show the stages and colour changes that occur during a mixed halide Perovskite anneal. A) Perovskite at room temperature hold for 10 minutes. B) Perovskite at the start of the annealing stage, temperature 100 °C. C) After 2-5 seconds at 100 °C. D) Final stage after annealing for 10 minutes at 100 °C.

1.3.5 Deposition Methods for Perovskites

Since 2012 the variety of techniques used to deposit perovskites has increased significantly. Techniques include spin coating, atomic layer deposition, sequential deposition, vapour deposition, spray coating, slot dye coating and bar casting to name but a few. Each technique along with the annealing or drying phase has a significant impact on thin film morphology, crystallography and hence the electronic properties observed in the perovskite absorber layer.

1.3.5.1 Spin Coating

Spin coating is a widespread method used in many laboratories to deposit thin film electronics and semiconductors. It is possible to deposit the whole perovskite cell via spin coating and most laboratory small scale devices follow this method. The application of a thin film evenly across a surface relies on centrifugal force to cast a solution of the desired material carried in a solvent (or ink). As the substrate is in motion, airflow then dries the majority of the solvent leaving behind a plasticised film as seen in figure 1.14 and figure 1.15. A secondary heating step is applied in some instances to drive off higher boiling point solvents and induce desired crystallisation. The high-speed rotation of the substrate, controlled by the revolutions per minute, means centripetal forces combined with surface tension pulls the solution across the substrate to form a uniform coating. It is during the drying stage where many of key processes of film formation occur, namely; π - π stacking or crystallisation of small molecules, self-assembly of block materials, phase separation of dual solution materials (such as polymer blends) and aggregation and assembly of nanoparticles and colloids.

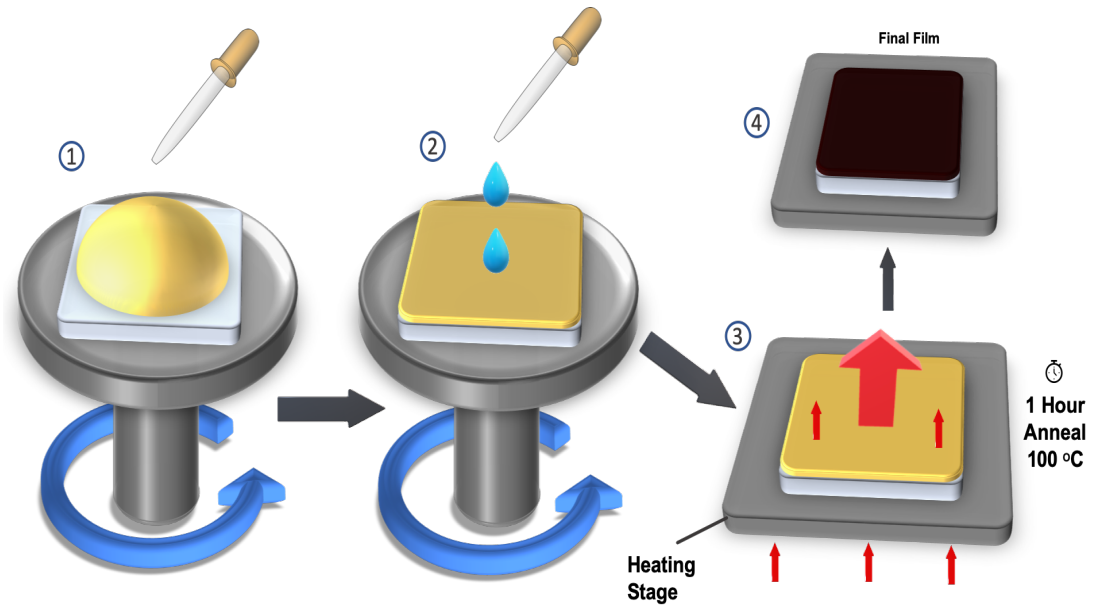

Figure 1.15: A diagram of the spin coating antisolvent process: 1) Initial perovskite precursor solution is deposited followed by spin coating 2) Application of the antisolvent while film is in motion 3) Annealing stage to dry excess solvent and aid with grain growth and crystallisation 4) Final annealed film showing the dark photoactive phase of perovskite.

In general, the thickness of a spin coated film is proportional to the inverse of the square of the spin speed as shown below: where "t" is thickness and w is the angular velocity:

$$t \cong \frac{1}{\sqrt{w}} \tag{1.1}$$

The graph below denotes this relationship and can be used as rough guide for thickness control for standard solvents. Solvent and solution viscosity, contact angle, atmospheric pressures, solution concentration, boiling points, vapour points and laboratory cleanliness are some of the key parameters to account for when fabricating a thin film device as they will have a determining impact on final film homogeneity and thickness.

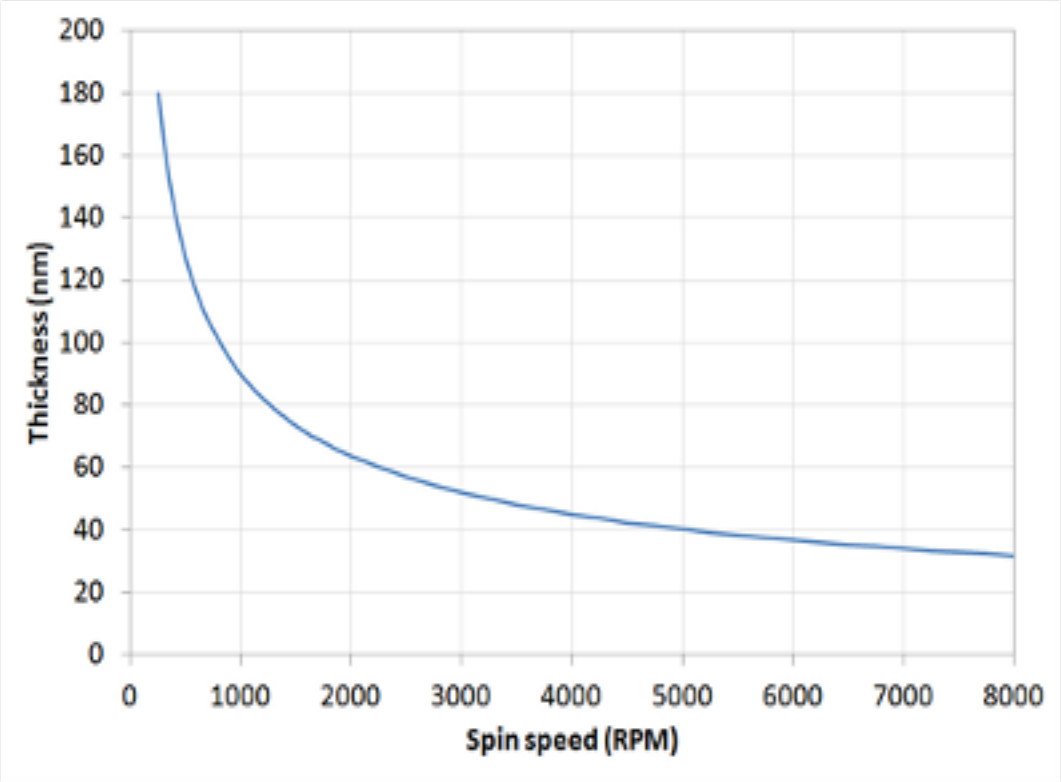

Figure 1.16: Example of a spin curve for a standard solution. [81]

Spin duration and spin speeds are the two parameters that the spin coating process can control independently of the solution. Spin durations are typically of the order of tens of seconds, but this will vary depending on the nature of the solvent (boiling point, vapour pressure, atmospheric conditions) used and spin speeds between an order of 10 magnitude (600rpm – 6000rpm) are commonly used to give uniform defect free thin films.

1.3.5.1.1 One and Two Step Deposition – The Antisolvent Drop Method

The initial papers on perovskites reported a processing method using what is commonly termed a single step spin coating procedure. In Kim et al [20] seminal paper from 2012, a perovskite solution consisting of CH_3NH_3I and PbI_2 dissolved in (N-N) Dimethylformamide was spin coated directed onto a TiO_2 coated substrate and then annealed to form the final film. This method was further

developed by Jeon et al in 2014 [25]. In this method a mixed perovskite precursor solution is used where dimethyl sulfoxide (DMSO) and ϒ butyrolactone (GBL) act as the carrier solvents. Spin coating causes much of the solvent to evaporate leaving behind the perovskite molecules and residual DMSO owing to its lower evaporation rate than GBL. To negate this Jeon et als method drips what is termed an antisolvent onto the sample while rotating. The solvent in case was toluene which is miscible with DMSO and GBL but does not dissolve the perovskite. The antisolvent removes excess DMSO and creates an intermediate phase of PbI_2-CH_3NH_3I-DMSO verified by XRD and FTIR spectroscopy. This was followed by an annealing stage at 100 °C to evaporate any residual solvents from the intermediate phase producing extremely uniform, defect free perovskite layers with equiaxed grain structures. The initial antisolvent used has now been expanded upon and a variety of low dielectric constants, low polarity, and low boiling point antisolvents have been reported as suitable for the preparation of perovskite films including chlorobenzene, ethyl acetate and diethyl ether [82].

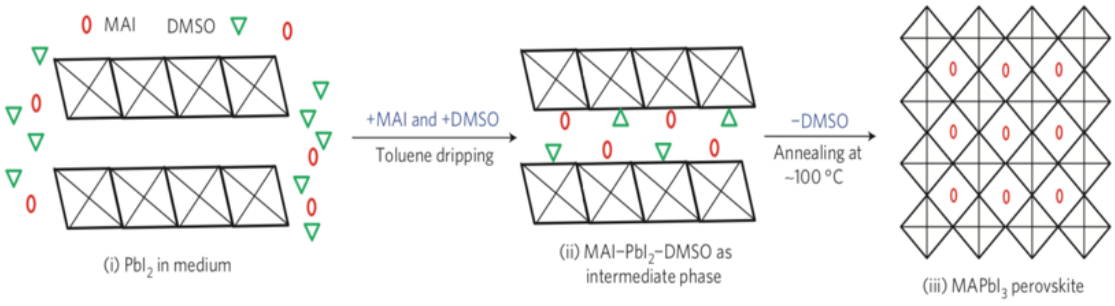

Figure 1.17: A demonstration of the antisolvent dropping technique as reported by Jeon et al. [25].

1.3.5.2 Annealing of Perovskite

The annealing stage of the perovskite film is critical to ensuring an efficient perovskite solar cell. The annealing phase will determine the morphological and crystallographic properties and hence optoelectronic properties of the perovskite absorber, so it is vital this stage is closely controlled and optimised.

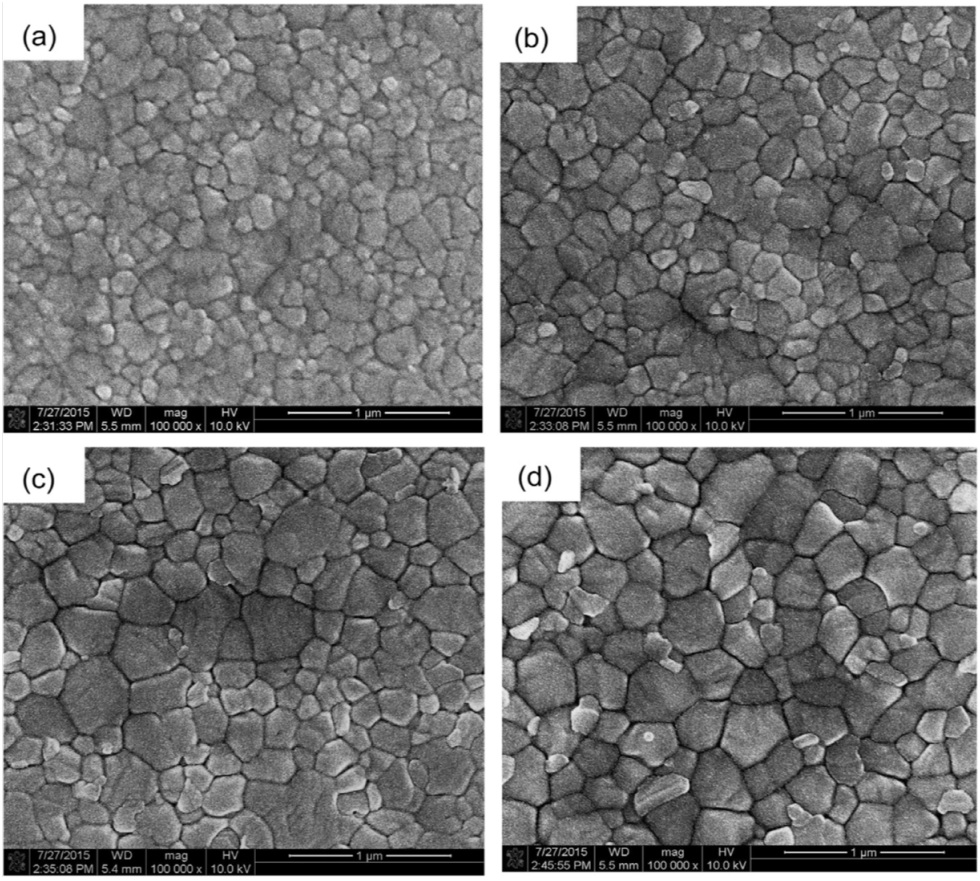

Figure 1.18: FEGSEM morphological image of perovskite film. (a) Thermal annealing to 80 °C. (b) Thermal annealing to 100 °C. (c) Thermal annealing to 120 °C. (b) Thermal annealing to 140 °C [83].

The heating regime of perovskites vary owing to the wide variety of chemistries now employed to induce crystallisation of the ABX_3 perovskite crystal structure. The most widely reported perovskite absorber material $CH_3NH_3PbI_2$ has an annealing temperature range between 80 - 140 °C over the course of 5 mins to several hours. In optimal conditions 100 °C significantly extends the exciton lifetime and yields devices with higher open circuit voltages. Although extended annealing temperatures of over 120 °C is sufficient to decompose the perovskite

where the organic species CH_3NH_3I is liberated from the perovskite film to form a distinctive yellow PbI_2 phase rendering the device ineffective. Different annealing temperatures have a profound effect on average perovskite crystal size ranging from 100 nm to 300 nm. Larger grains are postulated to improve performance owing to parasitic electron-hole recombination at grain boundary regions being reduced [83].

The presence of moisture in the fabrication environment also plays a significant role in perovskite film formation although the relationship isn't straight forward. In most standard lab devices, cells are fabricated in an inert atmosphere, usually conducted in a hermetically sealed glove box using nitrogen to remove oxygen and moisture that is reported to attack the surface of the films. Most small area record devices are therefore fabricated entirely in inert atmospheres with remarkably high PCE and stabilities reported. Moisture plays a determining role in the degradation of the hygroscopic methylammonium component of perovskites, conversely it also plays a role in the formation and film morphology of perovskites. Eperon et al. [84] demonstrated carefully controlled moisture exposure (<30% relative humidity) during fabrication results in a higher open circuit voltage, higher photoluminescence and longer photoluminescence lifetimes. The group concluded that the observations were attributed to reduced trap state densities within the perovskite film caused by partial solvation of the organic methylammonium component. Upon higher exposures the trend was reversed as excess moisture decreases the solubility of the dissolved perovskite constituents and causes them to crash out of solution. This result helped demonstrate it was possible to achieve high performing perovskite solar cells in an ambient environment, thus reducing the need for costly hermetically sealed inert environments that may cause bottlenecks in a large-scale production process. Although more work is needed to fully understand the effects of moisture during fabrication and long-term stability of encapsulated devices.

Conventional methods of annealing perovskites at 100 °C for 30 minutes typically rely on a heated hotplate or temperature-controlled oven with sufficient solvent extraction. These relatively slow processing times are another bottle neck in

largescale manufacture and other methods of annealing have been explored. Processing times have been a source of interest for the upscaling and engineering community, reports of near infrared processed perovskites have shown excellent PCEs by reducing the annealing time for perovskite down to around 3 seconds [85]. Troughton et al [86] further reduced processing times down to below 1 microsecond by employing a photonic flash sintering technique to crystallise the perovskite absorber layer with remarkable success compared to conventional hotplate annealed devices.

1.3.5.3 Sequential Deposition

Sequential deposition was first described as a method for depositing perovskite by Burschka et al in mid-2013 [87] to combat the effects of uncontrolled perovskite precipitation that lead to variations in photovoltaic performance. The method employed a nano-porous metal oxide (TiO_2) substrate that had a thin layer of PbI_2 coated to it. This was done by dissolving PbI_2 in dimethylformamide (DMF) and spin coating, followed by annealing at 100 °C to drive off the DMF. The PbI_2 film, bright yellow in colour immediately transformed to a black photoactive perovskite ($CH_3NH_3PbI_3$) upon submersion in a solution of CH_3NH_3I dissolved in isopropanol (IPA). In the analysis, Burschka, found the conversion occurred within the nano-porous host as soon as the two components came into contact with one another. After submersion for a period of time the films were removed and heated to drive off excess IPA. The result of which was a much higher degree of control of the perovskite morphology when compared to simple spin coating. The method produced reproducible devices with power conversion efficiencies in excess of 15% that have subsequently been bettered and continues to improve. The technique reported increased perovskite film stability and has the potential to be upscaled.

1.3.5.4 Atomic Layer Deposition

Atomic layer deposition involves the sequential deposition of a gas phase chemical process. Two precursors are used that react with the surface of a target substrate one at a time in a sequential, self-limiting process. Through repeated exposures to the precursors a thin film is slowly built up. ALD is compatible for a broad range of materials, works with low vacuum and low temperature depositions and can build up large areas with acute atomic thickness precision and superior homogeneity. Currently there are no processes for the growth of halide compounds via ALD which is a problem, however it can be achieved by going through a series of intermediary stages as explained in a paper by Edward H. Sargent et al. [88]. There they deposit a seed layer to form PbI_2 that can then be converted to $CH_3NH_3PbI_3$ thin films with the use of PbS (lead sulphide) as the other precursor.

1.3.5.5 Physical Vapour Deposition

Physical vapour deposition of perovskite involves using a dual source thermal evaporation system for depositing the perovskite absorber. Snaith et al reported the first use of this technology in late 2013, where they used methyl ammonium iodide as the organic source and lead chloride ($PbCl_2$) as the inorganic source to deposit the mixed chloride-iodide Perovskite onto a TiO_2 glass substrate. In doing so they achieved devices in excess of 15% PCE without the need for nano-structuring. The Perovskite films deposited ($CH_3NH_3PBI_{3-x}Cl_x$) were of extremely high uniformity with crystalline features of hundreds of nanometres in length and very few pinholes observed thus reducing the amount of shunting observed in the final devices. [84][90].

1.3.6 HTM layer / P-Type Contact

The hole transport material (HTM) otherwise known as the p-type contact plays an important role in the workings of a perovskite solar cell. Its role is similar to the n-type contact mentioned previously but varies in that its job is to aid in transporting the holes generated upon excitation and restrict the movement of electrons through to the cathode electrode. This is where the "p" type contact gets its name, from the transport of the "positive" holes from the valence band of the perovskite light absorbing material. This completes the circuit and thus allows the generated photocurrent to be conducted away to perform any number of useful tasks. An ideal p type material has a highest occupied molecular orbital (HOMO) slightly higher than that of the perovskite's valence band. It also needs to have a high hole carrier mobility and is thermally, electrically and chemically stable.

The most popular HTMs in the literature are organic hole conducting polymers such as PEDOT PSS, P3HT (Poly (3-hexylthiophene-2, 5-diyl)) although the most commonly used in literature is Spiro-OMeTAD (2,2',7,7'-Tetrakis-(N,N-di-4-methoxyphenylamino)-9,9'-spirobifluorene, see figure 1.19 and when used in conjunction with appropriate dopants that improve charge carrying properties, can efficiently extract and transfer holes from the valence band of the light absorber and achieve power conversion efficiencies above 20% with n-i-p heterojunction devices.[91] [92] [93].

Spiro-OMeTAD is material that can trace its use back to dye sensitised solar cells and was heavily used in the production of solid-state DSCs. It contains what is known as a Spiro central point, this comprises of a tetrahedral carbon that bonds it with two aromatic moieties. The Spiro centre accounts for the materials relatively high glass transition temperature (T_g = 120 °C) that is useful when considering processing constraints, however a higher glass transition may also be beneficial for future developments and stability. With a HOMO level of -5.22 eV, Spiro-OMeTAD couples well many perovskites, notably the commonly used $CH_3NH_3PbI_2$ (eV of -5.43) and dual and triple cation varieties. This contributes to

high open circuit voltages and PCE have been verified at over 20%. Spiro - OMeTAD is usually spin coated on top of the Perovskite layer, it is typically dissolved in solution before coating and the most common solvent used in the literature at the moment is chlorobenzene. This may pose a problem with scaling up as chlorobenzene is toxic to lifeforms and thus large-scale production poses a risk to health and safety as well damaging the atmosphere and ozone. If Perovskite are to be used at scale an alternative will most likely be needed in the future.

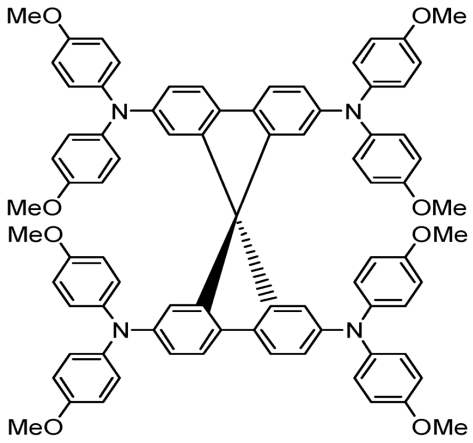

Figure 1.19: Molecule of Spiro-OMeTAD denoting the central point, comprised of a tetrahedral carbon that bonds it with two aromatic moieties.

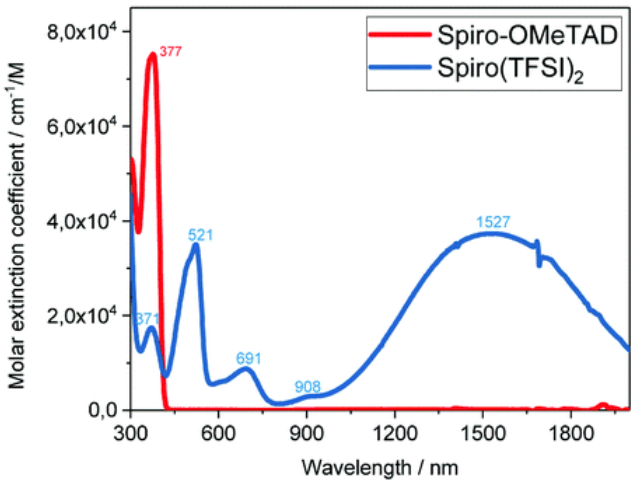

Figure 1.20: UV/visible absorption spectra of Spiro-OMeTAD and Spiro (TFSI)2 in acetonitrile solution. [94].

Perovskite devices based on the n-i-p architecture exhibit good PCEs, however the diffusion length of the holes are slightly shorter than that of the electron due

to the larger effective mass of the hole. [95]. Perovskites that employ the p-i-n architecture, where the "p" contact or HTM is layered on top of the FTO or TCO glass (followed by depositing the Perovskite on top of this) could therefore potentially exhibit more efficient hole extraction. This design would also allow for improved integration of perovskite solar cells with silicon or copper indium gallium selenide (CIGS) solar cells to build tandem devices. This can be done using organic hole conducting polymers like PEDOT PSS, commonly found in organic photovoltaics (OPV) as a HTM but is now used in perovskites for very similar purposed. Molecules such as PEDOT PSS are acidic and have the tendency to absorb water which can lead to degradation of the Perovskite absorber. Being organic in nature they are also susceptible to UV degradation over prolonged exposures. This poses a problem for perovskites becoming commercially successful in the long term. Thus, more stable HTMs are currently being researched for Perovskite based solar cells. The most promising of these are inorganic p-type semiconductors because of their high mobility, improved transparency (another issue concerning Spiro-OMeTAD when doped with Li-TFSI as seen in figure 1.20) in the visible region, good chemical stability and various combinations in terms of VB energy level matching. p-type metal oxide semiconductors used as HTMs include NIO, V_2O_5 and MoO_3. Other inorganics include CuI and CuSCN. Copper iodide was recently shown to have PCEs of around 6% and copper thiocyanate demonstrated good transparency throughout the visible and near infra-red spectrum along with a relatively high hole mobility and chemical stability when compared to Spiro-OMeTAD [95].

1.3.6.1 Additives – Li TFSI and tBP

Bis(trifluoromethane)sulfonamide lithium salt or Li TFSI is an additive commonly used to help improve the optoelectronic properties of the hole transport layer, in this case Spiro-OMeTAD. Li TFSI normally functions as the p-dopant, which improves the hole conductivity of this layer and is used to increase the stability of the photo-generated current as well as prevent charge recombination. It is also used to increase the cells potential by increasing the

degree of disorder amongst coulomb traps within the HTM. 4-tert-butylpyridine or tBP is another common additive added to Spiro-OMeTAD to help improve cell performance, the chemical structure is denoted in figure 1.21 alongside Li-TFSI. When the HTM is employed in the n-i-p architecture in conjunction with a Titania scaffold, the tBP can cause a positive shift in the conduction band in the TiO_2 (compared to the HTMs energy level) initiated by the pyridine molecules being weakly bound to the Titania surface. This produces a negative charge which removes protons from its surface thus determining the cells potential. It has been reported that tBP also enhances the hole extraction at the perovskite/HTL interface. The addition of tBP to Spiro allows more lithium ions to dissolve into the Spiro containing solution as it causes a change in the Spiro-OMeTAD dielectric properties. One drawback of using tBP is it's corrosive effect on the perovskite initiated by the uptake of water, however this can be alleviated by optimizing the molar ratios and thus complex formations of the tBP and Li TFSI molecules as outlined by Meng et al. [96][97]. The drawback to these additives is a lowering of the glass transition temperature of the Spiro molecule, making it more susceptible to degradation when exposed to temperatures above 70 °C which could have significant problems in real world applications where operating temperatures could well exceed this. Thus, effective heat displacing systems would be necessary. The addition of additives like Li-TFSI to Spiro increases the molar extinction coefficient over key wavelength ranges (300 nm to 800 nm) thus reducing the amount of light able to reach the Perovskite absorber when illuminated through the HTM as shown back in figure 1.20.

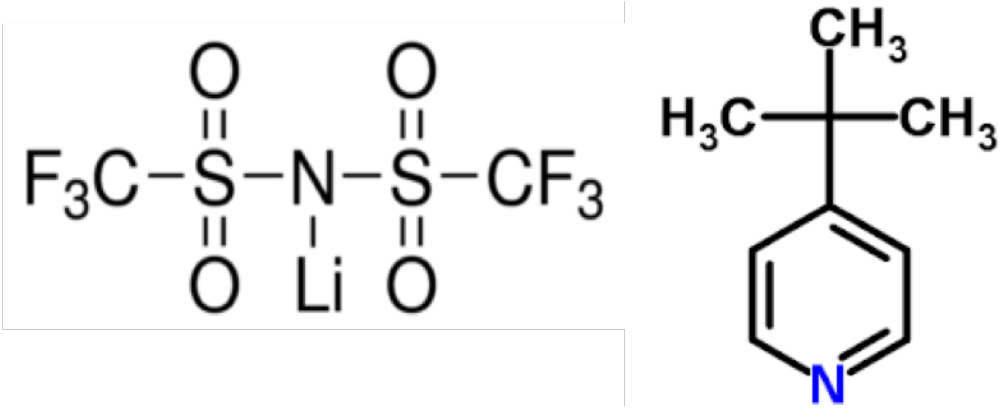

Figure 1.21: To the left a molecule of Li-TFSI and to the right a molecule of tBP.

1.3.7 PSC Transparent Counter Electrodes and Back Contacts

The final layer required to complete the Perovskite solar cell is the counter electrode or back contact sometime referred to as the cathode or anode depending the architecture. This layer is usually comprised of a highly conductive metal such as gold or silver. Its role is relatively simple; it has to conduct the photocurrent generated from either the HTM or ETM depending on the architecture to complete the circuit. Another property that is very desirable of this layer is for it to act as a reflector as well as a contact. This is because when constructing Perovskites solar cells on glass, a reflective back contact can reflect and scatter light back into the device thus improving the light harvesting capabilities which in turns leads to improved power conversion efficiencies through the plasmonic effect. [98]. The layer is relatively thin and can be applied in numerous different ways, the most common of which is via thermal evaporation onto the hole transport material (usually Spiro-OMeTAD) to a thickness of around 80 nm. One issue with evaporated metal back contacts is metal ion migration through the HTM and ETL materials. HTMs like Spiro-MeOTAD are soft polymer materials that become susceptible to metal ion migration under sustained heat and illumination over the course of a cell's lifetime. This creates a short circuit pathway where the metal contact is in direct contact with the perovskite material and recombination occurs rendering the cell ineffective, it also highlights the need for a defect free selective layer to ensure separation of the generated photocurrent [99].

One other potential back contact to mention is that of a conductive metal grid printed on polymer. This method has been employed when manufacturing flexible Perovskite devices using PEDOT PSS [100]. Where a conductive gold Epimesh grip is used to collect and conduct the photocurrent generated with the help of a conductive glue used to hold the device together. The added benefit of this material is it creates a transparent back contact so cells can be illuminated in reverse, allowing perovskites act as a window and or for use in tandem solar cell applications. A transparent contact also allows Perovskites to be fabricated onto

non transparent materials such as sheet metal. TCO materials have also received much attention for the same reason. Typically, these TCO materials are deposited by radio frequency magnetron sputtering to give precise thin film thickness with nanometre control in order to obtain optimised transmission of light. Difficulties arise as the high energy ions required to coat the surface in the sputtering process damage the perovskite absorber and can penetrate soft HTMs as mentioned previously. Semi-transparent perovskite solar cells using vacuum processed TCO materials such as indium doped tin oxide (ITO) [101], hydrogenated indium oxide (In_2O_3:H) [89] and aluminium doped zinc oxide (AZO)[102] have shown it is possible to apply a TCO material on top of a perovskite solar cell in both n-i-p and p-i-n architectures by using an additional sputtered buffer layer to protect the soft delicate under layers from high energy molecular ion penetration. These devices have demonstrated relatively high PCEs in both standard and reverse illuminations with good stability properties as the TCO materials are very stable under repeated thermal stress whilst being illuminated.

Silver nanowires (AgNW), graphene composites and single walled carbon nanotubes (SW-CNT) have also been shown to act as effective charge collectors while maintaining a high degree of optical transparency. The ease of which they are processed is seen as an advantage as this is typically done via solution processing with relatively earth abundant materials. Their matrix structure, with individual nanowire/ nanotubes allows for precise control of layer thickness with light allowed to pass through large areas of their surface unimpeded while acting as effective charge collection sites to negate parasitic recombination. Although ingress of metal components is still an issue, so long term stability is brought into question when used in conjunction with perovskite solar cells. [103] [104]. The mechanism by which they bond to substrates involves Van der Waals forces, which include attraction and repulsions between atoms, molecule and surfaces. The key difference between these and ionic and covalently bonded structures is they are much weaker and are caused by correlations in the fluctuating polarisations of nearby particles. Van Der Waals are essentially weak electrostatic forces that attract neutral molecules to one another. When these neutral particles reach within critical distance, electrons from one particle are

pulled towards the nucleus of the other particle, this creates a transient polarization and an electron-rich domain: δ− and electron deficient domain: δ+ are set up. The δ+ side of one particle attracts the δ− side of another (London dispersion interaction). Particle vibration or motion breaks the interparticle interaction and the particles separate. Van Der Waal interactions have an attractive interaction between atoms, which results from the induced dipoles, and a repulsive interaction, which results from the overlap of the electron clouds of the two atoms, when they get too close to each other. It is this force that AgNW and SW-CNT use to attach to substrates like glass when opposite domains pull one another together. The deposition and interaction of both AgNW and SW-CNT can be used to form a matrix of over lapping tubes/ wires with an increased dislocation density that increases the ability of the composite to attach to the substrate of choice once a sufficient layer thickness is fabricated [105] [106]. The optical properties of these composites can be controlled with spray pyrolysis by varying the amount of spray passes used and the carrier gas flow, as we will see in chapter 5.

1.4 Applications

A key aspect to the commercialisation of perovskite solar cells will be to demonstrate a variety of potential applications to encourage widespread up-take of the technology. One intriguing prospect is the use as building as power stations. SPECIFIC IKC has set out a pioneering vision that incorporates the use of perovskite solar cells and other means of energy generation into the fabric of a building (BIPV – Building Integrated Photovoltaics). In addition, battery technology will be used to store the excess energy produced in times of plentiful sunlight so a store of energy can be retained for use when needed in the winter months when light levels are typical much lower. This reduces a building's need for grid scale energy as it becomes self-sustaining and the need for an expensive network grid system to distribute energy isn't required.

Perovskites have the ability to fine-tune their chemistries to produce a wide range of colours [107], this will hopefully enable larger scale up take of the technology as they can then be employed as windows with a dual function. By fabricating them into double glazed window units they can provide a means to generate electricity as well as provide a source of insulation as those architectures employing TiO_2 have the ability to act as good thermal insulators, keeping buildings cool in the summer and warm in the winter in addition to being aesthetically pleasing.

Perovskite have the ability to be fabricated directly onto metal as well as glass, this means it can be integrated with large-scale roofing for supermarkets and other industry with large warehouse styled buildings. An example of the potential can be seen with Bentley Motors where 20,000 solar PV panels have been installed on otherwise unused roofing to generate electricity adequate to power over 1,200 households. During peak periods this was enough to meet up 40% of Bentley's energy requirements. So the cost benefits to businesses with large expansive metals roofs are clear. [108].

Perovskites also have the potential to be used in tandem solar cell devices along with CIGS and traditional silicon based solar cells. They have the added benefit that absorb in a specific region of the electromagnetic spectrum that differs slightly to that of other PV devices. This means more electricity can be generated in the same area with the same amount light as before. Another promising application for Perovskites is use in low light conditions. Perovskites are one of only a few solar cell technologies that have the ability to be able to function relatively well under low light, meaning indoor applications are an exciting prospect.

1.5 The problem of Scale

If perovskite solar cell technology is to be commercially successful it must address the need to scale up the outstanding lab-based efficiencies to large scale. Cells of area 1cm^2 already achieve a PCE of 15%, produced by the research group at the NIMS Photovoltaic Materials Unit, led by Dr Liyuan Han. Manufacturing large scale homogenous crystalline and uniform thin films is a challenge as defect tolerances are small when considering the scale is only few hundred nanometres thick for an entire device. Toxicity, film stability and the requirement for high throughput (continuous manufacture) and high yields complicate the matter further. A wide range of solution processed deposition methods have been explored for the various different layers that comprise a perovskite solar cell.

Slot dye coating is one such method that offers fully printed, scalable perovskite solar cells. A vacuum free process that has the ability to deposit all but the counter electrode makes it a versatile technique that can be used in a role to roll design to reduces process bottlenecks and time to manufacture. Relying on the visco-capillary model, a solution or "ink" of known viscosity and composition is loaded into a well in the head of the die and a wet film meniscus forms between the die head and the substrate. Careful control of the height and speed of the head over the coated substrate along with the width at the tip of die opening allow for carful control of the layer thickness. In addition, the temperature of the nozzle and bed itself can be carefully controlled to suit the layer being deposited. Perovskite cells produced using this method initially achieved PCEs of nearly 12% [109] and devices with 4 slot die coated layers (ETL, mesoporous scaffold, Perovskite absorber and HTM) have been demonstrated with stabilised power conversion efficiencies of 7% over a large area [110]. The system can be adapted and modulated with the addition of air knives to help control uniform distribution of precursors over a large area.

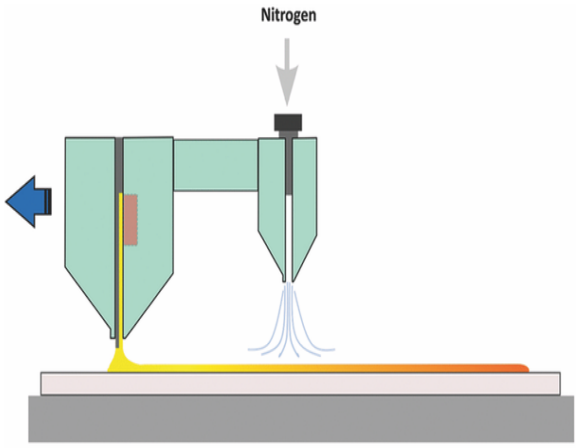

Figure 1.22: A schematic diagram for a slot-die coater with a gas quenching process for the fabrication of pinhole free PbI_2 layer [109].

Screen printing in a clean room environment is another deposition technique that has the capability to manufacture perovskite solar cells at scale via a batch to batch process or continuous process depending on the set-up. Screen printing can also deposit multiple layered thin films sequentially which helps to reduce processing times and simplify a route to manufacture. Screen printing typically falls into three categories; screen printing, relief printing and Gravure printing. Screen printing relies on the image to be printed first being engraved onto an image carrier before being applied to a suitable substrate. This image carrier or mesh is equipped with a stencil defining the pattern to be printed and a blade is swept across the screen that distributes the ink over the mesh and substrate. Gravure and relief printing use a cylindrical image carrier if continuous production is desired. Screen printing has been widely used to deposit the HTL, ETL and mesoporous scaffolds and PCE have exceeded 15% [103]. Examples of these techniques is illustrated in figure 1.23.

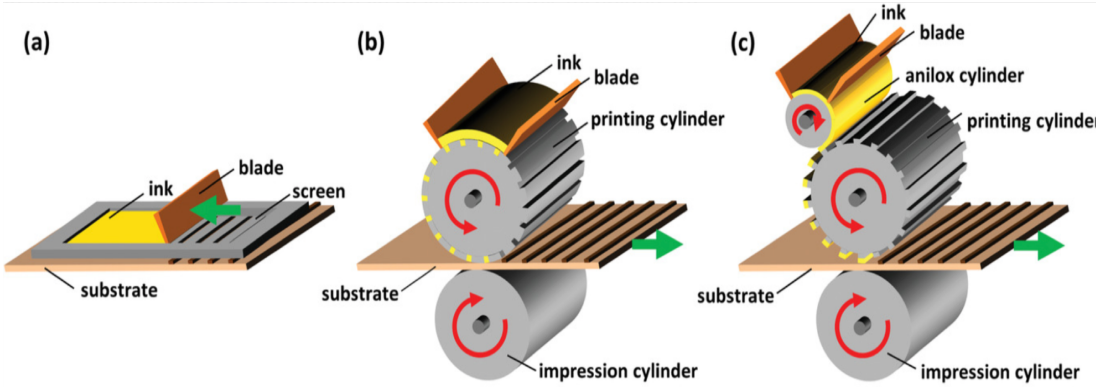

Figure 1.23: Screen printing, gravure printing, and relief printing. a–c) Schematic illustration of screen printing (a), gravure printing (b), and relief printing (c) processes [111].

Other methods to scale up perovskite solar cell technology include spray coating, inkjet printing and blade coating. All provide good throughput processing times, are roll to roll compatible given certain modifications, can deposit multiple homogeneous layers (thin film) and demonstrate excellent power conversion efficiencies [112] [113][114]. The use of LASER technologies to ablate materials in order to create the interconnects of modules helps to improve precision over more tradition mechanical scribing methods and allows a more scalable method for high production volumes [115]. The suitability and toxicity of the materials used in the scale up of perovskites must also be taken into account. Solvents choice is of paramount importance, solvents such chlorobenzene and materials such as lead metal both pose significant risks to human health and safety, so will need careful planning and control when it comes to up scaling. The same can be said when processing any flammable, toxic and corrosive agents. Much work has been done looking into safe solvent systems to process perovskite solar cells, replacing DMF with non-toxic alternative such as DMSO and GBL [116].

1.6 Characterisation

1.6.1 JV or Current Voltage Measurements

The performance of a solar cell is a measure of its ability to convert light energy from the sun into electricity via the photovoltaic effect (defined as the creation of a voltage and electrical current in a material upon exposure to light). Also known as the power conversion efficiency (PCE), it is the ratio of incident light power to output electrical power. PCE is determined via current-voltage (IV) measurements, where a series of voltage biases are applied to a cell under a known illumination and the output current measured at each voltage step. The resulting IV curve is the ubiquitous form of displaying solar cell performance in literature and an example can be seen in figure 1.24 along with other key photovoltaic properties that can be deduced from the IV measurement. The convention to use current density (J) instead of current (I), is common when characterising solar cells as the area of the cell has an impact on the output current and thus performance. These measurements allow for a direct comparison of devices manufactured at different laboratories and allow different PV technologies to be compared under similar conditions.

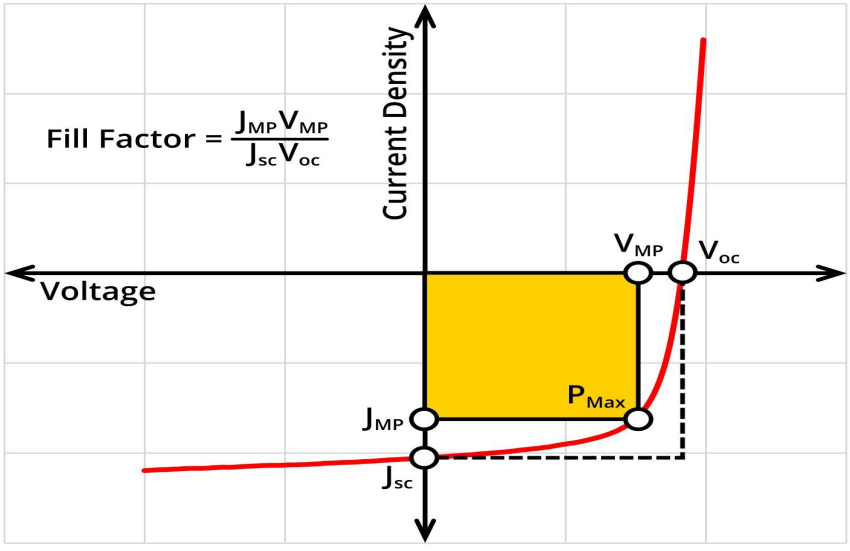

Figure 1.24: A typical JV curve of a solar cell plotted using current density, highlighting the short-circuit current density (Jsc), open-circuit voltage (Voc), current and voltage at maximum power (JMP and VMP respectively), maximum power point (PMax), and fill factor (FF) [117].

From figure 1.24 the following key characteristics can be extracted:

- V_{OC} – Open circuit voltage is defined as the voltage measured when the current (or current density) is equal to 0. In this case the applied electric field cancels out the built-in electric field, removing the driving force needed to move the charge carriers and resulting in a current equal to 0. This is influenced by the energy levels of the photoactive materials, the work functions of the chosen electrodes and charge carrier recombination rates.
- J_{SC} – Short circuit current is defined as the current (A) or current density (Acm^{-2}) measured when the voltage is equal to 0. In this case the electric field within the cell drives charge carriers to the electrodes. This is influenced by the photoactive layer's absorption properties and charge generation, transport and extraction efficiency.
- P_{Max} – The maximum output power (or max power point).
- V_{MP} – Voltage measured at maximum power.
- J_{MP} – Current or current density measured at maximum power.

The fill factor (FF) is the ratio of the actual maximum power point and theoretical maximum power point if there was no series resistance and infinite shunt resistance (ideally as close to 1 as possible). Series and shunt resistances can be approximately calculated from the inverse of the gradient of a cell's JV curve at the V_{OC} and J_{SC} respectively. Fill factor is calculator as follows:

$$FF = \frac{J_{MP} \cdot V_{MP}}{J_{SC} \cdot V_{OC}} \tag{1.2}$$

Power conversion efficiency is subsequently calculated from the equation shown below:

$$PCE = \frac{P_{out}}{P_{in}} = \frac{J_{SC} \cdot V_{OC} \cdot FF}{P_{in} \cdot 100} \tag{1.3}$$

In the equation above P_{in} is the power associated with the intensity of the incident light on the cell and P_{out} is the electrical power generated by the cell.

A solar cell is regarded as a diode in parallel with a current source and a resistor (shunt resistance) as well as a resistor connected in series (series resistance). The Shockley diode equation can help us model the electrical behaviour of an ideal solar cell. This can be modified in order to address the fact that no device is ideal, so to include potential loses that arise from series resistance and the impact of reduced shunt resistance the following equation is often cited:

$$J(V) = J_{ph} - J_0 \left[\exp\left(\frac{e(V + JR_s)}{n \cdot k_B \cdot T}\right) - 1\right] - \frac{V + JR_s}{R_{sh}} \tag{1.4}$$

Where: J_{ph} = Photogenerated current density, J_D = Diode current density, V = Voltage , T = Device temperature, R_s = Series resistance, R_{sh} = Shunt resistance, k = elementary charge constant ~ 1.6 x 10^{19} C, B = Boltzmann constant ~ 1.38 x 10^{-23} m^2 kg s^{-2} K^{-1}, n = diode idealistic factor derived from the slope of the dark IV measurement, suns V_{OC} and occasionally the light IV curve and J_0 = Dark saturation current density which is measured from the current density through the diode in the dark while under reverse bias.

The expression above is often incorporated into the equivalent circuit of a simplified solar cell shown below in figure 1.25:

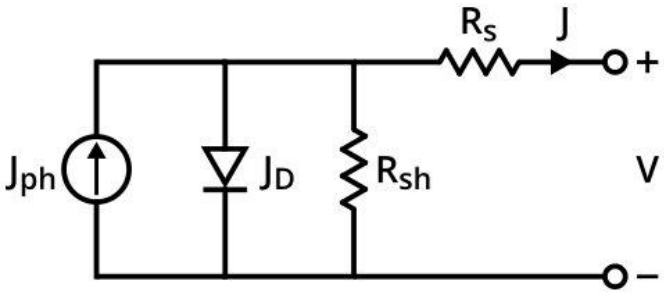

Figure 1.25: a simplified circuit diagram for a solar cell [117].

The modified Shockley diode equation shows the effect increased series resistance has on reducing power conversion efficiency. Series resistance is associated with energetic barriers at interfaces and internal bulk resistances within layers (e.g. layers that are too thick). Increased series resistance leads to an increase in charge carrier recombination thus reducing performance. This can

be negated by ensuring energy level alignment within the cell complement one another so that charge carriers are not impeded. The modified Shockley diode equation also shows us an increase in shunt resistance causes a direct increase in power conversion efficiency by disrupting alternative pathways through the cell which aids to prevent charge leakage. Short circuiting is a result of low shunt resistance often due to pinhole formation within layers that allows unwanted contact between conducting layers.

In order to measure a solar cells performance accurately it must be exposed to a known intensity of light and spectral output. The spectrum of our sun peaks in the visible range (400 – 700 nm) and has a long infra-red tail which is like that of black body with a temperature of 5780 K. It's important to note that the earth's atmosphere absorbs a significant portion of our suns solar radiation before it reaches the earth's surface. This must be considered when measuring solar cell performance. The industry standard spectral intensity used for characterising solar cells is known as AM1.5G (air mass 1.5 global, shown below in figure 1.26), it correlates to the average global solar spectrum after passing through 1.5 atmospheres. Commonly denoted as "1 sun" it has a power density of 1000 W m^{-2} (conforming to ASTM G173-03 as defined by IEC 60904-3 with a device temperature of 25 °C) and replicates average solar radiation at mid latitudes in regions such as the USA and Europe.

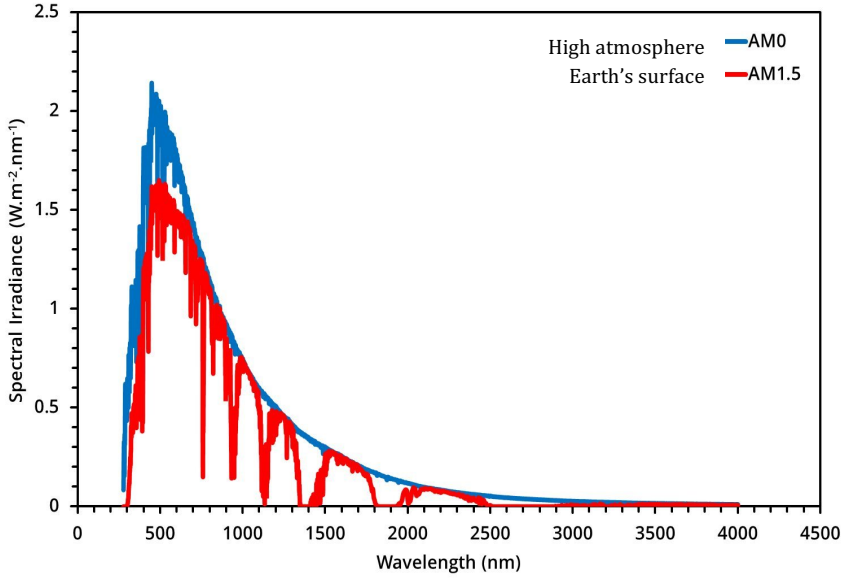

Figure 1.26: AM0 and AM1.5 solar spectrum. Data courtesy of the National Renewable Energy Laboratory, Golden, CO [118].

Solar simulators are used to replicate this AM1.5G specification in order to measure solar cell performance. Solar simulators are typically divided into three categories: continuous, flashed and pulsed. Continuous solar simulators are most commonly used to replicate between under 1 sun to several suns and typically employ a xenon arc lamp as they offer high intensities and an unfiltered spectrum that reasonably matches that of our sun. Solar simulators for photovoltaics comply with IEC 60904-9 and ASTM E927-10 standards. The light from these solar simulators is controlled in three dimensions: spectral content, spatial uniformity and temporal stability and each is classified A to C (or AAA to CCC). AAA is seen as the gold standard by which measurements are made and in order to achieve this the spectral match must not deviate from 0.75 to 1.25 times the ideal percentage in 6 spectral intervals. The irradiance spatial non-uniformity must not exceed 2% (over the working area) and temporal stability (output intensity) 2% over the agreed testing timeline. These guidelines were intended for use with silicon photovoltaics but still apply well (but not ideal) for perovskites and other thin technologies whose spectral absorption range is between 300 to 1000nm (Perovskites ~ 250- 800 nm).

1.6.1.1 Hysteresis

When measuring solar cell efficiencies from forward to reverse voltage biasing, there can be a discrepancy between the two resulting J-V scans and subsequently the calculated performances. The effect is termed Hysteresis and has been observed in silicon solar cells and dye sensitised solar cells to some degree. Perovskite solar cells are known to exhibit this effect to a greater extent, particularly when the scan speed is slowed down to the millisecond and testing periods extended while under illumination. This poses a significant risk to the long-term stability of the perovskite solar cell. In 2016, Chen et al [119] reviewed the origins of hysteresis with perovskite solar cells and drew upon research from the field that suggested the four mechanisms linked with J-V hysterias were a slow transient capacitive current, dynamic trapping and de-trapping processes of charge carriers, band bending due to ion migration, and band bending due to

ferroelectric polarization. The predominant mechanism connected to (J-V) hysteresis in perovskite solar cells has been attributed to ion migration within the perovskite layer [120]. Here ionic species (such as methylammonium and iodide species [121] are free to move throughout the perovskite film, although the exact mechanism of migration and whether through the bulk material or via grain boundaries and or interfaces can vary depending on composition and processing conditions. The main contributing factor to ion migration is the low activation energies associated with the halide ions. Mechanisms for hysteresis also postulate hopping via vacancies or via interstitial species [122]. In this scenario mobile ions moving on a millisecond to second timescale at the electrodes shield the electric field in the perovskite layer. This screening has been observed at both short circuit and open circuit voltages and causes modification in the charge extraction efficiency and recombination pathways inside the absorber layer as the photocurrent becomes dependent on the voltage scan direction. Weber et al [123] surmised J-V hysteresis is dominated by the dynamics of the formation and release of ionic charges at the interfaces based on Kelvin probe force microscopy that enables mapping charge redistribution in an operating device during an applied voltage or light pulse with sub-millisecond resolution.

It is therefore crucial that the electron and hole selective contacts are fine-tuned and engineered in such a way to reduce the effects of hysteresis at interfacial regions within the solar cell. With metal halide perovskites being somewhat ionic in nature, ionic movement within the layer itself it likely to persist in one form or another. Much progress has been made on the ETL/HTM front and such architectures employing a mesoporous TiO_2, PCBM and SnO_2 result in little to no hysteresis. In SnO_2 this is attributed to an extremely efficient electron extraction process that eliminated recombination losses [124][125]. PCBM's reduction in hysteresis was attributed to the passivation of interfacial defects and thus suppressing ion migration [126]. Hole transport materials have been shown to reduce the effects of hysteresis by fine tuning the energy levels so that band alignment between the HOMO level of the extraction layer and the valence band

of the perovskite can suppress hysteresis by evading charge accumulation at the interfaces [127].

1.6.1.2 Stabilised Power Measurements – Steady State

Hysteresis imposes problems when trying to measure the output of solar cell under equilibrium conditions (steady state) as the photocurrent and voltage can vary over time. Ideally maximum power point tracking methods are used to determine the maximum power voltage (V_{MPP}) prior to recording the steady state power output of a device. More simply, by taking a V_{MPP} measurement from a non-biased (non-preconditioned) J-V scan and holding the device at this V_{MPP} while under illumination for a given period of time (several tens of seconds or longer), and measuring the resulting photocurrent until it stabilises or plateaus can be used to determine a steady state efficiency. Close agreement between the values of the steady state measurement and the J-V scan derived efficiency gives a more valid representation of device performance under working conditions, a large divergence can indicate poor interface, bulk material properties with a strong ionic influence as reported by S. N. Habisreutinger et al [128].

1.6.2 Spectrophotometry (UV – Visible – NIR)

When considering perovskites, it's important to understand how they react to different parts of the electromagnetic spectrum – this is where Spectrophotometry comes in. By directing UV-Vis-NIR light at a sample and measuring the transmittance through it, the transmittance (T) can be used to calculate absorbance (A) as it is equal to the minus of log (T). An absorbance spectrum is obtained that shows the relative absorbance of a compound at different wavelengths which is dictated by the compounds molecular structure. When a photon is absorbed by a molecule, it's promoted into a more excited energetic state, UV-Vis-NIR wavelengths have the energy needed to promote an electron from the highest occupied molecular orbital (HOMO) to the lowest unoccupied molecular orbital (LUMO), the difference between the two is termed the band gap

and these orbitals are often referred to as the bonding and anti-bonding orbitals. Characteristic spectra are formed as different chemical structures have different energy band gaps.

Absorption follows Beer's Law:

$$A = \varepsilon b C \tag{1.5}$$

1.6.3 Cyclic Voltammetry (CV)

Cyclic voltammetry is a versatile electrochemical technique commonly used to investigate the reduction and oxidation processes of molecular species. It can also be used to study electron transfer initiated chemical reactions including catalysis. In Perovskite solar cells, electron transport layers and hole transport materials are key components to highly efficient cells. These thin films need to be uniform and homogenous; any defects or pinholes can act as sites for potential trap states and or recombination pathways that compromise the efficient extraction of charge.

Cyclic voltammetry works by applying a linearly changing voltage to an electrode, usually in the range of ±3 V from an appropriate rest potential to cover most important electrode reactions. As the applied voltage reaches that of the reversible potential for the electrode process, a small current flows. It increases rapidly but is then limited at a potential slightly beyond the standard potential (caused by a depletion of reactants as seen in chronopotentiometry). Past this point current decreases with decreasing diffusive transports available to the electrode and thus the current passes through a peak. Depending on the scan direction this is either termed the cathodic trace, also known as the forward scan where the potential is swept negatively from the starting potential (E_i) to the switching potential E_{ii}. The scan direction can then be reversed, and the potential swept positively back to E_i, and this is referred to as the anodic trace or reverse scan.

The potential sweep is represented by :

$$E = E_i - v\,T \tag{1.6}$$

Where E_i = Initial potential, T = Time, V = rate of potential change or sweep rate (v/s). The resulting shape of a cyclic voltammogram can often look like a "duck shape" and this can be related to the Nernst equation (for a one electron process):

$$E = E^0 - \frac{k\,T}{n\,e} \ln \frac{Red}{Ox} = E^{0,} - \frac{R\,T}{F} \ln \frac{Red}{Ox} \tag{1.7}$$

Where F = Faraday's constant, k = Boltzmann's constant, e = electron charge, R = universal gas constant, E^0 = standard potential, $E^{0,}$ = formula potential, n = number of electrons, T = Temperature, E = Potential of an electrochemical cell, Red = Relative activity of the reduced analyte in the system, Ox = Relative activity of the oxidised analyte in the system.

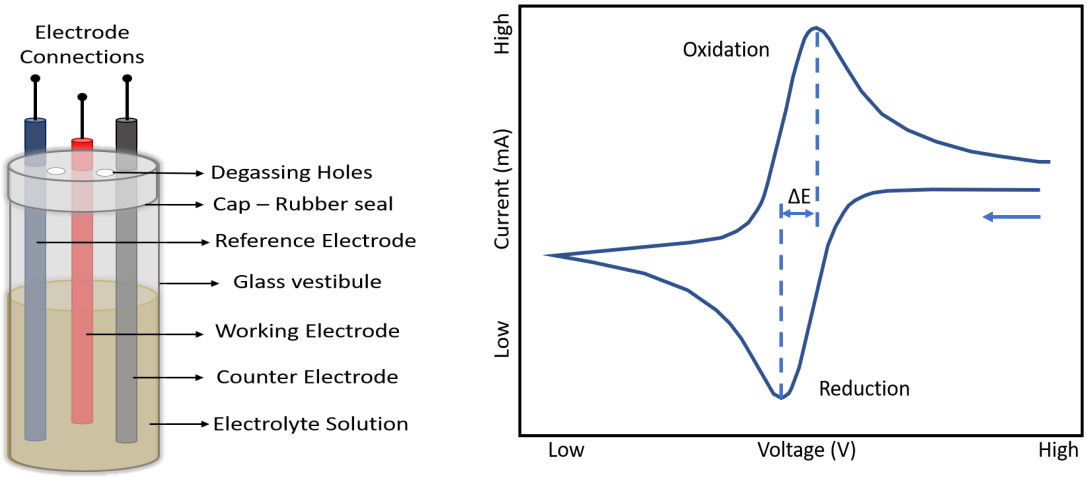

Figure 1.27: Left) A typical setup used in cyclic voltammetry, electrodes will be connected to a potentiostat and computer. Right) A typical duck shaped cyclic voltammogram.

The Nernst equation can help us to predict how a sample will respond to a change in concentration of a species in solution or a change in the electrode potential. If

the reduction process is chemically and electrochemically reversible, the difference between the cathodic and anodic peak potentials (ΔE_p) is 57 mV at room temperature and the width at half max on the forward scan of the peak is 59 mV [129][130].

The current measured (i.e. ohmic dropping) can be influenced by scan rates, faraday cages, atmosphere, electrode and electrolyte choices. These are important factors to consider when setting up a cyclic voltammetry experiment as seen in figure 1.27 along with the resulting voltammogram. Cyclic voltammetry can be employed to assess the homogenous quality of layers such as TiO_2 coated onto of a conductive substrate. Uniform, homogenous thin films with no defects/ pinholes make a rectifying interface, at which no anodic current of oxidation can occur as the material is in the depletion regime. The onset of the cathodic current reduction appears at the potentials negative to the flat band potential, Φ_{FB}, when the material is in the accumulation regime, i.e. displaying a metallic behaviour. Defects such as pinholes, cracks and voids etc can be detected with a high degree of accuracy and precision with nanometre resolution when the selection of appropriate sweeping voltages, electrolyte composition and electrode selection is optimal. Oxidation occurs at bare or exposed conductive surfaces such as the TCO. At these regions an anodic current is produced and by using a potentiostat, even minute currents can be measured and displayed on the cyclic voltammogram thus highlighting potential pinhole/defects etc. [131][132].

1.6.4 Transient Photovoltage Measurements

Transient photovoltage measurements (TPV) is a technique often employed to determine charge carrier lifetimes generated by the photovoltaic effect in thin film solar cells. This lifetime is often incident light intensity dependant and by coupling this with charge extraction measurements to determine photocurrent charge density, the resulting recombination rate constant and its order can be obtained.

TPV works by placing a semiconducting material between two extracting electrodes (FTO and gold being common in solar cells). By using a background LED to provide a background illumination to give a steady state V_{OC} (this measurement is usually performed over a range of different background light intensities to ensure accuracy) and a short-pulsed laser diode (in the order of femtosecond or nanoseconds) to generate excess charge carriers in the sample. These excess charge carriers are extracted by the sandwiching electrodes and the resulting increase in voltage (V_{OC}) is detected using an oscilloscope in the form of a voltage across a resistor. The oscilloscope records what is termed the transient and typically has a 1 MΩ input resistance which holds the sample at open circuit. An InGaN source (520 nm and 100 ns^{-1}) is used and the short pulse is generated via a function generator that gives a square wave that simulates "on off" (0 to 5 Volts applied to the cell) conditions. When the laser pulse is switched off the excess charge carriers recombine, and the decay is fitted by an exponential function (with perovskites this usually takes the form of a single exponential time constant) where the time constant usually relates to the electron lifetime. It is important to note that although recombination can be measured, electron transport occurs too quickly to be measured via TPV. An example of an annotated TPV sample can be seen in figure 1.28.

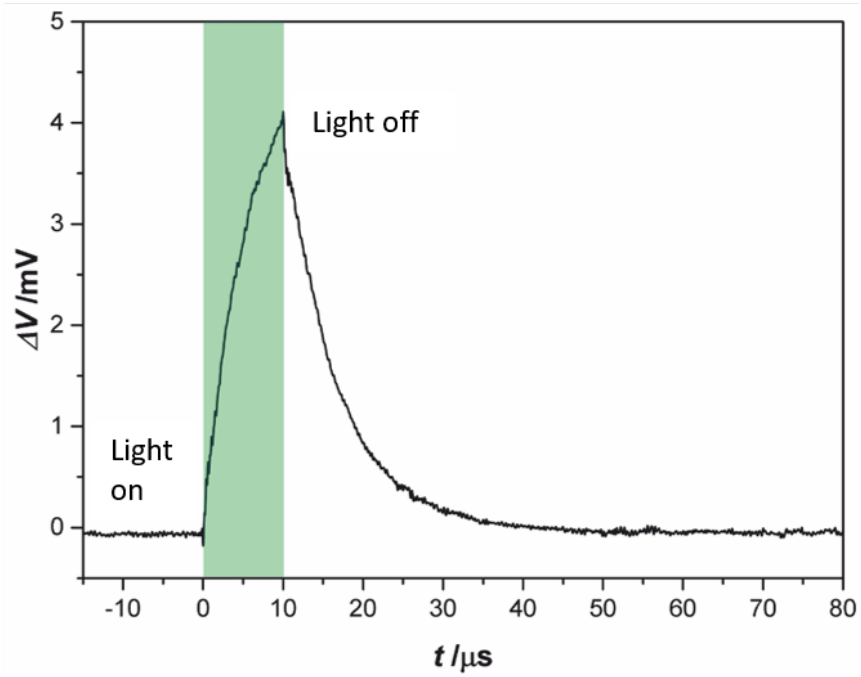

Figure 1.28: Typical plot of a transient photovoltage measurement where the laser pulse is denoted in the off and on regime.

1.7 Stability

To date the most challenging aspect of commercialising perovskite solar cells revolves around the stability of the material itself and the architectures employed in its fabrication. Now that efficiencies and processing techniques have seen much improvement in a relatively short space of time the last hurdle to clear is that of stability if perovskites are to compete in a crowded photovoltaics market. Whether perovskites are configured in planar, mesoporous structure, n-i-p or p-i-n all are prone to degradation in severe environments. Parameter know to have detrimental consequences include exposure to thermal stress at elevated temperatures, oxidation, illumination, the effects of ion migration, UV degradation and lastly excess humidity [133]. Nearly all of the mechanisms related to the instability of perovskites can be linked to ion migration within the perovskite material and at the interfaces of the p and n type contacts. The component largely associated with this movement is the small halide ions in perovskites, namely the iodides which features in most perovskites solar cell architectures. Low activation energies mean the requirements for ion migration can be met by the aforementioned degradation mechanisms. Although humidity has been reported to be beneficial when fabricating devices in a controlled environment, leading to yield enhancement and beneficial perovskite crystal formation and growth. Excess humidity, leads to degradation due to ion migration and phase separation [93]. Excess humidity and moisture ingress after fabrication results in a degradation of the crystallinity of the prepared films and hence most fabrication is carried out under dry atmospheric conditions [134].

This moisture instability is due to the hygroscopic nature of the amine salt used in the preparation of most perovskite materials. The commonly reported MAPI (methyl ammonium lead triiodide) perovskite and its derivatives that incorporate other halides (usually chlorine and bromine) show a degradation

process where the methylamine sublimates, and PbI_2 is formed, thus destroying the ABX_3 crystal structure and the resulting film appears yellow [135]. Other hydration products such as $(CH3NH3)_4PbI_6.2H_2O$ have also been reported. The process through which this occurs has been linked to the hydrogen bond between organic and inorganic units in the perovskite being strongly affected by the high polarity of water molecules [136]. The presence of oxygen and moisture leads to a further breakdown of the methylammonium group to form hydrogen iodide which further reacts with oxygen to form hydrogen gas and free iodide. The organic cation is entirely consumed as the degradation process progresses [137][138]. This has led to considerable research to engineer perovskite chemistries with variants such as formamidinium and caesium to replace the relatively unstable methylammonium group. A promising development in the long-term stability of the perovskite absorber material has been combination of stable 2D and 3D structures. Architectures and materials that show higher tolerances to oxygen, UV light, thermal stress and moisture degradation will be necessary for successful commercialisation. In addition, more effective methods of hermetic sealing of perovskite devices to protect them from severe environments to prolong device lifetimes will be key to commercial success [139][140][141][142][143][144][145][146].

Solar cells require a thermal stability of at least 85 °C (0.0093 eV) under standard working conditions (IEC 61656 climatic chamber tests) [147]. The decomposition of MAPI based perovskite has been established between 100 and 140 °C. The organic methyl ammonium (MA) component is cited as the initiation point for thermal degradation where it decomposes to form lead iodide and hydrogen gas. These products further accelerate decomposition process. Other mechanisms of thermal decomposition suggest it initiates at grain boundaries has been reported in the literature [148][149]. It has also been shown that sustained annealing of perovskite (MAPI) even in inert (N_2) atmospheres for a period of only 24 hours was sufficient to induce the organic decomposition of MA as the formation energy of MAPI is 0.11 - 0.14 eV, close to that of the required 0.093 eV for thermal stability under normal working conditions [150]. It has also been reported that the tetragonal structure of $CH_3NH_3PbI_3$ will undergo a phase

transition to a cubic structure at temperatures of around 330K. This temperature could be exceeded under real world operating conditions and thus casts considerable concern about the stability of this Perovskites at elevated temperatures. [151]. To negate this, various studies into thermally resistant compositions of perovskite have yielded materials with relatively high thermal stability. This has been achieved by removing or replacing the organic components with more thermally stable inorganic materials such as formamidinium lead iodide (bandgap 1.48 eV). Thermal stability has been further enhanced with the additions of various halides and substitutions ions such as rubidium into the perovskite composition [27][152].

Decomposition via ultraviolet light exposure is a common mechanism for failure in most solar cell technologies. Photogenerated electrons can combine with oxygen present to form superoxide's, which can then react with the organic components in perovskites (methylammonium) to degrade the film [153]. Again, organic substitution (methyl ammonium free perovskite) has been reported as solutions to this issue [154] .

It is also important to consider the stability of the other materials and or structures and interfaces (selective contacts; ETL, HTM, and electrodes like gold and FTO, ITO) when designing a perovskite solar cell in order to ensure excellent cell lifetimes with minimal drop-offs in power conversion efficiency. Materials like the dopants in Spiro-MeOTAD, UV stability of TiO_2 and metal ion migration in contact electrodes are prime examples in this case that has been addressed in literature with inorganic p type semiconductors (HTM) like copper thiocyanate, chemically and thermally stable graphene contacts and UV stable SnO_2 ETLs. [155][156] [157].

1.8 References/ Bibliography

[1] D. B. Botkin *et al.*, "Forecasting effects of global warming on Biodiversity,"

Bioscience, vol. 57, no. 3, pp. 227–236, 2007.

[2] P. M. Vitousek, “Beyond global warming: ecology and global change,” *Ecology*, vol. 75, no. 7, pp. 1861–1876, 1994.

[3] J. Tsao, N. Lewis, and G. Crabtree, “Solar FAQs,” *US Dep. Energy*, pp. 1–24, 2006.

[4] K. A. Tsokos, *Physics for the IB Diploma*. Cambridge: Cambridge University Press, 2010.

[5] F. Huang, M. Li, P. Siffalovic, G. Cao, and J. Tian, “From scalable solution fabrication of perovskite films towards commercialization of solar cells,” *Energy Environ. Sci.*, pp. 0–66, 2019.

[6] B. O’Regan and M. Grätzel, “A low-cost, high-efficiency solar cell based on dye-sensitized colloidal TiO2 films,” *Nature*, vol. 353, pp. 737–740, 1991.

[7] M. Green, K. Emery, Y. Hishikawa, W. Warta, and E. Dunlop, “Solar Cells efficiency tables 42,” *Prog. Photovolt Res. Appl.*, 2013.

[8] K. Hara and H. Arakawa, *Handbook of Photovoltaic Science and Engineering*. Chichester, UK: John Wiley & Sons, Ltd, 2003.

[9] M.-H. Li, J.-H. Yum, S.-J. Moon, and P. Chen, “Inorganic p-Type Semiconductors: Their Applications and Progress in Dye-Sensitized Solar Cells and Perovskite Solar Cells,” *Energies*, vol. 9, no. 5, p. 331, Apr. 2016.

[10] U. Bach *et al.*, “Solid-state dye-sensitized mesoporous TiO2 solar cells with high photon-to-electron conversion efficiencies,” *Nature*, vol. 395, no. 6702, pp. 583–585, Oct. 1998.

[11] Y. Cao *et al.*, “11% efficiency solid-state dye-sensitized solar cells with copper(II/I) hole transport materials,” *Nat. Commun.*, vol. 8, no. 1, p. 15390, Aug. 2017.

[12] C. Helbig, A. M. Bradshaw, C. Kolotzek, A. Thorenz, and A. Tuma, “Supply risks associated with CdTe and CIGS thin-film photovoltaics,” *Appl. Energy*, vol. 178, pp. 422–433, Sep. 2016.

[13] NREL, “http: // www. nrel. gov/ ncpv/ images/ efficiency_chart,” 2019. .

[14] J. D. M. Tom Baines, Thomas P. Shalvey, *A Comprehensive Guide to Solar*

Energy Systems. Elsevier, 2018.

[15] J. Liang, E. A. Schiff, S. Guha, B. Yan, and J. Yang, "Hole-mobility limit of amorphous silicon solar cells," *Appl. Phys. Lett.*, vol. 88, no. 6, p. 063512, Feb. 2006.

[16] R. C. Chittick, J. H. Alexander, and H. F. Sterling, "The Preparation and Properties of Amorphous Silicon," *J. Electrochem. Soc.*, vol. 116, no. 1, p. 77, 1969.

[17] A. Kojima, K. Teshima, Y. Shirai, and T. Miyasaka, "Novel Photoelectrochemical Cell with Mesoscopic Electrodes Sensitized by Lead-halide Compounds (11)," *Meet. Abstr. Electrochem. Soc.*, vol. MA2008-02, no. 1, p. 27, 2008.

[18] A. Kojima, K. Teshima, Y. Shirai, and T. Miyasaka, "Organometal Halide Perovskites as Visible-Light Sensitizers for Photovoltaic Cells," *J. Am. Chem. Soc.*, vol. 131, no. 17, pp. 6050–6051, May 2009.

[19] J.-H. Im, C.-R. Lee, J.-W. Lee, S.-W. Park, and N.-G. Park, "6.5% efficient perovskite quantum-dot-sensitized solar cell," *Nanoscale*, vol. 3, no. 10, p. 4088, 2011.

[20] H.-S. Kim *et al.*, "Lead Iodide Perovskite Sensitized All-Solid-State Submicron Thin Film Mesoscopic Solar Cell with Efficiency Exceeding 9%," *Sci. Rep.*, vol. 2, no. 1, p. 591, Dec. 2012.

[21] M. M. Lee, J. Teuscher, T. Miyasaka, T. N. Murakami, and H. J. Snaith, "Efficient hybrid solar cells based on meso-superstructured organometal halide perovskites.," *Science*, vol. 338, no. 6107, pp. 643–7, Nov. 2012.

[22] D. Burkitt, J. Searle, D. A.Worsley, and T. Watson, "Sequential slot-die deposition of perovskite solar cells using dimethylsulfoxide lead iodide ink," *Materials (Basel).*, 2018.

[23] D. Di Girolamo *et al.*, "Dual effect of humidity on cesium lead bromide: enhancement and degradation of perovskite films," *J. Mater. Chem. A*, vol. 7, no. 19, pp. 12292–12302, 2019.

[24] Z. Ku, Y. Rong, M. Xu, T. Liu, and H. Han, "Full Printable Processed Mesoscopic CH3NH3PbI3/TiO2 Heterojunction Solar Cells with Carbon

Counter Electrode," *Sci. Rep.*, vol. 3, no. 1, p. 3132, Dec. 2013.

[25] N. J. Jeon, J. H. Noh, Y. C. Kim, W. S. Yang, S. Ryu, and S. Il Seok, "Solvent engineering for high-performance inorganic–organic hybrid perovskite solar cells," *Nat. Mater.*, vol. 13, no. 9, pp. 897–903, Sep. 2014.

[26] M. Saliba *et al.*, "Cesium-containing triple cation perovskite solar cells: improved stability, reproducibility and high efficiency," *Energy Environ. Sci.*, vol. 9, no. 6, pp. 1989–1997, 2016.

[27] T. Matsui *et al.*, "Effect of Rubidium for Thermal Stability of Triple-cation Perovskite Solar Cells," *Chem. Lett.*, vol. 47, no. 6, pp. 814–816, Jun. 2018.

[28] J.-W. Lee, D.-H. Kim, H.-S. Kim, S.-W. Seo, S. M. Cho, and N.-G. Park, "Formamidinium and Cesium Hybridization for Photo- and Moisture-Stable Perovskite Solar Cell," *Adv. Energy Mater.*, vol. 5, no. 20, p. 1501310, Oct. 2015.

[29] I. Benabdallah, M. Boujnah, A. El Kenz, A. Benyoussef, M. Abatal, and A. Bassam, "Lead-free perovskite based bismuth for solar cells absorbers," *J. Alloys Compd.*, vol. 773, pp. 796–801, Jan. 2019.

[30] Oxford PV ltd., "The perovskite-silicon tandem," *The perovskite-silicon tandem*, 2019. [Online]. Available: https://www.oxfordpv.com/perovskite-silicon-tandem.

[31] L. K. Ono, N.-G. Park, K. Zhu, W. Huang, and Y. Qi, "Perovskite Solar Cells—Towards Commercialization," *ACS Energy Lett.*, 2017.

[32] P. Gerhardinger and D. Strickler, "Fluorine Doped Tin Oxide Coatings - Over 50 Years and Going Strong," *Key Engineering Materials*, vol. 380. pp. 169–178, 2008.

[33] G. Yang, H. Tao, P. Qin, W. Ke, and G. Fang, "Recent progress in electron transport layers for efficient perovskite solar cells," *J. Mater. Chem. A*, vol. 4, no. 11, pp. 3970–3990, 2016.

[34] M. J. Carnie *et al.*, "A one-step low temperature processing route for organolead halide perovskite solar cells.," *Chem. Commun. (Camb).*, vol. 49, no. 72, pp. 7893–5, 2013.

[35] J. F. Banfield, B. L. Bischoff, and M. a. Anderson, “TiO2 accessory minerals: coarsening, and transformation kinetics in pure and doped synthetic nanocrystalline materials,” *Chem. Geol.*, vol. 110, no. 1–3, pp. 211–231, 1993.

[36] N. G. Park, “Organometal Perovskite Light Absorbers Toward a 20% Efficiency Low-Cost Solid-State Mesoscopic Solar Cell,” *J. Phys. Chem. Lett.*, vol. 4, no. 15, pp. 2423–2429, 2013.

[37] Q. Dong *et al.*, “Insight into Perovskite Solar Cells Based on SnO 2 Compact Electron-Selective Layer,” *J. Phys. Chem. C*, vol. 119, no. 19, pp. 10212–10217, May 2015.

[38] H.-S. Rao *et al.*, “Improving the Extraction of Photogenerated Electrons with SnO 2 Nanocolloids for Efficient Planar Perovskite Solar Cells,” *Adv. Funct. Mater.*, vol. 25, no. 46, pp. 7200–7207, Dec. 2015.

[39] A. J. Nozik and R. Memming, “Physical Chemistry of Semiconductor–Liquid Interfaces,” *J. Phys. Chem.*, vol. 100, no. 31, pp. 13061–13078, Jan. 1996.

[40] L. Huang *et al.*, “UV-Sintered Low-Temperature Solution-Processed SnO 2 as Robust Electron Transport Layer for Efficient Planar Heterojunction Perovskite Solar Cells,” *ACS Appl. Mater. Interfaces*, vol. 9, no. 26, pp. 21909–21920, Jul. 2017.

[41] K.-H. Jung, J.-Y. Seo, S. Lee, H. Shin, and N.-G. Park, “Solution-processed SnO 2 thin film for a hysteresis-free planar perovskite solar cell with a power conversion efficiency of 19.2%,” *J. Mater. Chem. A*, vol. 5, no. 47, pp. 24790–24803, 2017.

[42] W. Ke *et al.*, “Cooperative tin oxide fullerene electron selective layers for high-performance planar perovskite solar cells,” *J. Mater. Chem. A*, vol. 4, no. 37, pp. 14276–14283, 2016.

[43] J. T.-W. Wang *et al.*, “Low-Temperature Processed Electron Collection Layers of Graphene/TiO 2 Nanocomposites in Thin Film Perovskite Solar Cells,” *Nano Lett.*, vol. 14, no. 2, pp. 724–730, Feb. 2014.

[44] J. Xie *et al.*, “Enhanced Electronic Properties of SnO 2 via Electron

Transfer from Graphene Quantum Dots for Efficient Perovskite Solar Cells," *ACS Nano*, vol. 11, no. 9, pp. 9176–9182, Sep. 2017.

[45] L.-C. Chen and Z.-L. Tseng, "ZnO-Based Electron Transporting Layer for Perovskite Solar Cells," in *Nanostructured Solar Cells*, InTech, 2017.

[46] D. Liu and T. L. Kelly, "Perovskite solar cells with a planar heterojunction structure prepared using room-temperature solution processing techniques," *Nat. Photonics*, vol. 8, no. February, pp. 133–138, 2014.

[47] Q. Gao *et al.*, "An Effective TiO₂ Blocking Layer for Perovskite Solar Cells with Enhanced Performance," *Chem. Lett.*, vol. 44, no. 5, pp. 624–626, 2015.

[48] a. M. Peiró, J. Peral, C. Domingo, X. Domènech, and J. a. Ayllón, "Low-temperature deposition of TiO2 thin films with photocatalytic activity from colloidal anatase aqueous solutions," *Chem. Mater.*, vol. 13, no. 8, pp. 2567–2573, 2001.

[49] B. Smith *et al.*, "Mass Manufactured Glass Substrates Incorporating Prefabricated Electron Transport Layers for Perovskite Solar Cells," *Adv. Mater. Interfaces*, 2019.

[50] J. Jang, S. H. Hwang, J. Roh, J. Lee, J. Ryu, and J. Yun, "Size-controlled SiO2 nanoparticles as scaffold layers in thin-film perovskite solar cells," *J. Mater. Chem. A*, p. Ahead of Print, 2014.

[51] O. Malinkiewicz *et al.*, "Perovskite solar cells employing organic charge-transport layers," *Nat. Photonics*, vol. 8, no. 2, pp. 128–132, Feb. 2014.

[52] J. T. W. Wang *et al.*, "Low-temperature processed electron collection layers of graphene/TiO 2 nanocomposites in thin film perovskite solar cells," *Nano Lett.*, vol. 14, no. 2, pp. 724–730, 2014.

[53] D. Ramirez *et al.*, "Meso-Superstructured Perovskite Solar Cells: Revealing the Role of the Mesoporous Layer," *J. Phys. Chem. C*, 2018.

[54] A. Matas Adams, J. M. Marin-Beloqui, G. Stoica, and E. Palomares, "The influence of the mesoporous TiO 2 scaffold on the performance of methyl ammonium lead iodide (MAPI) perovskite solar cells: charge injection, charge recombination and solar cell efficiency relationship," *J. Mater.*

Chem. A, vol. 3, no. 44, pp. 22154–22161, 2015.

[55] U. A. Joshi, J. S. Jang, P. H. Borse, and J. S. Lee, “Microwave synthesis of single-crystalline perovskite BiFeO3 nanocubes for photoelectrode and photocatalytic applications,” *Appl. Phys. Lett.*, 2008.

[56] M. O. Jarligo, D. E. Mack, R. Vassen, and D. Stöver, “Application of plasma-sprayed complex perovskites as thermal barrier coatings,” in *Journal of Thermal Spray Technology*, 2009.

[57] J. G. Bednorz and K. A. M□ller, “Possible highT c superconductivity in the Ba?La?Cu?O system,” *Zeitschrift f□r Phys. B Condens. Matter*, vol. 64, no. 2, pp. 189–193, Jun. 1986.

[58] W. Zhang, G. E. Eperon, and H. J. Snaith, “Metal halide perovskites for energy applications,” *Nature Energy*. 2016.

[59] J. Will *et al.*, “Evidence of Tailoring the Interfacial Chemical Composition in Normal Structure Hybrid Organohalide Perovskites by a Self-Assembled Monolayer,” *ACS Appl. Mater. Interfaces*, vol. 10, no. 6, pp. 5511–5518, Feb. 2018.

[60] S. D. Stranks *et al.*, “Electron-hole diffusion lengths exceeding 1 micrometer in an organometal trihalide perovskite absorber.,” *Science*, vol. 342, no. 6156, pp. 341–344, 2013.

[61] G. Xing *et al.*, “Long-Range Balanced Electron- and Hole-Transport Lengths in Organic-Inorganic CH3NH3PbI3,” *Science (80-.).*, vol. 342, no. 6156, pp. 344–347, Oct. 2013.

[62] S. Ravishankar *et al.*, “Influence of Charge Transport Layers on Open-Circuit Voltage and Hysteresis in Perovskite Solar Cells,” *Joule*, vol. 2, no. 4, pp. 788–798, Apr. 2018.

[63] I. Mora-Seró, “How Do Perovskite Solar Cells Work?,” *Joule*, vol. 2, no. 4, pp. 585–587, Apr. 2018.

[64] E. M. Barea *et al.*, “Energetic factors governing injection, regeneration and recombination in dye solar cells with phthalocyanine sensitizers,” *Energy Environ. Sci.*, vol. 3, no. 12, p. 1985, 2010.

[65] Y. Tidhar *et al.*, “Crystallization of Methyl Ammonium Lead Halide Perovskites: Implications for Photovoltaic Applications,” *J. Am. Chem. Soc.*, vol. 136, no. 38, pp. 13249–13256, Sep. 2014.

[66] W. Zhang *et al.*, “Ultrasmooth organic-inorganic perovskite thin-film formation and crystallization for efficient planar heterojunction solar cells,” *Nat Commun*, vol. 6, p. 6142, 2015.

[67] D. T. Moore *et al.*, “Crystallization Kinetics of Organic–Inorganic Trihalide Perovskites and the Role of the Lead Anion in Crystal Growth,” *J. Am. Chem. Soc.*, vol. 137, no. 6, pp. 2350–2358, Feb. 2015.

[68] A. Buin *et al.*, “Materials processing routes to trap-free halide perovskites,” *Nano Lett*, vol. 14, no. 11, pp. 6281–6286, 2014.

[69] S. T. Williams, F. Zuo, C. C. Chueh, C. Y. Liao, P. W. Liang, and A. K. Jen, “Role of chloride in the morphological evolution of organo-lead halide perovskite thin films,” *ACS Nano*, vol. 8, no. 10, pp. 10640–10654, 2014.

[70] N. Kitazawa, Y. Watanabe, and Y. Nakamura, “Optical properties of CH 3 NH 3 PbX 3 (X = halogen) and their mixed-halide crystals,” *J. Mater. Sci.*, vol. 7, pp. 3585–3587, 2002.

[71] E. Mosconi, A. Amat, M. K. Nazeeruddin, M. Grätzel, and F. De Angelis, “First-principles modeling of mixed halide organometal perovskites for photovoltaic applications,” *J. Phys. Chem. C*, vol. 117, no. 27, pp. 13902–13913, 2013.

[72] S. D. Stranks and H. J. Snaith, “Metal-halide perovskites for photovoltaic and light-emitting devices,” *Nat. Nanotechnol.*, vol. 10, no. 5, pp. 391–402, 2015.

[73] W. S. Yang *et al.*, “High-performance photovoltaic perovskite layers fabricated through intramolecular exchange,” *Science (80-.).*, p. science.aaa9272-, 2015.

[74] G. E. Eperon, S. D. Stranks, C. Menelaou, M. B. Johnston, L. M. Herz, and H. J. Snaith, “Formamidinium lead trihalide: a broadly tunable perovskite for efficient planar heterojunction solar cells,” *Energy Environ. Sci.*, vol. 7, no. 3, p. 982, 2014.

[75] F. C. Hanusch *et al.*, “Efficient Planar Heterojunction Perovskite Solar Cells Based on Formamidinium Lead Bromide,” *J. Phys. Chem. Lett.*, p. 140724113526001, 2014.

[76] W. Ke and M. G. Kanatzidis, “Prospects for low-toxicity lead-free perovskite solar cells,” *Nat. Commun.*, vol. 10, no. 1, p. 965, Dec. 2019.

[77] F. Hao, C. C. Stoumpos, D. H. Cao, R. P. H. Chang, and M. G. Kanatzidis, “Lead-free solid-state organic–inorganic halide perovskite solar cells,” *Nat. Photonics*, vol. 8, no. 6, pp. 489–494, Jun. 2014.

[78] C. C. Stoumpos, C. D. Malliakas, and M. G. Kanatzidis, “Semiconducting Tin and Lead Iodide Perovskites with Organic Cations: Phase Transitions, High Mobilities, and Near-Infrared Photoluminescent Properties,” *Inorg. Chem.*, vol. 52, no. 15, pp. 9019–9038, Aug. 2013.

[79] B. Vargas, E. Ramos, E. Pérez-Gutiérrez, J. C. Alonso, and D. Solis-Ibarra, “A Direct Bandgap Copper–Antimony Halide Perovskite,” *J. Am. Chem. Soc.*, vol. 139, no. 27, pp. 9116–9119, Jul. 2017.

[80] C. C. Stoumpos *et al.*, “Hybrid Germanium Iodide Perovskite Semiconductors: Active Lone Pairs, Structural Distortions, Direct and Indirect Energy Gaps, and Strong Nonlinear Optical Properties,” *J. Am. Chem. Soc.*, vol. 137, no. 21, pp. 6804–6819, Jun. 2015.

[81] Oscilla, “Spin coating_ a guide to theory and techniques – Ossila.” [Online]. Available: http://www.ossila.com/pages/spin-coating?gclid=Cj0KEQiA496zBRDoi5OY3p2xmaUBEiQArLNnK9t4ZNydBJ1CHOvcrQaSjRuJ3mic63CMm_tCTBbk3rUaAvJK8P8HAQ.

[82] M. Xiao *et al.*, “Selection of an anti-solvent for efficient and stable cesium-containing triple cation planar perovskite solar cells,” *Nanoscale*, vol. 10, no. 25, pp. 12141–12148, 2018.

[83] L.-C. Chen, C.-C. Chen, J.-C. Chen, and C.-G. Wu, “Annealing effects on high-performance CH 3 NH 3 PbI 3 perovskite solar cells prepared by solution-process,” *Sol. Energy*, vol. 122, pp. 1047–1051, Dec. 2015.

[84] G. E. Eperon, V. M. Burlakov, P. Docampo, A. Goriely, and H. J. Snaith, “Morphological Control for High Performance, Solution-Processed Planar

Heterojunction Perovskite Solar Cells," *Adv. Funct. Mater.*, vol. 24, no. 1, pp. 151–157, Jan. 2014.

[85] J. Troughton, C. Charbonneau, M. J. Carnie, M. L. Davies, D. A. Worsley, and T. M. Watson, "Rapid processing of perovskite solar cells in under 2.5 seconds," *J. Mater. Chem. A*, vol. 3, no. 17, pp. 9123–9127, 2015.

[86] J. Troughton *et al.*, "Photonic flash-annealing of lead halide perovskite solar cells in 1 ms," *J. Mater. Chem. A*, vol. 4, no. 9, pp. 3471–3476, 2016.

[87] J. Burschka *et al.*, "Sequential deposition as a route to high-performance perovskite-sensitized solar cells.," *Nature*, vol. 499, no. 7458, pp. 316–9, 2013.

[88] B. R. Sutherland *et al.*, "Perovskite Thin Films via Atomic Layer Deposition," *Adv. Mater.*, vol. 27, no. 1, pp. 53–58, 2014.

[89] F. Fu *et al.*, "Low-temperature-processed efficient semi-transparent planar perovskite solar cells for bifacial and tandem applications," *Nat. Commun.*, vol. 6, no. 1, p. 8932, Dec. 2015.

[90] M. Liu, M. B. Johnston, and H. J. Snaith, "Efficient planar heterojunction perovskite solar cells by vapour deposition.," *Nature*, vol. 501, no. 7467, pp. 395–8, 2013.

[91] Q. Hu *et al.*, "P3HT/Phthalocyanine Nanocomposites as Efficient Hole-Transporting Materials for Perovskite Solar Cells," *Sol. RRL*, vol. 3, no. 1, p. 1800264, Jan. 2019.

[92] A. M.-O. and N. M. Javier Urieta-Mora, Ines Garcia-Benito, "Hole transporting materials for perovskite solar cells: a chemical approach," *Chem. Soc. Rev.*, vol. 11, no. 2, p. P003, 1982.

[93] H. Zhou *et al.*, "Interface engineering of highly efficient perovskite solar cells," *Science (80-.).*, vol. 345, no. 6196, pp. 542–546, 2014.

[94] W. Zhang *et al.*, "Single crystal structure and opto-electronic properties of oxidized Spiro-OMeTAD," *Chem. Commun.*, vol. 56, no. 10, pp. 1589–1592, 2020.

[95] M. Li, P. Shen, K. Wang, T. Guo, and P. Chen, "Inorganic p-type contact

materials for perovskite- based solar cells," *J. Mater. Chem. A Mater. energy Sustain.*, vol. 00, pp. 1–9, 2015.

[96] M. K. Nazeeruddin *et al.*, "Conversion of Light to Electricity by SCN-) on Nanocrystalline Ti02 Electrodes," *J. Am. Chem. Soc.*, vol. 115, no. 4, pp. 6382–6390, 1993.

[97] H. J. Snaith, A. J. Moule, C. Klein, K. Meerholz, R. H. Friend, and M. Grätzel, "Efficiency enhancements in solid-state hybrid solar cells via reduced charge recombination and increased light capture.," *Nano Lett.*, vol. 7, no. 11, pp. 3372–6, 2007.

[98] M. Grätzel, "Recent advances in sensitized mesoscopic solar cells," *Acc. Chem. Res.*, vol. 42, no. 11, pp. 1788–1798, 2009.

[99] K. Domanski *et al.*, "Not All That Glitters Is Gold: Metal-Migration-Induced Degradation in Perovskite Solar Cells," *ACS Nano*, vol. 10, no. 6, pp. 6306–6314, Jun. 2016.

[100] J. Troughton *et al.*, "solar cells employing metallic substrates †," *J. Mater. Chem. A Mater. energy Sustain.*, vol. 3, pp. 9141–9145, 2015.

[101] S. Chattopadhyay *et al.*, "Quantification of PV Module Discoloration Using Visual Image Analysis," in *2017 IEEE 44th Photovoltaic Specialist Conference (PVSC)*, 2017, pp. 1850–1854.

[102] F. Fu *et al.*, "High-efficiency inverted semi-transparent planar perovskite solar cells in substrate configuration," *Nat. Energy*, vol. 2, no. 1, p. 16190, Jan. 2017.

[103] C. D. Bailie *et al.*, "Semi-transparent perovskite solar cells for tandems with silicon and CIGS," *Energy Environ. Sci.*, vol. 8, no. 3, pp. 956–963, 2015.

[104] Z. Li *et al.*, "Laminated Carbon Nanotube Networks for Metal Electrode-Free Efficient Perovskite Solar Cells," *ACS Nano*, vol. 8, no. 7, pp. 6797–6804, Jul. 2014.

[105] F. Jiang *et al.*, "Metal electrode–free perovskite solar cells with transfer-laminated conducting polymer electrode," *Opt. Express*, vol. 23, no. 3, p. A83, Feb. 2015.

[106] F. Lang *et al.*, “Perovskite Solar Cells with Large-Area CVD-Graphene for Tandem Solar Cells,” *J. Phys. Chem. Lett.*, vol. 6, no. 14, pp. 2745–2750, Jul. 2015.

[107] C. O. Ramírez Quiroz, C. Bronnbauer, I. Levchuk, Y. Hou, C. J. Brabec, and K. Forberich, “Coloring Semitransparent Perovskite Solar Cells via Dielectric Mirrors,” *ACS Nano*, vol. 10, no. 5, pp. 5104–5112, May 2016.

[108] Decc, “UK Solar PV Strategy Part 1: Roadmap to a Brighter Future,” no. October, pp. 1–38, 2013.

[109] K. Hwang *et al.*, “Toward large scale roll-to-roll production of fully printed perovskite solar cells,” *Adv. Mater.*, vol. 27, no. 7, pp. 1241–1247, 2015.

[110] DECC, “UK solar PV strategy part 2 : Delivering a brighter future,” *Dep. energy Clim. Chang.*, 2014.

[111] I. A. Howard *et al.*, “Coated and Printed Perovskites for Photovoltaic Applications,” *Adv. Mater.*, p. 1806702, Apr. 2019.

[112] J. E. Bishop, T. J. Routledge, and D. G. Lidzey, “Advances in Spray-Cast Perovskite Solar Cells,” *J. Phys. Chem. Lett.*, vol. 9, no. 8, pp. 1977–1984, Apr. 2018.

[113] Z. Wei, H. Chen, K. Yan, and S. Yang, “Inkjet Printing and Instant Chemical Transformation of a CH 3 NH 3 PbI 3 /Nanocarbon Electrode and Interface for Planar Perovskite Solar Cells,” *Angew. Chemie Int. Ed.*, vol. 53, no. 48, pp. 13239–13243, Nov. 2014.

[114] S. Tang *et al.*, “Composition Engineering in Doctor-Blading of Perovskite Solar Cells,” *Adv. Energy Mater.*, vol. 7, no. 18, p. 1700302, Sep. 2017.

[115] G. Mincuzzi, A. L. Palma, A. Di Carlo, and T. M. Brown, “Laser Processing in the Manufacture of Dye-Sensitized and Perovskite Solar Cell Technologies,” *ChemElectroChem*, vol. 3, no. 1, pp. 9–30, Jan. 2016.

[116] Z. Bi *et al.*, “Defect tolerant perovskite solar cells from blade coated non-toxic solvents,” *J. Mater. Chem. A*, vol. 6, no. 39, pp. 19085–19093, 2018.

[117] Oscilla, “Solar Cells : A Guide to Theory and Measurement,” 2018. [Online]. Available: https://www.ossila.com/pages/solar-cells-

theory?fbclid=IwAR0oTqeF4Nk01oEF_AOz3WVh48zNNKqCuBspWS6DA4ka-OwOFoWt6NbYBIE#first.

[118] NREL, "Reference Air Mass 1.5 Spectra," *Grid Modernization*, 2019. [Online]. Available: https://www.nrel.gov/grid/solar-resource/spectra-am1.5.html.

[119] B. Chen, M. Yang, S. Priya, and K. Zhu, "Origin of J-V Hysteresis in Perovskite Solar Cells," *Journal of Physical Chemistry Letters*. 2016.

[120] W. Tress, "Metal Halide Perovskites as Mixed Electronic–Ionic Conductors: Challenges and Opportunities—From Hysteresis to Memristivity," *J. Phys. Chem. Lett.*, vol. 8, no. 13, pp. 3106–3114, Jul. 2017.

[121] J. L. Minns, P. Zajdel, D. Chernyshov, W. van Beek, and M. A. Green, "Structure and interstitial iodide migration in hybrid perovskite methylammonium lead iodide," *Nat. Commun.*, vol. 8, no. 1, p. 15152, Aug. 2017.

[122] Y. Yuan and J. Huang, "Ion Migration in Organometal Trihalide Perovskite and Its Impact on Photovoltaic Efficiency and Stability," *Acc. Chem. Res.*, vol. 49, no. 2, pp. 286–293, Feb. 2016.

[123] S. A. L. Weber *et al.*, "How the formation of interfacial charge causes hysteresis in perovskite solar cells," *Energy Environ. Sci.*, vol. 11, no. 9, pp. 2404–2413, 2018.

[124] Q. Jiang, X. Zhang, and J. You, "SnO 2 : A Wonderful Electron Transport Layer for Perovskite Solar Cells," *Small*, vol. 14, no. 31, p. 1801154, Aug. 2018.

[125] Q. Jiang *et al.*, "Enhanced electron extraction using SnO2 for high-efficiency planar-structure HC(NH2)2PbI3-based perovskite solar cells," *Nat. Energy*, vol. 2, no. 1, p. 16177, Jan. 2017.

[126] J. Xu *et al.*, "Perovskite-fullerene hybrid materials suppress hysteresis in planar diodes," *Nat. Commun.*, 2015.

[127] A. Guerrero *et al.*, "Switching Off Hysteresis in Perovskite Solar Cells by Fine-Tuning Energy Levels of Extraction Layers," *Adv. Energy Mater.*, 2018.

[128] S. N. Habisreutinger, N. K. Noel, and H. J. Snaith, “Hysteresis Index: A Figure without Merit for Quantifying Hysteresis in Perovskite Solar Cells,” *ACS Energy Lett.*, vol. 3, no. 10, pp. 2472–2476, Oct. 2018.

[129] J.-M. Savéant, *Elements of Molecular and Biomolecular Electrochemistry*. Hoboken, NJ, USA: John Wiley & Sons, Inc., 2006.

[130] L. Kavan and M. Grätzel, “Highly efficient semiconducting TiO2 photoelectrodes prepared by aerosol pyrolysis,” *Electrochim. Acta*, vol. 40, no. 5, pp. 643–652, Apr. 1995.

[131] L. Kavan, M. Zukalova, O. Vik, and D. Havlicek, “Sol-Gel Titanium Dioxide Blocking Layers for Dye-Sensitized Solar Cells: Electrochemical Characterization,” *ChemPhysChem*, vol. 15, no. 6, pp. 1056–1061, Apr. 2014.

[132] L. Kavan, B. O’Regan, A. Kay, and M. Grätzel, “Preparation of TiO2 (anatase) films on electrodes by anodic oxidative hydrolysis of TiCl3,” *J. Electroanal. Chem.*, vol. 346, no. 1–2, pp. 291–307, Mar. 1993.

[133] J. A. Christians, P. A. Miranda Herrera, and P. V. Kamat, “Transformation of the Excited State and Photovoltaic Efficiency of CH 3 NH 3 PbI 3 Perovskite upon Controlled Exposure to Humidified Air,” *J. Am. Chem. Soc.*, vol. 137, no. 4, pp. 1530–1538, Feb. 2015.

[134] K. K. Bass, R. E. McAnally, S. Zhou, P. I. Djurovich, M. E. Thompson, and B. C. Melot, “Influence of moisture on the preparation, crystal structure, and photophysical properties of organohalide perovskites,” *Chem. Commun.*, vol. 50, no. 99, pp. 15819–15822, 2014.

[135] B. Philippe *et al.*, “Chemical and Electronic Structure Characterization of Lead Halide Perovskites and Stability Behavior under Different Exposures—A Photoelectron Spectroscopy Investigation,” *Chem. Mater.*, vol. 27, no. 5, pp. 1720–1731, Mar. 2015.

[136] A. M. A. Leguy *et al.*, “Reversible Hydration of CH 3 NH 3 PbI 3 in Films, Single Crystals, and Solar Cells,” *Chem. Mater.*, vol. 27, no. 9, pp. 3397–3407, May 2015.

[137] G. Niu, X. Guo, and L. Wang, “Review of recent progress in chemical

stability of perovskite solar cells," *J. Mater. Chem. A*, vol. 3, no. 17, pp. 8970–8980, 2015.

[138] G. Niu, W. Li, F. Meng, L. Wang, H. Dong, and Y. Qiu, "Study on the stability of CH 3 NH 3 PbI 3 films and the effect of post-modification by aluminum oxide in all-solid-state hybrid solar cells," *J. Mater. Chem. A*, vol. 2, no. 3, pp. 705–710, 2014.

[139] Y. Hou *et al.*, "Enhanced moisture stability of metal halide perovskite solar cells based on sulfur–oleylamine surface modification," *Nanoscale Horizons*, 2019.

[140] P. M. Hangoma *et al.*, "Improved Moisture Stability of Perovskite Solar Cells with a Surface-Treated PCBM Layer," *Sol. RRL*, vol. 3, no. 2, p. 1800289, Feb. 2019.

[141] S. Emami *et al.*, "Development of hermetic glass frit encapsulation for perovskite solar cells," *J. Phys. D. Appl. Phys.*, vol. 52, no. 7, p. 074005, Feb. 2019.

[142] E. Ramasamy, V. Karthikeyan, K. Rameshkumar, and G. Veerappan, "Glass-to-glass encapsulation with ultraviolet light curable epoxy edge sealing for stable perovskite solar cells," *Mater. Lett.*, vol. 250, pp. 51–54, Sep. 2019.

[143] R. Cheacharoen *et al.*, "Encapsulating perovskite solar cells to withstand damp heat and thermal cycling," *Sustain. Energy Fuels*, vol. 2, no. 11, pp. 2398–2406, 2018.

[144] G. Grancini *et al.*, "One-Year stable perovskite solar cells by 2D/3D interface engineering," *Nat. Commun.*, vol. 8, no. 1, p. 15684, Aug. 2017.

[145] I. Poli *et al.*, "Graphite-protected CsPbBr3 perovskite photoanodes functionalised with water oxidation catalyst for oxygen evolution in water," *Nat. Commun.*, vol. 10, no. 1, p. 2097, Dec. 2019.

[146] W. Luo *et al.*, "Efficient and Stable Perovskite Solar Cell with High Open-Circuit Voltage by Dimensional Interface Modification," *ACS Appl. Mater. Interfaces*, vol. 11, no. 9, pp. 9149–9155, Mar. 2019.

[147] H.-S. Kim, J.-Y. Seo, and N.-G. Park, "Material and Device Stability in

Perovskite Solar Cells," *ChemSusChem*, vol. 9, no. 18, pp. 2528–2540, Sep. 2016.

[148] T. Supasai, N. Rujisamphan, K. Ullrich, A. Chemseddine, and T. Dittrich, "Formation of a passivating CH 3 NH 3 PbI 3 /PbI 2 interface during moderate heating of CH 3 NH 3 PbI 3 layers," *Appl. Phys. Lett.*, 2013.

[149] T. T. Ava, A. Al Mamun, S. Marsillac, and G. Namkoong, "A Review: Thermal Stability of Methylammonium Lead Halide Based Perovskite Solar Cells," *Appl. Sci.*, vol. 9, no. 1, p. 188, Jan. 2019.

[150] B. Conings *et al.*, "Intrinsic Thermal Instability of Methylammonium Lead Trihalide Perovskite," *Adv. Energy Mater.*, vol. 5, no. 15, p. 1500477, Aug. 2015.

[151] P. P. Boix, S. Agarwala, T. M. Koh, N. Mathews, and S. G. Mhaisalkar, "Perovskite Solar Cells: Beyond Methylammonium Lead Iodide," *J. Phys. Chem. Lett.*, vol. 6, no. 5, pp. 898–907, 2015.

[152] R. J. Sutton *et al.*, "Bandgap-Tunable Cesium Lead Halide Perovskites with High Thermal Stability for Efficient Solar Cells," *Adv. Energy Mater.*, vol. 6, no. 8, p. 1502458, Apr. 2016.

[153] Q. Sun *et al.*, "Role of Microstructure in Oxygen Induced Photodegradation of Methylammonium Lead Triiodide Perovskite Films," *Adv. Energy Mater.*, 2017.

[154] S.-H. Turren-Cruz, A. Hagfeldt, and M. Saliba, "Methylammonium-free, high-performance, and stable perovskite solar cells on a planar architecture," *Science (80-.).*, vol. 362, no. 6413, pp. 449–453, Oct. 2018.

[155] N. Arora *et al.*, "Perovskite solar cells with CuSCN hole extraction layers yield stabilized efficiencies greater than 20%," *Science (80-.).*, vol. 358, no. 6364, pp. 768–771, Nov. 2017.

[156] X. Hu *et al.*, "Air and thermally stable perovskite solar cells with CVD-graphene as the blocking layer," *Nanoscale*, vol. 9, no. 24, pp. 8274–8280, 2017.

[157] K. Choi *et al.*, "Thermally stable, planar hybrid perovskite solar cells with high efficiency," *Energy Environ. Sci.*, vol. 11, no. 11, pp. 3238–3247, 2018.

Chapter 2

Experimental Procedures

2.1 Fabricating Perovskite Solar Cells

2.1.1 Laser processing of TCO materials

In order to fabricate perovskite solar cells it is necessary to isolate desired regions of the TCO material in order to complete the electronic circuitry and reduce the chance of short circuiting the cell. This is done with the use of a nanosecond air cooled Rofin Power line E diode end pumped solid state laser. The power line E has a Neodynium: yttrium vanadate (Nd: YVO_4) source, frequency doubled to 532 nm and operating at an output power of 10 – 40 Watts. The Pulse frequency (pulse repetition rate) was varied between 1 – 200 kHz depending on the materials being etches as in chapters 3, 4, 5 and 6 (Pilkington TEC15 ™ (<15 Ωcm^{-2}) glass, Pilkington

Eclipse ™ Advantage and TEC15-D ™). Laser width and line speed was control by reducing the aperture of the beam to 0.01 cm and 20 mms^{-1} in order to isolate in the regions.

The system comes with Visual LaserMarker (VLM), an application software which allows the layout, generation and transfer of the required marking data to be sent straight from the PC to the laser marker.

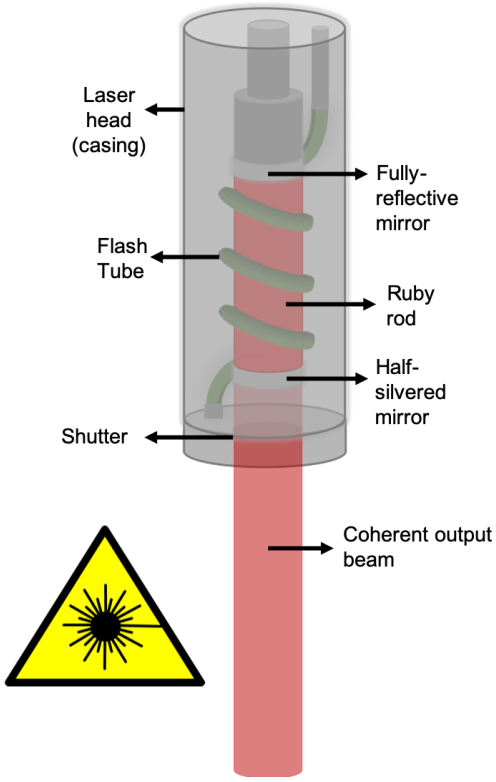

Figure X: Schematic of a laser used to pattern TCO and Perovskite solar cell materials.

2.1.2 TCO Surface Treatments

2.1.2.1 General TCO cleaning

Pilkington TEC15 ™ (<15 Ωcm^2) glass, Pilkington Eclipse ™ Advantage and TEC15-D ™ were submerged in 5 % hellmanex ™ de-ionised water solution (<18 mΩ) at 80

ºC for 20 minutes and subsequently rinsed with de-ionised water, acetone, ethanol and isopropanol. The substrates were then blown dry with a nitrogen air knife and placed into an oxygen plasma cleaner for 10 minutes and UV ozone treated for 20 minutes to remove any residual carbon contaminants and make the surfaces more hydrophilic. Power setting for the plasma cleaning were kept constant at 100 % power, see model number and settings in 2.1.2.1 for equipment details.

2.1.2.2 Oxygen Plasma Treatment

Oxygen plasma treatment was conducted using a diener electronics plasma etcher surface technology -HF-Generators. Serial number 040127, type NANO-LF, Manuf: 2004. (U [V]: 230, I [A] 16, f[Hz] 50. Full power was always applied unless otherwise stated. This was used to remove any residual organic compounds after general TCO cleaning.

2.1.2.3 Ultraviolet ozone treatment

UV ozone cleaning was done by a UVO Cleaner, Model: 144AX-220 supplied by Jelight Compnay Inc. 230 V / 50 HZ, 3 A. This ensured good wetting capabilites of subsequent layers with use of the corona effect and removed any residual carbon missed by previous treatments.

2.1.3 Electron Transport Layer Fabrication

2.1.3.1 TiO_2 preparation

Electron transport layers (ETL) (where used) were prepared by diluting a solution of 0.2 M titanium di-isopropoxide bis(acetylacetonate) (or TAA) in ethanol and filtered with a 0.2 μm PTFE filter. The deposition of these layers was achieved via manual spraying with an art spray gun (Sealey, Model No. AB932) over the conductive surface of a fluorine-doped tin oxide (FTO)-coated glass. The substrate

was pre-heated and maintained at 300 °C on a hotplate during spraying and a subsequent annealing stage at 550 °C was carried out for 30 minutes to crystallise the TiO_2 to the anatase phase. A series of 25 sprays were applied successively at 5 s intervals to build up a layer thickness of approximately 40-50 nm.

2.1.3.2 SnO_2 Preparation

SnO_2 ETL layers were prepared by diluting (44592) Tin (IV) oxide, 15% in H_2O colloidal dispersion procured from Alfa Aesar further in de-ionised water to the ratio 1: 2.6 ml to give a final solution of 4.2 wt.%. These were then deposited via spin coating immediately after UV-Ozone treatment of the FTO was finished. We note that the increased wetting effects of UV-Ozone on FTO films lasts no longer than 10 minutes, we found it imperative that films were spin coated before this time limit elapsed. 150 µl of the final ETL solution was spin coated onto a 28 mm by 28 mm glass/ FTO substrate at 2000 rpm / 2000rpms^{-1} for 30 s, we noted improved surface coverage by depositing the solution dynamically at 25 s. The substrates were then placed on a hotplate at 110 °C for 10 minutes then a 5-minute ramp to 180 °C for 1 hour to anneal the final films. We note that processing conditions in the laboratory are critical to good film formation, noting that a very dry room (<25 % RH) coupled with a nitrogen flowed Laurel (Model: WS-650Mz-23NPPB spin processor) spin coater contributed to rapid drying of the film, resulting in detrimental pin hole defects. Increased humidity of >30 % RH and no nitrogen flowing in the spin coater resulted in more homogenous films. These conditions should be considered when trying to fabricate such a layer as the effects can be easily negated although are not obvious during manufacture.

2.1.4 Mesoporous Scaffold

The 200 nm mesoporous TiO_2 scaffold was fabricated by diluting a TiO_2 paste, 30-NRD, procured from Greatcell Solar, in a mixture of isopropanol and terpineol (Ratio 30-NRD: terpineol: isopropanol 2:6:4.5 by weight) to produce a 200 nm thick layer via solution processed spin coating (6000 rpm, 2000 rpms^{-1}, 30 s). Initial heating

immediately after spin coating was done at 100 °C followed by a gradual ramping over 15 minutes to 550 °C to remove any organic binder present.

2.1.5 Perovskite Deposition and Formulation

2.1.5.1 Caesium Doped Triple and Rubidium Doped Quadruple Cation Perovskite

The triple and quadruple cation perovskite film was fabricated according to the procedures in the literature [1][2]. The desired triple cation composition consisted of a 5 % addition of CsI solution (1.5 M stock solution in DMSO) dispersed in a 95% mixed perovskite precursor to obtain the final composition, $Cs_{0.05}(MA_{0.17}FA_{0.83})_{(0.95)}Pb(I_{0.83}Br_{0.17})_3$. The solution was then filtered using a 0.2 μm PTFE filter and deposited via solution processed spin coating (150 μL, 1000 rpm/ 1000 $rpms^{-1}$ for 10 s followed immediately by a 4000 rpm/ 4000 $rpms^{-1}$ for 20 s). During the spin coating process, 200 μL of chlorobenzene was deposited dynamically onto the spinning substrate 10 s before the end the second spin program. Upon addition of the anti-solvent (chlorobenzene) the perovskite film immediately turned dark and once the spin coating procedure had finished the films were transferred to a hotplate and annealed at 100 °C for 1 hour. The entire perovskite procedure was carried out in nitrogen filled glove-box.

2.1.5.2 Methylammonium Lead Iodide Perovskite

MAPI perovskite was prepared by dissolving 605 mg of Lead Iodide (1.1 M PbI_2 5 %) procured from TCI America and 199 mg of methylammonium iodide (1.0 M MAI) procured from GreatCellSolar in 1 ml of 4:1 ratio of Dimethylformamide: Dimethyl Sulfoxide. We noted that by dissolving the inorganic PbI_2 at elevated temperatures >150 °C resulted in better perovskite film formation with fewer pinholes as reported in literature [1][3] . The solution was then filtered using a 0.2 μm PTFE filter and deposited on top of the SnO_2 via solution processed spin coating (125 μL, 4000 rpm/

2000 $rpms^{-1}$ for 30 s). During the spin coating process, 200 µL of ethyl acetate procured from Sigma Aldrich was deposited dynamically onto the spinning substrate 22 s before the end the second spin programme. Once the spin coating procedure had finished the films were transferred to a hotplate and annealed at 100 °C for 1 hour. The entire perovskite procedure was carried out in nitrogen filled glove-box.

2.1.6 Hole Transport Material Formulation and Deposition

2.1.6.1 Spiro-MeOTAD

For the hole transporting material (HTM), a Spiro-OMeTAD solution (100 mg of Spiro-OMeTAD, 36 µL of 4-tert-butylpyridine (tBP), 20 µL of a lithium-bis(tri-fluoromethanesulfonyl)imide (Li- TFSI) solution (516 mg Li-TFSI in 1 mL acetonitrile) and 8 µL of a FK209 (300 mg in 1 mL of acetonitrile) in 996 µL of chlorobenzene) was spin-coated dynamically at 4000 rpm, 4000 $rpms^{-1}$ for 12 s on top of the annealed perovskite.

2.1.6.1 PCBM

PCBM Layer: 10 mg per ml in chlorobenzene. C60 PCBM, filtered. All PCBM films annealed for an hour at 100 degrees Celsius. All depositions used 150 ul of solution. Optimum speed speeds 4000 rpm, 4000 $rpms^{-1}$ for 30 seconds dynamically for a resulting film thickness of approximately 20 nm.

2.1.7 Top Electrode Preparation

2.1.7.1 Evaporated Metal Contacts

70-80 nm of gold or silver top electrode was thermally evaporated under high vacuum (5 x 10^{-6} torr) using an Edwards E306A Thermal Evaporator. The evaporation rate was estimated at between 15-20 nm per second to avoid overheating of the perovskite substrates. Pixel Mask area were 0.09cm^2.

2.1.7.2 Silver Nanowire (AgNW) Carbon Nanotube (CNT) Composite

Optimised mixtures of Silver nanowires procured from sigma aldrich (product number 739421) where mixed with single walled carbon nanotubes (containing Tuball^{TM}) dispersed in IPA procured from Oscial Europe. The mixture was diluted in IPA further so spray coating could be used to deposit the desired layer thickness using a nitrogen carrier gas pressurised at 25 psi. Masking was used to deposit in the desired regions to complete cell architecture. Other suppliers of silver nanowires were ASC Materials and Novarials, discussed further in chapters 5.2 and 5.3. Thickness was controlled by varying the number of passes rather than varying carrier gas pressure or composition/ dilution. Optimal concentrations used ratios containing a 2:1:2 solution (Silver nanowires: Single walled carbon nanotubes: IPA). 1:1: was also used effectively.

2.1.7.3 TCO Encapsulating Electrode (IZO) with Orotective Layer MoO_3 and SnO_2

The molybdenum oxide (MoO_x, STREM, 99.95%) and silver (Ag, Kurt Leskar, 99.99%) films were thermally evaporated using a MBRAUN evaporator with evaporation rate of 0.5 Å s^{-1} and 0.25 Å s^{-1}, respectively. The indium and tin (ITO target, Plasmaterial 99.99%) films were Radio Frequency magnetron sputtered

using Moorfield Nanolab 60 at 0.37 Wcm^{-2} and 2.46 Wcm^{-2} for the bottom and top layers.

2.2 Chemical Vapour Deposition Process

CVD processes where carried out by NSG Pilkington in St Helens UK on an industrial float glass line (also reffered to as UK5) and various locations in Germany and the USA. All lines are equipped with low vacuum chemical vapour deposition using precise precursor formulations and processing temperatures that cannot be disclosed owing to a prior non disclosure agreement. (tempertures where replicated when processing both TiO_2 and SnO_2 variants that would be similar to lab manufacture).

2.3 Sheet Resistance Measurements (4-point probe)

Sheet resistance and conductivity measurements were obtained using a four point probe head procured and commercially available from Jandel. The head had soft tip gold contacts spaced 1.00 mm (for small samples) and 5 mm (for larger samples) apart. This was connected to a resistance test unit also procured and commerciall available from Jandel, model RM3000. The four point probe was calibrated using a sheet of FTO-coated glass of known resistance at several different currents. For the measurements obtained in Chapter 6, the current was sweeped from 1 μA to 10A in order to attain optimised conductivity measurements. It works by forcing current through two outer probes and reading the voltage across the two inner probes. The equation below is used to calculate the sheet resistance, where $\frac{\pi}{ln2} = 4.53$.

$$p_0 \quad \frac{\Omega}{\square} = \frac{\pi}{ln2} \cdot \frac{V}{I} \tag{2.1}$$

2.4 Profilometry Measurements

Profilometry of methylammonium lead triiodide films spin coated onto clean plain glass (microscope slides) measuring 2.5 x 2.5 cm2. A stylus force of 5 mg was used in order not to damage the perovskite surface and 3 forward scans of 2 mm in length spaced 0.7 cm apart were conducted across samples with a range of 10 μm and a speed of 0.1 mms-1. Data was filtered with an 8-point average using a KLA, Tencor, D600 profilometer.

2.5 X-ray Photoelectron Spectroscopy (XPS)

X-Ray Photoelectron Spectroscopy (XPS) was carried out using a Kratos Axis Supra (Kratos Analytical) using a monochromated Al Kα source. All data was analysed on CasaXPS (2.3.17dev6.4k) using the Kratos sensitivity factor library. Samples sizes for mapping as seen in chapter 3 and point maps in chapter 4 was 800 nm by 800nm. Samples were precleaned using a gentle (50%) argon gun plasma clean to remove surface carbon contaminants for 5 minutes. All samples were prepared on the day of analysis.

2.6 X-Ray Diffraction Crystallography (XRD)

The crystalline properties of the samples were determined by glancing angle X-ray diffraction crystallography (XRD) measurements taken with a D8 Discover instrument from Bruker (Germany) with a CuKα beam at 40 kV, 40 mA and scan parameters of 0.1 s per step at 0.01 2θ step size. (Radiation λ = 1.5406 Å).

2.7 Scanning Electron Microscopy (SEM)

The cross-sectional SEM imagery in chapter 3 was performed on a Zeiss Crossbeam 540-47- 51 ultra-high resolution FEG SEM FIB using a focused ion beam (FIB) probe (30kV:50p) with a working distance of approximately 5.1 mm. The morphology of films in chapter 6 was studied using a JEOL-JSM-7800F field emission scanning electron microscope (5 kV acceleration voltage, a working distance of 10 mm and a magnification of x 50, 000)

2.8 Atomic Force Microscopy (AFM)

All Atomic Force Microscopy (AFM) imagery was taken using a JPK Nanowizard 3 AFM, using a 0.8 newton meter tip in contact mode. Typical dimensions of 7.5 μm by 7.5 μm for comparative purpose.

2.9 Cyclic Voltammetry (CV)

Cyclic voltammetry (CV) was conducted using a potassium ferro/ ferri cyanide electrolyte couple. In the experiment, the $Fe(CN)_6^{3-/4-}$ solution acts as a model redox system in a three-electrode cell, with the coated FTO glass substrates acting as a working electrode and a calomel electrode acting as a reference electrode. Voltages were typically swept through at least 3 complete cycles over the range of +1.0V and -0.7V and the resulting anodic and cathodic activities measured using a potentiostat connected to a personal computer running CorrWare software.

2.10 Tensile Adhesion Testing

The adhesive force of the AgNW, CNT composite was measured using a Hounsfield tensile tester with the tape attached to the sample stage at a 90 degree angle. Each sample was glued with a thin layer of epoxy to the stage to ensure and even surface.

2.11 Current-Voltage Sweep Measurements (JV)

For current-voltage measurements of solar cells, devices were masked to 0.1 cm^2 and tested under a class AAA solar simulator (Newport Oriel Sol3A) at AM1.5 and 100 $mWcm^{-2}$ illumination conditions calibrated against a KG5 filtered silicon reference cell (Newport Oriel 91150-KG5) using a Keithley 2400 source meter. Current-voltage sweeps were performed from both V_{OC} to J_{SC} and vice versa at a rate of 0.1 Vs^{-1} unless otherwise stated. For stabilized power output measurements, device bias was set to the maximum power point voltage determined by the J-V sweep and current monitored under 100 $mWcm^{-2}$ illumination. Data was tabulated in box plots for analysis which displays the first quartile, median and third quartile as well as maximum and minimum values for the data presented.

Stability measurements in chapter 6 were performed on unencapsulated devices kept at open circuit in a light soaking unit (Solaronix Solixon A20), at 25 °C and ambient humidity (approximately 45 %), under 1 sun illumination: both reverse and forward scans, at 15mV/s scan rate, were carried at every hour.

2.12 Transient Photovoltage & Transient Photocurrent Decay (TPV, TPC)

Transient photovoltage measurements were performed using a commercially available transient measurement system (Automatic Research GmbH). This system uses a 635 nm red laser diode driven by a waveform generator (Keysight 33500B). The laser pulse length was 10 µs. Background illumination was provided by a white LED with its intensity calibrated to generate the same device photocurrent as measured using the solar simulator. This intensity is referred to as 1 Sun equivalent. Transient responses were captured by a digital storage oscilloscope (Keysight

DSOX2024A), the number of sample averages being adjusted to optimize signal noise and measurement time. The device under test is assumed to be held at open-circuit by the 1 MΩ oscilloscope input. Transient photo voltage (TPV) decays were fitted using a single exponential function. Open-circuit photovoltage decay (OCVD) measurements were performed using the same white LED and oscilloscope.

2.13 CIE Colour Analysis

CIE colour analysis was done by photo spectrometry according to the CIE color model. A color space model created by the International Commission on Illumination known as the Commission Internationale de l'Elcairage (CIE). It is also known as the CIE XYZ color space or the CIE 1931 XYZ color space.

2.14 UV-Visible-Near Infrared Spectrophotometry (UV-Vis-NIR)

UV-Vis-NIR spectroscopy was carried out using a Perkin Elmer UV/VIS/NIR spectrophotometer Lambda 750 with a 100 mm InGaAs integrating sphere used for routine diffuse reflectance and diffuse transmittance measurements. Scans from 900-250 nm were taken with a 1 nm data interval at 266.75 nm/ min with transmission mode.

2.15 Incident Photon to Electron Conversion Efficiency (IPCE)

IPCE measurements were performed in 10 nm increments on a PV Measurements QEX10 in DC mode calibrated against a NIST-traceable photodiode. Measurements were carried out over the range of 300 to 850 nm.

2.16 Raman Spectroscopy

Raman spectroscopy measurements were taken using a Renishaw Invia Raman microscope. (Operating power: 30 mW, Objective lens 50 x magnifications with a 1 μm spot-size, working wavelength 532 nm).

2.17 Haze and Clarity Measurements

Haze and clarity measurements performed at NSG Pilkington's European technical research centre using a Haze meter. Haze relates to the amount of light that is subject to wide angle scattering at an angle greater than 2.5° from normal (ASTM D1003). Total haze is a combination of both transmission and reflection whereas clarity relates to the amount of light that is subject to narrow area scattering at an angle less than 2.5° from normal

2.18 Stability Measurements

The stability for devices with IZO/MoOx top electrode was performed under continuous one-sun equivalent illumination in a nitrogen atmosphere without additional encapsulation. All the devices were illuminated on whole pixel area (0.24 cm2) rather than masked area (0.09 cm2) through either IZO or FTO during the stability test. Oxygen and water concentrations were esitmated to be below 100ppm during testing. A continuous flow of nitrogen (flow rate 20ml/ min) was used to control measurement conditions.

Bibliography

[1] M. Saliba *et al.*, “Cesium-containing triple cation perovskite solar cells: improved stability, reproducibility and high efficiency,” *Energy Environ. Sci.*, vol. 9, no. 6, pp. 1989–1997, 2016.

[2] T. Matsui *et al.*, “Effect of Rubidium for Thermal Stability of Triple-cation Perovskite Solar Cells,” *Chem. Lett.*, vol. 47, no. 6, pp. 814–816, Jun. 2018.

[3] B. Park *et al.*, “Understanding how excess lead iodide precursor improves halide perovskite solar cell performance,” *Nat. Commun.*, vol. 9, no. 1, p. 3301, Dec. 2018.

Chapter 3

3. Eclipse Advantage – A Dual Purpose Mass Manufactured Electron Transport Material Based on TiO_2

Work in this chapter was published in Advanced Materials Interfaces (Benjamin Smith, Joel Troughton, Anthony Lewis, James McGettrick, Adam Pockett, Matthew Carnie, Cecile Charbonneau, Cameron Pleydell-Pearce, Justin Searle, Paul Warren, Su Varma and Trystan Watson, *Adv. Mater. Interfaces* **2019**, 1801773).

3.1 Introduction

Perovskite solar cells (PSCs) have seen a meteoric rise in prominence amongst the photovoltaic community with power conversion efficiencies increasing from 3.8% in 2009, [1]to over 22% in 2017. [2] [3] [4] One of the challenges facing PSCs and other emerging thin film photovoltaics is the scaling up of lab-scale devices to commercial production using inexpensive roll-to-roll or sheet-to-sheet manufacturing techniques as seen in chapter 1.5. Recently, an article by Youn-Jung Heo and co-workers has demonstrated a fully printed PSC fabricated through the use of slot die coating with a PCE of 14.4%. [6] [7] [8] [9] With these large scale-compatible deposition methods, coupled with novel fast processing techniques, [10] [11] [12] [13] the future looks bright for PSCs.

PSCs are typically fabricated by solution processing layers onto transparent conducting oxide (TCO)-coated glass. Common TCOs used include fluorine-doped tin oxide (FTO) and tin-doped indium oxide (ITO): FTO-coated glass, in particular, is already produced inexpensively on industrial scales using a chemical vapor deposition technique integrated within the glass production process. Depending on the architecture of the PSC, either a p-type (in the case of "inverted"-type devices) or n-type (in the case of "normal"-type devices) semiconducting layer is deposited onto the TCO-coated substrate. Currently, the majority of "normal" structure devices report TiO_2 as an n-type, electron selective contact; usually in the form of a compact layer followed by a thicker mesoporous layer. [14] [15] The most common reported means of depositing high quality compact layers of TiO_2 at lab scale involve spray pyrolysis of a metal-organic precursor solution. [16] In spray pyrolysis, this solution is sprayed onto a heated substrate, typically at temperatures in excess of 300 °C to remove the carrier solvent as well as organic ligands associated with the precursor. A subsequent annealing step in excess of 450 °C is also required to sinter and crystallize the amorphous titanium dioxide into a crystalline anatase form. Although the deposition and heating of such a layer may be scaled up, it may be dangerous owing to the presence of flammable

solvent vapor in close contact with heated substrates, as well as being difficult to replicate consistently. This poses a potentially significant bottleneck to the realization of mass-produced perovskite photovoltaics. In this report, we demonstrate efficient PSCs fabricated on a commercially available glass substrate known as "Pilkington Eclipse TM Advantage" (EA) that is commonly used in solar control products. EA is produced by the glass conglomerate NSG Pilkington and consists of 1.9 mm thick glass with a base layer of 25 nm SnO_2 followed by another 25 nm of SiO_2. On top of this base layer is a 200-250 nm thick FTO layer subsequently overlaid with a 20-40 nm thick TiO_2 layer via CVD (chemical vapor deposition at temperatures estimate to be in excess of 550 degrees Celsius). During standard operation the EA functions as a solar control product allowing the control of heat and light into a building, primarily in warmer climates, where the aforementioned TiO_2 is used to control the optics in the system. EA is manufactured at large scale and is presently commercially available, however although its stack is ordered appropriately and in the correct thickness range for a PSC charge-selective layer, EA has yet to be realized in the use of PSC. In this chapter we investigate the potential of using EA as a substrate in perovskite solar cells and characterise its suitability as an electron transport layer (ETL) using techniques including X-ray photoelectron analysis (XPS), Raman spectroscopy, scanning electron microscopy (SEM) and X-ray diffraction analysis (XRD) as well as cyclic voltammetry (CV) and transient photovoltage measurements (TPV). The setup parameters for these measurements can be found in chapter 2 – Experimental methods under the relevant subsections.

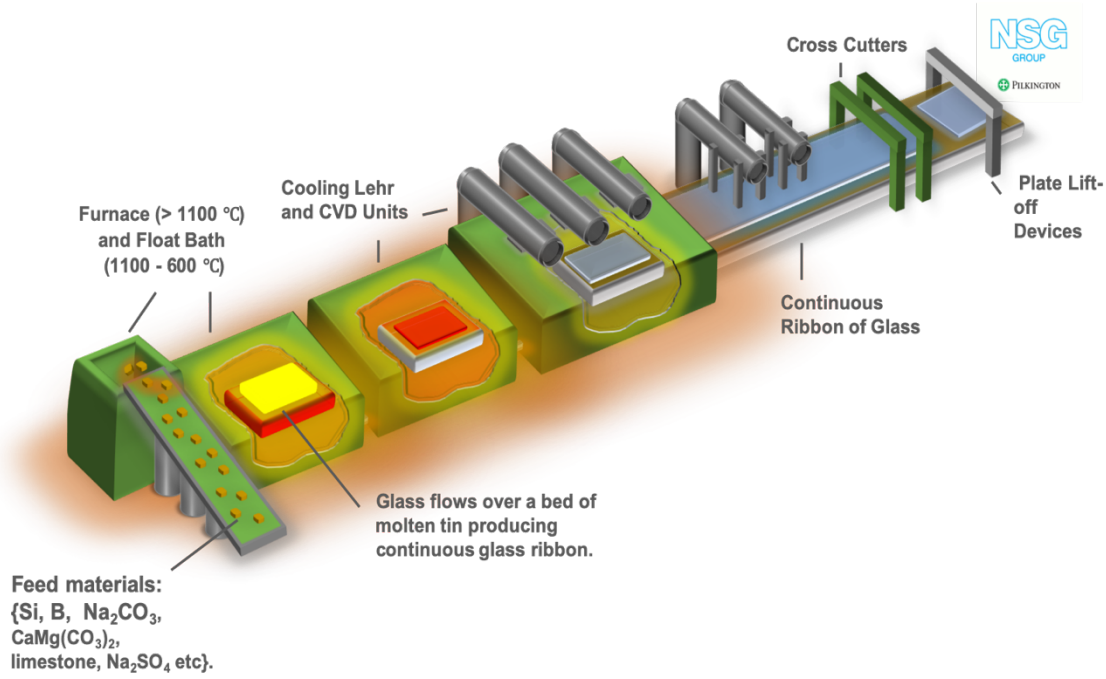

Figure 3.1: A simplified schematic diagram detailing the CVD production process used by NSG Pilkington to produce Eclipse Advantage.

3.2 Experimental

As Eclipse Advantage was supplied as bulk homogenous layers sequentially layered via the CVD process, Laser processing was necessary in order to isolate the desired regions of the TCO materials in order to complete electronic circuitry of the cell and reduce the possibility of short circuiting the cell. This process is outlined in section 2.1.1. Conventional acid (4.0 M concentrated hydrochloric acid, HCL) etching with a base metal (Powdered Zinc) is normally employed when trying to remove TCO materials like fluorine doped tin oxide. This isn't possible with an inert and chemically stable TiO_2 over layer hence the laser process is preferred for all scenarios, this is futhur outlined in figure 3.2, along with the device's pixel layout.

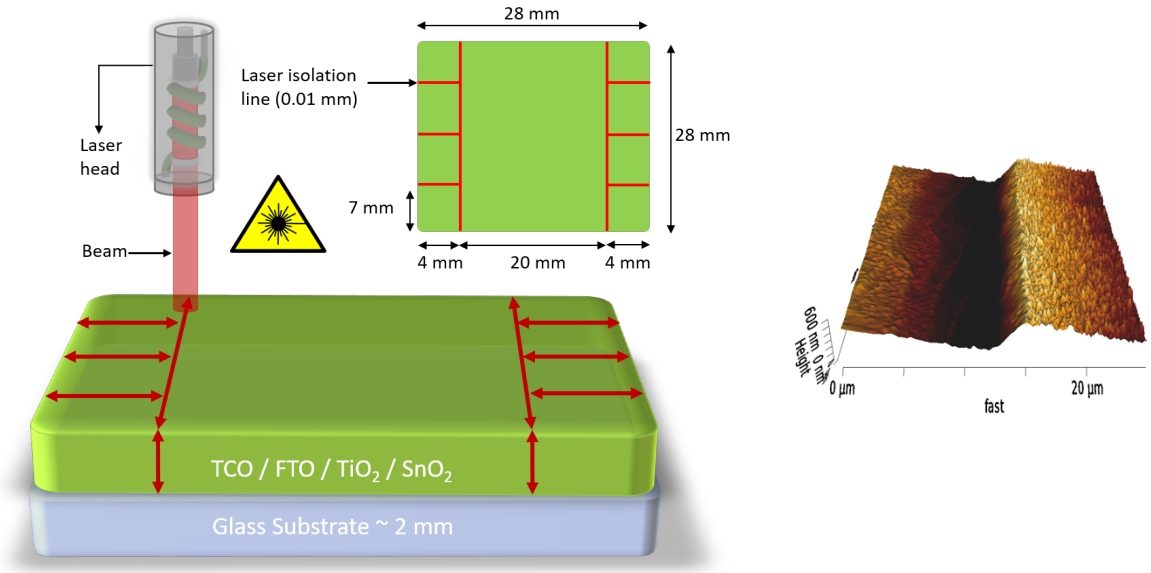

Figure 3.2: A schematic to show how the lasering process was used to isolate the desired regions of TCO/ ETL materials in Eclipse Advantage and TEC15 glass and to the right an AFM image of an ablated trench.

It was noted that the pulse repetition rate needed to be increased for bare FTO when compared to FTO/TiO_2 substrates. The increase was attributed to higher transmission of the laser's 532 nm frequency through FTO as opposed to being absorbed by the TiO_2 in Eclipse Advantage substrates. Pulse repetition rates of 20,000 Hz and 15,000 Hz respectively gave a similar ablation depth (>600 nm) as seen in figure 3.2.

Full details of the fabrication methods used to build the devices displayed in this chapter are provided in chapter 2.1. Eclipse Advantage based devices were compared against a standard laboratory TiO_2 ETL layer processed via spray pyrolysis outline in chapter 2.1.3.1. All devices incorporated a mesoporous TiO_2 scaffold, Triple cation-based perovskite absorber layer, Spiro-MeOTAD HTM and evaporated metal back contacts as described in section 2.1.4, 2.1.5.1, 2.1.6.1 and 2.1.7.1 respectively. Mesoporous TiO_2 was incorporated into the architecture as lab scale reproducibility was greatly enhanced by the addition of the mesoporous scaffold. Near record PCEs have been reported using this architecture [14] and

the mesoporous layer has the added benefit of separating the ablation regions from TCO/ Perovskite contact while exhibiting no blocking effect as discussed in more detail in chapter 3.3.

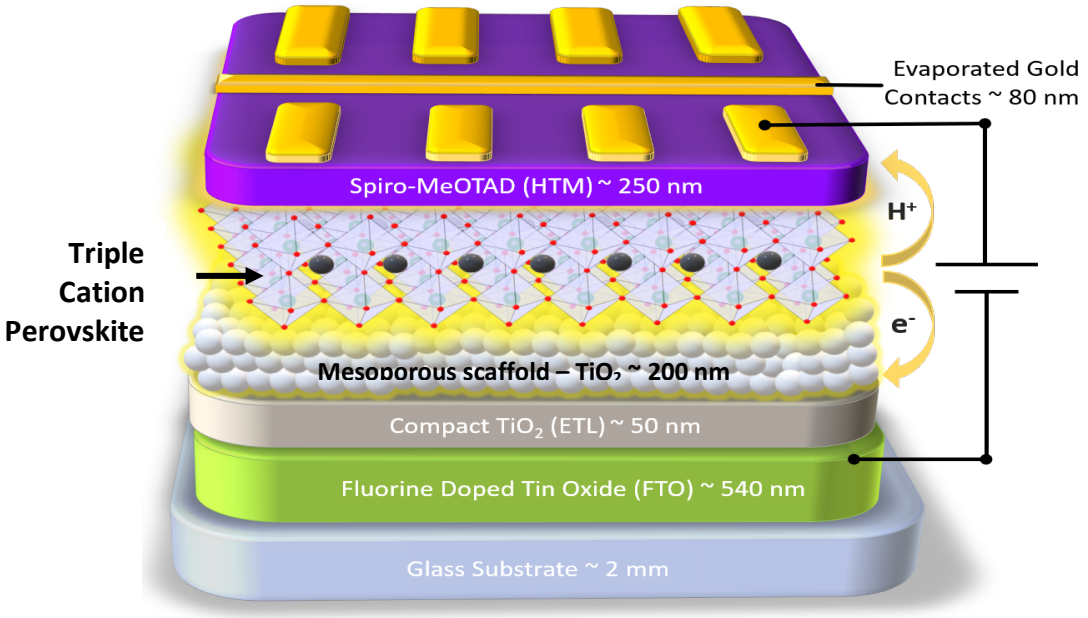

Figure 3.3: A simplified schematic diagram of the architectures employed in fabricating lab based sprayed pyrolysis TiO_2 ETLs and Eclipse Advantage.

3.3 Results and Discussion

During the operation of a PSC, illumination occurs through the glass/ FTO substrate interface thus confirming the importance of optical characterization of these and subsequent layers. Figure 3.4 shows optical transmission spectra for both EA and a conventional spray pyrolysis processed compact (c)-TiO_2 layer (50 nm) on FTO-coated glass as well as a plain FTO glass (TEC15) sample. It is apparent that both EA and spray pyrolysis processed c-TiO_2 layers on FTO glass exhibit very similar optical transmission between 250 nm and 800 nm. In both cases, the transmission through EA and conventionally coated substrates is markedly reduced compared to FTO glass without a c-TiO_2 layer, especially at shorter wavelengths. Average transmission (AT) values of EA are fractionally lower than that of conventional spray pyrolysis with an AT of 59.52% compared

to 60.85%. The difference in the FTO glass and the spray pyrolysis, EA samples is attributed to the material's refractive indexes. SnO_2 has a refractive index around n = 2 whereas TiO_2 has a noticeably higher refractive index at around n = 2.5. The higher the refractive index the slower the light travels, thus causing an increase in the change of the direction of the light within the material, thus higher refractive indexes will have lower transmissions through the sample when the detected and incident beam are parallel (or in line with each other). There is a small blue shift at the band absorption edge in the EA, this is likely due to the variation in glass substrate. EA consists of 1.9 mm thick glass with a base layer of 25 nm SnO_2 followed by another 25 nm of SiO_2. On top of this base layer is a 200-250 nm thick FTO layer subsequently overlaid with a 20-40 nm thick TiO_2 layer via CVD. The spray pyrolysis sample was produced on TEC15 glass that consists 2.2mm thick glass and an FTO film overlaid with a 40-50 nm of spray pyrolyzed TiO_2. The variation in the two samples is likely due to the nature of the glass substrate and thickness of TiO_2. The corresponding sheet resistances of the TCO in both the EA and spray pyrolysis-processed substrate (Solaronix), were measured at 15 Ω sq. cm^{-1} ($\pm$0.75) using a Jandel four-point probe.

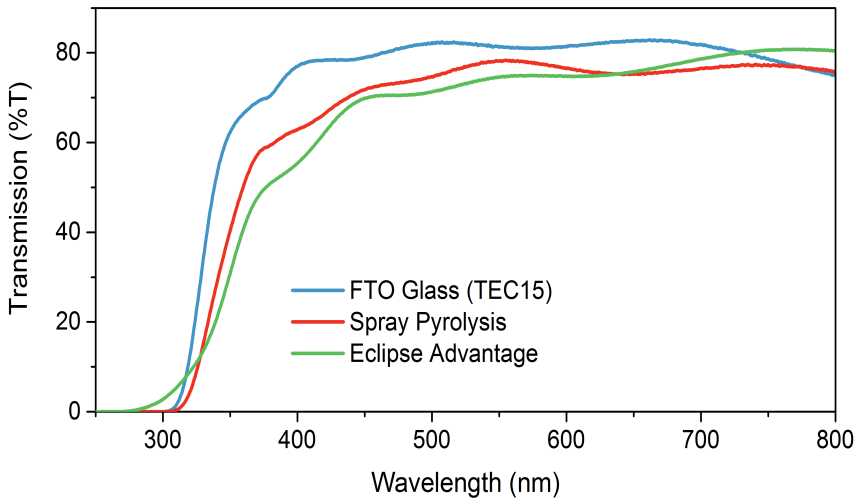

Figure 3.4: UV-Visible transmission spectra for Pilkington Eclipse Advantage, conventionally processed c-TiO_2 via spray pyrolysis on FTO TEC 15 and bare FTO on glass (TEC15). Note: All glass substrates are 1.8-2.1 mm in thickness.

Surface morphology and topography of the ETL layer is crucial when fabricating PSCs. The interface between the ETL and mesoporous TiO_2 overlaid is critical to ensuring efficient charge transfer and reducing potential sites for trap states. Any pin holing in the ETL surface can provide a mechanism for parasitic charge recombination of photo-generated electron hole pairs which results in a decreased photocurrent observed by a lower short circuit current density. Thus, a highly conformal TiO_2 layer, with no pinholes is required to assess these properties. Cross sectional SEM images were taken using a Zeiss Cross beam 540 ultra-high resolution FEG SEM FIB of EA and Atomic Force Microscopy (AFM) imagery taken using a JPK Nanowizard 3 AFM, using a 0.8 newton meter tip in contact mode can also be seen in Figure 3.5 and 3.6 respectively.

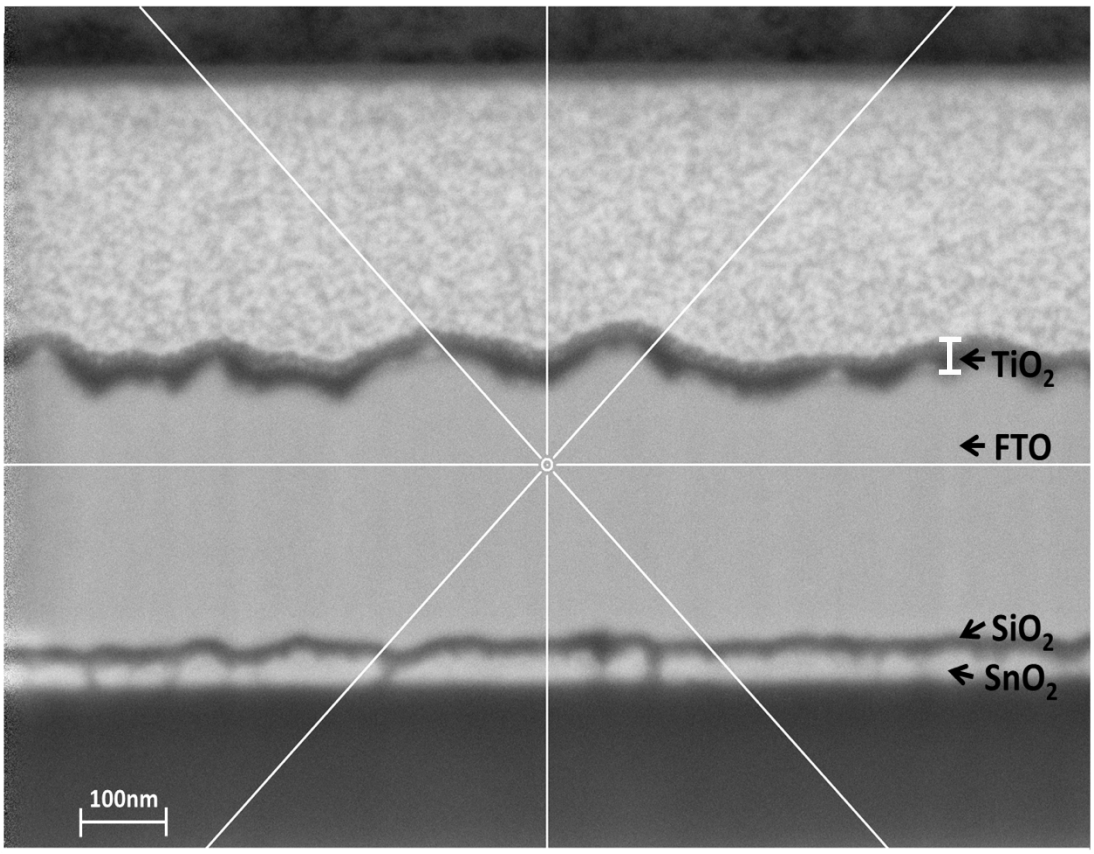

Figure 3.5: Cross sectional SEM of Pilkington Eclipse Advantage taken using a Zeiss cross beam 540 ultra high resolution FEG SEM FIB.

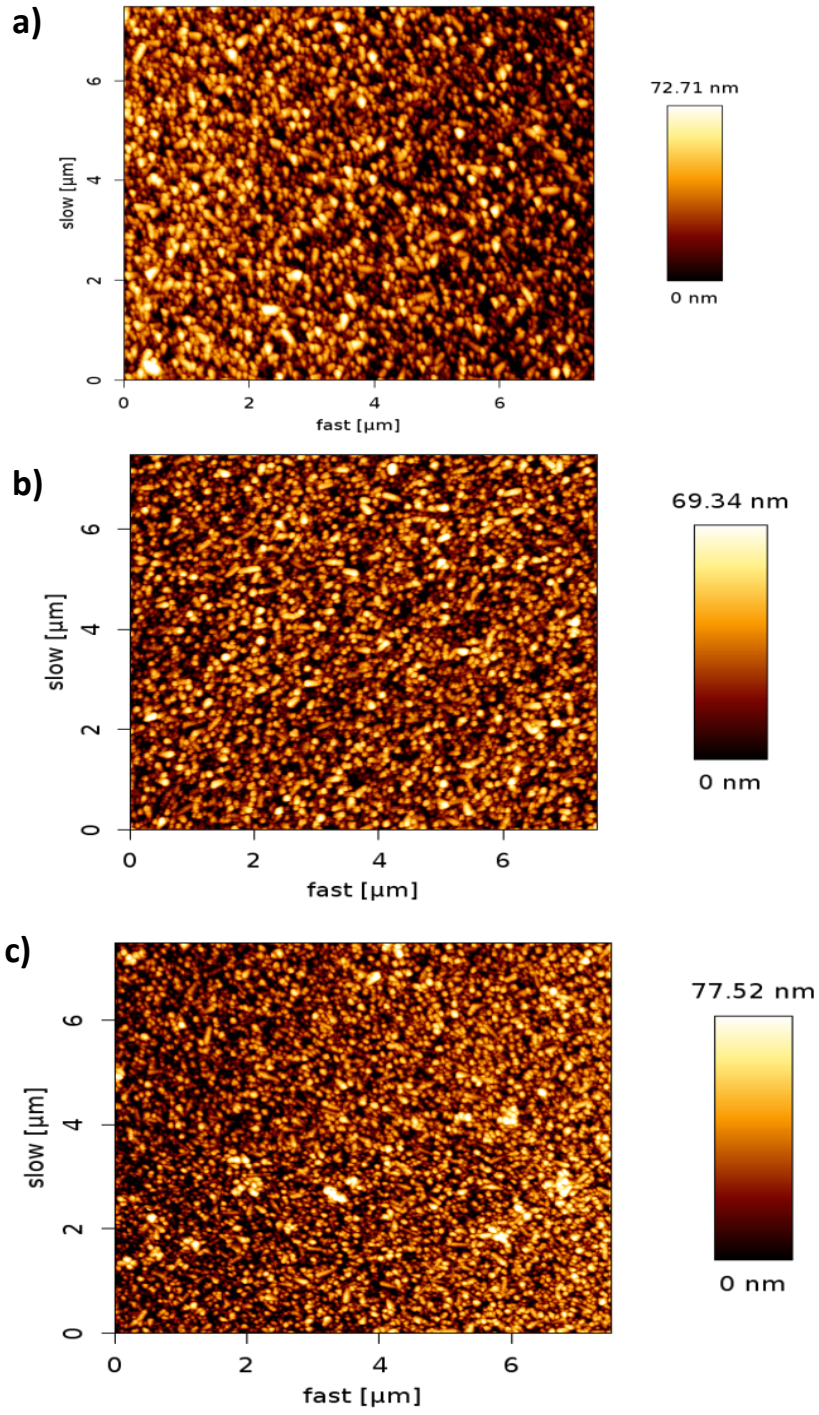

Figure 3.6: AFM imagery taken using a JPK Nanowizard 3 AFM, using a 0.8 newton meter tip in contact mode. All images taken are of dimensions 7.5 μm by 7.5 μm for comparative purposes. a) TEC15 FTO glass, b) TEC15 FTO overlaid with 50 nm of spray pyrolysis deposited TiO_2, c) Pilkington Eclipse Advantage.

The observations in Figure 3.5 confirm that the EA sample has a very thin but highly conformal and homogeneous thickness of TiO_2 overlaid upon the relatively large FTO grains. Cross-sectional SEM measurements confirm that the TiO_2 layer is thin, around 20 nm thick. It should be noted that there is only the one material layer overlaying the FTO and the layer seen above in the background TiO_2/ FTO of the cross-section sample as a tilt 50 degrees. The cross-sectional SEM also shows the FTO, SiO_2, SnO_2 present in eclipse advantage as described by the parent company NSG Pilkington in the technical specifications mentioned the introduction of chapter 3.1. It is important to note that although EA has a thinner FTO layer (~200 nm) compared to TEC15 samples for spray pyrolysis and standard lab devices (540 nm) the conductivity remains unaffected as confirmed by the four-point probe measurements. The average roughness values (ARV) calculated via AFM analysis (multiple line analysis – inbuilt into the AFM software, Nanowizard) show very little difference in EA, Spray pyrolysis and bare FTO glass with ARVs of 14.03, 12.57 and 13.15 nm respectively. The difference in the values is down to natural variation in roughness seen in the FTO. All three show a maximum peak – trough roughness of around 70 nm, slightly more with regards to EA (6 nm to 8 nm) but again this is attributed to natural variation in FTO, these figures indicate that subsequent layer processing will not be hindered by a surface morphology that is too rough to coat over large areas via solution processing.

In order to quantitatively determine the surface elemental composition of the TiO_2 layer applied to the EA substrate, x-ray photoelectron spectroscopy (XPS) was employed. Figure 3.7 shows an elemental map of a mechanically scribed region of the EA in order to expose the underlying surface. On the sample surface Ti is observed (highlighted in red), with exposed Sn (highlighted in blue) seen in the scribed areas, the dark areas are contaminants/ debris left over as a result of the scribing process. The analysis showed Ti and Oxygen peaks, with the Ti peaks being consistent with Ti (IV) present in TiO_2. With the EA substrate, a significant amount of Sn and C was detected at the surface. These are a result

of sample contamination during the manufacturing process. In addition, XPS depth profiling revealed that the Ti layer found on EA is thinner than what might be preferred in PSCs according to literature, [17] estimated to be around 20 nm which confirms the measurements taken with the Zeiss cross beam SEM. Recent work has shown that highly efficient PSCs utilizing ultra-thin TiO_2 electron transport layers as low as 2 nanometers can produce excellent PCEs [18] [21]. It has also been demonstrated that a compact TiO_2 may not be required at all to achieve reasonable PCEs, but such devices seldom reach PCEs of over 14 %. [20]

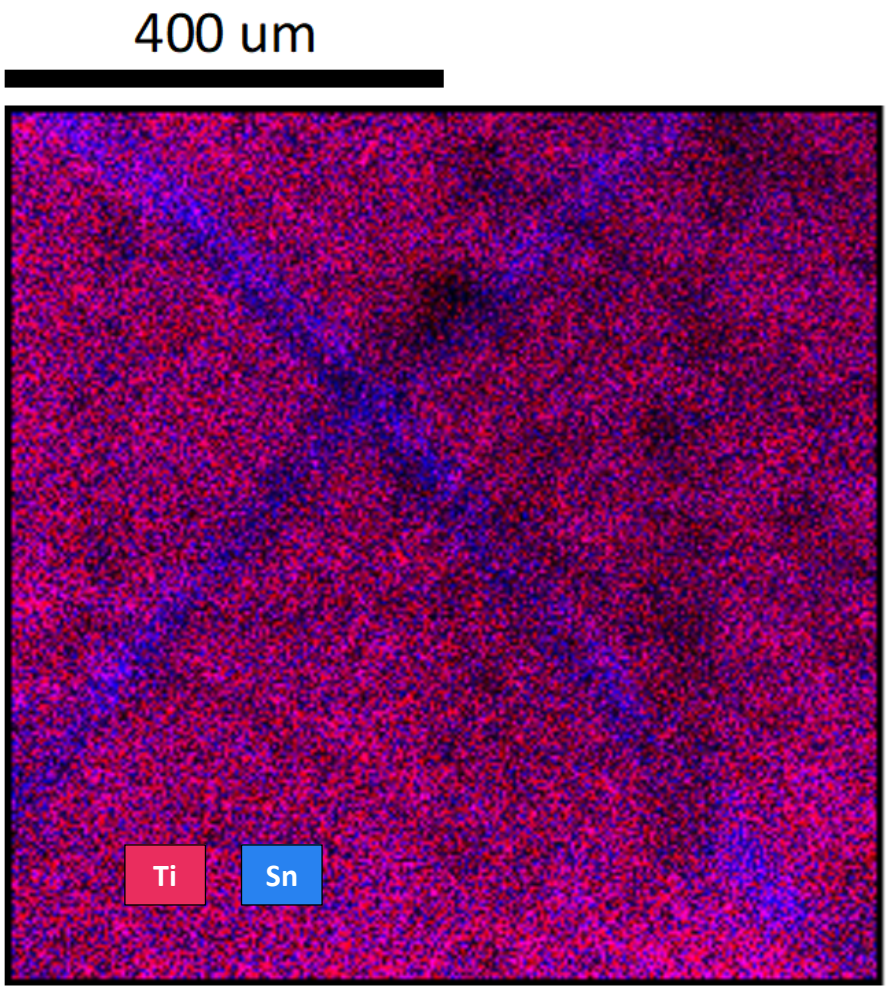

Figure 3.7: XPS elemental mapping of a scratched Pilkington Eclipse Advantage surface. Red indicates the presence of Ti whereas blue indicated the presence of Sn.

Raman spectroscopy was used to further identify the presence of TiO_2, and any associated crystalline behavior. Sharp intense peaks give an insight into the degree of crystallinity within a film, while broad, less intense peaks are indicative of amorphous materials. A plot of Raman shift intensity for both a 50 nm spray pyrolysis processed c-TiO_2 and EA substrates is shown in Figure 3.8. Interestingly, while the TiO_2 indicative peak at 145 cm^{-1} is present for the conventionally processed c-TiO_2 layer via spray pyrolysis, no such peak is present in the EA sample [22]. Figure 3.8 also shows the spectra of a EA sample having undergone an additional heat treatment at 550 °C in order to induce a crystallographic transformation of any TiO_2 present to the anatase polymorph. Despite a drop in Raman shift intensity around 445 cm^{-1} and 550 cm^{-1} indicating the presence of SnO_2 (FTO) the anticipated TiO_2 peak fails to manifest itself following heat treatment.

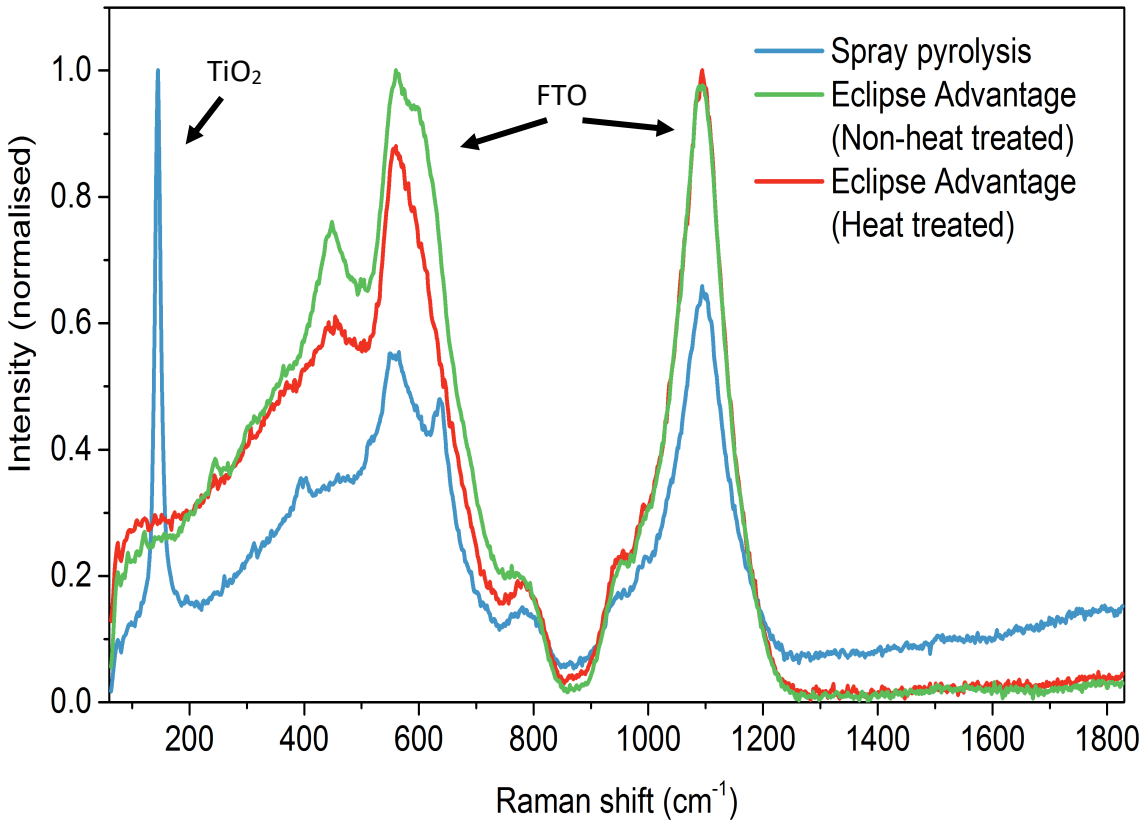

Figure 3.8: Raman spectra measured for a standard control c-TiO_2 layer on FTO-coated glass processed via spray pyrolysis as well as pre and post heat treated

(550 °C for 30 minutes) Pilkington Eclipse Advantage.

X-ray diffraction (XRD) was employed to probe further the presence of crystalline TiO_2 on both EA and spray pyrolysed processed films as seen in figure 3.9 below:

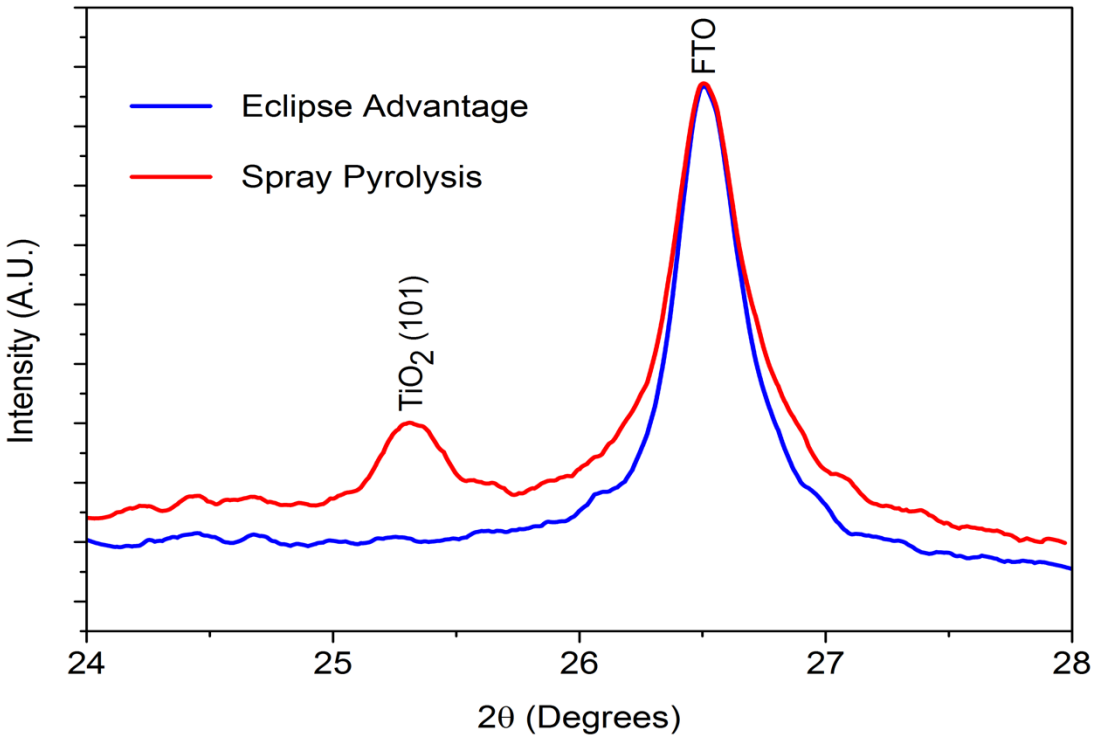

Figure 3.9: XRD plot to show the relative peak intensities for Pilkington Eclipse Advantage and Spray Pyrolysis TiO2 on FTO-coated glass.

The data suggests that the c-TiO_2 in the spray pyrolysed films is crystalline in nature as suggested by the peak around 25.25 degrees which correlates to the anatase TiO_2 (101) atomic planes. The corresponding peak for FTO at 26.5 degrees can be observed in both samples; the intensity and sharpness of both peaks indicate a highly crystalline film, corroborated by the Raman spectra in Figure 3.8. The Raman and XRD show no characteristic crystalline TiO_2 traces in EA suggesting an amorphous, disordered structure in nature, as the corresponding peaks at 25.24 degrees and 125 cm^{-1} for crystalline TiO_2 fail to manifest. It is worth mentioning that Raman spectroscopy and XRD are limited in the analysis of very thin films (<20 nm) especially where the crystalline range is

very small. Work carried out by Chandiran et al. and Tilley et al. demonstrated that Raman and XRD are known to suggest very thin films of c-TiO_2 are amorphous in nature. [23] [24] [25]. It has also been demonstrated that the crystallinity of such thin layers may not be a barrier to solar cell performance, with PCEs of 19.2% achievable on planar heterojunction devices utilizing an atomic layer deposited amorphous TiO_2. [19] The presence of TiO_2 proves difficult to identify through x-ray diffraction and Raman spectroscopy as has been shown previously for ultra-thin layers (less than 20 nm), this is remedied by the XPS data discussed previously

Cyclic voltammetry (CV) is an electrochemical technique that can uncover the characteristic hole-blocking properties (pinhole densities and coverage yield) of TiO_2 in the EA and spray pyrolysis substrates when present on an conductive (FTO) surface. It can also be used to examine larger areas of coated substrates for defects than is possible with technique such as SEM, XRD, Raman and XPS which are limited to finite small areas in the region of a few microns.

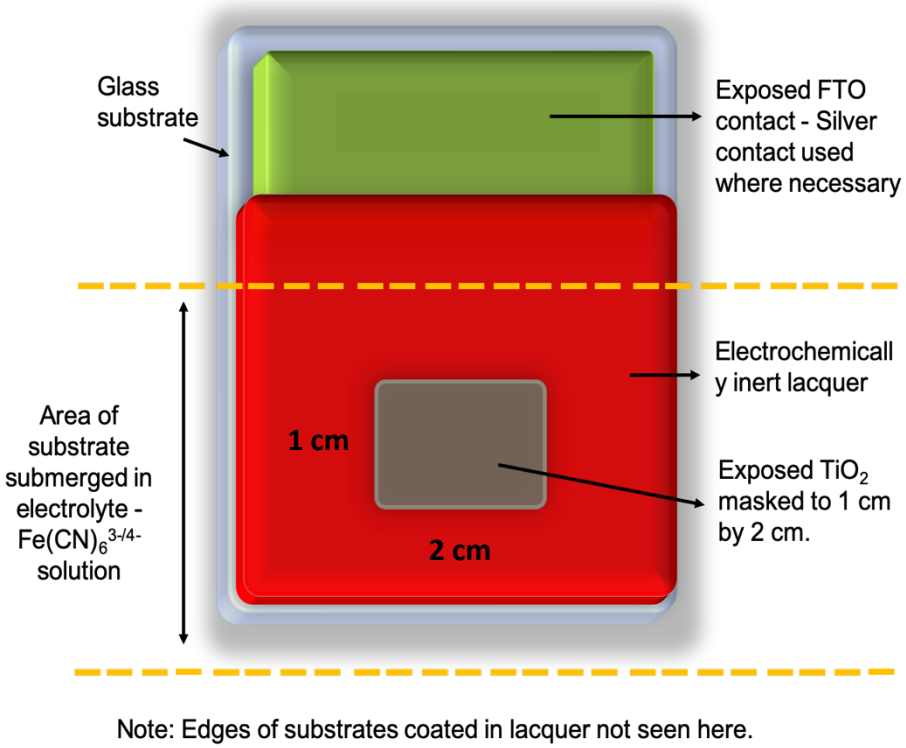

Note: Edges of substrates coated in lacquer not seen here.

Figure 3.10: Schematic to show how samples were prepared for cyclic voltammetry. Exposed sample areas were 1 cm by 2 cm as shown above.

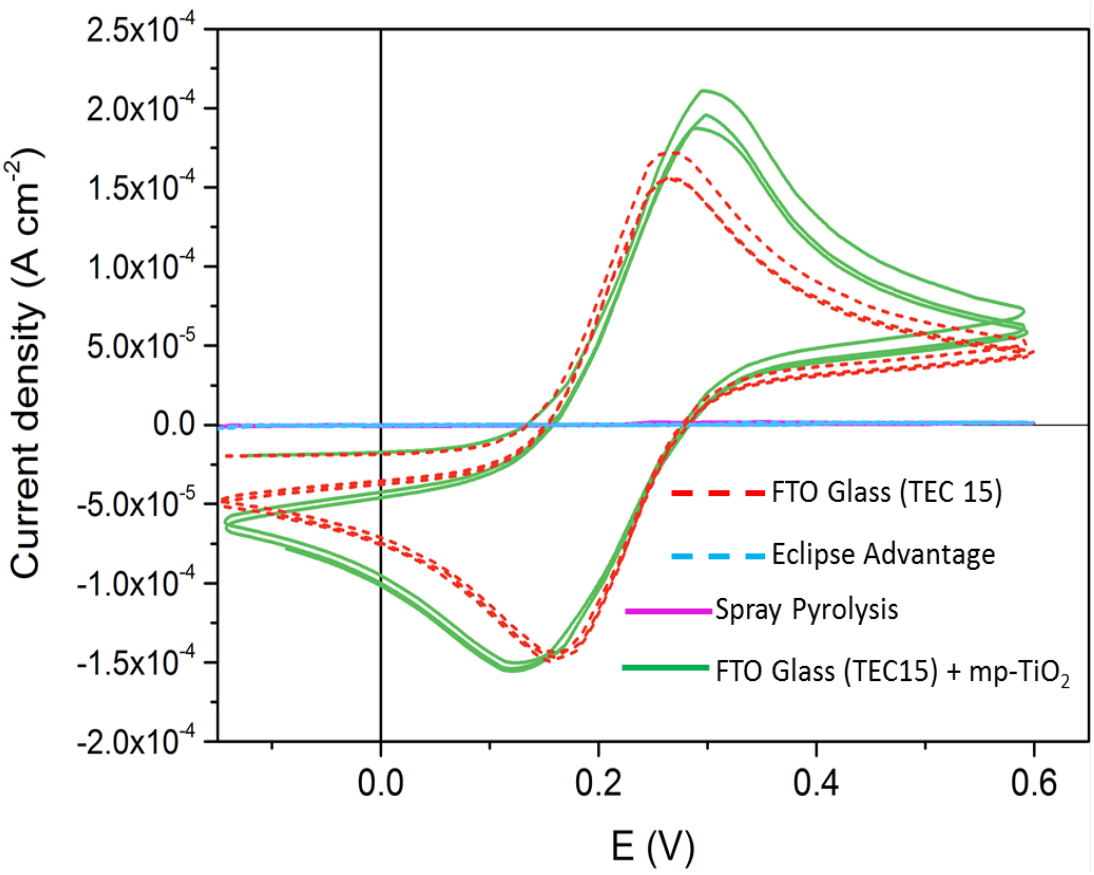

Figure 3.11: Cyclic voltammograms of Pilkington Eclipse Advantage and spray pyrolysis processed c-TiO_2 layers, including additional mesoporous (mp) TiO_2 layers. Note: The Eclipse Advantage trace (blue) and Spray pyrolysis trace (purple) virtually overlap one another and no anodic or cathodic activity is detected over the voltage range.

Figure 3.11 and 3.12 shows cyclic voltammograms of different TiO_2 films exposed to a potassium ferro/ ferri cyanide electrolyte couple. In this experiment, the $Fe(CN)_6^{3-/4-}$ solution acts as a model redox in a three-electrode cell, with the TiO_2 coated FTO glass acting as a working electrode. CV was carried out on several different areas of the eclipse advantage sheets (numerous samples taken from different sheets of 30 cm x 30 cm) supplied by NSG Pilkington to test the effectiveness of the ETL over a large area and compared to similar large area spray pyrolysis device. Each CV measurement was masked with an electrochemically inert lacquer to 1 cm x 2 cm. EA and a 50 nm thick spray pyrolysis processed compact TiO_2 layer both show a strong blocking effect over the voltage range as there is minimal current activity, indicating good quality TiO_2 blocking layers

with high film coverage that make a rectifying interface. At this point no anodic currents of Ferro cyanide oxidation can flow because TiO_2 is in the depletion regime (i.e. no current can flow/ be detected) at these potentials (-0.15V to 0.6V). If the CV scan were to be extended down to -0.7 V, the cathodic current would be detected meaning the TiO_2 layer is in the accumulation regime i.e. exhibiting metallic behaviour as described by Kavan et al. [26] [27] Pin holes and defects were monitored by measuring any anodic current response; the current measured from these effects arises from the ferrocyanide oxidation at the bare FTO regions, thus indicating an inhomogeneity within the film. Our results for FTO are within good agreement to that published by Tzu-Sen Su and Kavan et al. in that a clear anodic current and subsequent cyclic voltammogram mirrored that reported previously. [27] [28]. One of the major drawbacks to spray pyrolysis has been its unreliability to reproduce homogeneous films due to operator and human area. The sensitivity of the CV measurement reveals the presence of defects within the c-TiO_2 otherwise undetectable with the electron microscopy. Characteristic signs of pin holes were deduced from the corresponding increase in anodic activity resulting from ferrocyanide oxidation occurring at uncoated FTO regions as seen in Figure 3.12. An increase in cathodic activity (current increase), also described in section 1.6.3, indicated a relatively poor film coverage for this sample as shown by Tzu-Sen-Su and co-workers. [28] Conversely; EA showed no appearance of defects or pinholes under CV across all samples tested, giving further credence to the reproducible nature of chemical vapor deposition. Bare FTO does not have any hole blocking layer characteristics as evidenced by the Nernstian response in the CV pot in Figure 3.11. The cathodic (Epc) and anodic peak potential (Epa) are separated by 92.00 mV. The ΔEP is within a reasonable degree to that of the theoretical value of 56.00 mV for a one-electron reversible reaction. This is because the theoretical value of 56.00 mV is an ideal situation, whereas under our set-up conditions resistances associated with the solution; contacts, area masking, barrier layer lacquer, lack of a faraday cage and wiring were not accounted for in these calculations and thus increased the ΔEP . This means the redox reaction of the electrolyte is electrochemically reversible on

bare FTO, suggesting no blocking effect. This result is also within good agreement to that published by Tzu-Sen Su and Kavan et al. [27] [28] The blocking effect of mesoporous TiO_2 scaffolds were also investigated in full devices. 30NRD, procured from Dyesol was prepared by diluting its paste with a mixture of Terpineol and (IPA) to produce a 200 nm thick layer via spin coating. 30NRD has an average Nano-particle size of 30 nm, and gives a transparent Titania film with a large surface area to volume ratio upon sintering at 550 °C. The resulting voltammograms in Figure 3.11 show that a 30NRD mesoporous TiO_2 scaffold exhibits no blocking effect. The porous nature of the film exposes bare FTO to the electrolyte that gives rise to a substantial anodic and cathodic current being observed, much the same as with bare FTO. Again, the behaviour is Nernstian and the redox reaction reversible. We attribute the very small amount of current (of the order of micro-amperes) observed in the EA and homogeneous spray pyrolysis samples to be down to capacitive charge effects as the number of voltage cycles increases. The small currents detected are a consequence of the lack of Faraday cages used in our set-up which results in small currents being detected from the surrounding environment, this is also close to the instruments resolution. [29]

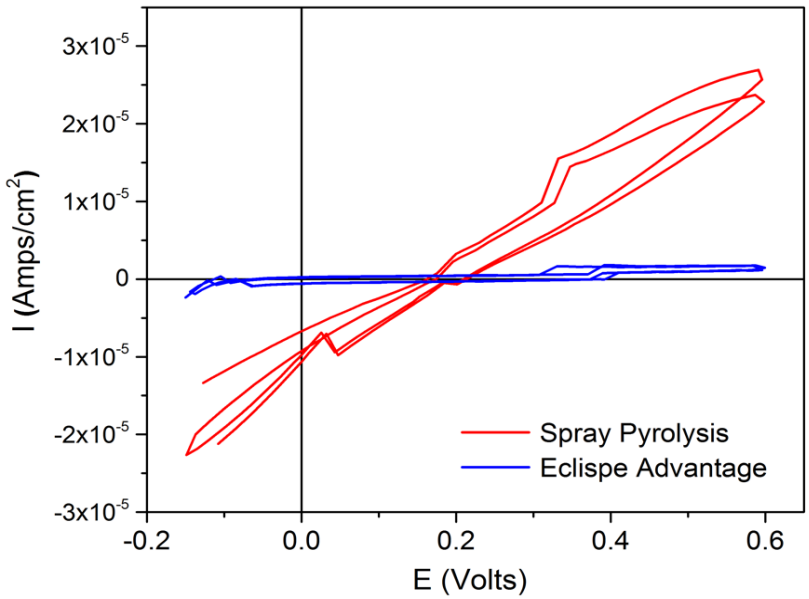

Figure 3.12: Characteristic pinholes found in a spray pyrolysis TiO_2 as demonstrated by cyclic voltammetry, highlighted by the inert Eclipse advantage over the same voltage range.

Following confirmation of a blocking function on EA, full devices based on a mixed cation composition were fabricated. The device architecture can be seen in Figure 3.3, with the perovskite based around published work by Saliba et al. [14] The resulting caesium containing triple cation perovskite of composition $Cs_{0.05}(MA_{0.17}\ FA_{0.83})_{(0.95)}Pb(I_{0.83}\ Br_{0.17})_3$ produces excellent films for power conversion efficiencies as can be seen in Figure 3.16. As explained in chapter 3.2 we chose to employ the mesoporous scaffold (30RND) into both spray pyrolysis and EA architectures. One key difference in the processing of EA involves the electronic isolation of the cells which is necessary to enable electrode contacting in solar cell fabrication; this is done in spray pyrolysis usually by etching a masked area of FTO with a suitable acid, usually concentrated hydrochloric acid in combination with a reactive metal powder such as Zinc. In order to electrically isolate the desired regions of FTO in EA, one must additionally remove the TiO_2 layer deposited on top of it by the CVD process. We achieved this through the use of a neodymium sourced YVO_4 yttrium orthovanadate laser with wavelength of 532 nm, operating at 32 Amperes, line speed of 20 mms^{-1} and a pulse repetition rate of 20,000 Hz and 15,000 Hz for Eclipse Advantage and FTO respectively.

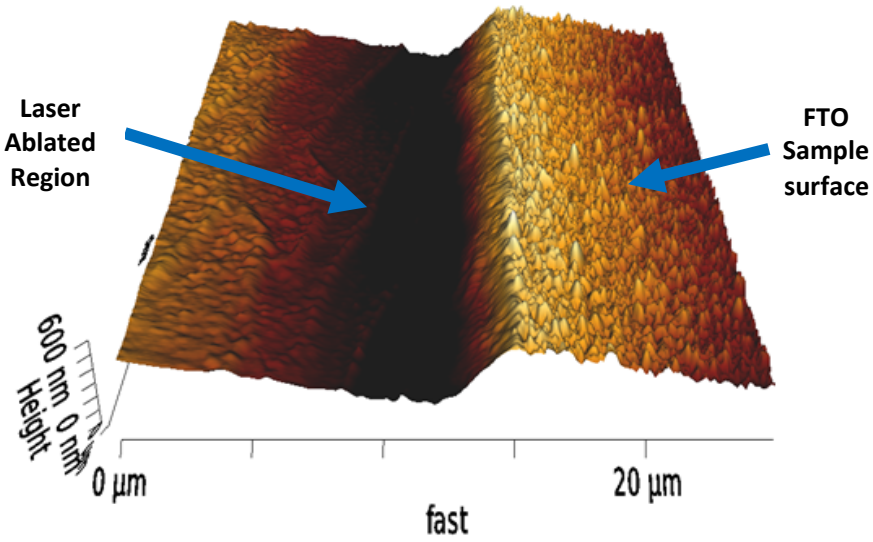

Figure 3.14: AFM imagery post Laser ablation of TEC15 FTO using a neodymium sourced YVO_4 yttrium orthovanadate laser.

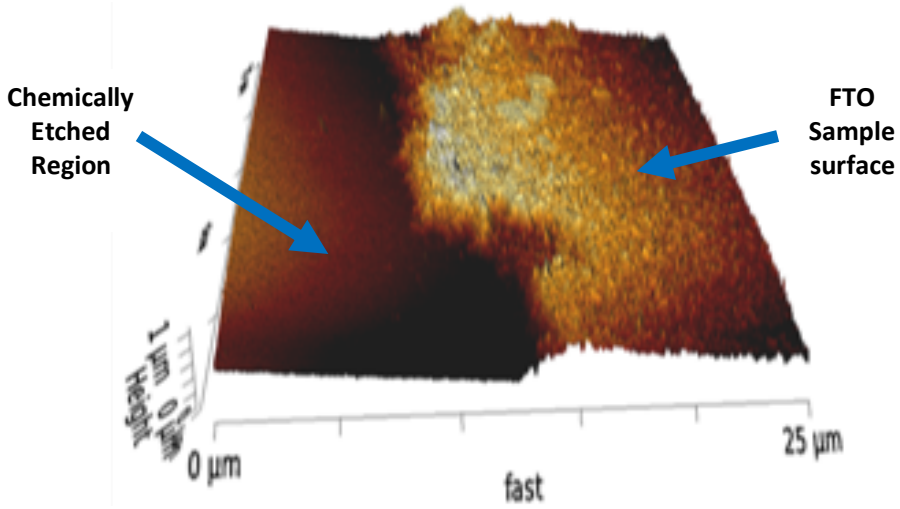

Figure 3.15: AFM imagery post chemical etching of FTO regions using concentrated hydrochloric acid and powdered zinc.

The ablation depth of this process is seen in figure 3.14 and a comparison made with conventional chemical etching of FTO in figure 3.15. From the two AFM images it is clear to see laser ablation allows for a higher degree of morphological surface control and precise removal of FTO and ETL materials while also reducing the chance of contamination. The substrate is ablated enough so that the FTO in both cases is completely removed without unnecessarily damaging the base material of the glass that could induce thermal stresses and eventful cracking in the glass during annealing and cooling stages.

An analysis of Current-Voltage (J-V) statistics for EA devices is presented in Figure 3.16 and Table 3.1. Device performance for EA and spray pyrolysis were characterized by illuminating each 0.1 cm^2 pixel with a solar simulator (Oriel Sol AAA 940238) and tested under 1 sun illumination in air. It can be seen that EA marginally outperforms spray pyrolysis cells in terms of power conversion efficiencies (+1.1 % for champion devices and +1.9 % on maximum stabilized power outputs), the record device for EA achieved a stabilized power conversion efficiency of just under 15% over 180 s of maximum power point tracking (J_{mpp}), the maximum PCE achieved in a single unstabilised device was 15.9% whereas devices with a spray pyrolysis blocking layer achieved a maximum PCE of 14.8%.

that reduced to 13.1% on stabilized measurement. Overall batch data using the median for EA (median PCE 12.1) and spray pyrolysis (median PCE 11.2) were notable similar but again on average eclipse advantage outperformed spray pyrolysis by 0.9 %. The no ETL sample "Mesoporous TiO_2" displayed a slightly lower PCE again with a record PCE of 12.9 % and a median PCE of 10.9 %. A high V_{OC} in both spray pyrolysis (Peak V_{OC} 1.04 V) and EA (Peak V_{OC} 1.06) demonstrate two effective blocking layers with good band gap alignment.

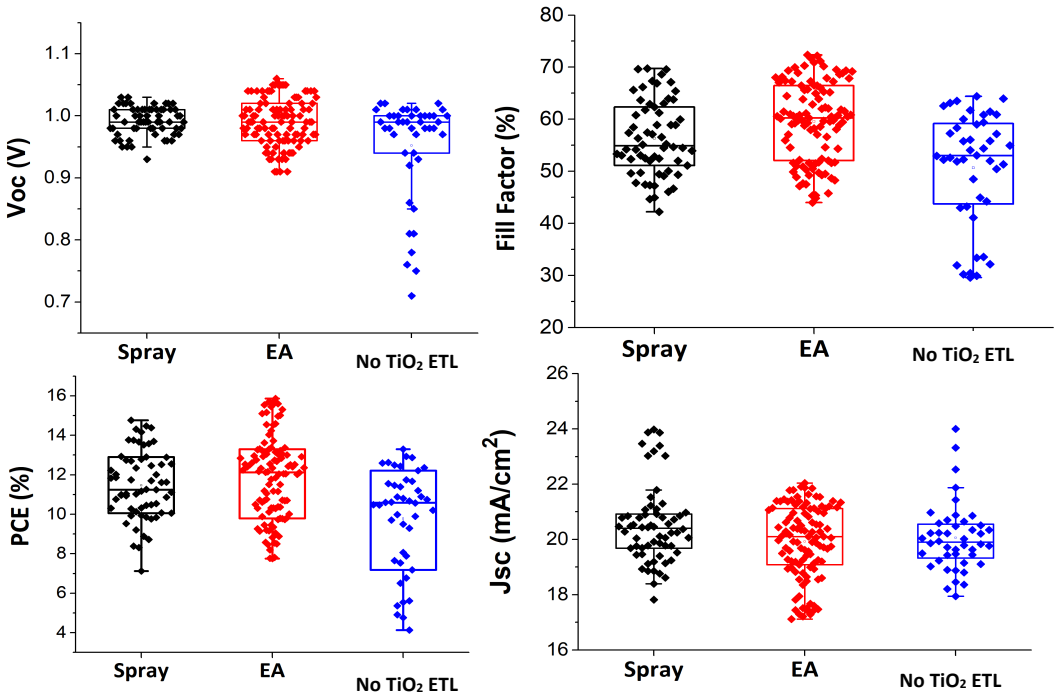

Figure 3.16: Statistical analysis of J-V parameters for spray pyrolysis processed TiO_2, Pilkington Eclipse Advantage and samples without a compact TiO_2 ETL (labelled Meso). All Devices were built and tested concurrently to avoid batch to batch variation. Forward and reverse measurements are highlighted below in table 3.1.

Table 3.1: Summary of the best performing devices for Pilkington Eclipse Advantage (EA), Spray pyrolysis deposited TiO_2 and blocking layer free devices (Meso)

Cell Variant	Voc (mV)	Jsc (mAc m^{-2})	Fill Factor (%)	Max PCE (%)	Stabilized PCE (%)
EA (Reverse)	1040	21.4	71.2	15.9	14.9
EA (Forward)	1000	21.2	59.3	12.5	
Spray (Reverse)	990	21.3	69.7	14.8	13.1
Spray (Forward)	990	20.7	54.7	11.2	
No TiO_2 ETL (Reverse)	980	20.5	64.4	12.9	10.7
No TiO_2 ETL (Forward)	1000	19.5	48.5	9.5	

The resulting EA JV curve shown in Figure 3.17 shows there is some residual hysteresis, but it appears to be limited and the same can be observed in the spray pyrolysis cells shown in figure 3.18. The hysteresis observed is common in TiO_2 based devices and can be attributed to a lack of optimization in the perovskite film processing conditions, such as residual solvents present in our glove box due to a lack of laminar flow capabilities. It can be seen that the origin of the hysteresis is not due to the TiO_2 ETLs as both TiO_2 ETL deposition methods and devices without a compact ETL show similar levels of hysteresis. The origin of the observed hysteresis lies primarily in the mobility of halide ions present within the perovskite material, this coupled with the aforementioned unoptimized processing conditions, with residual solvents allowing for greater ion mobility. We postulate a higher degree of surface recombination at the perovskite Spiro-OMeTAD and mesoporous TiO_2 interfaces. 30] [31] [32] [33]. The V_{OC} for all devices is relatively high; this would indicate high perovskite film coverage and a low defect density. This is because poor coverage and a high degree of pin holes has been shown to cause a reduction in voltages in perovskite devices through

recombination at the interface between the compact TiO2 blocking layers and Spiro-OMeTAD that arises inside pinholes

as reported by Carnie et al. [34]

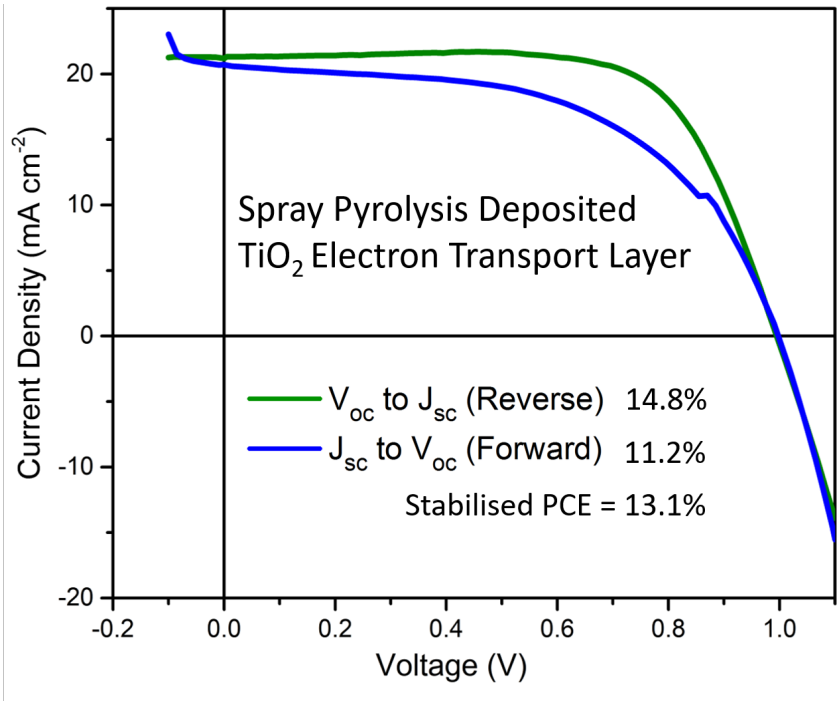

Figure 3.17: JV curves and stabilised measurements for champions device incorporating Pilkington Eclipse Advantage.

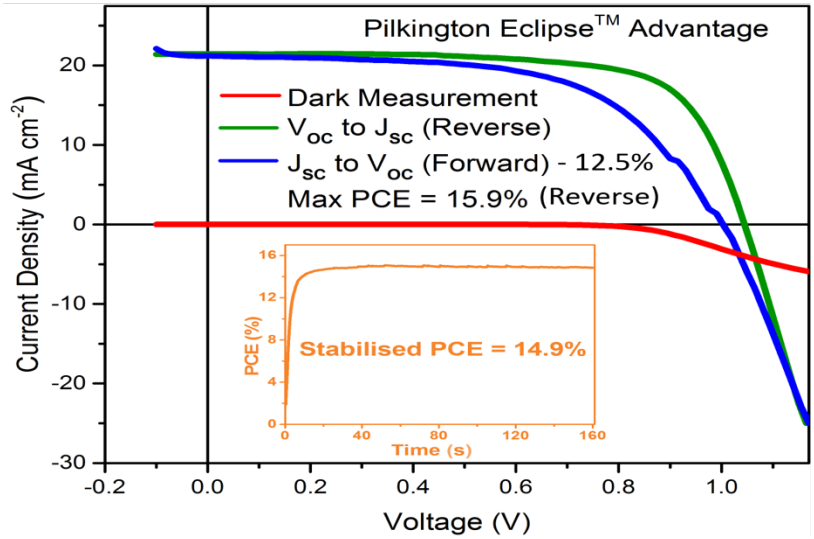

Figure 3.18; JV curves of champion device incorporating a TiO_2 ETL via spray pyrolysis.

The high (>20 mA cm^{-2}) associated J_{SC} across all samples indicate that there is a sufficient capping layer of perovskite above the mesoporous scaffold that allows for large current densities to be generated through maximum absorption of incident light. The fill factors for all samples (EA, spray pyrolysis and meso TiO_2) could be considered an area for improvement. Though not low, it appears fill factors have been reduced by the effect of increased series resistance as evidenced in table 3.1. We attribute this to poor contact at the perovskite/ Spiro-OMeTAD interface and a lack of optimised Spiro-OMeTAD processing conditions within our labs as reported by Troughton et al. [11]. Occasional pin holing was noticed in devices and this was attributed to the lack of a laminar flow glovebox, allowing a solvent build up as well as unoptimized Spiro-OMeTAD additives such as Li-TFSI. Saliba et al [30] reported that heating of the Li-TFSI to temperatures in excess of 180 degrees Celsius ensured complete dissolving of the Li-TFSI salt in acetonitrile., whereas dissolving at room temperature could leave trace Li-TFSI salt behind suspended in solution and not dissolved. Our labs, at the time of processing did not use solution heating so we highly suspect undissolved Li-TFSI salt molecules present in the unheated solution were added to the Spiro-OMeTAD solution, which when spin coated onto perovskite were later observed as having a small concentration of pin holes. Devices were also fabricated onto FTO (TEC15) with no compact TiO_2 blocking layer whatsoever; these cells again incorporated a mesoporous TiO_2 scaffold into the cell architecture. These devices performed higher when scanned from V_{OC} to J_{SC}. Where a peak PCE was observed at 12.9%, but under testing in the forward direction (J_{SC} to V_{OC}) PCEs reduced to nearly half that when tested in the reverse scan (V_{OC} to J_{SC}). In addition to this, stabilized PCEs were noticeably lower than both spray pyrolysis and EA with a maximum stabilized PCE of 10.7% achieved indicating hysteresis within the cell. We attribute this to increased recombination of electron-hole pairs due to the lack of blocking effect and subsequent charge separation at the FTO/ Mesoporous TiO_2 / perovskite interfaces within the device. Perovskite film morphology could be further optimised on the EA substrate (for example by varying the deposition process of perovskite) to improve performance as processing conditions for both

planar TiO_2 and mesoporous TiO_2 devices is critical [35]. In this study EA still outperforms our optimized spray pyrolysis samples, the mesoporous TiO_2 layer has been optimized for use with spray pyrolysis and not EA. Given the resulting Jsc for both EA and Spray pyrolysis are very similar (21.4 and 21.3 $mAcm^2$ respectively) and the much higher V_{OC} in EA compared to spray pyrolysis in our labs (1040mV and 990 mV) this demonstrates that the perovskite microstructure is not hampered by the EA but rather charge extraction is enhanced and recombination pathways are mitigated.

Further analysis on the devices was carried out using steady state and transient photo-voltage measurements to understand the effect of blocking layer quality on recombination. The light intensity dependence of the open circuit voltage, as seen in Figure 3.19 demonstrates the similarities between the two types of cell employing a blocking layer. Both the spray pyrolysis TiO_2 and EA devices have a similar dependence over two decades of light intensity. The mesoporous-only cell without a blocking layer exhibits a similar trend at high light intensity, with the voltage dropping off sharply below 10% intensity. This suggests that a different recombination process dominates at low light intensity when the cell has no blocking layer. This affect appears to be similar to the case for Dye Sensitized Solar Cells (DSSC) at low intensity without a blocking layer. In DSSC and PSCs this is attributed to recombination processes including the back reaction of electrons via the substrate to the oxidized electrolyte species, [36] or recombination via trap states in the TiO_2 bandgap. [37] The impact of blocking layers on PSC device performance at low intensity has not been extensively studied, but it is possible that there could be a similar DSSC-like behaviour. Gouda et al. [38] have also

observed several distinct regions in the trend of open-circuit voltage on light intensity and showed that the electron selective interface has a strong influence

Figure 3.19: V_{OC} verses Intensity measurements of Pilkington Eclipse Advantage, conventional spray blocking layers and mesoporous TiO_2 only devices that employ no compact ETL.

upon it. It has also been shown that the underlying TiO_2 blocking layer is more influential than the type of mesoporous oxide used. [10] Recombination processes have been shown to be affected by ion migration and the associated build-up of charged species at the interfaces of the device. [39] [40] [41] [42] It is possible that without the presence of a blocking layer this accumulation of ions

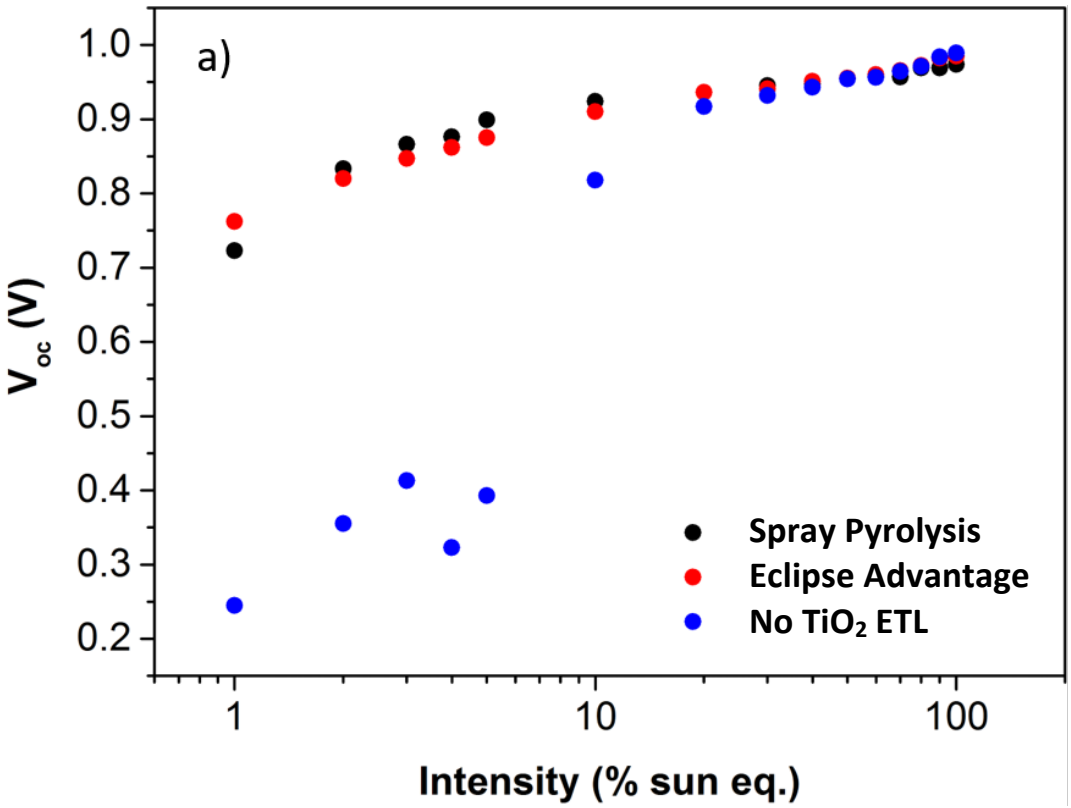

is unable to sustain a stable layer and therefore causes a less favourable band structure at the interface resulting in higher recombination. This instability may also be evidenced by the variation in open-circuit voltage at low intensity where a smooth trend is not observed. Further analysis is beyond the scope of this work, but it is clear that a good quality blocking layer is needed to produce cells that

will work efficiently over a wide range of light intensities. The transient photovoltage decays displayed simple mono exponential behaviour at all light intensities for the cells containing a blocking layer. At lower intensities the decay transients for the cell without a blocking layer showed double exponential characteristics, similar to previous work considering modifications to reduce interfacial recombination. [36] Again this data shows the almost identical performance of the two blocking layers. The increased rate of recombination at low light intensity for the cell without a blocking layer is evidenced by the sudden tailing off of the lifetime below 0.9 V as seen in Figure 3.20.

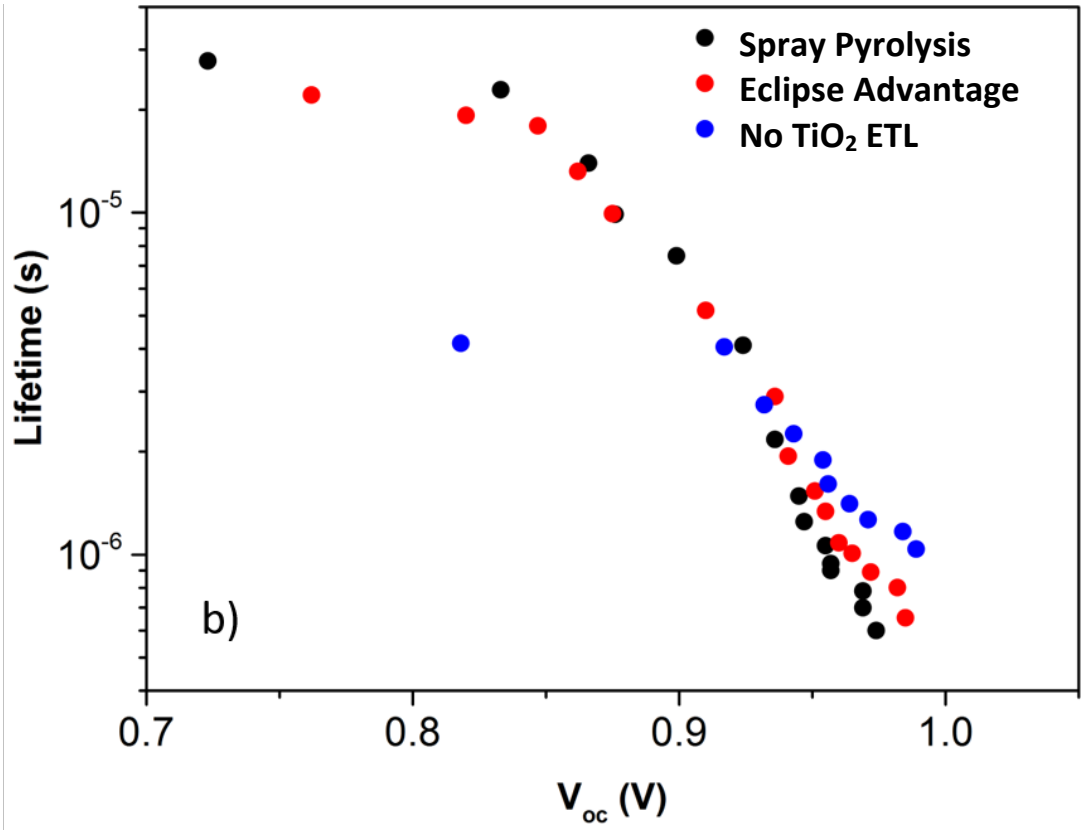

Figure 3.20: Lifetime verses VOC measurements of Pilkington Eclipse Advantage, conventional spray blocking layers and mesoporous TiO_2 only devices that employ no compact ETL.

At low light intensity the VOC could be reduced by recombination involving trap states in the TiO_2, shunting via the substrate or band edge changes due to ionic migration that are somehow mitigated by the presence of a blocking layer. The

emergence of multiple recombination processes at low intensity in the blocking layer free cell is suggested by the transition to double exponential decays. The cells with a blocking layer EA and spray pyrolysis once again show near identical characteristics in open-circuit photovoltage de- cay (OCVD) measurements, as seen in Figure 3.21. These cells exhibit a slow decay in V_{OC}, taking over 1 minute to decay to zero. In contrast, the absence of a blocking layer causes the VOC to decay completely in around 1 s. This striking difference in OCVD behaviour has been reported previously in cells that are seemingly identical at 1 sun intensities. [43] The results here suggest that the blocking layer is highly influential for the V_{OC} decay, so this technique may be very useful in analysing the quality and reproducibility of these layers. It should be noted that the voltage in these devices had a higher initial voltage than those in figure 3.20. The reason being is that 2 champion cells were taken from each sub-set (EA, Spray pyrolysis and Mesoporous TiO_2) post JV testing. The repeated testing, lack of encapsulation and wear on the evaporated contacts is postulated to the reason for the discrepancy.

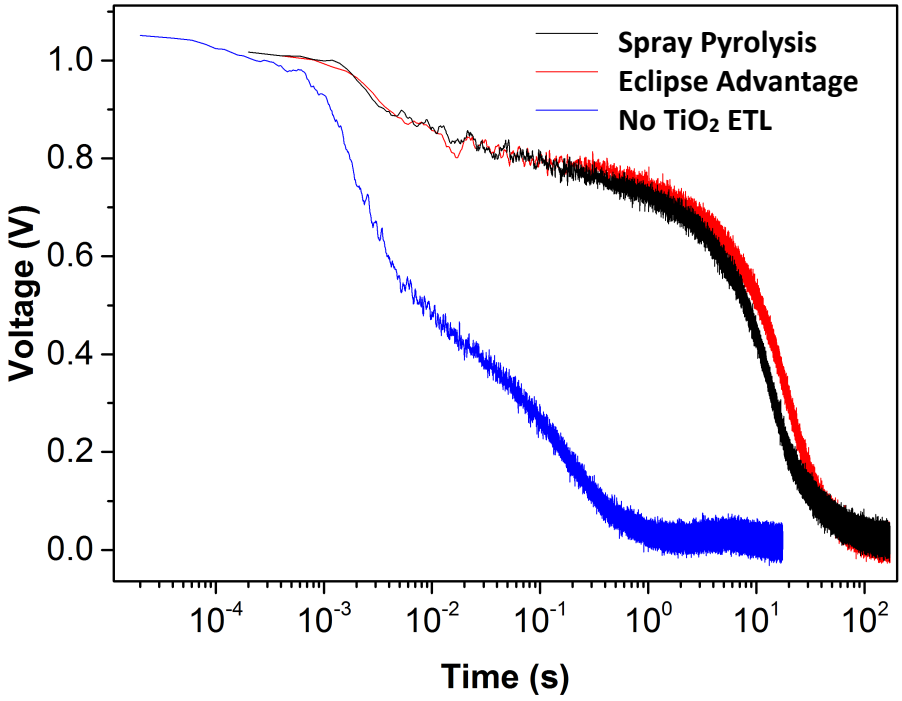

Figure 3.21: Open circuit photovoltage decay measurements of Pilkington Eclipse Advantage, conventional spray blocking layers and mesoporous TiO_2 only devices that employ no compact ETL.

3.4 Conclusions

The work in this chapter presents an alternative technology to depositing compact TiO_2 spray pyrolysis blocking layers. EA originally designed for use as a solar control product, utilizes a thin, < 20 nm CVD TiO_2 compact blocking layer and conductive FTO base layer to perform remarkably well in a mesoporous triple cation perovskite device with PCE up to 15.9%, this is higher than that produced via spray pyrolysis within our research group. Cross sectional SEM and XPS, confirm that the layer of TiO_2 in EA is very thin (<20 nm). The crystalline nature of the TiO_2 proved difficult to surmise via XRD and Raman owing to the thin nature of the film and the aforementioned limitations of techniques used, however no crystalline TiO_2 manifest itself for the EA sample suggesting it is amorphous in nature, despite the processing temperature being in excess of 550 degrees Celsius, in line with anatase TiO_2. Despite being designed as a solar control product, EA makes a highly suitable, mass manufacturable perovskite photo voltaic substrate, performing well under standard testing conditions, with relatively high short circuit currents, open current voltages and fill factors. There is potential for even better performances by tuning the physical and optical TiO_2 parameters. The substrate has the potential to remove process bottlenecks such as the laborious spraying and sintering of blocking layers while at the same time streamlining the fabrication process to reduce total build times. The use of cyclic voltammetry indicated EA shows a strong blocking effect similar to that found in spray pyrolysis TiO_2 layers sintered at 550°C. TPV and CV analysis shows TiO_2 films on the EA substrate have fewer pinholes and stronger rectifying behaviour compared to conventionally processed c-TiO_2 layers prepared via spray pyrolysis. EA doesn't suffer with the inconsistencies and technical difficulties associated with the lab produced spray pyrolysis (principally glass cracking and inhomogeneity of film coverage etc.). Automated spray pyrolysis could reduce these inconsistence at the process would be time consuming and involve the addition of a further annealing stage when compared to CVD straight off the

glassfloat line. In summary EA proves superior to spray pyrolysis for the large-scale production of effective electron transport layers based on TiO_2.

3.5 References

[1] A. Kojima, K. Teshima, and Y. S. T. Miyasaka, Journal of the American Chemical Society, 2009, 131, 6050.

[2] S. S. Shin, E. J. Yeom, W. S. Yang, S. Hur, M. G. Kim, J. Im, J. Seo, and J. S. I. Seok, Science 2017, 356,167.

[3] D. Tobergate and S. Curtis in Climate Change 2013 - The Physical Science Basis, Cambridge University Press, Cambridge, England 2013, pp. 1-30.

[4] T. Leijtens, K. A. Bush, R. Prasanna, and M. D. McGehee, Nature Energy, 2018, 3, 828.

[5] Z. Song, C. L. McElvany, A. B. Phillips, I. Celik, P. W. Krantz, S. C. Watthage, G. K. Liyanage, D. Apul, and M. J. Heben, Energy & Environmental Science, 2017, 10, 1297.

[6] K. Hwang, Y. S. Jung, Y. J. Heo, F. H. Scholes, S. E. Watkins, J. Subbiah, D. J. Jones, D. Y. Kim, and D. Vak, Advanced Materials, 2015, 27, 1241.

[7] I. Hwang and K. Yong, ACS applied materials & interfaces, 2016, 8, 4226.

[8] Y. J. Heo, J. E. Kim, H. Weerasinghe, D. Angmo, T. Qin, K. Sears, K. Hwang, Y. S. Jung, J. Subbiah, D. J. Jones, M. Gao, D. Y. Kim, and D. Vak, Nano Energy, 2017, 41, 443.

[9] D. Burkitt, J. Searle and T. Watson, Royal Society Open Science, 2018, 5, 172158.

[10] J. Troughton, D. Bryant, K. Wojciechowski, M. J. Carnie, H. Snaith, D. A. Worsley, and T. M. Watson, J. Mater. Chem. A, 2015, 3, 9141.

[11] J. Troughton, M. J. Carnie, M. L. Davies, C. Charbonneau, E. Jewell, D. A. Worsley, and T. M. Watson, J. Mater. Chem. A, 2016, 4, 3471.

[12] M. J. Carnie, C. Charbonneau, M. L. Davies, J. Troughton, T. M. Watson, K. Wojciechowski, and H. S. Worsley, Chemical Communications, 2013, 49, 7893.

[13] J. Hou, H. Y. Chen, S. Zhang, R. I. Chen, Y. Yang, Y. Wu, and G. Li, Journal of the American Chemical Society, 2009, 131, 15586.

[14] M. Saliba, T. Matsui, J. Y. Seo, K. Domanski, J. P. Correa-Baena, M. K. Nazeeruddin, S. M. Zakeeruddin, W. Tress, A. Abate, and A. H. M. Grätzel, Energy Environ. Sci, 2016, 1989.

[15] J. H. Heo, S. H. Im, J. H. Noh, T. N. Mandal, C.-S. Lim, J. A. Chang, Y. H. Lee, H. jung Kim, A. Sarkar, M. K. Nazeeruddin, M. Grätzel, and S. I. Seok, Nature Photonics, 2013, 7, 486.

[16] L. Kavan and M. Grätzel, Electrochimica Acta, 1995, 40, 643.

[17] C. Charbonneau, P. J. Cameron, A. Pockett, A. Lewis, J. R. Troughton, E. Jewell, D. A. Worsley, and T. M. Watson, Ceramics International, 2016, 42, 11989.

[18] A. K. Chandiran, A. Yella, M. T. Mayer, P. Gao, M. K. Nazeeruddin, and M. Grätzel, Advanced Materials, 2014, 26, 4309.

[19] X. Yin, C. Battaglia, Y. Lin, K. Chen, M. Hettick, M. Zheng, C.-Y. Chen, D. Kiriya, and A. Javey, ACS Photonics, dec 2014, 1, 1245.

[20] D. Liu, J.Yang and T. L. Kelly, Journal of the American Chemical Society, 2014, 136, 17116.

[21] J. T.-W. Wang, J. M. Ball, E. M. Barea, A. Abate, J. A. Alexander-Webber, J. Huang, M. Saliba, I. Mora-Sero, J. Bisquert, H. J. Snaith, and R. J. Nicholas, Nano Letters, 2014, 14, 724.

[22] A. Lewis *et al.*, "In-depth analysis of defects in TiO2 compact electron transport layers and impact on performance and hysteresis of planar perovskite devices at low light," *Sol. Energy Mater. Sol. Cells*, 2020.

[23] S. D. Tilley, M. Schreier, J. Azevedo, M. Stefik, and M. Graetzel, Advanced Functional Materials, 2014, 24, 303.

[24] A. K. Chandiran, A. Yella, M. Stefik, L. P. Heiniger, P. Comte, and M. K. Nazeeruddin, M. Grätzel, ACS Applied Materials & Interfaces, 2013, 5, 3487.

[25] J. F. Banfield, B. L. Bischoff, and M. a. Anderson, Chemical Geology, 1993, 110, 211–231.

[26] L. Kavan, N. Tetreault, T. Moehl and M. Graetzel, The Journal of Physical Chemistry C, 2014, 118, 16408.

[27] L. Kavan, M. Zukalova, and O. Vik, D. Havlicek, ChemPhysChem, 2014, 15, 1056.

[28] T. S. Su, T. Y. Hsieh, and C. Y. Hong, T. C. Wei, Scientific Reports, 2015, 5, 16098.

[29] D. J. Wiedemann, K. T. Kawagoe, R. T. Kennedy, E. L. Ciolkowski, and R. M. Wightman, Analytical chemistry, 1991, 63, 2965.

[30] M. Saliba, J. P. Correa-Baena, C. M. Wolff, M. Stolterfoht, N. Phung, S. Albrecht, D. Neher, and A. Abate, Chemistry of Materials, 2018, 30, 4193.

[31] F. Giordano, A. Abate, J. P. C. Baena, M. Saliba, T. Matsui, S. H. Im, S. M. Zakeeruddin, M. K. Nazeeruddin, A. Hagfeldt, and M. Graetzel, Nature Communications, 2016, 7, 10379.

[32] M. Abdi-Jalebi, M. I. Dar, A. Sadhanala, S. P. Senanayak, F. Giordano, S. M. Zakeeruddin, M. Grätzel, and R. H. Friend, Journal of Physical Chemistry Letters, 2016, 7, 3264.

[33] H.-S. Kim and N.-G. Park, The journal of physical chemistry letters, 2014, 5, 2927.

[34] M. J. Carnie, C. Charbonneau, M. L. Davies, B. O. Regan, D. A. Worsley, and T. M. Watson, J. Mater. Chem. A, 2014, 2, 17077.

[35] G. E. Eperon, V. M. Burlakov, P. Docampo, A. Goriely, and H. J. Snaith, Advanced Functional Materials, 2014, 24, 151.

[36] P. J. Cameron, L. M. Peter and S. Hore, Journal of Physical Chemistry B, 2005, 109, 930.

[37] P. Salvador, M. G. Hidalgo, A. Zaban. J. Bisquert, Journal of Physical Chemistry B, 2005, 109, 15915.

[38] L. Gouda, R. Gottesman, A. Ginsburg, D. A. Keller, E. Haltzi, J. Hu, S. Tirosh, A. Y. Anderson, A. Zaban, P. P. Boix, Journal of Physical Chemistry Letters, 2015, 6, 4640.

[39] S. V. Reenen, M. Kemerink and H. J. Snaith, Journal of Physical Chemistry Letters, 2015, 6, 3808.

[40] G. Richardson, S. E. J. O'Kane, R. G. Niemann, T. A. Peltola, J. M. Foster, and P. J. C. A. B. Walker, Energy Environ. Sci, 2016, 9, 1476.

[41] A. Pockett and M. J. Carnie, ACS Energy Letters, 2017, 2, 1683.

[42] P. Calado, A. M. Telford, D. Bryant, X. Li, J. Nelson, B. C. O'Regan, and P. R. Barnes, Nature Communications, 2016, 7, 13831.

[43] A. Pockett, G. E. Eperon, T. Peltola, H. J. Snaith, A. Walker, L. M. Peter and P. J. Cameron, The Journal of Physical Chemistry C, 2015, 119, 3456.

Chapter 4

TEC15-D: A Dual-Purpose Mass Manufactured Electron Transport Layer Based on SnO_2

Work in this chapter used as a basis for a paper published in the Journal of Materials Chemistry C (Wei Zhengfei, Smith Benjamin, De Rossi Francesca, Searle Justin, Worsley David, Watson Trystan). J. Mater. Chem. C, 2019,7, 10981-10987.

4.1 Introduction

In chapter 3 we presented a mass manufactured TiO_2 based substrates that although originally designed for use in thermal control windows proves an excellent ETL and is able to achieve PCEs up to 15.1 % [1]. There is however a drawback to using TiO_2 in a perovskite solar cells, crystalline TiO_2 is photoactive in the UV region of the electromagnetic spectrum where free radicals are often formed. When irradiated free radicals are formed when UV light breaks an outer electron pair of a TiO_2 molecule. The term free radical refers to an atom, molecule, or ion that has an unpaired valence electron. With some exceptions, these unpaired electrons make radicals highly chemically reactive. When a particle of dirt lands on the TiO_2 coated window in the presence of UV light from the sun the free radical, attacks the weak bonds of the dirt molecule binding to the window, (usually Van der Waal forces) and subsequent rainfall washes the dirt molecule off the window. However, in PSC these free radicals and can attack and break the weakly bonded crystalline structure of perovskites such as methylammonium lead triiodide, specifically the weakly bonded smaller halide ions thus degrading the perovskite film and comprising long term stability [2][3]. Proper UV filtration would likely be needed for any commercial perovskite solar cell based around crystalline TiO_2, this could be achieved with well designed glass encapsulation and strong UV absorbing films. Furthermore, TiO_2 based PSC tend to exhibit a hysteresis behaviour more strongly than other ETL materials [4]. Finally, high temperatures associated with the fabrication of Tio_2 ETLs can be a barrier to commercialisation, although recent research has shown that low temperature processed TiO_2 are possible and produce reasonable power conversion efficiencies of around 14% [5].

SnO_2 has recently emerged as promising new alternative to the conventionally used TiO_2 although these cells still boast some of the highest efficiencies ever recorded for a perovskite solar cell [6] with promising short to medium term stability (< than 1 year). SnO_2 was described by Qi Jiang et al. [7] as a wonderful ETL material, owing to an improved band alignment with the perovskite

absorption layer, high electron mobility and high conductivity that aids with efficient electron extraction. It can also be processed at low temperature (< 200 °C) and via solution processing with dispersed nanoparticles amongst other methods, meaning that the defects and high energy costs associated with annealing TiO_2 and even ZnO at temperatures above 300 °C are mitigated. [8]. Extremely high efficiencies have also been published using SnO_2 and PCEs regularly top 20 % for even planar based architectures [9]. Planar structures are simpler and faster to process as extra steps like mesoporous scaffolds can be bypassed.

Hysteresis, the difference in I-V curves from reverse (V_{OC} to J_{SC}) and forward scan (J_{SC} to V_{OC}) causes problems when trying to evaluate the real performance of devices. Hysteresis can regularly be seen in planar based PSC as well as mesoporous and inverted architectures although the presence of which is less obvious. Many hypotheses have been postulated as to what causes this effect such as charge trapping at interfaces and along grain boundaries. More recent studies have suggested charge accumulation could be the main culprit via ion migration and some hypothesis suggest ferroelectric polarisation effects, where the hysteresis in I V curves is found to greatly depend on the scan range as well as the velocity, which can, according to some be explained by the ferroelectric diode model [10][11]. SnO_2 planar ETLs have shown much less hysteresis than other metal oxides like TiO_2 and in n-i-p architectures, hysteresis is almost negligible when using SnO_2.

NSG Pilkington currently have a product known commercially as TEC15-D , which consists of 500 nm of FTO with 50 nm of SnO_2 overlaid via a CVD process controlled during the float line production of glass, very similar to the processes used to produce Eclipse Advantage ™ that was presented in chapter 3. This is of particular interest because research is scarce for depositing SnO_2 onto FTO via chemical vapour deposition, although ALD and aerosol assisted CVD (AACVD) has been achieved but the PCE of AACVD was relatively low at 10.2 % in 2018[12][13]. In this chapter we look at the processing required to fabricate PSC

using TEC15-D and subsequently characterise the suitability of the substrate for use in perovskite solar cells.

4.2 Experimental

Perovskite solar cells were fabricated in two principle architectures as laid out in figure 4.1 and 4.2. Laser processing of the films was also required in order electronically isolated desired regions of the solar cell, the details for this can be seen in chapter 2.1.1. Because TEC15-D was supplied by NSG Pilkington as blanket deposited layers on top of each other (the same as in chapter 3), lasering processing would also cut through the ETL layer meaning an intermediate would be needed again as with the mesoporous TiO_2 used in chapter 3. It was decided to use [6,6]-phenyl-C61-butyric acid methyl ester or PCBM as described in chapter 2.1.6.1.

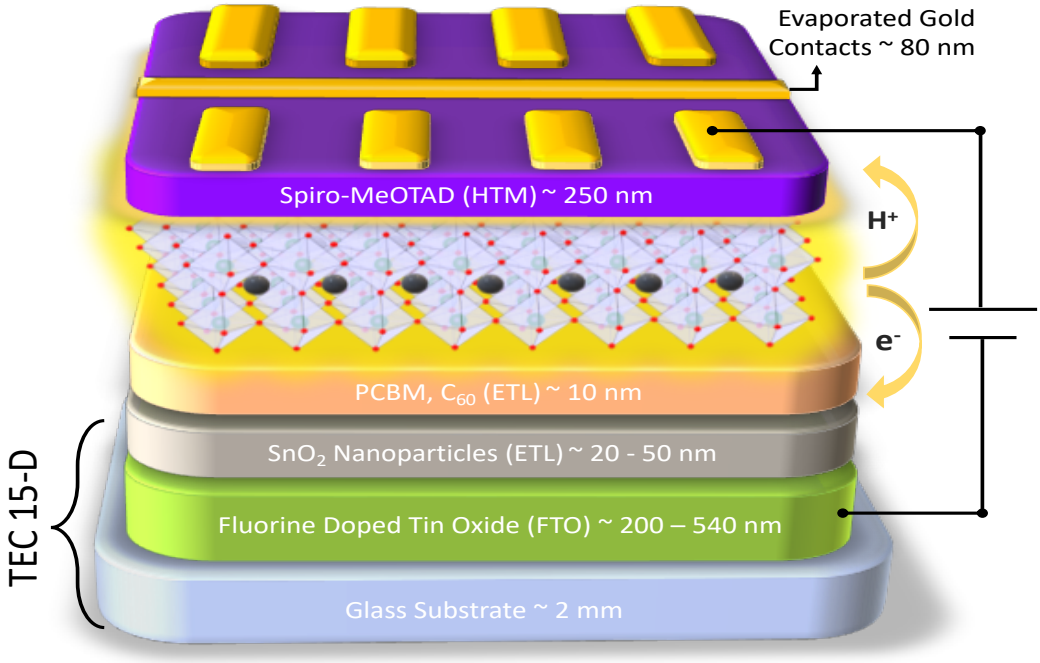

Figure 4.1: A schematic diagram showing the device architecture for cells that use TEC15-D as a TCO and ETL. NSG Pilkington TEC 15-D, consists of 50 nm of SnO_2 on top of FTO deposited via CVD. Laser processing is then used to pattern it with PCBM overlaid.

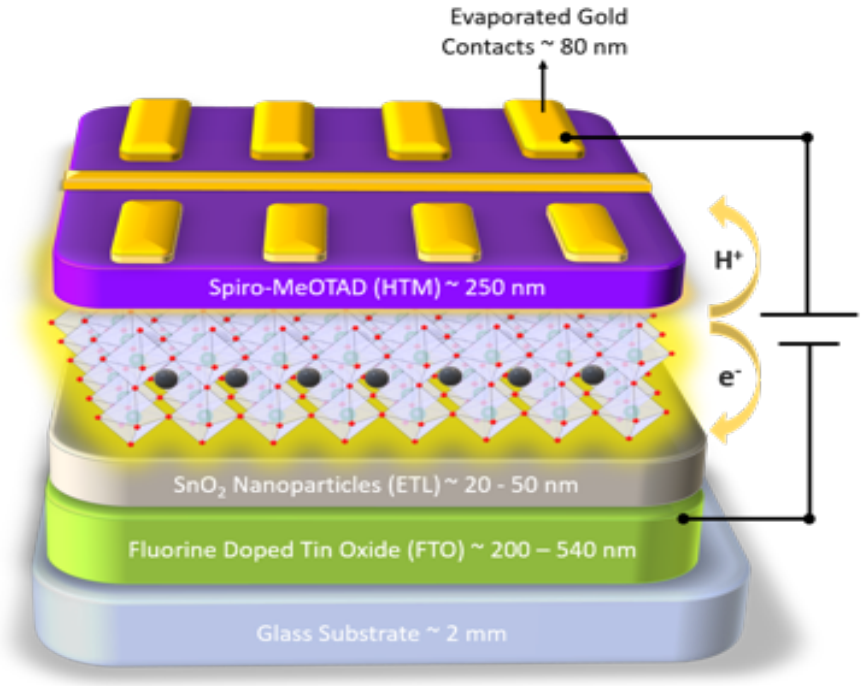

Figure 4.2: A schematic diagram of control devices prepared by depositing a solution processed SnO_2 nanoparticles, the ETL on top of FTO TEC15 glass.

Control and TEC15-D devices as seen in figure 4.1 and 4.2 were fabricated according to experimental methods 2.2, 2.1.1, 2.1.2, 2.1.3.2, 2.1.5.2, 2.1.6.1, 2.1.7.1. The control devices used an optimised solution prepared by diluting (44592) Tin (IV) oxide, 15 w/w in H_2O colloidal dispersion procured from Alfa Aesar further in de-ionised water to a final v/v ratio of 1: 2.6 and a solid content of 4.2 wt.%. This solution was then deposited via strict spin coating and cleaning parameters. (20 mins of Oxygen plasma treatment at full power followed by 15 minutes of UV ozone treatment and immediate deposition of the pre-prepared SnO_2 solution).

Characterisation methods included UV-Visible spectrophotometry (2.16), cyclic voltammetry (2.10), XPS (2.6), current-voltage sweep measurements (2.12), TPV (2.14), IPCE (2.17), 4 point probe conductivity measurements (2.3).

4.3 Results and Discussion

In order to have a control cell in which to compare TEC15-D with it was necessary to develop a laboratory based FTO/ SnO_2 substrate. It was also useful to try to optimise this system before fabricating cells of TEC15-D due to the lack of substrate available at the time and in order to inform decisions on processing when cells on TEC15-D were required. We eventually settled on using a SnO_2 ETL layer prepared by diluting (44592) Tin (IV) oxide, 15% in H_2O colloidal dispersion procured from Alfa Aesar further in de-ionised water to the ratio 1: 2.6 ml to give a final solution of 4.2 wt.%. The process of depositing a thin film (< 20 nm) NPs (Particle size 1 to 100 nm) to homogenously coat a TEC15 substrate was a technical challenge due to the roughness of the FTO. Average rough for a sample of TEC15 was measured in chapter 3 to be approximately 13.15 nm respectively, with peaks of 70 nm via AFM. During fabrication trials it was noted that in order to obtain a homogenous SnO_2 film, a minimum of 15 minutes of UV ozone cleaning was needed followed by immediate deposition afterwards. The humidity within the room must also be above 30 % RH because below this and without the added wettability benefit from the corona treatment via UV ozone, the water-based film dries too quickly during spin coating resulting in a film with an exceptionally high density of pin holes.

Optimised films of TEC15-D, FTO (TEC15), TEC15-D & PCBM and Alfa Aesar NPs were examined using UV-Visible spectrophotometry as seen in figure 4.3. The substrates all show a high average transmission (AVT) across the UV-Visible spectrum. This is critical for high short circuit currents and thus efficient solar cells. It is noticeable that the films that use PCBM have a slightly lower AVT of around 67 % compared to those that don't > than 70 % on average. The Alfa Aesar NPs and TEC15-D samples have a slighter higher transmission than plain FTO glass (72.3 % and 71.6 % for Alfa Aesar NPs and TEC15-D respectively, compared to 70.7 % for FTO). This is attributed to the relative refractive indexes of the materials used. SnO_2 has a refractive index of approximately 2 to 2.2, whereas air

has a refractive index of 1. The Alpha Aesar NPs and TEC15-D reduce reflectance of light at the FTO , SnO_2 , air interface compared to bare FTO, thus there is a small incremental increase in transmission of light through those samples.

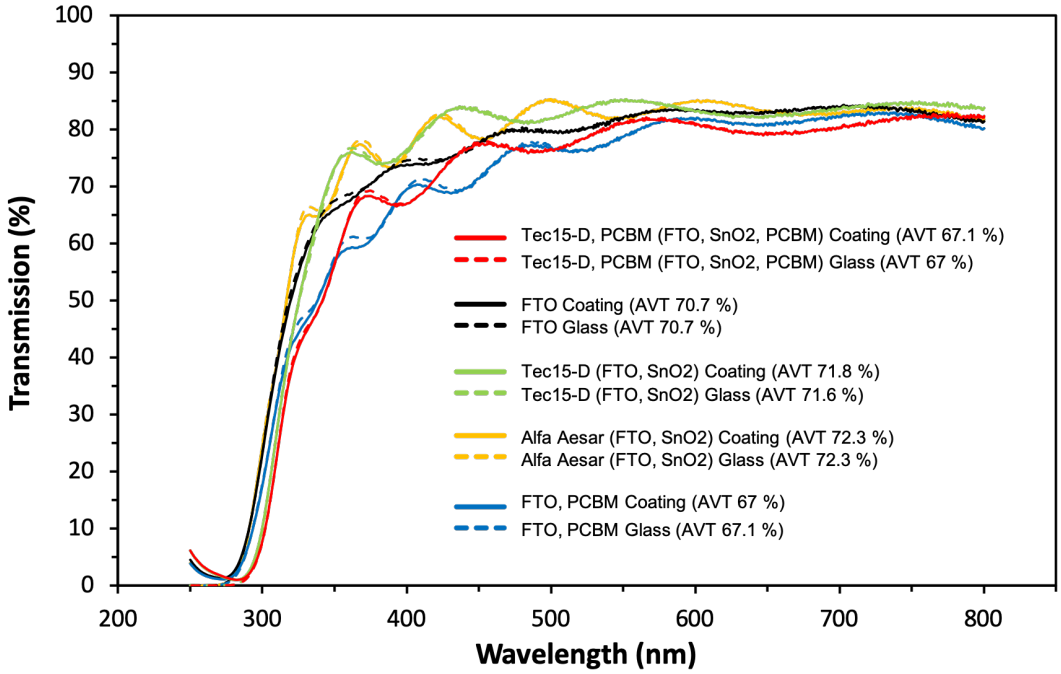

Figure 4.3: UV-Visible spectrophotometry to access the behaviours of TEC15-D, PCBM, Alfa Aesar SnO_2 films and FTO glass over the range 250 nm to 800 nm. Data was collected at 1 nm intervals at 266.75 nm/ min with transmission mode. Note: in the legend of figure 4.3, glass and coating refers to the incident light being transmitted through this layer first, i.e. what orientation the sample was loaded into the spectrometer.

It is also important to point out that small discrepancy between the Alfa Aesar and TEC15D films is due to minor variations in the glass bases of the substrate, depending on thickness and composition of the glasses used. But the fact the Alfa Aesar NPs are deposited on top of the same FTO as the reference suggests the SnO_2 is the dominant force for the slight increase in optical transmission.

Table 4.1: A summary of the relative amounts of C, Ca, F, K, N, O and Sn as measured by XPS for samples of TEC15-D pre and post a 20-minute UV ozone cleaning regime. The measurements were used to quantify the chemical composition of TEC15-D supplied by NSG Pilkington.

Sample Identifier	Carbon	Calcium	Fluorine	Potassium	Nitrogen	Oxygen	Tin
TEC-15-D-UV_ozone 1	11.6	0.1	2.1	0.5	0.0	58.5	27.2
TEC-15-D-UV_ozone 2	12.6	0.2	2.3	0.6	0.0	57.7	26.6
TEC-15-D-UV_ozone 3	12.5	0.1	2.1	0.5	0.0	57.4	27.5
TEC-15-D-UV_ozone 4	12.2	0.1	2.2	0.6	0.0	57.6	27.3
TEC-15-D-UV_ozone 5	13.0	0.1	2.4	0.6	0.0	57.1	26.7
TEC-15-D-no_treatment 1	32.2	1.1	0.0	0.0	0.4	45.8	20.5
TEC-15-D-no_treatment 2	39.2	1.4	0.0	0.0	0.3	41.0	18.1
TEC-15-D-no_treatment 3	26.1	0.8	0.0	0.0	0.4	50.0	22.7
TEC-15-D-no_treatment 4	34.1	1.4	0.0	0.0	0.9	45.0	18.8
TEC-15-D-no_treatment 5	31.2	1.2	0.0	0.0	0.5	46.6	20.5

Compositional analysis of the TEC15-D substrate was determine using XPS. Results are presented in table 4.1 where a summary of relative amounts of measured elements are listed. There are two sample sets, one that exposed the TEC15-D to 25 minutes of UV Ozone treatment, and one taken from a store and only a solvent rinse used to clean the sample prior to analysis. From table 4.1 we see the UV-Ozone treatment works well to remove carbon contamination from a high of 39.2 to 11.6 before and after treatment, other contaminants such as calcium and nitrogen are also removed but this may be down to natural variation due to the low levels present initially. There is very small, but noticeable rise in fluorine post UV ozone treatment, but it is very minimal, we attribute this to variations in the TEC15-D substrates and the presence of a very small fraction of pinholes in CVD deposited SnO_2 present on a clean/ impurity free substrate (we would expect to observe the same effect in SnO_2 deposited via nanoparticle solution processing). This phenomenon is further investigated using cyclic voltammetry discussed later. Although the amounts are low, an increased conductivity (associated with fluorine) could aid with electron mobility in small enough quantities even though TEC15-D has a relatively low sheet resistance of

~ 27 Ωcm^{-2} (± 4.2) as measured with a Jandel 4-point probe. Literature suggest UV-ozone treatment for even a few minutes is beneficial for SnO_2 based n-i-p PSCs by helping to passive trap states and oxygen vacancies and ensuring good conformal of the proceeding layer through the increased wettability. [7] Optimisation for the amount of UV-ozone treatment would help to improve performance. Fully fabricated devices of TEC15-D were exposed to a 10-15-minute UV-Ozone treatment and the PCE seen in Figure 4.5 seems to indicate limited if any damage was done to the devices. Lastly the oxygen and tin levels recorded in table 4.1 indicated a good ratio of nearly 2:1 for oxygen to tin suggesting that the of the TEC-15D sample supplied by NSG Pilkington is likely contains SnO_2 in the first 10-20nm of the resulting sample.

Cyclic voltammetry (CV) was used to investigate the blocking effects of all the ETL used in device fabrication. It was successfully used to model the hole blocking behaviour of TiO_2 in chapter 3. Figure 4.4 shows cyclic voltammograms of the various ETL films (TEC15-D, Alfa Aesar NPs on TEC15, PCBM on FTO and TEC15-D & PCBM combined) exposed to a potassium ferro/ ferri cyanide electrolyte couple. In this experiment, the $Fe(CN)_6^{3-/4-}$ solution acts as a model redox in a three-electrode cell, with the ETL coated, FTO glass acting as a working electrode. In this round of CV scan ranges were extended from -0.8 V to +0.8 V in order to ascertain full working principles, although during JV testing PSC solar cells are usually swept in the range of -0.2 V to 1.2 to 1.4 V depending on the absorber material. Pin holes and defects were monitored by measuring any anodic current response over the range of +0.8 V to -0.1 V. The current measured from these effects arises from the ferrocyanide oxidation at the bare FTO regions, thus indicating an inhomogeneity within the film. Across all 4 films there appears very few if any pin holes indicating strongly homogenous defect free layers. It is important to note that that even with homogenous thin films by CVD and Nanoparticle solution processing, there will be a very small degree of pinholes. This is picked up in cyclic voltammetry, but it is at the limit of accuracy for the setup. These small pinholes can help explain the fluorine observed in table 4.1 for UV ozone treated TEC15-D where the XPS is able to pick up very faint traces of fluorine under small the pinholes.

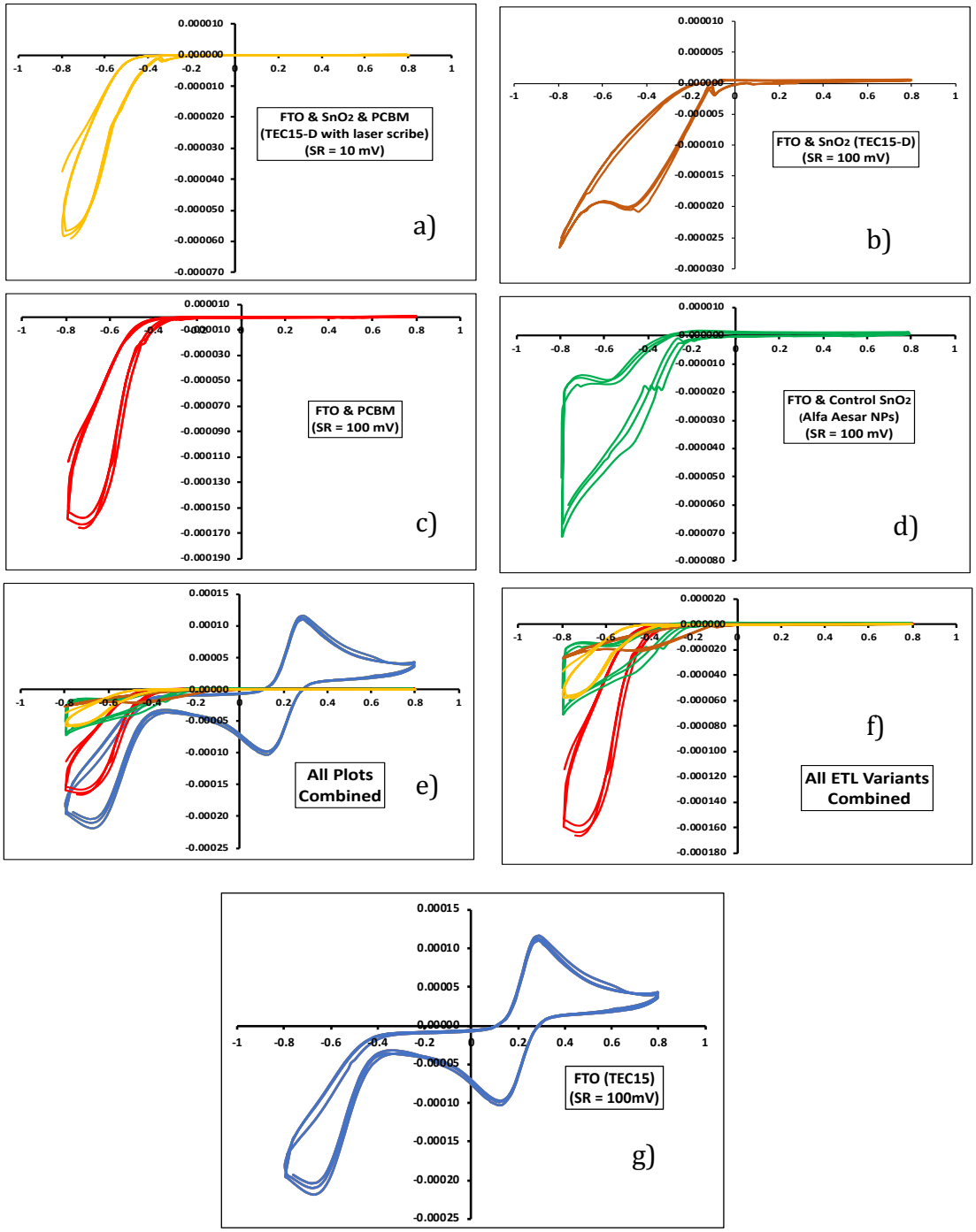

Figure 4.4: Cyclic voltammograms showing the blocking function of various ETLs based on SnO_2 and PCBM. a) FTO & SnO_2 & PCBM – using laser scribed TEC15-D, b) TEC 15-D only (un pattered FTO and 50 nm of CVD SnO_2), c) FTO and PCBM only, d) FTO and control SnO_2 ETL based on Alpha Aesar Nanoparticles dispersed in water, e) Is all combined plots onto one single plot for comparison, f) IS all ETL variants combined onto one plot for comparison and g) Plain FTO glass for reference. All samples were measured using a sweep rate (SR) of 100 mVs^{-1}.

The 4 samples TEC15-D, Alfa Aesar NPs on TEC15, PCBM on TEC15 and TEC15-D & PCBM all show a strong blocking effect over the positive voltage ranges as very little is detected, below microamps 2 (mA), this is in contrast to the FTO reference sample that shows current activity over the positive voltage range orders of magnitude higher than that observed in 4 ETL measured. This strong blocking effect demonstrates TEC15-D, PCBM on TEC15, Alfa Aesar NPs on TEC15 and TEC15-D & PCBM all have a high degree of film coverage that make a rectifying interface. At this point no anodic currents of Ferro cyanide oxidation can flow because ETLs are in the depletion regime at these potentials, this is denoted by the flat line between -0.15 V to +0.8 V. As the CV scan is extended towards -0.8 V the cathodic current is detected meaning the ETLlayers are in the accumulation regime i.e. exhibiting metallic behaviour as described by Kavan et al. [14][15] and a negative current is measured as seen in figure 4.4f). This is where small differences begin to manifest between the 4 ETL samples. PCBM by itself exhibits the strongest blocking effect, the accumulation regime (cathodic current increases as voltage gets more negative) only begins when the negative potentials start to go beyond the -0.4 V to 0.8 V. This can be seen in both samples incorporating PCBM if we refer to figures 4.4 a) and 4.4 c). The Alfa Aesar and TEC15-D samples enter the accumulation slightly earlier at the negative potentials, with accumulation onset estimated around -0.1 to -0.2 V, in fact the two samples respond almost identically to each other up until the point of the accumulation regime as seen in figures 4.4d) and 4.4b). Combining the TEC15-D and PCBM has much the same trace as PCBM by itself, exhibiting a very strong blocking effect all the way to -0.4 V as seen if 4.4a). Figure 4.4 f) depicts all the ETLs plotted concurrently, from here we notice how much more current is measured at the lower potential (beyond -0.4 V) for the PCBM cell as seen in figure 4.4 c). Additionally, TEC15-D shows the lowest measured cathodic current activity beyond -0.4 V compared to all other samples as seen 4.4f). Although the accumulation does start at slightly lower potentials (0.2 V) than PCBM FTO (0.4V).

To fabricate devices on TEC15-D laser processing had to be used to isolate the desired regions of the working cell, this meant ablating through the ETL and creating a short circuit pathway if perovskite were deposited directly on top. From the literature it has been shown that fullerenes like PCBM combine well when used in tandem with SnO_2 n-i-p structures. The PCBM reportedly aids by forming a strong electronic coupling with the fullerene monolayer to adjust the surface properties of SnO_2, such as passivating surface defects and recombination at the interface. [7] [16]. Process optimisation was carried out on the Alfa Aesar nanoparticles in order to find the correct spin parameters for an approximate 20 nm film of PCBM to overlay the SnO_2. The details can be seen in table 4.2.

Table 4.2: A table detailing the PCBM spin coating process parameters as seen in figures 4.5 and 4.6. Dynamic deposition refers to depositing the PCBM while the sample is spinning for 30 seconds.

Sample ID	PCBM Processing Parameters (Spin Coating)
Control: TEC15 & Alfa Aesar NPs	No PCBM Layer Deposited
TEC15-D & PCBM (1S)	2000 rpm / 2000rpms^{-1} / 30 seconds / Static Deposition
TEC15 & Alfa Aesar NPs & PCBM (1S)	2000 rpm / 2000rpms^{-1} / 30 seconds / Static Deposition
TEC15-D & PCBM (1D)	2000 rpm / 2000rpms^{-1} / 30 seconds / Dynamic Deposition
TEC15-D & PCBM (2S)	4000 rpm / 4000rpms^{-1} / 30 seconds / Static Deposition
TEC15-D & PCBM (2D)	4000 rpm / 4000rpms^{-1} / 30 seconds / Dynamic Deposition

Remarkably the cells employing TEC15-D and PCBM produced excellent PCEs. The results of which can be seen in figures 4.5, 4.6, 4.7 and table 4.2. JV statistical analysis suggests there is a correlation between increasing spin speed and acceleration of PCBM with an increase in performance of over 1.5 % for record V_{OC} to J_{SC} measurements linked to an increase in short circuit current. The effect of dynamic spinning isn't apparent although there was a small increase in the very highest short circuit currents within this group.

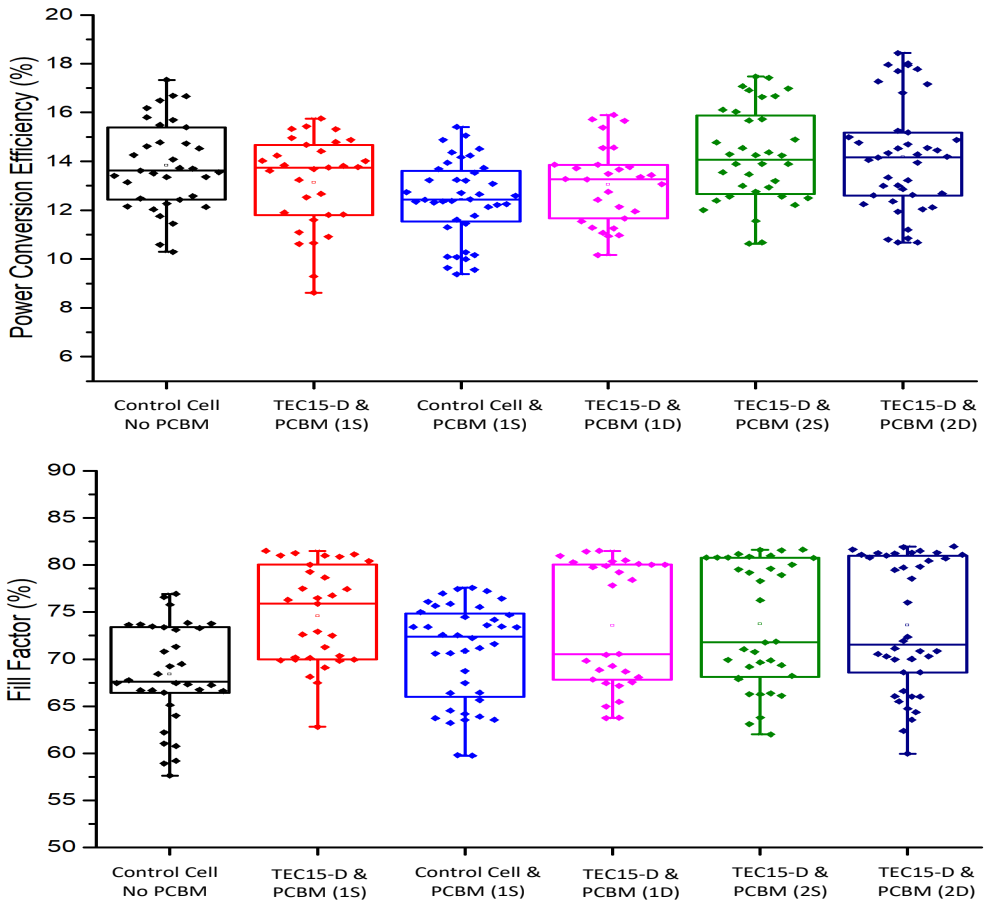

Figure 4.5: Box plot JV data for variations in PCBM processing conditions. displayed is PCE data and associated Fill Factors. Both forward (J_{SC} to V_{OC}) and reverse (V_{OC} to J_{SC}) are plotted together. Key to variations can be seen in table 4.2.

The effect of PCBM across all devices when compared to the control cells without PCBM is an increase in FF and V_{OC} but this is counter acted by an overall drop in short circuit current. The increases in V_{OC} can be attributed to PCBM having a better band alignment with the perovskite (-3.9 to -5.7) than SnO_2 (-3.90 to -5.96 for PCBM and -4.5 to -8 eV for SnO_2). With the increase in V_{OC} comes the drop in J_{SC} for the PCBM films that we attribute to the charge recombination at the spiro perovskite interface due to the narrowing of the band gap, the opposite effect is true for the cell without PCBM, the larger bandgap of SnO_2 reduces recombination at the HTM and increases recombination at the ETL and hence we see an increase in J_{SC} and a lowering of V_{OC}. There is a small amount of hysteresis observed in all films which we attribute to un-optimised selective contact layers like PCBM and

Spiro-MeOTAD. The likely root cause charge trapping at interfaces. Physically, we observe occasional small pinholing in the Spiro film, resulting from undissolved Li-TFSI present in the Spiro layer, this is attributed to not heating the solution to high enough temperatures (approximately 180 degrees Celsius). Charge trapping at the interface builds up at the interface during the first reverse scan and again during the second forward scan resulting in a PCE discrepancy in the forward scan. This is levelled out over time as seen in the stabilised PCE in Figure 4.8.

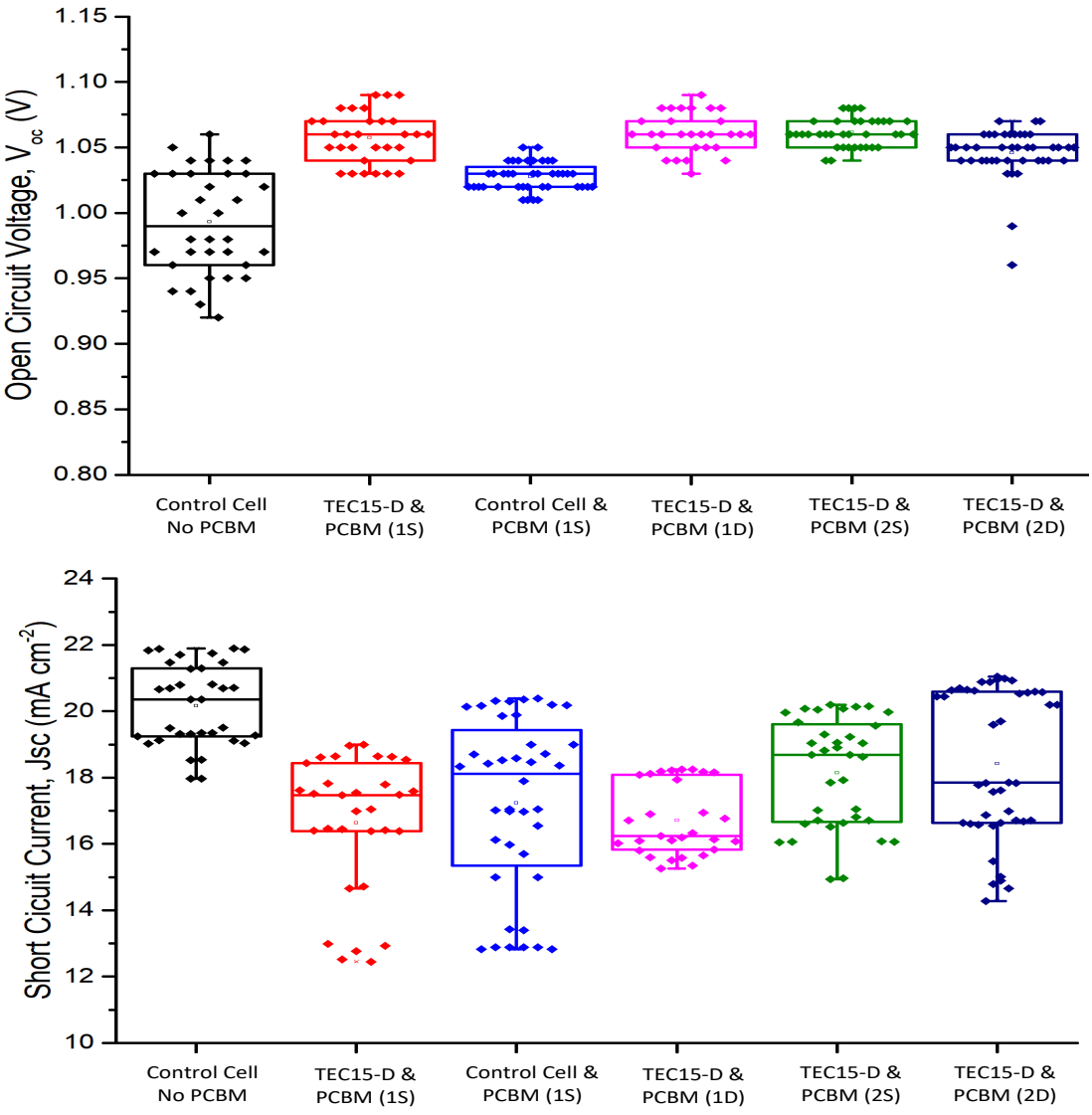

Figure 4.6: Statistical analysis of JV data for variations in PCBM processing conditions. Displayed is J_{SC} data and associated V_{OC} Both forward (J_{SC} to V_{OC}) and reverse (V_{OC} to J_{SC}) are plotted together. Key to variations can be seen in table 4.2.

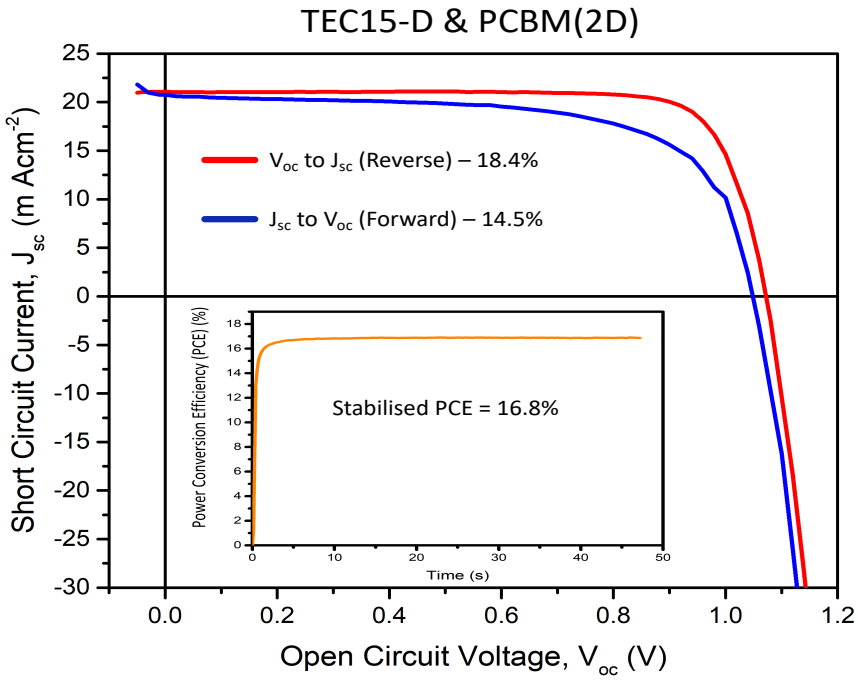

Figure 4.7 JV curve for the best performing TEC15-D & PCBM cell. PCBM was spun dynamically at 4000 rpm, 4000 rpms^{-1} for 30 seconds.

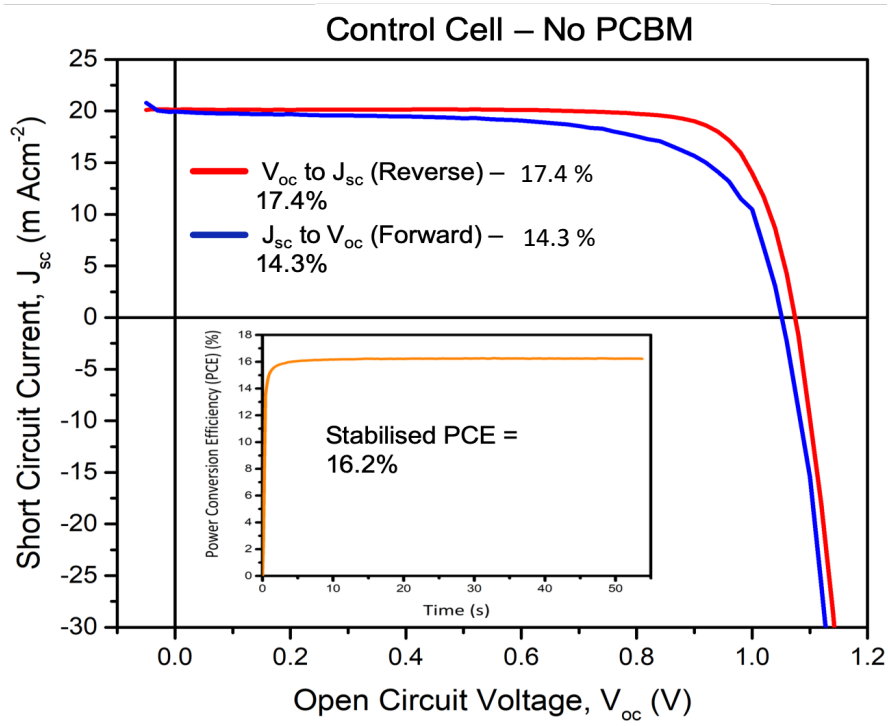

Figure 4.8: JV curve for the best performing control cell with no PCBM. The SnO_2 was fabricated from a solution processed low temperature SnO_2 nanoparticle dispersion procured from Alfa Aesar.

Overall the TEC15-D and PCBM films performed very similarly to that of the control cells using no PCBM and solution process SnO_2 nanoparticles deposited and annealed at low temperature. At higher spin speeds and acceleration PCBM produced cells with a small increase in PCE than that of the highest control cell, Alfa Aesar NPs with no PCBM(17.4 % to 18.4%).

From the relationship between V_{OC} and light intensity shown in Figure 4.9 it is clear that devices that contain PCBM behave similarly, at least at open circuit. The TEC15D devices without PCBM have a slightly lower V_{OC} for a given light intensity which might suggest that the PCBM has a slight energy offset relatively to the SnO_2 and/or that the PCBM reduces the rate of interfacial recombination, although it is difficult at this stage to prove whether this is occurring in the bulk or at the bulk/ HTM (Spito-OMeTAD) interface. A comparison device using a non ETL material, KOH, instead of PCBM was fabricated and tested to see if it could act as a passivator for the etched TEC15-D. Shunting is seen for device with KOH where V_{OC} drops suddenly below 0.3 suns proving that KOH is not an appropriate alternative to PCBM. The perovskite is able to contact the FTO in the etched zones, hence the shunting observed.

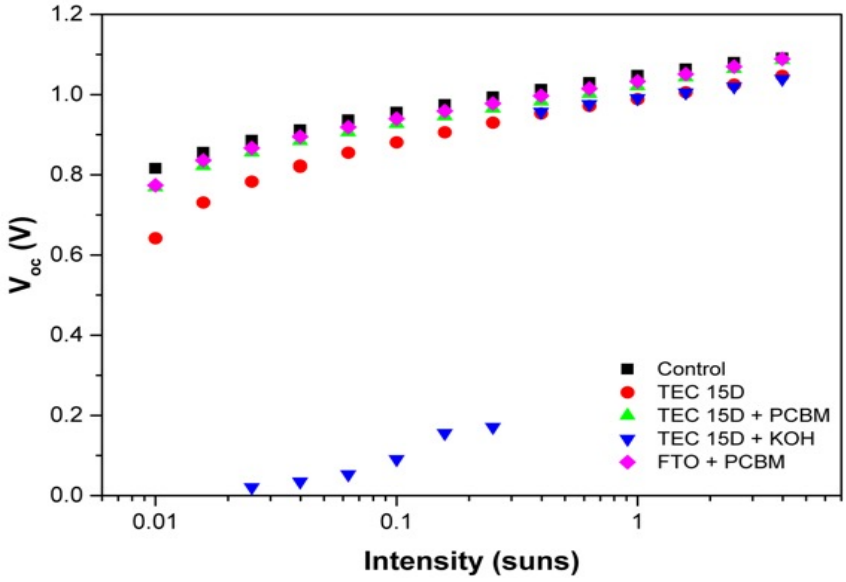

Figure 4.9: V_{OC} versus light intensity for TEC15-D and PCBM based cells, a non PCBM cell and one using TEC15-d and KOH instead of PCBM is also recorded. (Note: Control device in black is TEC15 & Alfa Aesar NPs)

The graphs in figure 4.10 are matched so a side by side comparison can be made. For the devices without PCBM a bi-exponential fitting was used which suggests the presence of two recombination processes. The slower of these time constants (open symbols) is on a similar time scale to the control device in right hand graph. We postulate this is either a slower time constant that can therefore be attributed to bulk/ HTM (Spiro-OMeTAD) recombination, or a state we are not passivating. The faster time constant for the devices without PCBM can therefore be attributed to fast interfacial recombination. KOH does not appear to passivate this affect as before. The addition of PCBM on TEC15-D seems to remove this faster component (decays are monoexponential) and the recombination behaviour pretty much follows that of the control device – bulk/HTM (Spiro-OMeTAD) recombination dominates.

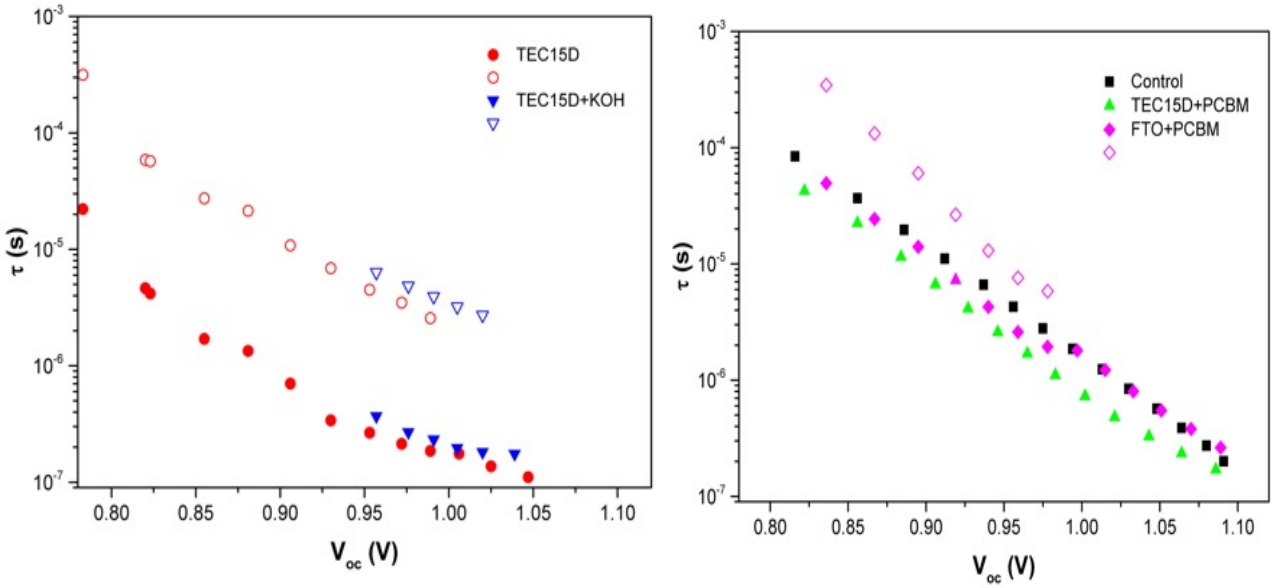

Figure 4.10 Recombination lifetime versus V_{OC} for devices without PCBM (top) and with PCBM (Bottom). Open symbols represent second time constant when bi- exponential fitting is required. (Note: Control device in black is TEC15 & Alfa Aesar NPs).

4.4 Conclusions

SnO_2 is rightly being hailed as a wonder material in the world of perovskite solar cells. Its excellent band alignment, high electron mobility, ease of manufacture and stability compared to other metal oxide ETL give real promise for the commercialisation of perovskite solar cells. We further this cause by presenting another versatile mass manufactured electron transport layer based on SnO_2 deposited via CVD on TEC glass, that, when incorporated into a perovskite solar cell achieves a maximum PCE of 18.4 % with very little optimisation. By combining TEC15-D with the organic fullerene PCBM, the obstacles of processing during manufacture are mitigated where laser ablation is needed to complete the cell circuitry. Cyclic voltammetry demonstrates that TEC15-D alone acts an effective hole blocking layer over the range -0.8 to +0.8 V and compares well with that achieved in chapter 3 with TiO_2. This is combined with impressive optical transmission, conductivity. While open circuit voltage verses sun intensity TPV suggests that an unoptimized TEC15-D compares well to optimised control cells and those with PCBM have a reduced rate of parasitic interfacial recombination. The work from this chapter on SnO_2 based perovskites feed well into the next body of work by applying transparent bifacial contact to it for window applications.

4.5 Bibliography

[1] B. Smith *et al.*, "Mass Manufactured Glass Substrates Incorporating Prefabricated Electron Transport Layers for Perovskite Solar Cells," *Adv. Mater. Interfaces*, 2019.

[2] S. W. Lee *et al.*, "UV Degradation and Recovery of Perovskite Solar Cells," *Sci. Rep.*, 2016.

[3] G. Niu, X. Guo, and L. Wang, “Review of recent progress in chemical stability of perovskite solar cells,” *J. Mater. Chem. A*, 2015.

[4] A. K. Jena, H. W. Chen, A. Kogo, Y. Sanehira, M. Ikegami, and T. Miyasaka, “The interface between FTO and the TiO2 compact layer can be one of the origins to hysteresis in planar heterojunction perovskite solar cells,” *ACS Appl. Mater. Interfaces*, 2015.

[5] X. Huang, Z. Hu, J. Xu, P. Wang, J. Zhang, and Y. Zhu, “Low-temperature processed ultrathin TiO2for efficient planar heterojunction perovskite solar cells,” *Electrochim. Acta*, 2017.

[6] M. Saliba *et al.*, “How to Make over 20% Efficient Perovskite Solar Cells in Regular (n-i-p) and Inverted (p-i-n) Architectures,” *Chem. Mater.*, 2018.

[7] Q. Jiang, X. Zhang, and J. You, “SnO 2 : A Wonderful Electron Transport Layer for Perovskite Solar Cells,” *Small*, vol. 14, no. 31, p. 1801154, Aug. 2018.

[8] W. Ke *et al.*, “Lowerature solution-processed tin oxide as an alternative electron transporting layer for efficient perovskite solar cells,” *J. Am. Chem. Soc.*, 2015.

[9] E. H. Anaraki *et al.*, “Highly efficient and stable planar perovskite solar cells by solution-processed tin oxide,” *Energy Environ. Sci.*, vol. 9, no. 10, pp. 3128–3134, 2016.

[10] W. Tress, N. Marinova, T. Moehl, S. M. Zakeeruddin, M. K. Nazeeruddin, and M. Grätzel, “Understanding the rate-dependent J–V hysteresis, slow time component, and aging in CH 3 NH 3 PbI 3 perovskite solar cells: the role of a compensated electric field,” *Energy Environ. Sci.*, vol. 8, no. 3, pp. 995–1004, 2015.

[11] Y. Zhao *et al.*, “Anomalously large interface charge in polarity-switchable photovoltaic devices: an indication of mobile ions in organic–inorganic halide perovskites,” *Energy Environ. Sci.*, vol. 8, no. 4, pp. 1256–1260, 2015.

[12] J. P. Correa Baena *et al.*, “Highly efficient planar perovskite solar cells through band alignment engineering,” *Energy Environ. Sci.*, 2015.

[13] M. F. Mohamad Noh *et al.*, “Eliminating oxygen vacancies in SnO 2 films via aerosol-assisted chemical vapour deposition for perovskite solar cells and photoelectrochemical cells,” *J. Alloys Compd.*, 2019.

[14] L. Kavan, N. Tétreault, T. Moehl, and M. Grätzel, “Electrochemical Characterization of TiO 2 Blocking Layers for Dye-Sensitized Solar Cells,” *J. Phys. Chem. C*, p. 140114142307002, 2014.

[15] L. Kavan, M. Zukalova, O. Vik, and D. Havlicek, “Sol-Gel Titanium Dioxide Blocking Layers for Dye-Sensitized Solar Cells: Electrochemical Characterization,” *ChemPhysChem*, vol. 15, no. 6, pp. 1056–1061, Apr. 2014.

[16] W. Ke *et al.*, “Cooperative tin oxide fullerene electron selective layers for high-performance planar perovskite solar cells,” *J. Mater. Chem. A*, 2016.

Chapter 5

A Transparent Conductive Adhesive Contact Based on a Silver Nanowire Carbon Nanotube Composite

Work in this chapter was presented and included in the conference proceedings at the Annual Hybrid Organic Photovoltaic Conference in Benidorm, Spain, 2019.

5.1 Introduction

Chapters 3 and 4 demonstrate just a fraction of the material sets available when fabricating high efficiency perovskite solar cells. This plethora of potential materials is both an advantage and disadvantage when it comes to commercialising perovskite based solar cells. With new materials currently being developed at an astonishing rate, it can be difficult to decide on a material set to upscale knowing the technology may be rendered obsolete in just a few years. It is therefore essential to consider processing techniques that are versatile enough to switch between different materials at a cost that doesn't impede the route to commercialisation. In section 1.4 and 1.5 we discussed the potential applications and the problem of scale for perovskite solar cells, certain processing technologies are more versatile than others. Two potential applications for perovskite solar cells are semi-transparent windows and tandem applications with other commercially available PV technologies. The idea of a window that functions as a dual-purpose material is attractive to glass manufacturing companies like NSG Pilkington as shown in Figure 5.2. Current window technologies predominantly focus on optimising both optical and thermal properties for building and automotive purposes using thin TCO materials to control the solar spectrum for desired purposes. Recent innovations have opened the possibility of windows that not only control optical and thermal properties but also include a self-cleaning element. The use of photoactive TiO_2 to break down dirt particles with the use of the UV component of light and water from precipitation to clean windows without the need for additional manual labour [1], [2]. The idea of using a window that can control optical, thermal, self-cleaning and energy generating properties is therefore of considerable interest. By generating renewable and usable power from excess solar radiation and external lighting sources during periods when the sun isn't shining offers a chance to reduce the impact of a buildings CO_2 on the environment as a whole. The power generated can either be stored in conventional battery technologies or be used to power low energy consumer electronics and Internet-Of-Things (IOT) devices. Perovskites also have the added bonus that they absorb a different part of the solar spectrum (Infrared and visible ranges) than other commercial PV

technologies like crystalline silicon. This makes them ideal for tandem applications and new records have been recorded by using a silicon-perovskite multijunction tandem solar cells [3]–[6].

In order to function as dual purpose windows (energy generating) and tandem applications, perovskites solar cells must replace the solid, opaque metal electrodes used in conventional architectures with a conductive transparent electrode that doesn't fatally inhibit the performance of the cell. Several electrode materials are suitable for use within perovskites, whilst also beneficial for technology development [7].

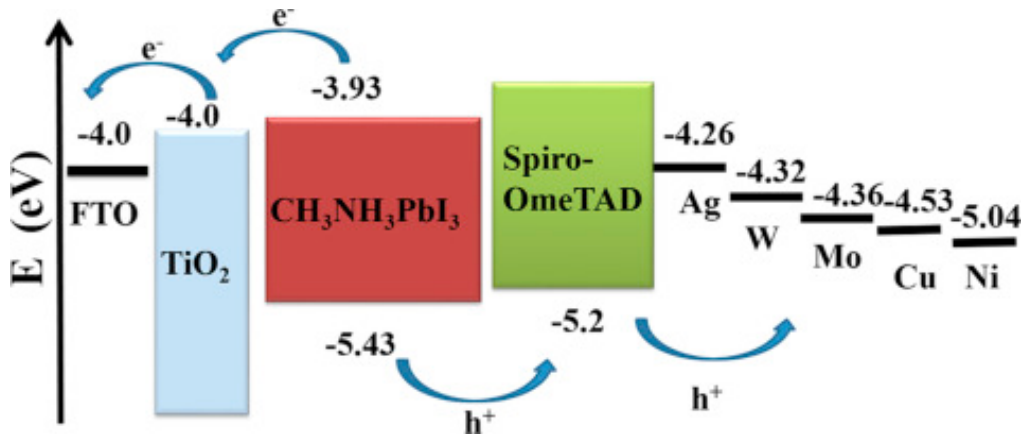

Figure 5.1: An energy diagram of electron-hole generation and charge flow through a typical perovskite solar cell with respect to the work functions of those materials. Highlighted on the right is a range of metal electrodes (Ag, W, Mo, Cu and Ni) that can be used to extract charges. [7]

There is an inevitable trade-off between the transparency of the contact and performance. This is due to the loss of the reflective properties of an opaque, metal contact that reflects transmitted photons back onto the perovskite absorber material that boosts short circuit current. The transparency of the perovskite absorber material can be controlled through the thickness of the material. Ellipsometry models suggest the perovskite material needs to be around 370 nm thick and homogenous to absorb all incident photons of light for maximum efficiency as reported by Phillips et al [8]. Increasing thickness beyond this threshold starts to induce series resistances with the cell and efficient charge

extraction becomes more difficult. Again, there will be a compromise between transparency of absorber material and performance as more photons of light pass through the cell without reflection and short circuit current is again reduced.

A variety of methods have been explored to replace the conventionally evaporated solid opaque metal contacts including solution processed silver nanowires, [4] carbon nanotubes, [9]PEDOT:PSS, [10]. Laminated graphene [11] or Ni-mesh [12] top electrodes have been used to fabricate efficient semi-transparent perovskite solar cells; however these devices suffer hysteresis and tend to have low reproducibility. Vacuum processed transparent conductive oxides (TCO) are investigated in chapter 6, but to date indium tin oxide (ITO), [13] hydrogenated indium oxide (In_2O_3:H)[14] and aluminium doped zinc oxide (AZO) [15] have been reported with relatively stable semi-transparent perovskite solar cells and encouraging PCEs. Another approach involves using ultra-thin (<10 nm)evaporated metal electrodes [16] to produce high efficiencies but they do suffer long-term stability issues due to moisture diffusion and gold (Au) diffusion. Although vacuum processes produce homogenous thin films with excellent conductivity and optical properties, they are expensive to implement and maintain in a production facility; production rates aren't as high as that of continuous roll to roll manufacture.

In this chapter we present a solution processed, non-vacuum, ambient air processed silver nanowire/ carbon nanotube composite material that can replace the evaporated opaque metal electrodes for window and tandem applications. The film is easily processed with non-toxic solvents at scale and uses a simple spray coating technique at low temperatures to ensure ease of manufacture. The resulting thin films produce an excellent sheet resistance which can be controlled via layer thickness to achieve a film that is highly transparent, conductive and robust enough to withstand difficult manufacturing procedures. From figure 5.1 it can be seen that silver; Ag has a work function of around (-4.26 eV) that corresponds well with HTM materials like Spiro-MeOTAD (-5.07 eV), ensuring effective charge conduction and extraction. Silver is also a relatively inexpensive conductive metal when compared to gold. AgNW do have one drawback, the

silver will readily react with the halides present in the perovskite, which can lead to short circuit pathways, water ingress, ion migration and degradation of the cell. In order to combat that this a barrier layer or composite will have to be delveoped to mitigate this chemical instability. Silver nanowires by themselves can act as an effective transparent electrode material but the nanowires themselves can be easily damaged during processing owing to the fact they do not adhere well to relatively smooth thin films like FTO glass and HTM/ ETL materials. This is because they rely on relatively weak Van Der Waals forces to attach onto substrates, the uniformity and regularity of individual nanowires, they don't form particular strong matrixes owing to lack of size variation needed to increase dislocation density. They are also relatively weak when compared to structures like single walled carbon nanotubes(SW-CNT). Some SW-CNT have a young's modulus (YM) of 10^{12} pascals and a yield strength of 53 x 10^{9} Pascals, whereas steel by comparison silver nanowires by comparison have a YM of 90 x 10^{9} Pascals and a yield strength of around 2 x10^{9} Pascals [17] [18]. By incorporating a carbon nanotube matrix into the layer this problem is partially alleviated and the excellent conductivity of the silver nanowires helps to compensate for the relatively poor electrical conductivity of some thin film single walled carbon nanotubes and an excellent compromise is reached. Carbon nanotubes are robust structurally and don't break easily due to the covalent bonds linking individual carbon atoms together. Silver nanowires and Carbon nanotubes have been deposited via several methods including spray pyrolysis and inkjet printing [19][20].

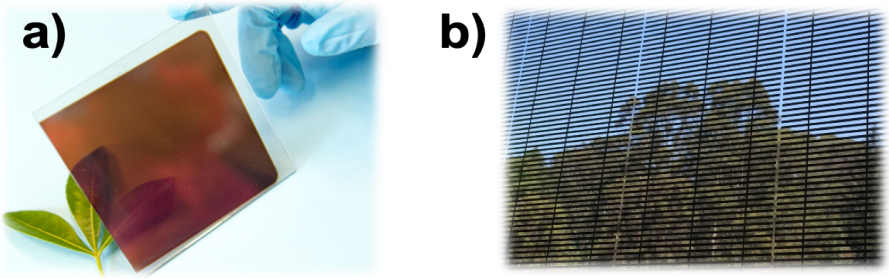

Figure 5.2: A diagram to show a) True semi transparency – No patterning of the device, layer allows given amount of light to transmit through and b) Quasi transparent – Usually patterned (mechanical or via LASER) photovoltaics with regions left uncoated for light to transmit through.

5.2 Experimental

The silver nanowire carbon nanotube composite material was fabricated by mixing optimum amounts of silver nanowires procured from Sigma Aldrich, diameter: × Length 60 nm × 10 µm, 0.5% (isopropyl alcohol suspension) product number 739421, 0.05 % single walled carbon nanotubes (diameter 2 nm, length > 5um) (containing Tuball™) dispersed in IPA procured from Oscial Europe. The ideal mixture was further dispersed in IPA (to act as a carrier solvent) in order to spray coat multiple layers to give the desired thickness. Dry Nitrogen was used as the carrier gas at 25 psi and sprayed with a spray gun (Sealey, Model No. AB932) by hand from a height of 10 cm from the substrate surface to cover the entire device. Substrates where placed on a heated hotplate at < 50 °C while being sprayed to aid with evaporation of the carrier solvent. A mask cut from an adhesive acrylic was applied to each device to give the desired pixel layout (0.9 cm by 2 cm as with all previously measured devices). A number of different suppliers of silver nanowires were sourced in order to optimise conductivity, adhesion and transparency. These are discussed later in the chapter and listed below for clarity:

- Novarials - Silver Nanowires diameter: × Length 50 nm × 40 µm, 0.5% (isopropyl alcohol suspension 10mg/ ml) NovaWire-Ag-A50.
- Sigma Aldrich – Silver Nanowires, diameter: × Length 60 nm × 10 µm, 0.5% (isopropyl alcohol suspension) product number 739421.

A schematic diagram of the spray coating procedure and subsequent adhesion testing is displayed below in figure 5.3 and detailed in chapter 2.11. Optical, compositional, topographical and electrical properties were measured via 4-point probe conductivity testing, profilometry, UPS work function measurements, XPS, AFM, Kelvin probe, CIE colour analysis, UV-Visible spectroscopy, haze and clarity measurements and device performance measured outlined in chapters 2.3, 2.4, 2.5, 2.6, 2.9, 2.13, 2.15, 2,16, 2.19 and 2.12 respectively.

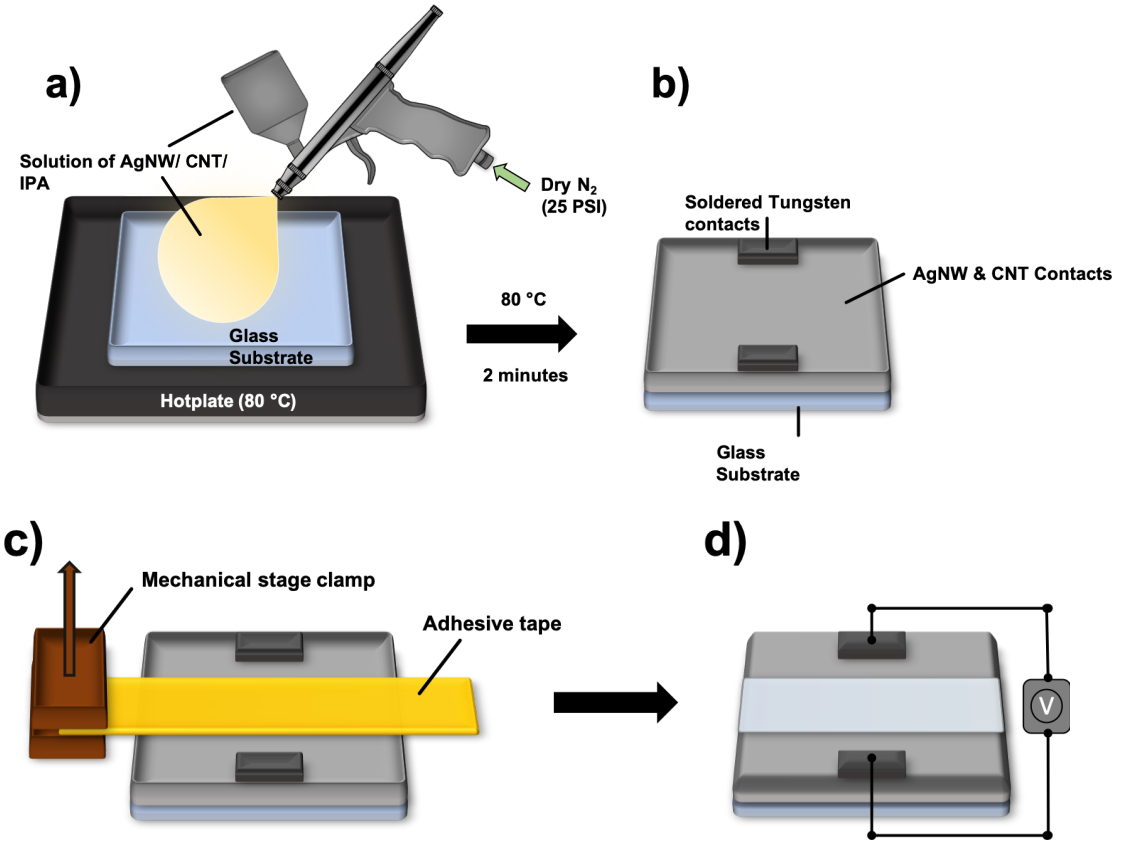

Figure 5.3: Schematic diagram to show adhesive strength testing of the contact and its variation with composition. a) spray coating of the silver nanowire, carbon nanotube composite dispersed in IPA using dry nitrogen as a carrier solvent onto a heated hotplate at 80 °C b) Finished contact with soldered tungsten contacts for subsequent testing, this was chosen for the robustness of the contact under repeated resistance and mechanical testing c) Mechanical testing using a tensile tester to remove adhesive tape at 90 ° to the substrate, force measured to remove tape is recorded d) Subsequent conductivity testing to see if the force used to remove the tape has broken the contact. It was decided to use scotch masking tape with a 1.37 N adhesive strength and bonding mechanisms used across optimised substrates.

Adhesive tapes used:

- Scotch Magic tape (Scotch® Magic™ Tape 810 - 62.5 micron x 12mm x 33mm) (Adhesive force 1.37 N)

Full details of the fabrication methods used to build the devices displayed in this chapter can be seen in chapter 2.1. It was decided to take base line laboratory cells seen in figure 5.4 and replace the evaporated gold contacts with the composite material as reported in chapter 2.1.7.2 in order to attain an optimised cell before trying to optimise the optical transparency of the devices discussed later in the chapter. All devices incorporated a mesoporous TiO_2 scaffold, Triple cation or MAPI based perovskite absorber layer, Spiro-MeOTAD HTM and evaporated metal back contacts as described in section 2.1.4, 2.1.5.1, 2.1.6.1 and 2.1.7.1 respectively. Mesoporous TiO_2 was incorporated into the architecture as lab scale reproducibility was greatly enhanced by the addition of the mesoporous scaffold as mentioned in chapter 3.2.

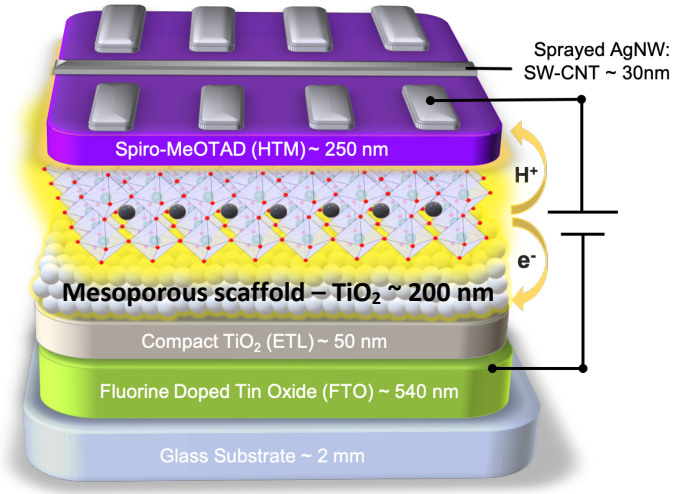

Figure 5.4: A simplified schematic diagram of the architectures employed in fabricating lab based base line devices before replacing the evaporated gold contacts with the composite material and optimising optical transparency.

<u>Chapter 5: Naming Convention:</u>

TC = Triple Cation Perovskite

ST = Semi Transparent (diluted films)

C = Control (non-diluted films)

SW CNT = Single Walled Carbon Nanotubes

AgNW = Silver Nanowires

PVD = Physical Vapour Deposition

MAPI = Methylammonium lead triiodide.

5.3 Results and Discussion

As mentioned in the introduction, silver nanowires have the ability to act as an efficient electrical contact material but are relatively weak when compared to other nanotube/ nanowire materials and do not adhere well to smooth surfaces due to the dominance of Van Der Waals forces[17] . Thus, the electrical contact can be easily broken, rendering devices such as PSC ineffective. Deposition involves spray coating a solution of these nanowires in a solvent such as IPA using an inert dry carrier gas such as nitrogen flowing at a controlled rate. This process is outlined in section 5.2. By building up a matrix of spray passes, the nanowires overlap one another to create a lattice like network that can conduct electrons across an extended area once the carrier solvent has evaporated. Atomic force microscopy was used to image the silver nanowire patterns that could be applied to PSCs.

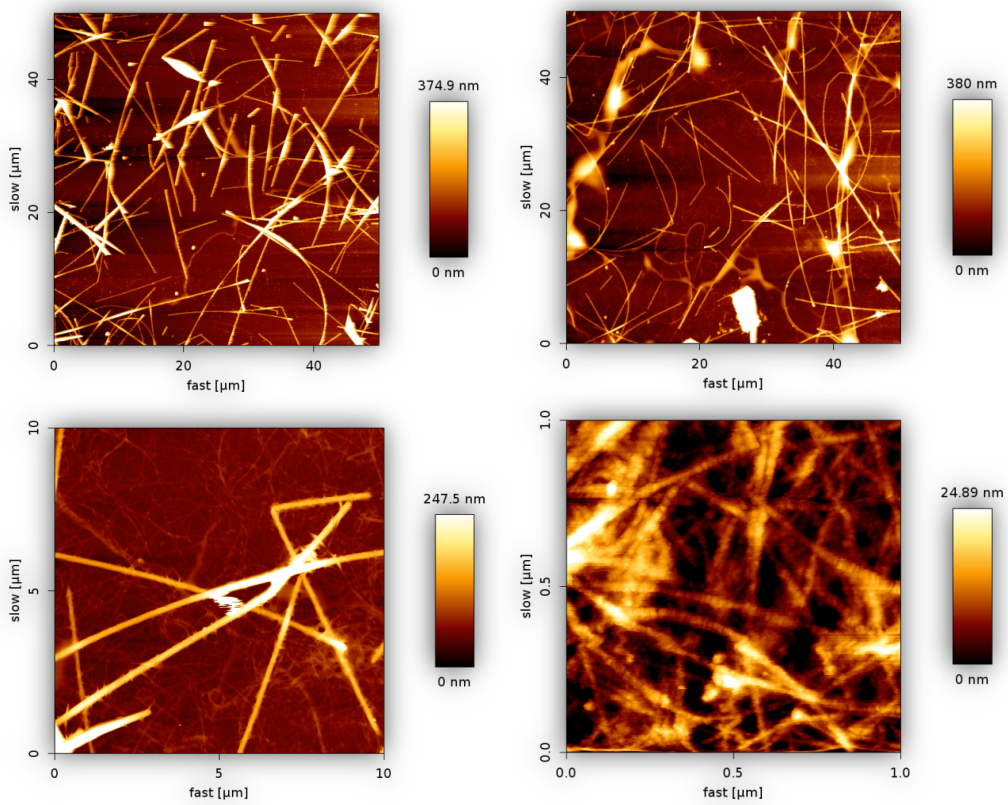

Figure 5.5: AFM images of silver nanowires deposited on a plain glass microcope slide substrate via spray coating 3 passes at 10 PSI using dry nitrogen, followed by heating at 80 °C to remove the carrier solvent. 4 regions are mapped at 3 magnifications (50 x 50 µm, 10 x 10 µm and 1 x 1 µm).

From the images in the bottom right of Figure 5.5 the lattice network can clearly be seen creating good electrical contacts across the samples. However, the uniformity of the nanowire's small size and dimensions makes it easy for individual nanowires to move and slide past one another within the lattice with relatively little force. This is compounded by the thin nature of the film, which is necessary for maximum optical transmission of light.

Single walled carbon nanotubes adhere well to smooth surfaces and are relatively robust compared to silver nanowires due to covalent sp^2 bonds formed between the individual carbon atoms and the carbon nanotubes ability to exhibit bundling driven by inter-tube bonding, which causes bundles of carbon nanotubes that can even consist of hundreds or even thousands of individual nanotubes. The high axial strength of the individual carbon nanotubes is difficult to utilize, but it it has been observed that bundles comprised of larger single-walled nanotubes tend to be stronger than smaller ones [18][21]. But when processing a large area electrical conductivity can be affected even though individual carbon nanotubes are either metallic or semiconducting by nature. Resistive nanotube-to-nanotube junctions and impurities are both known to lower the electrical conductivity of the macroscopic nanotube wires by orders of magnitude, as compared to the conductivity of the individual nanotubes.

By combining the single walled carbon nanotubes and silver nanowires a compromise can be made. The Initial work involved ascertaining the optimum formulation of silver nanowires and carbon nanotubes that would yield the best compromise between conductivity, transparency and durability (physical adhesion to smooth surfaces). Various manufactures of silver nanowires were sourced in order optimise cost effectiveness, conductivity and reproducibility of the final solutions. These were combined with precise amounts of single walled carbon nanotubes procured from Tuball™ dispersed in IPA. IPA was then used to further dilute the solutions for spray coating onto cleaned glass substrates at 80 °C to drive off any carrier solvent as outline in section 5.2. It was found that between 5 to 7 passes were needed to build up sufficient layer thicknesses for

testing with a Jandel 4-point probe to determine conductivity. The results of which can be seen below, summarised is table 1.

Table 5.1: A summary table denoting the resistivity, R_{sh} (Ωcm^{-2}) of various formulations of silver nanowires (AgNW), single walled carbon nanotubes (SW-CNT) and IPA measured using a Jandel 4-point probe.

Sample Name or Ratio Denotation	**AgNW Vendor**	**AgNW Solution (µl)**	**Tuball™ SW-CNT Solution (µl)**	**IPA Solution (µl)**	**Resistivity, R_{sh} (Ωcm^{-2}) 5 passes**	**Resistivity, R_{sh} (Ωcm^{-2}) 7 passes**
2:1:2	Sigma Aldrich	500	250	500	7.7 (±1.5)	6.3 (±0.6)
1:1:1		500	500	500	35 (±2.0)	13.7 (±1.2)
1:2:1		500	1000	500	52 (±2.7)	30.3 (±2.5)
1:0:1		500	0	500	9.3 (±0.6)	5.3 (±1.2)
0:1:1		0	500	500	>300	>300
2:1:2	Novarials	500	250	500	>300	>300
1:1:1		500	500	500	>300	>300
1:2:1		500	1000	500	>300	>300
PVD Evaporated Ag (80 nm)	N/A	N/A	N/A	N/A	3.7 (±0.6)	3.7 (±0.6)

These results where compared to an 80 nm thermally evaporated PVD metal silver contact deposited on glass with a measured sheet resistance of 3.7 (±0.6) Ωcm^{-2}, measured using the same Jandel 4-point probe. From table 5.1, there is a clear trend between SW/CNT content and resistivity across the film. When the solution is comprised of entirely SW-CNT, resistivity jumps to over 300 Ωcm^{-2},

rendering it unsuitable for a transparent contact material due to resistive nanotube-to-nanotube junctions lowering the electrical conductivity of the macroscopic nanotube wires by orders of magnitude. Increasing the AgNW content has the opposite effect of increasing conductivity by lowering the resistivity across the final film. A solution comprised entirely of silver nanowires demonstrated a conductivity or shunt resistance of just 5.3 Ωcm^{-2} after 7 spray passes. However, the adhesion and strength of this material has come into question and is discussed later in the chapter.

Interestingly a solution containing a 2:1:2 ratio of AgNW: SW-CNT: IPA demonstrated an excellent sheet conductivity of 6.3 Ωcm^{-2} after 7 spray passes. The film matched the result of the solid evaporated silver metal contact within ± 1 Ωcm^{-2} across the whole substrate (3 sites on a microscope slide measuring 75 x 25 mm) and even to the human eye clearly displayed an excellent level of transparency as demonstrated in figure 5.6 below.

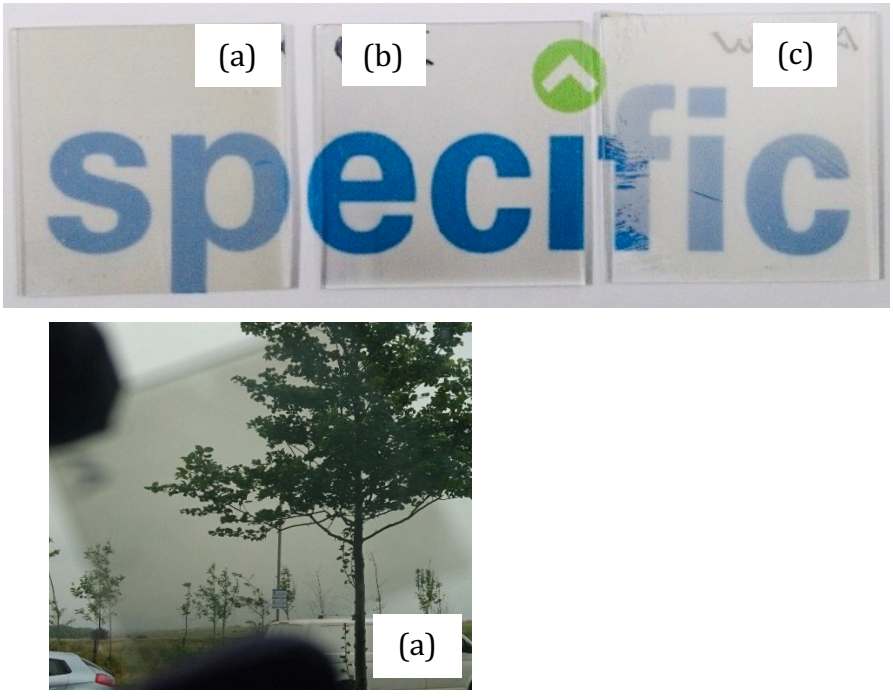

Figure 5.6: Optical images of processed films: (a) represents a film a 2:1:2, AgNW: SW-CNT: IPA solution at 5 passes, (b) represents a 0:1:1, AgNW: SW-CNT: IPA at 7 spray passes and (c) represents a 1:0:1, AgNW: SW-CNT: IPA solution at 7 spray passes.

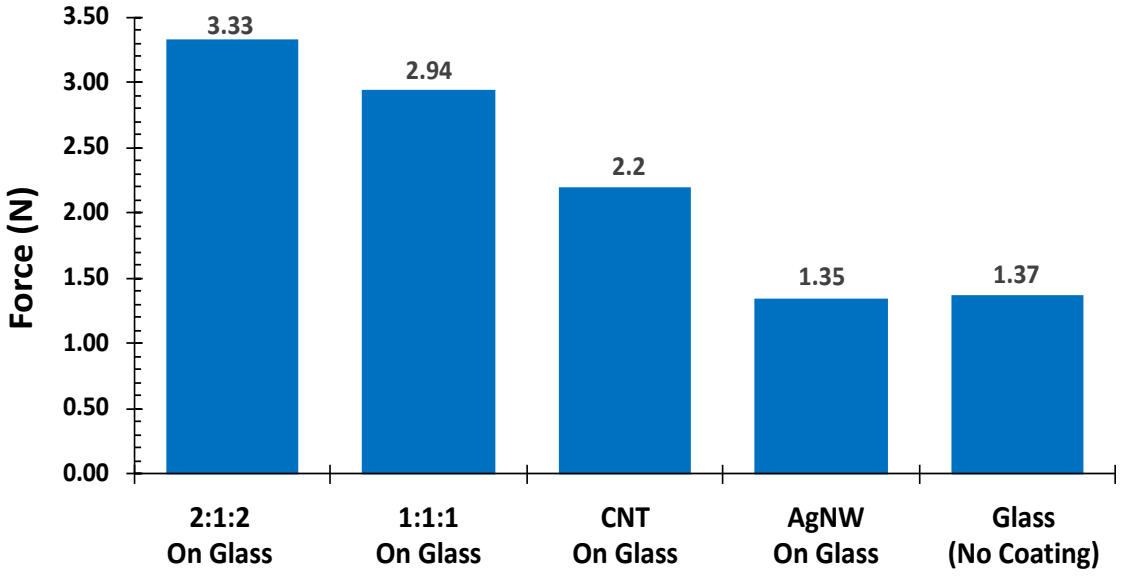

Figure 5.7: Adhesion testing of AgNW: CNT contact materials performed by measuring the force taken to remove Masking Tape of known strength and adhesive at a 90° angle to a fixed platform. (10 spray were used to build up sufficient thickness)

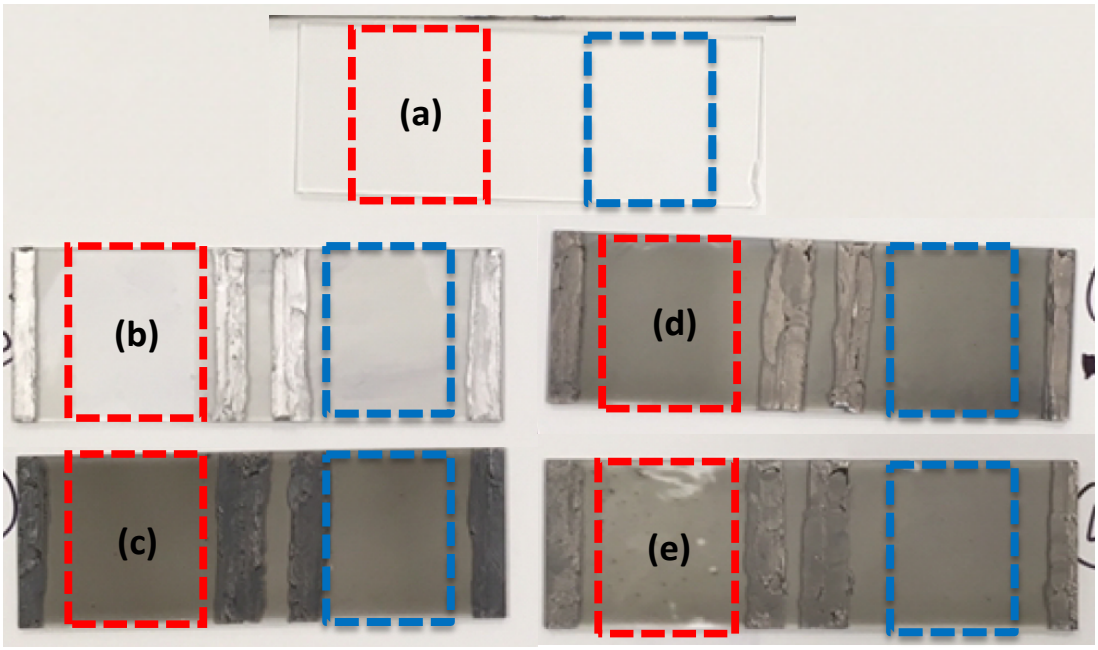

Figure 5.8: Imagery of AgNW: CNT contacts on glass microscope slides with solder. The red dashed lined area indicates the test area post mechanical testing and blue dashed area indicates a coated but untested region for comparison. (a) a clean microscope slide, (b) AgNW on glass, (c) CNT on glass, (d) 1:1:1 AgNW: CNT: IPA on glass, (e) 2:1:2 AgNW: CNT: IPA. 10 spray passes were used for samples (b) – (e) to ensure sufficient layer thickness for testing.

Figure 5.7 shows the relative adhesion strength of each constituent of the AgNW: CNT contact. By measuring the force required to remove a known strip of masking tape at 90 ° using a standard tensile test we can derive a value of relative adhesive strength of each material to a given substrate, in this case glass microscope slides. From the results it becomes clear AgNW by themselves have a negligible adhesive strength to glass as the force required to remove the tape is equivalent to that required for removing the tape directly from an uncoated microscope slide, 1.35 N and 1.37 N respectively. The CNT deposited directly onto glass show an improved adhesive strength of 2.2 N, this result shows the added advantage of using CNT in order to enhance the adhesive strength of the contact. The van Der Waals bonding forces coupled with the nanowires due to covalent sp^2 bonds formed between the individual carbon atoms and the carbon nanotubes ability to exhibit bundling driven by inter-tube bonding, which causes bundles of carbon nanotubes that can even consist of hundreds or even thousands of individual nanotubes. The shorter, narrower, higher surfaced area and more numerous CNTs form more stronger bonds (Van Der Waals, bundling and inter tube bonding) to the surface of the glass due to a higher degree of cross linking between individual CNT whereas the longer AgNW form loose sheets stacked on top of each other with minimal cross linking and contact area. The reduced surface area of the AgNW means less opportunities to force Van Der Waals bonds/ force. The results for the CNT was below expected and this was ascribed to a poor contact between the tape and the surface of CNT, figure 5.8 (c) shows the CNT remains relatively unmoved post tensile testing whereas the AgNW samples seen in figure 5.8 (b) have been completely removed. Subsequent conductivity measurements between the two soldered contacts either side of the test area confirm the AgNW contact has been lost and no charge can flow.

When combining the CNT and AgNW as seen in figure 5.7 and 5.8 the effect combines the adhesive properties of the CNT and the conductivity of the AgNW seen in table 5.1. A higher ratio of AgNW to CNT yielded a higher adhesive force needed to remove the masking tape than one where an equal ratio of AgNW and CNT was employed, with adhesive forces of 3.33 N and 2.94 N recorded respectively. When comparing the red dashed test area and blue dashed coated

but untested areas in Figure 5.8, the samples with a higher ratio of AgNW to CNT display a higher degree of coating removal compared to samples using equal ratios of AgNW and CNT as seen in figure 5.8 (d) and (e). Again, this could be attributed to a poorer contact between the tape and surface of the coating but both results demonstrated an adhesive force of more than double (210 %) increase than that of the AgNW alone. Crucially the contacts remained unbroken and functional (<50 Ωcm^{-2}) post tensile testing and this can be seen visually in figure 5.8. Further tests using a stronger adhesive duct tape were also carried and the AgNW: CNT contact remained functional again. The addition of AgNW to the carbon nanotubes introduces two different sizes of wire/ tube., the SW-CNT are longer than the shorter silver nanowires

With a working and reproducible method for producing a transparent and robust conductive coating, the next stage was to fabricate working PSC devices that incorporated the use of the AgNW: SW-CNT composite into its architecture and compare the resulting performance against our control laboratory devices. An important issue to consider at this stage was how to best optimise these devices for use as a semi-transparent solar window application that would fit into the sponsoring company's strategic objective, NSG Pilkington. The current design of perovskite solar cells maximises the absorption of light in order to generate a high-power conversion efficiency per unit area. Statistical modelling methodologies such as ellipsometry have accurately predicted that by carefully controlling film thickness (equal to 370 nm) and morphology, close to 100% of incident light can be absorbed by a homogeneous, pin hole free perovskite absorber layer [8]. The consequence of higher performance hinders the ability of a semi-transparent solar window because insufficient light is transmitted through the glass and PSC to illuminate the interior space. To this end, the perovskite absorber material needs to be thinned in order for adequate transmission of light for indoor lighting purposes. As laboratory-based devices done at small scale are deposited via spin coating, this thinning can be achieved by either increasing either or both spin speed and active time spinning or by lowering the concentration and hence viscosity and solution density of the perovskite precursor solution used in the coating process as defined in

Meyerhofer et al. work [22]; outlining the processing parameters governing spin coating [23][24][25]. We chose to opt for diluting the perovskite precursor solutions as this method can be applied to scaled methods of production (such as slot die coating) more easily than varying spin coating parameters that only apply to one technology that isn't favoured as a means of mass production for PSCs. The Perovskite precursor solution was diluted in ratios of (DMF: DMSO – 4:1) : (Triple cation precursor, $Cs_{0.05}(MA_{0.17}\,FA_{0.83})_{(0.95)}Pb(I_{0.83}\,Br_{0.17})$). Where 2:1 equates to 2 parts (DMF: DMSO – 4:1) to 1 part (Triple cation precursor - dry constituents) for an average film thickness on plain glass of 132 nm and a 1:1 control solution (TC dry constituents : DMF/DMSO – 4:1) has an average film thickness on plain glass of 315 nm (see table 5.4 for profilometry results). TC denotes triple cation, PVD Ag denotes thermally evaporated opaque metal contacts, AgNW denotes silver nanowires and CNT denotes single walled carbon nanotubes.

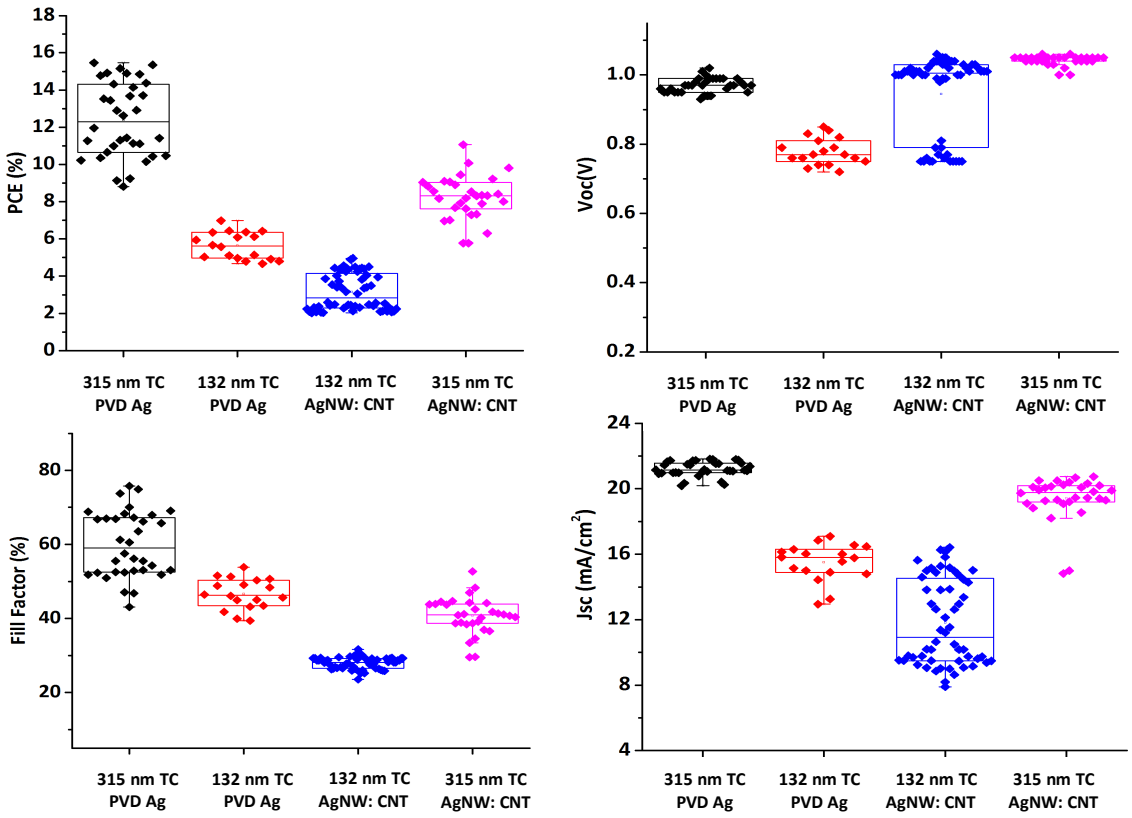

Figure 5.9: Initial J-V results comparing evaporated metal contacts and a 2:1:2 AgNW: SW-CNT: IPA solution at 7 passes annealed at 50 °C. All PSCs incorporate a triple cation-based (TC) perovskite absorber material (Refer to figure 3.3 for the full architecture of these devices).

Table 5.2: Summary of device performance for reverse bias results comparing evaporated metal contacts and a 2:1:2 AgNW: SW-CNT: IPA solution at 7 passes annealed at 50 °C. All PSCs incorporate a triple cation-based (TC) perovskite absorber material

Cell Variant	Voc	Jsc	Fill Factor	PCE
	(mV)	($mAcm^{-2}$)	(%)	(%)
315 nm TC PVD Ag (AVR)	990	21.8	68.2	14.5
315 nm TC PVD Ag (Max)	1020	24.7	76.3	15.7
132 nm TC PVD Ag (AVR)	800	16.2	50.1	6.2
132 nm TC PVD Ag (Max)	855	17.0	54.2	7.0
315 nm TC AgNW: CNT (AVR)	1060	20.4	46.7	9.2
315 nm TC AgNW: CNT (Max)	1070	21.0	53.5	11.1
132 nm TC AgNW: CNT (AVR)	1030	14.0	29	4.1
132 nm TC AgNW: CNT (Max)	1080	16.5	32	5.0

To ascertain whether the AgNW: SW-CNT can be used as an effective charge conducting electrode, devices were fabricated using two principle perovskite absorbing materials; a triple cation-based perovskite and the conventionally used MAPI or methylammonium lead triiodide-based perovskite. Both exhibits reproducibly high PCEs (>20%) and both were thinned to enhance light transmission through the cell and compared to standard or normal thickness devices. Refer to section 5.2 and 3.2 for fabrication methodologies of PSC. Interestingly, both perovskite thickness variations exhibit better than expected initial PCEs when combined with the AgNW: SW-CNT (2:1:2) as seen in figure 5.9 and table 5.2. The control thickness devices showed an average reverse bias PCE of 9.2 % compared to 14.5 % for control devices with evaporated, opaque metal contacts. Whereas the thinned devices achieved an average reverse PCE of 4.1 % compared to 6.2 % with an evaporated, opaque metal contact. Overall the thinned perovskite devices demonstrated wider variance in JV parameters such as short circuit current density, J_{SC} and open circuit voltage V_{OC}. Most noticeable is the reduction in fill factor for the diluted, thinned perovskite films. This can be attributed to the difficulties in controlling a uniform thickness of the triple cation film using more dilute solutions. Thinner regions and poor conformal coating leads to regions across the cell that have a reduced J_{SC} as seen in figure 5.9, while

pinholing and increased defects densities contributing to parasitic recombination and internal series resistances [26][27][28]. The uniformity of the AgNW: SW-CNT could cause poor J_{SC} and FFs across certain regions, but this can be attributed to human/ operator error during spray coating. Due to the use of IPA as the carrier solvent, prolonged exposure of the Spiro /perovskite films in IPA without adequate and fast drying when sprayed by hand led to degradation of the surface of the tripe cation/ Spiro OMeTAD layers and would likely contribute to interfacial defects, and complex impurities leading increased interface recombination and a reduction in fill factor. Thus, automation would be needed for larger scale devices to be reproducible, this can explain the difference seen between the sprayed silver nanowire/CNT devices to some extent. The V_{OC} across both AgNW: SW-CNT appears high, greater than 1.0 V showing that when homogeneous in coverage the composite acts as an efficient charge extraction contact and that the likely causes in the drop in performance can be linked in interfacial, parasitic recombination pathways. [29].

To analyse the optical performance of the fabricated devices, ultraviolet to visible spectrophotometry in the range 250 nm to 800 nm was employed and the resulting transmission spectra of full devices can be observed in figure 5.10. Reference guidelines from the spectra indicate that around 420 nm, transmission of light begins through the thinned film of perovskite, this increases up to around 10% around 550 nm. This wavelength is commonly quoted when describing the transparency or semi transparency of a window material. Tinted windows in automotive applications typically have a transmission of around 15 – 26% and are commercially available as low as 5 % transmission (also known as limo tint). This result bodes well for PSC as a potential dual-purpose building and automotive materials as layer thickness can be precisely controlled along with light transmission without compromising performance too severely.

Beyond 550 nm the semi-transparent diluted PSC employing AgNW-CNT contacts recorded a transmission of nearly 30% at the upper limit of the human eyes visible range (~700 nm). Further still into the NIR and transmission peaks at around 42 % at 800 nm. Average transmission value across the visible range (400 – 750 nm) was recorded at 14.5 % for the semi-transparent dilute PSC incorporating the AgNW-CNT contact.

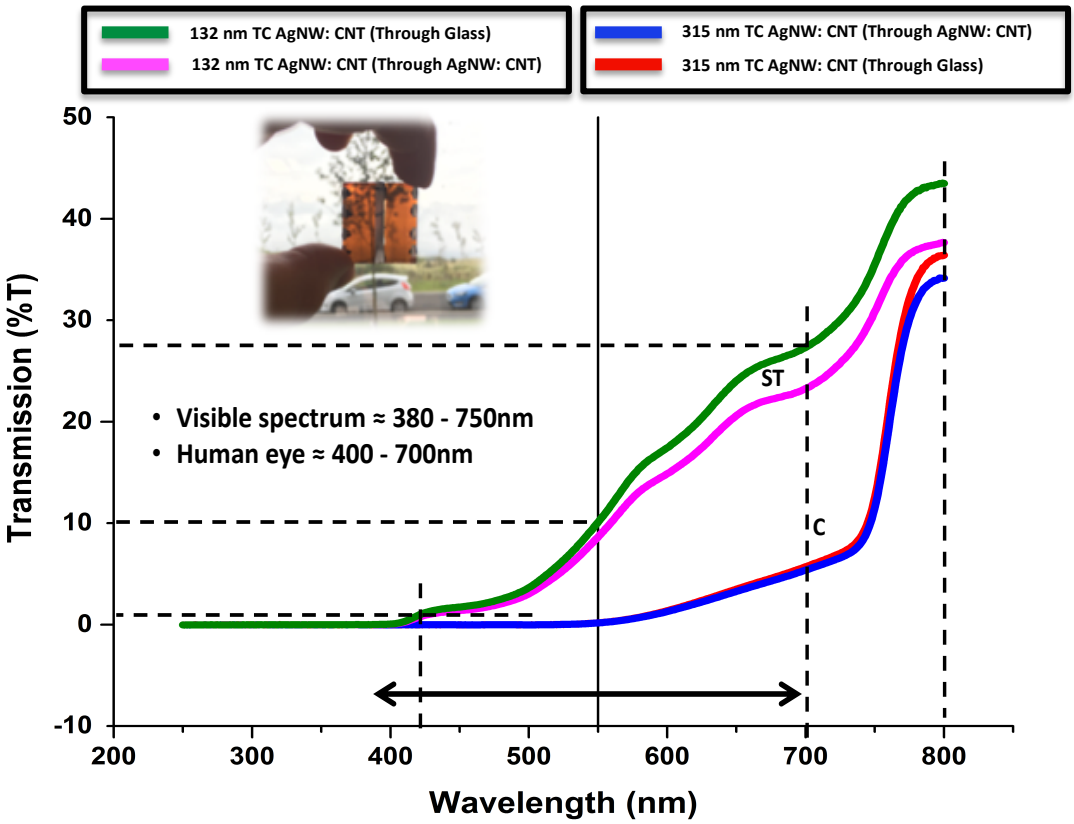

Figure 5.10: UV-Visible spectra analysis of full devices incorporating the AgNW: SW-CNT contact and a triple cation-based perovskite of varying thicknesses. ST denotes semi-transparent, where the perovskite solution has been diluted and C denotes non diluted control perovskites. A picture of a completed ST device is inserted for reference.

The resulting spectra for the 315 nm TC AgNW: CNT films show a marked increase in absorption and reduced transmission across the spectral range (250nm – 800nm). The thicker layer resulting in higher incident photon

absorption and subsequent power output as shown in figure 5.9 earlier. Transmission of light begins around 560 nm, increasing to around 5 % at 700nm and then sharply increasing over the NIR range up to 800 nm where a peak transmission of just over 30 % was observed. The sharp increase in transmission for the control cells from 750 nm to 800 nm is a key limiting factor for the final PCE, we postulate that in conventional cells employing an opaque reflective metal contact, these wavelengths would be reflected back towards the perovskite absorber material and allow for high photon absorption as seen in the increase short circuit current seen in figure 5.9. The result also indicates a potential area for optimisation, by indicating a perovskite thin film of insufficient thickness to absorb all incident photons.

One of the many attractive properties of Perovskites is the wide variety of chemistries that can be used to harvest light for energy. This wide array of materials means perovskites could be tuned for various applications depending on the product requirement. This is especially pertinent when considering semi-transparent photovoltaic windows where colour and over transmission of light of the visible spectrum are important. It was decided to compare multiple perovskite chemistries to see which would produce the best compromise of optical and electronic performance. The most commonly reported perovskite, MAPI was fabricated next. Again, it was decided to dilute the standard 1.1M perovskite precursor solution with excess DMF: DMSO – 4:1 in order achieve a semi-transparent thin film, with a thickness of 121 nm when profiled on plain glass as seen in table 5.4. Again, 2:1 equates to 2 parts (DMF: DMSO – 4:1) to 1-part MAPI precursor – 1.1 M dry constituents. This was compared to a 1:1 control solution (TC dry constituents: DMF/DMSO – 4:1) that has an average film thickness on plain glass of 296 nm (see table 5.4 for profilometry results). The full details of the fabrication process can be found in chapter (5.2. The devices were then combined with the AgNW: CNT: IPA (2:1:2) contact and JV measurements taken from 1.2 V to -0.1 V at a sweep rate of 10Wcm^2. A comparative JV summary of semi-transparent versus control thickness perovskites incorporating the AgNW: CNT contact and a control PVD evaporated Ag metal contact can be seen in Figure 5.11.

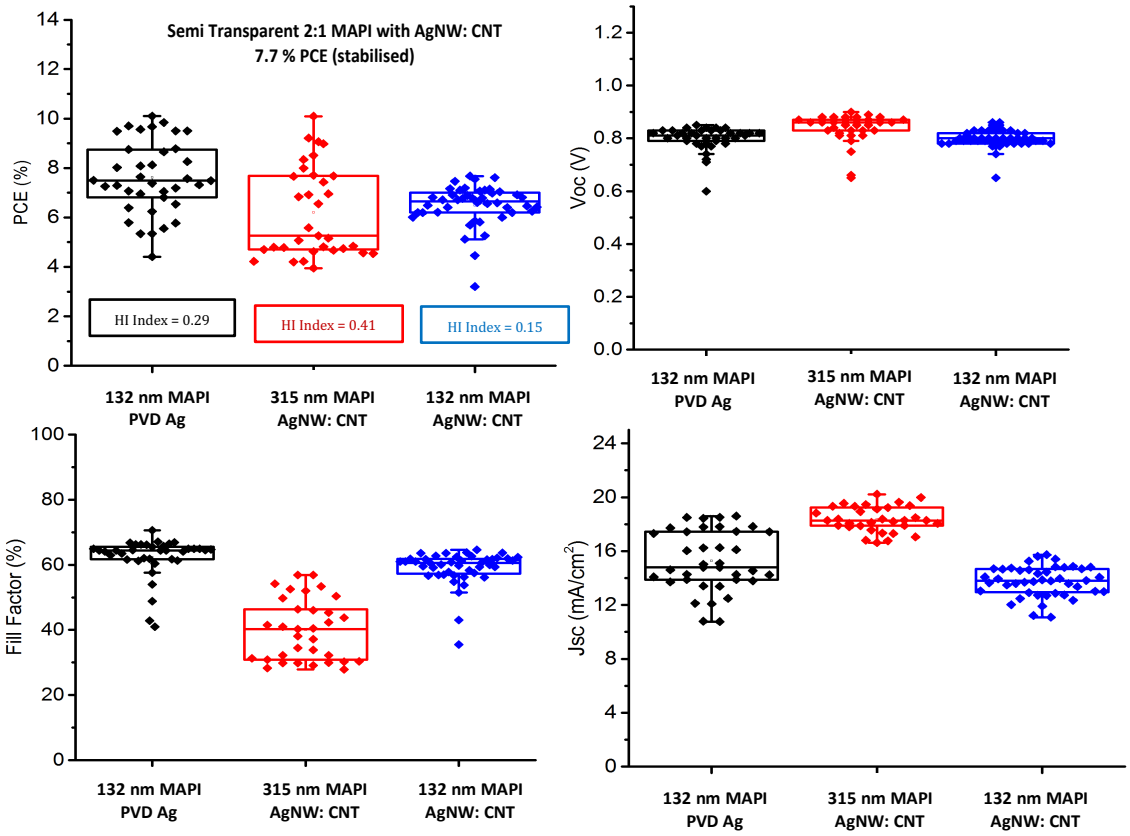

Figure 5.11: Resulting of J-V results comparing evaporated metal contacts and a 2:1:2 AgNW: SW-CNT: IPA solution at 7 passes annealed at 50 °C. All PSCs incorporate a MAPI-based perovskite absorber (Refer to figure 3.3 for the full architecture of these devices). The Perovskite precursor solution was also diluted in same ratios as previously stated in Figure: 5.7). AgNW denotes silver nanowires and CNT denotes single walled carbon nanotubes. HI Index denotes the Hysteresis index for champion device architectures, calculated by:

$(PCE_{reverse} - PCE_{forward} / PCE_{reverse})$.

Table 5.3: Summary of device performance for reverse bias results comparing evaporated metal contacts and a 2:1:2 AgNW: SW-CNT: IPA solution at 7 passes annealed at 50 °C. All PSCs incorporate a MAPI perovskite absorber material

Cell Variant	Voc	Jsc	Fill Factor	PCE
	(mV)	($mAcm^{-2}$)	(%)	(%)
132 nm MAPI PVD Ag (AVR)	820	17.5	66.1	8.9
132 nm MAPI PVD Ag (Max)	860	18.9	71.0	10.1
315 nm MAPI AgNW: CNT (AVR)	870	19.2	47.1	7.5
315 nm MAPI AgNW: CNT (Max)	900	20.2	58.0	10.1
132 nm MAPI AgNW: CNT (AVR)	812	14.3	62.3	7.0
132 nm MAPI AgNW: CNT (Max)	875	15.9	65.8	7.8

The standout result from table 5.2 and figure 5.11 a semi-transparent 132 nm thick MAPI device recorded a stabilised power conversion efficiency of 7.7 % over a duration of 30 seconds whilst being held at V_{max}. This result unexpectedly eclipsed that of the triple cation perovskite seen in Figure 5.9. The 132 nm MAPI devices incorporating the AgNW: CNT composite relatively consistently across all devices measured in the reverse direction with an average reverse bias PCE of 7.0%, and this can be seen in the corresponding tight distribution of the box plots. The box plots in figure 5.11 display both forward and reverse JV measurements, the more elongated the box, the higher the variance between forward and reverse scan biasing. A hysteresis index is included for champion device architectures in figure 5.11, comparing these results allows us to compare the forward and reverse scan differences across the samples. It can be seen the dilute MAPI with AgNW: CNT has a relatively low hysteresis index of 0.15 when compared to the evaporated Ag contacts, 0.29 and higher still was the undiluted MAPI devices with a HI index of 0.41. The tight box plots for the diluted semi-transparent, 132 nm thick MAPI devices indicate a close agreement for both forward and reverse measurements which lead us to conclude there is negligible hysteresis for these devices, this is corroborated by the narrow box plot representing fill factors in figure 5.11. This can be attributed to improved conformality of the diluted perovskite layer and hence improved interfacial connection between the perovskite absorbing material and hole transport material. This ensures less pinholing with a lower surface roughness and allows

for a more conformal Spiro HTL material to be deposited on top. These highly conformal layers mean that if a homogeneous AgNW: CNT contact film can be deposited on top; interfacial recombination pathways can be mitigated, and charge build up at interfaces reduced, provided the AgNW: CNT film is homogenous across the HTL with its lattice network. Breaks in the AgNW: CNT layers or poor coverage can lead to charge build up across the surface and interfacial recombination takes over. The overall effect here is a lowering of shunt resistance, increases in series resistance and a lowering of fill factor and a subsequent increase in the hysteresis index [28] [22] [23] [33]. This is supported with profilometry data from table 5.2 where the dilute perovskite layer on glass has an average step height thickness of 121 nm and the un-diluted perovskite layer has average of 296 nm with a larger thickness variation over the 2.5 x 2.5 cm^2 area. It should be noted the thicknesses in full devices may vary from the averages seen in table 5.3 due to the increased surface roughness of the mesoporous TiO_2 incorporated into the device structure but table 5.2 gives a strong indication of the likely film thicknesses in full devices.

Table 5.4: Profilometry of methylammonium lead triiodide and caesium containing triple cation films spin coated onto clean plain microscope slides, measuring 2.5 x 2.5 cm^2. A stylus force of 5 mg was used so not to damage the perovskite surface. 3 forward scans of 2 mm in length spaced 0.7 cm apart were conducted across samples with a range of 10 μm and a speed of 0.1 mms^{-1}. Data was filtered with an 8-point average using a KLA, Tencor, D600 profilometer.

Sample	**Step Height Thickness (nm)**			**Average (nm)**
(2:1) Dilute MAPI on plain glass – Semi Transparent	125	117	120	**121**
(1:1) MAPI on plain glass - Control Thickness	319	278	292	**296**
(2:1) Dilute TC on plain glass – Semi Transparent	131	135	130	**132**
(1:1) TC on plain glass - Control Thickness	311	305	330	**315**

The impressive film coverage and homogeneity of the diluted 121 nm MAPI films was noticeable as can be seen in the photographs in figure 5.13. We can link this to the precursor materials fully dissolving in the presence of excess solvent. This reduces the potential for defects during the critical perovskite deposition phase as undissolved constituents can lead to improper crystallisation of the perovskite film causing the formation of voids, pin holes that can detrimentally affect a cells performance. This could indicate why the PCE for the non-diluted films with AgNW: CNT contacts are lower than expected. Although J_{SC} and V_{OC} are relatively high, the fill factors are lower than that of the undiluted films. In addition this is likely associated to the poor coverage of the AgNW: CNT because of increased surface roughness and the associated operator error when spraying manual coating is involved in fabrication as explained above.

The MAPI JV data from figure 5.11 shows a similar correlation to that of figure 5.10 with the triple cation devices. There is decrease in J_{SC} in the diluted films compared to the non-diluted films due to the thinner, semi-transparent films allowing more light to pass through unabated (unabsorbed). Fill factors show less variation in the diluted films than non-diluted films. While V_{OC} appears to be more consistent across all the MAPI devices compared to the triple cation films owing to the unoptimized processing conditions of the triple cation-based devices.

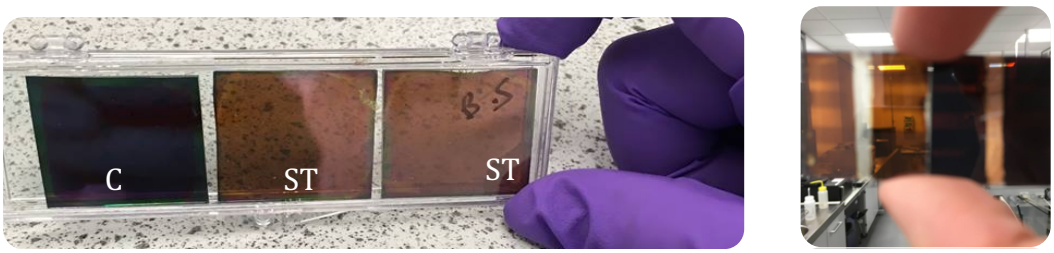

Figure 5.12: Imagery illustrating the comparative transparencies between the diluted and undiluted methylammonium lead triiodide films prior to deposition of contacts. The films demonstrated a glass like appearance with very few visual defects for the semi-transparent (ST) dilute (121 nm thick MAPI films). The thicker control (C) MAPI film (296 nm) can be seen on the far left and far right. Note: the ST film in the middle is partially shaded. The image on the right is finished device employing the AgNW: CNT composite contact.

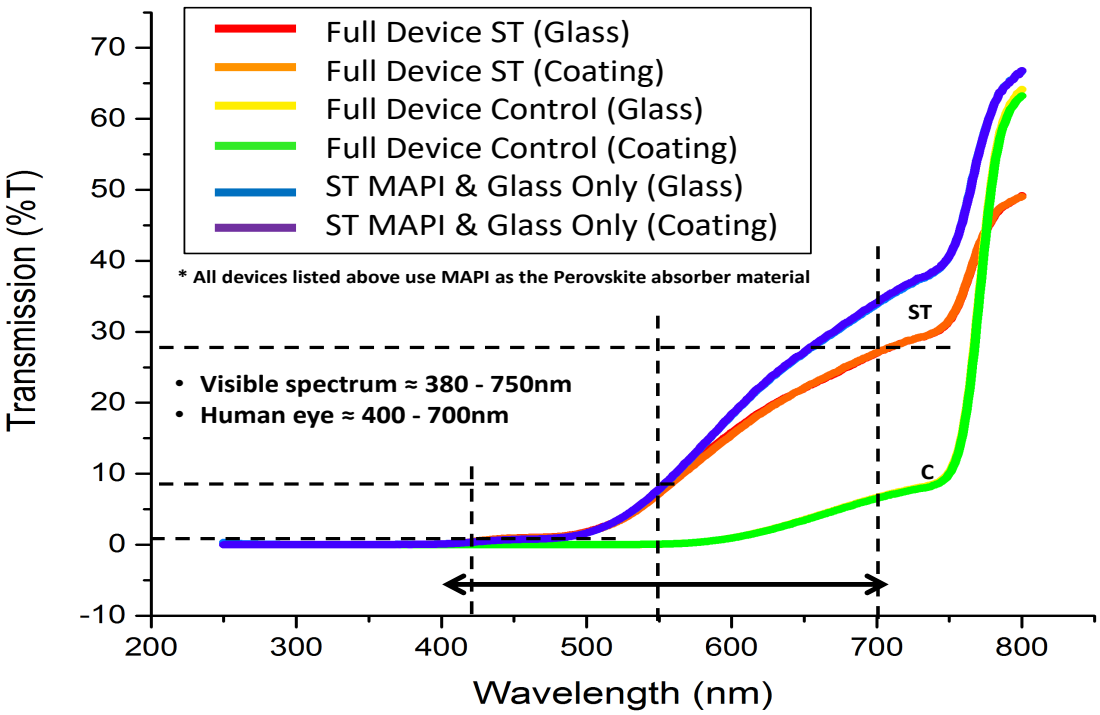

Figure 5.13: UV-Visible spectroscopic analysis of full devices incorporating the AgNW: SW-CNT composite material and variations in perovskite absorber material thickness using a methyl ammonium lead triiodide-based perovskite absorber (MAPI). ST denotes semi-transparent, perovskite solution diluted devices and C denotes non diluted control perovskites.

The optical properties of full MAPI based devices employing the AgNW: CNT composite contacts were analysed via spectrophotometry over the range 250 nm to 800 nm, as seen in figure 5.13. The undiluted films with the AgNW: CNT contacts indicated that transmission initiates around 600 nm and increases to around 5 % at the end of the visible spectrum (700 nm). Above 750 nm and into the near infra-red portion of the electromagnetic spectrum, transmission increases rapidly and reaches a maximum of 60 % at 800 nm. This transmission was greater than that observed for the triple cation-based perovskites (35 % at 800 nm as seen in figure 5.10) thus indicating how perovskite composition can be used to optimise absorption and transmission in a given region of the electromagnetic spectrum. MAPI has been shown in literature to have limitations in harvesting near infrared light in the solar spectrum whereas perovskites based

around a formamidinium mixed cation-based perovskite have more favourable band gaps (~ 1.45 eV) close to the ideal band gap (~1.2 to 1.3 eV). [34]

The diluted MAPI films incorporating the AgNW: CNT showed a similar trend to the triple cation films in figure 5.8. Transmission initiates around 420 nm and increases to ~ 8 % at 550 nm, increasing to just under 30 % at 700 nm and the end of visible spectrum. The average transmission over the visible range (400 nm to 750 nm) was calculated at 13 %. Slightly below the 14.5 % of that achieved by the triple cation film but with a marked improvement in PCE. Again, this figure of 13 % is well above the 5 % used in certain tinted window applications such as automobiles. Also measured was a film of diluted MAPI deposited on glass, c-TiO_2 and mesoporous TiO_2 to see the effect the HTM (Spiro-MeOTAD) and the AgNW: CNT have on overall transmission of full devices. The average transmission without the AgNW: CNT and HTM was slightly higher at 15.6 % thus demonstrating it is the perovskite material and base layers that have the single largest impact on transmission. The AgNW: CNT contact reduces overall transmission by much less than 2 % given oxidised Spiro-MeOTAD is known to absorb part of visible spectrum (400 - 750 nm) and significantly in the region of 600 nm to 750 nm as described by Fantacci et al. [35]. This absorption correlates to where the two transmissions lines diverge in figure 5.10.

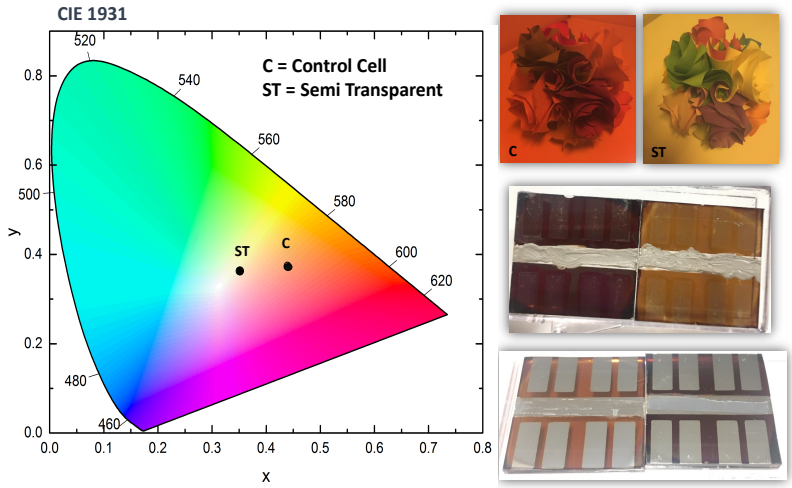

Figure 5.14: CIE (International commission on illumination) colour spectrum analysis and photographs of fabricated devices including perovskite thickness variations and a demonstration of the clarity of the films. C = control, 296 nm MAPI and ST = semi transparent, 121 nm Dilute MAPI.

The thin films of perovskite were investigated further by CIE International commission on illumination) colour analysis. Varying a materials thickness has the effect of changing certain optical properties. One such metric is colourimetry and when designing a transparent window for potential commercial applications, aesthetics is an important area to consider. Figure 5.14 shows CIE colour mapping of both the thinned, diluted perovskite material and compares it to that of the control cell, both are fully fabricated working devices employing the AgNW-CNT contact. The overall effect of thinning and diluting the perovskite material for a window application has shifted the colour spectrum towards the neutral centre point of the CIE plot when compared to the control cell that is shifted further towards the red or warmer portion of the CIE chart. This can be attributed to destructive interference as reflective wavelengths of light from the surface and back of the film have overlapping crests and troughs that cancel each other out and so dimming the colour of the thinned perovskite film. The opposite effect, constructive interference reinforces overlapping crests and results in the thicker non diluted samples exhibiting a stronger more pronounced red hue. This shift towards the neutral centre point is also advantageous as a potential commercial technology because products closer to the neutral or centre point have a stronger market appeal according to NSG Pilkington. Reference photos in figure and 5.13 and 5.14 demonstrate to the human eye how marked the difference in colour between the semi-transparent diluted perovskite and the control cells are when compared side by side. Although both are still clearly semi-transparent, and imagery can clearly be seen through the resulting films.

Table 5.5: Summary of Haze and Clarity measurements of constituent perovskites layers fabricated in the lab. Where CNT denotes single walled carbon nanotubes (Tuball™), AgNW denotes silver nanowires (Sigma Aldrich) and MAPI denotes methyl ammonium lead triiodide. All samples were fabricated onto clear plain glass (1.1 mm thick). Measurements were taken using a Haze Guard Plus from Garden.

Sample	**Haze**	**Clarity**
CNT Only	5.13	98.50
AgNW Only	25.75	99.10
AgNW & CNT (Composite)	12.10	99.00
Mesoporous TiO_2 & MAPI (Undiluted (≥ 296 nm))	11.8	99.52
Mesoporous TiO_2 & MAPI (Diluted 2:1 (≥ 125 nm))	6.91	99.80
Mesoporous TiO_2 & Triple Cation (Undiluted)	21.1	99.34
Mesoporous TiO_2 & Triple Cation (Diluted 2:1)	21.92	99.70
Mesoporous TiO_2 (200nm)	0.67	99.80
1.1mm Glass (reference)	0.13	99.98

The optics of the AgNW: CNT contact and perovskite films were further explored through haze and clarity measurements performed at NSG Pilkington's European technical research centre. Haze relates to the amount of light that is subject to wide angle scattering at an angle greater than 2.5° from normal (ASTM D1003). Total haze is a combination of both transmission and reflection whereas clarity relates to the amount of light that is subject to narrow area scattering at an angle less than 2.5° from normal. As can be seen in table 5.3, the AgNW by themselves exhibit a relatively high degree of haze compared to the CNT (25.75 and 5.13 respectively). This quantifies what can be seen in figures 5.13 and 5.14 presented earlier. The combination of AgNW and CNT compromises extremely well and a haze of just 12.10 was recorded for the contact on glass. The high degree of haze that can be seen in the AgNW can be attributed to the longer lengths of the nanowires (>50um) procured from Sigma Aldrich when compared to the shorter SW-CNT (>5um) which exhibits much less Haze, 5.13. Long AgNW lengths are ideal for use in solar cells due to the high transmission of visible light as

demonstrated by Yu et al. [36]. But the short length nature of the AgNW that give rise to high optical transparency also give rise to high haze, almost twice as much seen than if using longer AgNW (5-50 μm). as reported by Yu et al. This is because the short length of AgNW used have a higher relative density per area than longer AgNW (which would absorb more light thus less effective at transmitting it) and so wide-angle light scattering increases. The same reasoning can be applied for CNT. The longer length of the Tuball™ single walled CNTs reduces haze, seen in table 5.2 but also reduces the transmission of light overall as well as conductivity as seen in table 5.1. [36]. Interestingly there is a noticeable difference in the wide-angle light scattering between the two perovskite compositions. MAPI based devices show much lower haze (< 12) than the triple cation-based films (>21) for both diluted and undiluted samples. The haze in these triple cation films can be seen after spin coating and does not appear to have a detrimental effect on efficiencies although this could be limiting our triple cation films from reaching efficiencies of over 20 % but this is yet to be confirmed. We hypothesise the haze of the triple cation film comes from an increased surface roughness during the antisolvent drip and annealing process that scatters light at the surface of annealed film, thus giving it a slightly cloudy appearance. The fact that the haze remains present in both dilute and undiluted films suggests the origin of the hazing effect is not caused by undissolved precursors within the solution but rather processing conditions present within our laboratories glovebox, excess solvent levels is suspected but at the time of writing unconfirmed. It is also worth noting that the dilute MAPI recorded a lower haze than undiluted sample, potentially indicating undissolved precursors in the undiluted MAPI samples. This supports the JV statistical data. Analysis mentioned earlier.

The clarity, relating to the amount of light that is subject to narrow area scattering at an angle less than 2.5° from normal of all films was very high, meaning the amount of light subject to narrow area scattering at an angle less than 2.5° from normal was negligible. This is important when considering the design of a semi-transparent PV window as occupants need to be able to clearly see through the multiple layers within the device for the window to function properly.

5.4 Conclusions

The results presented in this chapter follow on well from the chapter 3 involving a mass manufactured electron transport layer based on CVD processed TiO_2. In order for Eclipse Advantage ™ to be used as a semi-transparent window, a transparent top contact material is needed to replace the conventional evaporated opaque metal contacts. The composite material based on AgNW and single walled CNTs presented in this chapter display key advantages over conventional metal nanowire-based contacts. The issue of poor adhesion related to AgNWs has been alleviated by incorporating a shorter length single walled CNT into a matrix design that adheres well even smooth substrates via the effects of increased surface area for Van Der Waals bonds, strong covalent bonding, high ultimate yield stress and inter tubular bonding and nanotube bundling. An increase in adhesion strength of 260 % was recorded for the optimal AgNW: SW CNT composite material (2:1) when dispersed in 2 parts IPA and sprayed at 25 psi. While at the same time demonstrating sheet resistances comparable to that of evaporated metal contacts. Sheet and shunt resistances (R_{SH}) were consistently lower than 10 Ωcm^{-2} across all samples. The processing technology used (spray coating) is relatively easy to upscale and simple to prepare, thus the issue of scale-up is also mitigated.The transparency of the contact allows a substantial portion of the electromagnetic spectrum to pass through unabated with excellent haze, clarity and optical (CIE colourimetry) performance. Full devices based on diluted MAPI perovskite absorbers demonstrated a stabilised PCE of over 7 % with an average transparency of 13 % over the visible spectrum. The development of multiple solution-processed semi-transparent perovskites prepared by diluting stock precursor solutions further enhances the possibility of using thinner layers of perovskites to improve the transmission of light without hampering performance catastrophically.

5.5 Bibliography

[1] X.-T. Zhang, O. Sato, M. Taguchi, Y. Einaga, T. Murakami, and A. Fujishima, "Self-Cleaning Particle Coating with Antireflection Properties," *Chem. Mater.*, vol. 17, no. 3, pp. 696–700, Feb. 2005.

[2] T. Watanabe *et al.*, "Photocatalytic activity and photoinduced hydrophilicity of titanium dioxide coated glass," *Thin Solid Films*, 1999.

[3] Oxford PV ltd., "The perovskite-silicon tandem," *The perovskite-silicon tandem*, 2019. [Online]. Available: https://www.oxfordpv.com/perovskite-silicon-tandem.

[4] C. D. Bailie *et al.*, "Semi-transparent perovskite solar cells for tandems with silicon and CIGS," *Energy Environ. Sci.*, vol. 8, no. 3, pp. 956–963, 2015.

[5] F. Lang *et al.*, "Perovskite Solar Cells with Large-Area CVD-Graphene for Tandem Solar Cells," *J. Phys. Chem. Lett.*, vol. 6, no. 14, pp. 2745–2750, Jul. 2015.

[6] T. Leijtens, K. A. Bush, R. Prasanna, and M. D. McGehee, "Opportunities and challenges for tandem solar cells using metal halide perovskite semiconductors," *Nature Energy*. 2018.

[7] L. Wang, G. R. Li, Q. Zhao, and X. P. Gao, "Non-precious transition metals as counter electrode of perovskite solar cells," *Energy Storage Mater.*, 2017.

[8] L. J. Phillips *et al.*, "Maximizing the optical performance of planar CH3NH3PbI3 hybrid perovskite heterojunction stacks," *Sol. Energy Mater. Sol. Cells*, 2016.

[9] Z. Li *et al.*, "Laminated Carbon Nanotube Networks for Metal Electrode-Free Efficient Perovskite Solar Cells," *ACS Nano*, vol. 8, no. 7, pp. 6797–6804, Jul. 2014.

[10] F. Jiang *et al.*, "Metal electrode–free perovskite solar cells with transfer-laminated conducting polymer electrode," *Opt. Express*, vol. 23, no. 3, p. A83, Feb. 2015.

[11] P. You, Z. Liu, Q. Tai, S. Liu, and F. Yan, "Efficient Semitransparent Perovskite Solar Cells with Graphene Electrodes," *Adv. Mater.*, vol. 27, no. 24, pp. 3632–3638, Jun. 2015.

[12] J. Troughton *et al.*, "Highly efficient, flexible, indium-free perovskite solar cells employing metallic substrates," *J. Mater. Chem. A*, vol. 3, no. 17, pp. 9141–9145,

2015.

[13] K. A. Bush *et al.*, "Thermal and Environmental Stability of Semi-Transparent Perovskite Solar Cells for Tandems Enabled by a Solution-Processed Nanoparticle Buffer Layer and Sputtered ITO Electrode SI," *Adv. Mater.*, 2016.

[14] F. Fu *et al.*, "Low-temperature-processed efficient semi-transparent planar perovskite solar cells for bifacial and tandem applications," *Nat. Commun.*, vol. 6, no. 1, p. 8932, Dec. 2015.

[15] F. Fu *et al.*, "High-efficiency inverted semi-transparent planar perovskite solar cells in substrate configuration," *Nat. Energy*, vol. 2, no. 1, p. 16190, Jan. 2017.

[16] B. Chen *et al.*, "Efficient Semitransparent Perovskite Solar Cells for 23.0%-Efficiency Perovskite/Silicon Four-Terminal Tandem Cells," *Adv. Energy Mater.*, 2016.

[17] Y. Zhu *et al.*, "Size effects on elasticity, yielding, and fracture of silver nanowires: In situ experiments," *Phys. Rev. B - Condens. Matter Mater. Phys.*, 2012.

[18] M. M. J. Treacy, T. W. Ebbesen, and J. M. Gibson, "Exceptionally high Young's modulus observed for individual carbon nanotubes," *Nature*, 1996.

[19] D. Bellet *et al.*, "Transparent electrodes based on silver nanowire networks: From physical considerations towards device integration," *Materials (Basel).*, 2017.

[20] J. W. Song, J. Kim, Y. H. Yoon, B. S. Choi, J. H. Kim, and C. S. Han, "Inkjet printing of single-walled carbon nanotubes and electrical characterization of the line pattern," *Nanotechnology*, 2008.

[21] M. F. Yu, B. S. Files, S. Arepalli, and R. S. Ruoff, "Tensile loading of ropes of single wall carbon nanotubes and their mechanical properties," *Phys. Rev. Lett.*, 2000.

[22] D. Meyerhofer, "Characteristics of resist films produced by spinning," *J. Appl. Phys.*, 1978.

[23] A. G. Emslie, F. T. Bonner, and L. G. Peck, "Flow of a viscous liquid on a rotating disk," *J. Appl. Phys.*, 1958.

[24] W. J. Daughton, F. L. Givens, W. J. Daughton, and F. L. Givens, "An Investigation of the Thickness Variation of Spun-on Thin Films Commonly Associated with the Semiconductor Industry," *J. Electrochem. Soc.*, 1982.

[25] Y. Mouhamad, P. Mokarian-Tabari, N. Clarke, R. A. L. Jones, and M. Geoghegan, "Dynamics of polymer film formation during spin coating," *J. Appl. Phys.*, vol.

116, no. 12, p. 123513, Sep. 2014.

[26] S. A. L. Weber *et al.*, "How the formation of interfacial charge causes hysteresis in perovskite solar cells," *Energy Environ. Sci.*, vol. 11, no. 9, pp. 2404–2413, 2018.

[27] B. Park *et al.*, "Understanding how excess lead iodide precursor improves halide perovskite solar cell performance," *Nat. Commun.*, vol. 9, no. 1, p. 3301, Dec. 2018.

[28] M. Saliba *et al.*, "How to Make over 20% Efficient Perovskite Solar Cells in Regular (n-i-p) and Inverted (p-i-n) Architectures," *Chem. Mater.*, 2018.

[29] S. Ravishankar *et al.*, "Influence of Charge Transport Layers on Open-Circuit Voltage and Hysteresis in Perovskite Solar Cells," *Joule*, vol. 2, no. 4, pp. 788–798, Apr. 2018.

[30] L. Gil-Escrig, A. Miquel-Sempere, M. Sessolo, and H. J. Bolink, "Mixed Iodide-Bromide Methylammonium Lead Perovskite-based Diodes for Light Emission and Photovoltaics," *J. Phys. Chem. Lett.*, 2015.

[31] M. Saliba *et al.*, "Cesium-containing triple cation perovskite solar cells: improved stability, reproducibility and high efficiency," *Energy Environ. Sci.*, vol. 9, no. 6, pp. 1989–1997, 2016.

[32] T. Matsui *et al.*, "Effect of Rubidium for Thermal Stability of Triple-cation Perovskite Solar Cells," *Chem. Lett.*, vol. 47, no. 6, pp. 814–816, Jun. 2018.

[33] B. Chen, M. Yang, S. Priya, and K. Zhu, "Origin of J-V Hysteresis in Perovskite Solar Cells," *Journal of Physical Chemistry Letters*. 2016.

[34] M. Azam *et al.*, "Highly efficient solar cells based on Cl incorporated tri-cation perovskite materials," *J. Mater. Chem. A*, 2018.

[35] S. Fantacci, F. De Angelis, M. K. Nazeeruddin, and M. Grätzel, "Electronic and optical properties of the spiro-MeOTAD hole conductor in its neutral and oxidized forms: A DFT/TDDFT investigation," *J. Phys. Chem. C*, 2011.

[36] X. Yu, X. Yu, J. Zhang, L. Chen, Y. Long, and D. Zhang, "Optical properties of conductive silver-nanowire films with different nanowire lengths," *Nano Res.*, 2017.

Chapter 6

A Bifacial Transparent Conductive Contact based on Indium doped Zinc Oxide and Molybdenum oxide for Window Applications

Work in this chapter has been submitted for publishing in Advanced Energy Materials (Zhengfei Wei, Benjamin Smith, Vasil Stoichkov, Harrison Ka Hin Lee, Jérémy Barbé, Wing C. Tsoi, David A. Worsley and Trystan M. Watson).

Work in this chapter was formulated around a previous piece of work published in the Journal of Materials Chemistry C (Wei Zhengfei, Smith Benjamin, De Rossi Francesca, Searle Justin, Worsley David, Watson Trystan). J. Mater. Chem. C, 2019,7, 10981-10987.

6.1 Introduction

Chapter 5 presented an efficient, highly conductive, adhesive transparent contact based on a silver nanowire and single walled carbon nanotube composite material. However, the use of silver within solar cells presents a problem as silver is known to degrade and poison the soft HTM Spiro-MeOTAD by migrating through the surface to create short circuit pathways that eventually cause failure of PSC over time. The lifetime is limited by this and affected by heat and light exposure and is of concern if the technology is to be adopted. Barrier layers are seen as a way to mitigate these problems [1]. In this chapter we present a radio frequency magnetron sputtered bifacial transparent conductive contact based on indium doped zinc oxide (IZO) and molybdenum trioxide (MoOx) that serves not only to act as an effective charge collecting contact but also aid with the encapsulation of the PSC leading to extended PSC lifetimes. This is coupled with the SnO_2 based ETL material presented in chapter 4 that has recently seen much attention due to its high associated PCE, hysteresis free behaviour and long-term stability when compared to devices based around a conventional TiO_2 structured device. Also incorporated into the device is the caesium doped triple cation-based perovskite that has shown much promise with high PCE and good thermal and optical stability.

By combining these technologies and the learnings from previous chapters, it is hoped that large scale semi-transparent dual functional PSC windows for structural and automotive uses can become a reality in the near future. The ability to harness the sun's energy in our everyday surroundings to reduce our consumption of fossil fuels and power the ever-growing new age of technology has much commercial promise. In this chapter we also look at the indoor performance of fabricated solar cells to ascertain if these perovskites can generate sufficient power from recycled indoor lighting source when the sun has set thus giving rise to the potential for longer power generating periods and powering low-power electronics such as wireless sensors and the internet of things (IOT) etc.

Bifacial solar cells (i.e. that can generate from both sides of the solar cell) have been reported with a 13.5 % PCE for window technologies [1]. But to fully utilise the solar spectrum for window applications a PSC should allow for efficient thermal energy transmission to ensure adequate heating of interior spaces, this means being highly NIR (near infrared) transparent in the range of 700 nm to 1 μm. However, the long-term operational stability of PSCs remains a primary focus. Current technologies have shown stabilities beyond 1000 hours but these are rarely aimed at the semi-transparent window market. [2]

Commercially available PV technologies require a lifetime warranty in excess of 25 years with less than a 10% reduction in performance over that lifetime. The cells and modules are assessed using the damp-heat test, following IEC 61215 industry standards issued by the International Electrotechnical Commission (IEC)[3][4] It would be difficult to convince customers and investors to accept PSCs in the market if they cannot pass the same strict stability test. Recently, stability studies have been carried out on perovskite solar cells that have attempted to track the origins of degradation induced by light, heat, moisture and other environmental conditions[5][6][7]. More generally, strategies to replace metal electrodes using conductive carbon [8][9][10], transparent conductive oxides (TCOs) [11] [12] and barrier layers, for example SnO_2 [13] have helped to solve the issue of metal ion migration from electrodes through transport materials to the perovskite that effectively creates short circuit pathways. The problem of metal contact corrosion from mobile halogen species is also reduced.

Previous reports of sputtering a TCO such as IZO onto perovskite or Spiro-OMeTAD for tandem applications have used a hole-selective layer (e.g. molybdenum oxide (MoOx) [14][15] to effectively extract charges and also alleviate the sputtering damage to underlying organic layers. Radio frequency magnetron sputtering of IZO even when done at room temperature produces high energy particles due to the high voltages required that are then subsequently deposited or directed onto the target. This high energy bombardment can damage soft materials such organic polymers and HTMs like Spiro-MeOTAD,

hence barrier or stronger materials are required such as MoOx in order to protect the soft organic HTMs like Spiro-OMeTAD. The thickness of the barrier layer is critical, too thick a MoOx layer could significantly reduce short-circuit current and fill factor and hence power conversion efficiency [12] [16] [14].

In this chapter we varied the MoOx thickness and combined it with a Glass/FTO/SnO_2/$Cs_{0.05}(MA_{0.17}FA_{0.83})_{0.95}Pb(I_{0.83}Br_{0.17})_3$/SpiroOMeTAD/MoOx/IZO in order to optimise the PCE, transmission and stability for use in dual functional PV windows. We demonstrate an optimised electrode that fulfils the requirements for a bifacial power generating window applications with excellent electrical properties, high NIR transparency, long-term stability, high performance at one sun and simple, reproducible low temperature coating processes. A subsequent record PCE cell with a PCE of 16.03% (13.8 % through the IZO coating) under one sun illumination through the FTO glass region and over 770 hours stability for cells optimised for long term stability. Our results compare well to others in the field who have report using a MoOx metal composite to improve the stability of perovskite solar cells by inhibiting decomposition [16]. Other have used MoOx as a barrier layer when trying to sputter TCO materials as reported by Werner et al. [14]

6.2 Experimental

Full details of the fabrication methods used to build the devices displayed in this chapter can be seen in chapter 2.1. It was decided to use the SnO_2 ETL architecture as employed in chapter 2.1 due to the reproducible high PCEs and associated stability with SnO_2 [17] and ease of processing. Refer to chapters 2.1.1, 2.12(2.1.2.1, 2.1.2.2, 2.1.2.3), 2.1.3.2, 2.1.5.1, 2.1.6.1, 2.1.7.1, 2.2 respectively for further details.

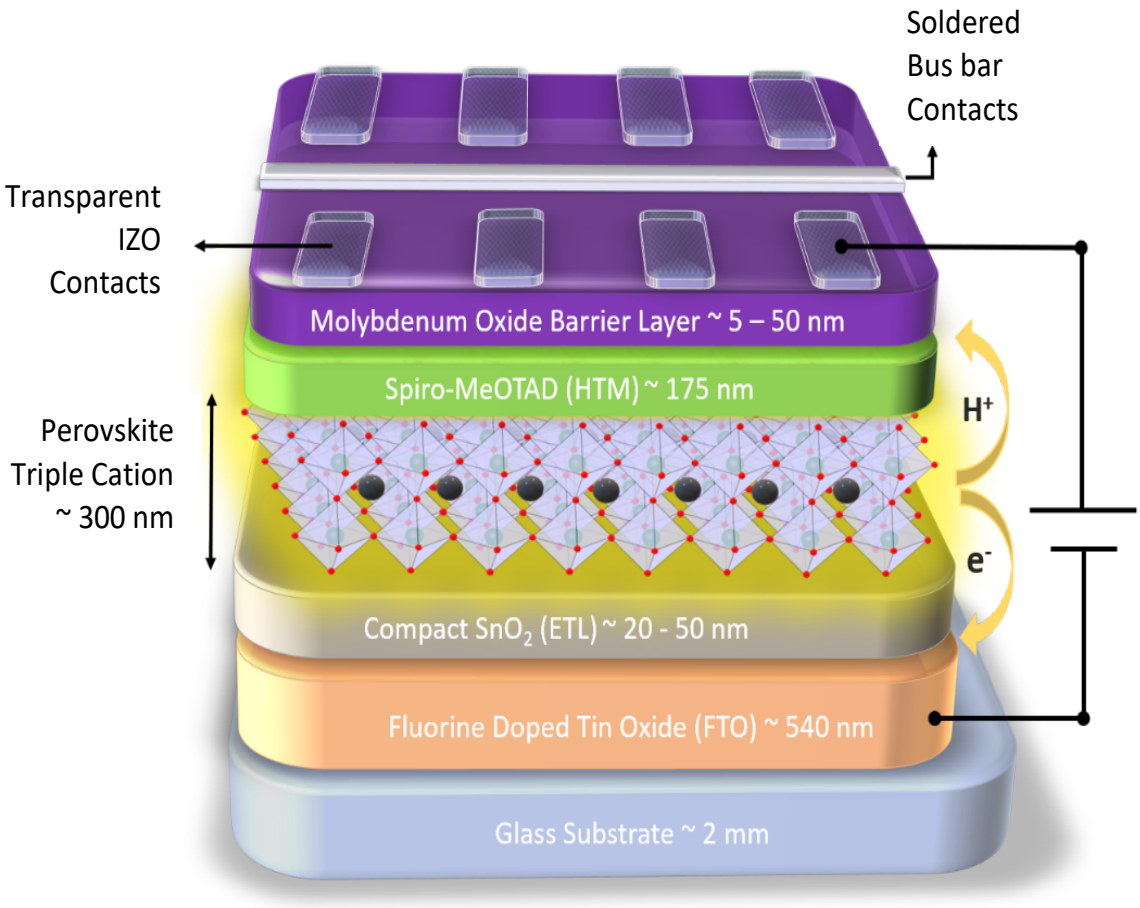

Figure 6.1: A schematic architecture of lab fabricated devices Glass/FTO/SnO_2/$Cs_{0.05}(MA_{0.17}FA_{0.83})_{0.95}Pb(I_{0.83}Br_{0.17})_3$/SpiroMeOTAD/MoOx/ IZO. The MoOx thickness was varied between 10 and 50 nm in order to optimise performance.

The molybdenum oxide (MoOx, STREM, 99.95%) films were thermally evaporated using a MBRAUN evaporator with evaporation rate of 0.50 Å s^{-1}, respectively. The indium zinc oxide (IZO target, Plasmaterial 99.99%) films were RF magnetron sputtered using a Moorfield Nanolab 60 sputtering system at 0.76 Wcm^{-2}. This is detailed in chapter 2.1.7.3 and carried out at Swansea University in a cleanroom glovebox.

The morphology of films was studied using a JEOL-JSM-7800F field emission scanning electron microscope (5 kV acceleration voltage, a working distance of 10 mm and a magnification of x 50, 000). The transmittance of the IZO films were scanned suing a PerkinElmer Lambda 750 UV/VIS/NIR Spectrometer. The sheet resistance of the IZO films were measured using a Jandel RM3000 four-point probe station. Refer to chapters 2.3 2.8, 2.16, 2,17.

For current-voltage measurements of solar cells, devices were masked to 0.09 cm2 and tested under a class AAA solar simulator (Newport Oriel Sol3A) at AM1.5 and 100 mWcm-2 illumination conditions calibrated against a KG5 filtered silicon reference cell (Newport Oriel 91150-KG5) using a Keithley 2400 source meter. Current-voltage sweeps were performed from both V_{OC} to JSC and vice versa at a rate of 0.1 Vs-1. For stabilized power output measurements, device bias was set to the maximum power point voltage determined by the J-V sweep and current monitored under 1000 Wm-2 illumination. Refer to chapter 2.12.

6.3 Results and Discussion

To access the optical performance of the TCO, 200 nm of IZO film was deposited via radio frequency magnetron sputtering at room temperature (RT) onto plain glass and spectroscopic analysis was performed over the UV to Near infra read regions (300 nm to 1300 nm).The results of this analysis can be seen below.

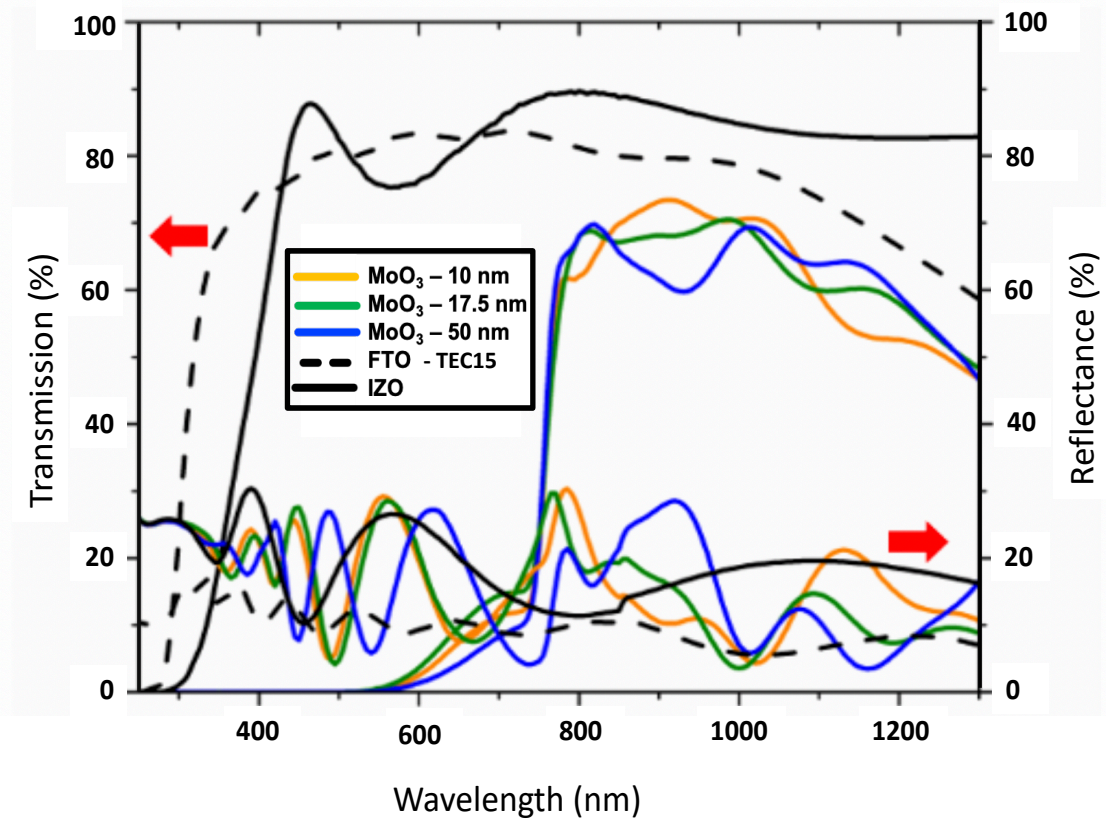

Figure 6.2: Transmittance and reflectance data measured through the IZO (solid black), the FTO (dotted black), the whole device stack with 10 nm-thick (solid orange), 17.5 nm-thick (solid green) and 50 nm-thick (solid blue) MoOx layers. (Device architecture: 2mm TEC15 FTO, SnO_2, Perovskite, Spiro-OMeTAD, MoOx, IZO).

The RT processed IZO on glass has an average transmittance over 85% across visible to NIR wavelengths. Notably, the NIR transmittance of IZO is remarkably higher than FTO as shown in Figure 6.1. The onset of the transmittance curve of IZO is around 320 nm which could serve as a UV light filter for the underlying layers as compared to 280 nm for FTO. It is well known that UV light is one of the main causes of degradation in PSC as high energy ultraviolet radiation is known to attack the

relatively weak bonds in the perovskite absorber material which leads to halogen ion migration [18]. So to have a contact that also acts as a filter to UV rays will help to improve the long term stability of the cell. This couple with relatively UV resistant selective contact materials such as SnO_2 could lead the way for stable long lifetime perovskite solar cells. This added UV shielding means that soft organic polymers like Spiro-MeOTAD that are known to suffer from UV attack could have a place in scaled up technologies, although the costs associated with producing molecules like Spiro-MeOTAD is too high for commercial use.

Figure 6.1 also elucidates that IZO has a significantly higher reflectance across the UV to NIR region than FTO, which is critical as IZO can be a more efficient back reflector for NIR photons and better front reflector for UV photons than FTO. Since both top and bottom electrodes are highly transparent, the total transmittances through the whole device stacks with 10 nm-, 17.5 nm- and 50 nm-thick MoOx interlayers are impressively high, with average value of 65% between 800-1200 nm compared to IZO alone at around 83 % average transmission over the same range. It shows a majority of visible light was absorbed in the whole device stack to generate electricity while leaving NIR photons transmit through and warm up interior spaces such as homes and automobiles.

We found adding MoOx is an effective way to enable us to fabricate efficient devices without any significant sputtering damage to either the soft organic HTMs like Spiro-OMeTAD and the perovskite absorber material. As the MoOx films get thicker the transmission is reduced with a noticeable shift in reflectance over the visible spectrum. There is also a noticeable shift in colour of the outward appearance of the solar cell with varying thickness of the MoOx barrier layer when viewed through the IZO. This is highlighted in figures 6.3 and 6.4 and is further investigated using CIE colourimetry. Figure 6.3 directly compares a 17.5 nm MoOx film next to a 50nm MoOx film and a green shift is observed with increasing film thickness. The obvious optical transparency of the device even with undiluted perovskite is clear to see even in full devices, this corroborates with the data collected in figure 6.1 and gives the impression

of a heavily tinted window as was the case with the AgNW: CNT contact presented in figure 5.10 and 5.13.

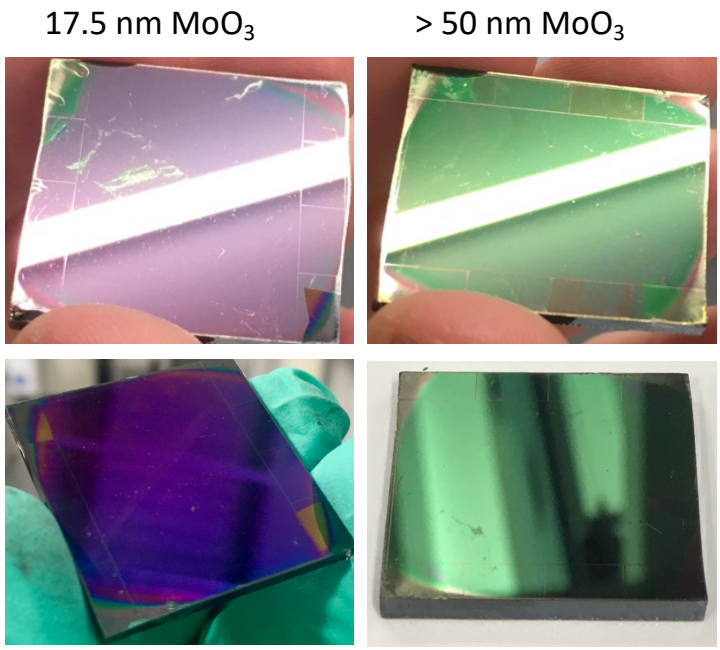

Figure 6.3: Photography of full devices with variances of MoOx thickness (17.5 and 50 nm. MoOx and IZO has been coated onto the entire surface of the cell in order for CIE measurements.

Figure 6.4: Photography of full stack perovskite solar cells taken with two different focal lengths. The IZO coatings can be seen as bus bar contacts and solder was used to complete the circuitry.

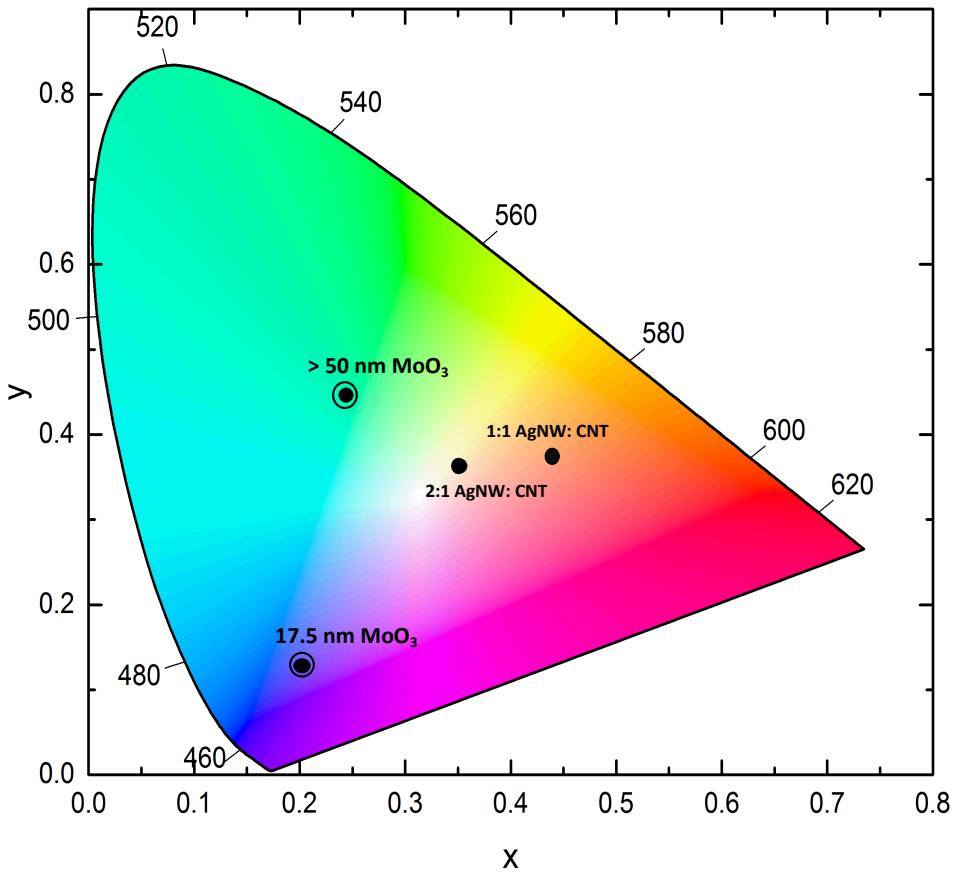

Figure 6.5: CIE colourimetry of full devices employing a 17.5 nm MoOx interlayer and a 50 nm MoOx interlayer measured through the IZO. Both are circled for highlighting in order to differentiate them from the full devices using the AgNW: CNT contacts as seen in figure 5.14. Note all devices used the same triple cation perovskite, although the ETL materials are different.

The CIE data present in figure 6.5 shows the apparent colour shift when different thickness of MoOx are employed. The thicker devices using 50 nm of MoOx show a shifted colour towards the green spectrum whereas the devices employing a thinner layer of MoOx appear to show a shift towards the purple section of the CIE chart. This correlates with the shift in reflectance's observed in figure 6.1, as the MoOx film thickness increases from 10 nm to 50 nm. This added advantage of being able to colour tune the perovskite final appearance is of particular importance to NSG Pilkington as was discussed in chapter 5. The ability to form a wide variety of colours without having a direct impact on the morphology and performance of the triple cation absorber layer is of added benefit as it means the colour can be tailored to suit the customers particular preference without having

to completely redesign the solar cell and makes best use of the most efficient perovskite absorber materials. Hue, colour, haze and clarity combined with optimal visible and NIR optical transmission are critical in the design of semi-transparent windows for building and automotive functionality and this variety and tunability of colour is a big advantage for this particular technology development.

Conductivity measurements were also performed on the as deposited films using a Jandel 4-point probe where the data is displayed in table 6.1. It can be seen that a 200 nm IZO film deposited on plain glass demonstrates an excellent sheet resistance of only 21.3 Ωcm^{-2}. The film appears to be fairly homogenous across all samples, although the range ± 1.85 isn't negliable at nearly 8.6 % compared to the reference at 3.5 %. This compares well with the AgNW: CNT presented in chapter 5 with a sheet resistance of just over 5 Ωcm^{-2} when optimised for electrical conductivity and thermally evaporated opaque metal contacts at less 5 Ωcm^{-2}.

Table 6.1: Conductivity (sheet resistance R_{sh}) measurements of a 200 nm IZO room temperature deposited film on plain glass of 2.8 x 2.8 cm^2. Measurements were taken using a Jandel 4-point probe and random areas at the edge and centre of the samples was taken.

Sample ID	**Sheet Resistance R_{sh} (Ωcm^{-2})**			**Average (Ωcm^{-2})**
Room temperature 200 nm IZO film deposited on plain glass of 2.8 x 2.8 cm^2	21.3	23.1	19.4	**21.3 (± 1.85)**
TEC15 Reference sample	16.4	15.8	15.3	**15.8 (±0.55)**

In order to fabricate full devices a 200 nm IZO film was deposited via radio frequency magnetron sputtering at room temperature as a top electrode by introducing a thin (10 nm to 50 nm) MoOx interlayer between the Spiro-MeOTAD and the IZO layer. The layered structured of the final devices was taken for SEM cross sectional analysis and the imagery can be seen in figure 6.6 below:

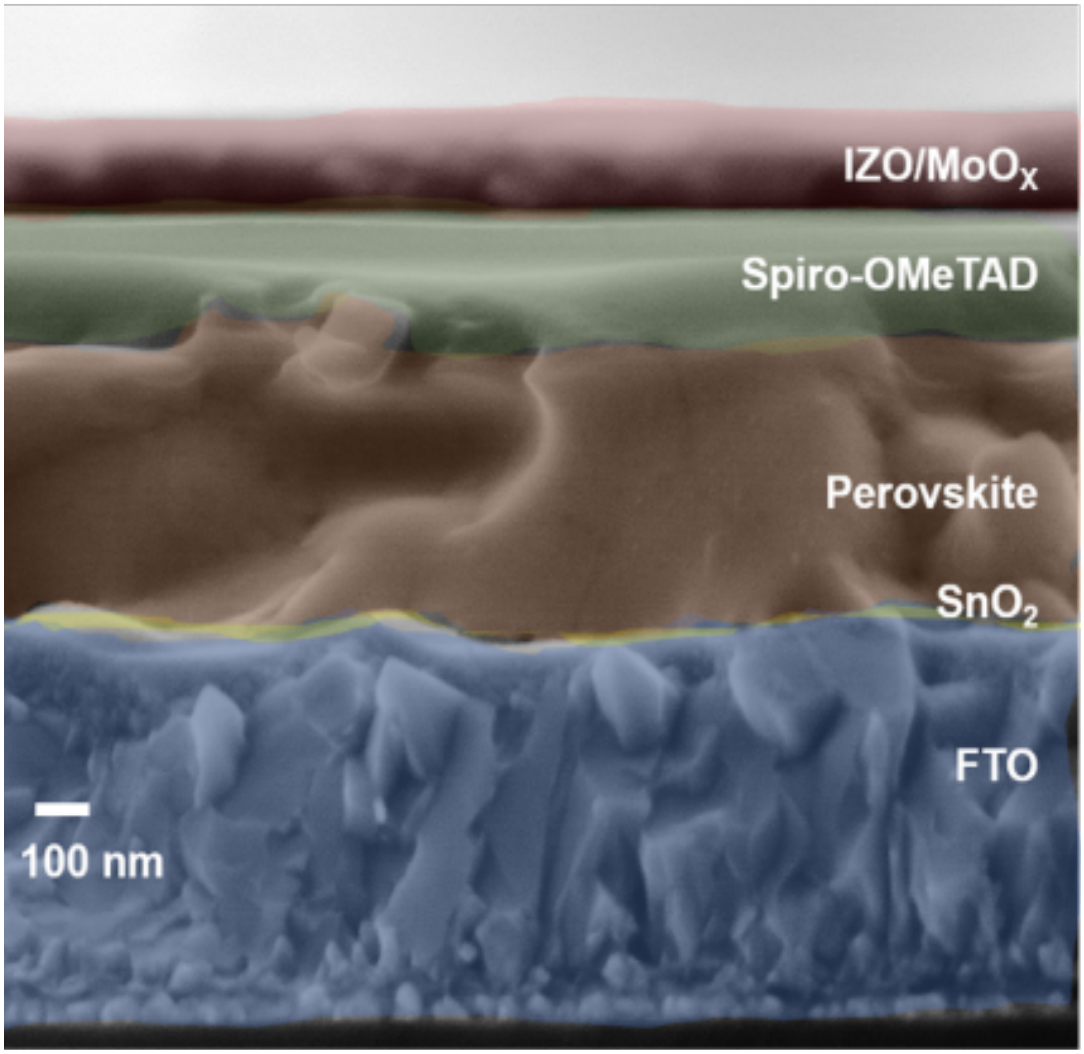

Figure 6.6: Cross-sectional SEM image of a completed perovskite solar cell with individual layers labelled. Taken using a JEOL-JSM-7800F field emission scanning electron microscope (5 kV acceleration voltage, a working distance of 10 mm and a magnification of x 50, 000). The perovskite used had a composition of $Cs_{0.05}(MA_{0.17}FA_{0.83})_{0.95}Pb(I_{0.83}Br_{0.17})_3$ as mentioned in chapter 6.2 and the MoOx thickness was targeted at 17.5 nm, corresponding to the cell with optimal performance.

The SEM imagery in figure 6.6 allows us to approximate the layer thicknesses of each individual layer although as it's just one image, it would be hard to ascertain how film coverage across the whole film. The MoOx proves difficult to distinguish here sa its targeted at only 17.5 nm thick. The deposition rate of IZO was 10 nm per minute for 10 mins so we surmise a layer thickness of approximately around 100 to 110 nm. From this initial image the IZO layer appears well deposited and conformal on top of the MoOx/ Spiro-OMeTAD. Although further imaging is necessary to confirm film homogeneity across the macro scale. The perovskite film thickness is estimated at around 400 nm so is well optimised to absorb the maximum number of photons in the visible region of the electromagnetic spectrum as modelled through ellipsometry where a film thickness of around 370 nm is desired [19]. Surprisingly the thickness of the HTM, Spiro-MeOTAD was below the desired thickness of 350 nm for smooth perovskite films and > 400 nm for rough perovskite films [20][21] although high efficiencies have been shown for thin films of Spiro-MeOTAD [22]. From figure 6.6 we estimate the HTM to be around 175 to 200 nm thick. This result was unexpected as our processing condition in the lab target 350 nm but when coupled with the additional MoOx layer which is also an efficient HTM, efficient hole extraction and charge carrier mobilities could well be possible and the resulting JV performances suggest this didn't have a detrimental effect on these devices. The SnO_2 layer thickness was too thin to determine but is estimated at less than 50 nm.

Figures 6.7 and table 6.2 and 6.3 summarise the JV performance of all variations of MoOx and from these we can see the average reverse bias for all devices is high, and consistent when compared to similar MoOx thicknesses. There are only marginal differences in V_{OC} and FF between all the devices with the bifacial illumination. This indicates there are no band alignment issues caused by light induced or MoOx thickness dependent band edge shifts. For devices employing a 10 nm MoOx film and IZO contact a record PCE of 16.0% measured from V_{OC} to J_{SC} through the FTO side with a stabilised efficiency of 15.2 % as seen in the JV curves plotted in figure 6.8. There was a very small decrease in performance for the marginally thicker 17.5 nm MoOx film, with a stabilised efficiency of 14.1 %. As the film thickness of the MoOx increased, PCE dropped accordingly with a 25

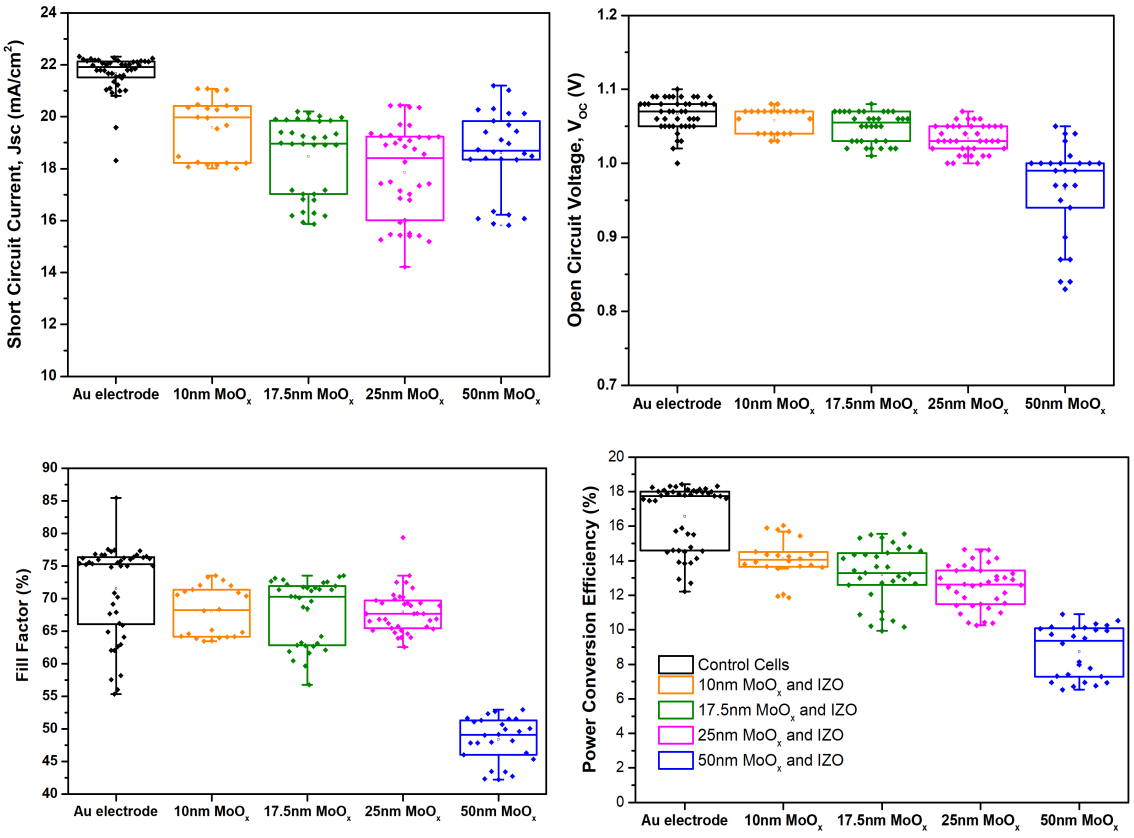

Figure 6.7: Statistical analysis of JV data of variations in MoOx thickness and its subsequent effect on performance measured through the FTO for comparison.

and 50 nm MoOx film obtaining a highest PCE of 14.7 % and 10.9 % respectively, although in the case of 50 nm film the forward scan J_{SC} to V_{OC} recorded the higher PCE. From the JV curves in figure 6.8 and table 6.2 and 6.3, once the MoOx thickness gets above 25 nm there is a direct increase in series resistance and reduction in shunt resistance as seen in table 6.1. The R at V_{OC} is around 5 ohm cm^{-2} at 10 nm MoOx thickness, and 15 ohm cm^{-2} at 50 nm. Resistance at I_{SC} is > 4000 ohm cm^{-2} for the reverse scan through the IZO at 10 nm MoOx, whereas this drops to <1900 ohm cm^{-2} for the corresponding measurement at 50 nm MoOx thickness. The valence band of MoOx is very deep (>7.5 eV) and increasing the thickness causes a change from an ohmic contact to a Schottky contact. Optoelectronic devices like perovskites require a low resistance ohmic contact between the active layers and any contact electrodes. When this is not the case, it usually denotes a Schottky barrier occurrence which inhibits charge extraction and thus reduces device performance. These Schottky barriers are clearly in

effect as the MoOx film thickness increases and is very pronounced in the 50 nm film. This is reflected in the decreasing J_{SC}, V_{OC} and FF observed as the MoOx increases as seen in figure 6.7 and table 6.2. A 25 nm MoOx recorded an average FF for both forward and reverse illumination (through FTO) of just under 70 % whereas the comparative value for 50 nm dropped to below 50 %.

Table 6.2: Summary of JV data of the best performing devices for each variation in MoOx thickness with associated series and shunt resistances.

Cell Variant	Scan Direction	V_{OC} (V)	J_{SC} (mA cm^{-2})	Fill Factor (%)	Efficiency (%)	Stabilised Efficiency (%)	R at I_{SC} (Ohms·cm^2)	R at V_{OC} (Ohms·cm^2)
Au electrode (Through FTO)	Forward	1.06	22.1	77.3	18.2	17.8	788	2.7
	Reverse	1.08	22.2	76.8	18.3		4769	3.2
10 nm MoO_3 (Through FTO)	Forward	1.04	21.1	65.2	14.3	15.2	618	5.5
	Reverse	1.07	21.0	71.1	16.0		1821	5.2
10 nm MoO_3 (Through IZO)	Forward	1.04	17.5	63.2	11.5	12.6	824	6.4
	Reverse	1.07	17.5	73.6	13.8		4194	5.9
17.5 nm MoO_3 (Through FTO)	Forward	1.03	20.0	64.2	13.3	14.1	573	7.1
	Reverse	1.08	20.0	71.9	15.6		2420	5.0
17.5 nm MoO_3 (Through IZO)	Forward	1.02	17.2	62.1	10.9	11.8	555	8.0
	Reverse	1.07	17.2	73.3	13.4		3347	6.1
25 nm MoO_3 Through FTO)	Forward	1.01	20.4	65.7	13.5	13.7	644	6.1
	Reverse	1.04	20.4	69.3	14.7		1607	6.3
25 nm MoO_3 (Through IZO)	Forward	1.01	17.4	64.0	11.3	11.9	571	7.4
	Reverse	1.05	17.4	72.5	13.3		5401	6.5
50 nm MoO_3 (Through FTO)	Forward	1.00	21.2	51.5	10.9	8.6	463	13.2
	Reverse	1.00	21.0	49.1	10.3		643	13.4
50 nm MoO_3 (Through IZO)	Forward	0.95	16.1	45.4	6.9	6.6	252	22.6
	Reverse	0.99	16.1	46.1	7.3		1849	21.9

Table 6.3: Summary of average device performance for reverse bias results for each variation in MoOx thickness. All PSCs incorporate a triple cation-based (TC) perovskite absorber material. Measured through the FTO.

Cell Variant	Voc	Jsc	Fill Factor	PCE
	(mV)	($mAcm^{-2}$)	(%)	(%)
Control Cell, Au Electrode (AVR)	1080	22.1	76.1	17.9
10 nm MoOx & IZO (AVR)	1071	20.2	72.4	15.0
17.5 nm MoOx & IZO (AVR)	1062	19.6	71.9	14.2
25 nm MoOx & IZO (AVR)	1049	19.2	69.9	13.3
50 nm MoOx & IZO (AVR)	1010	19.9	51.8	10.1

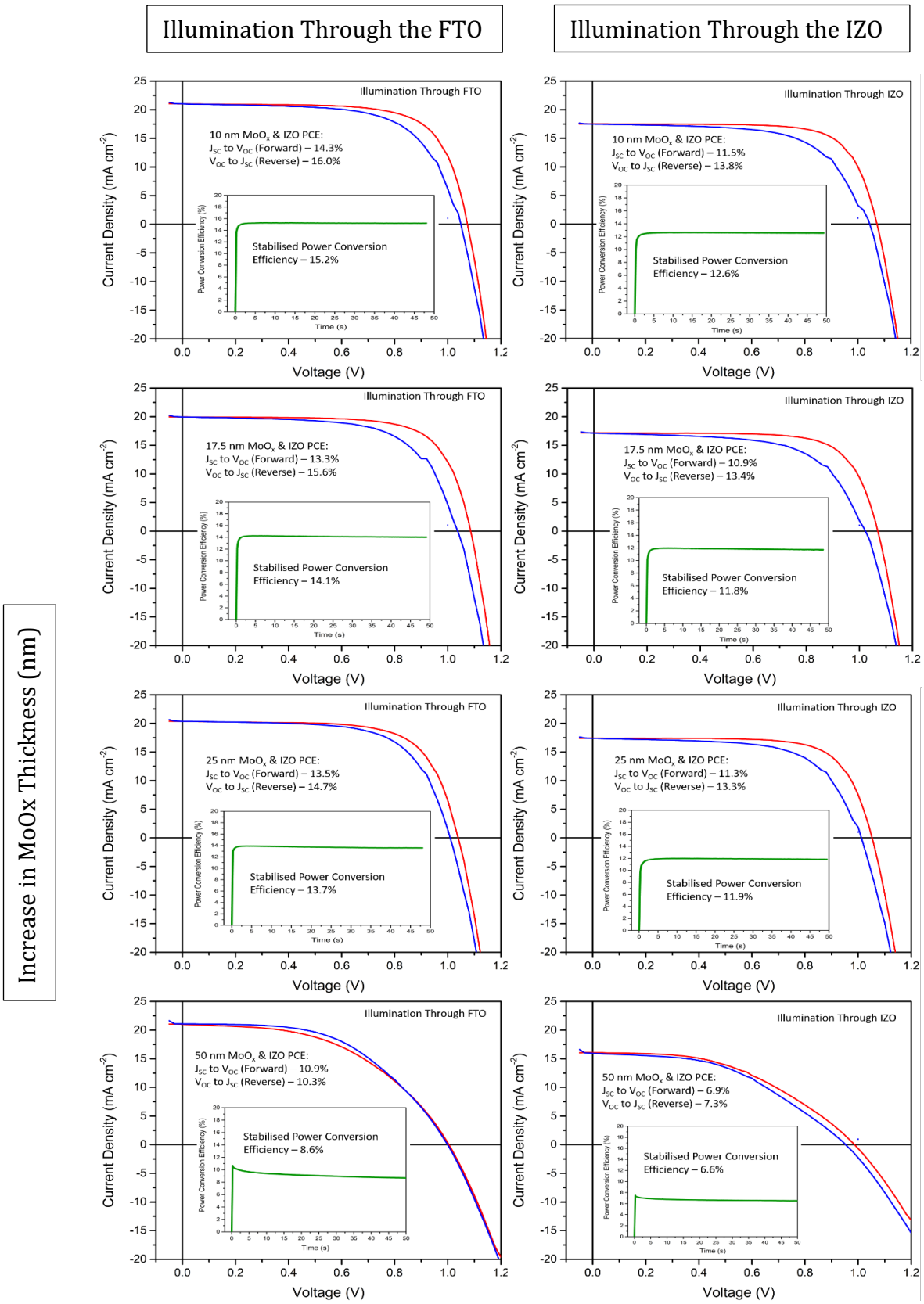

Figure 6.8: JV curves showing variations of MoOx thickness variation and its subsequent effect on performance of completed devices illuminated through the glass and IZO coating. Forward scan shown in red and reverse scan shown in blue. The accompanying stabilised plot is also attached.

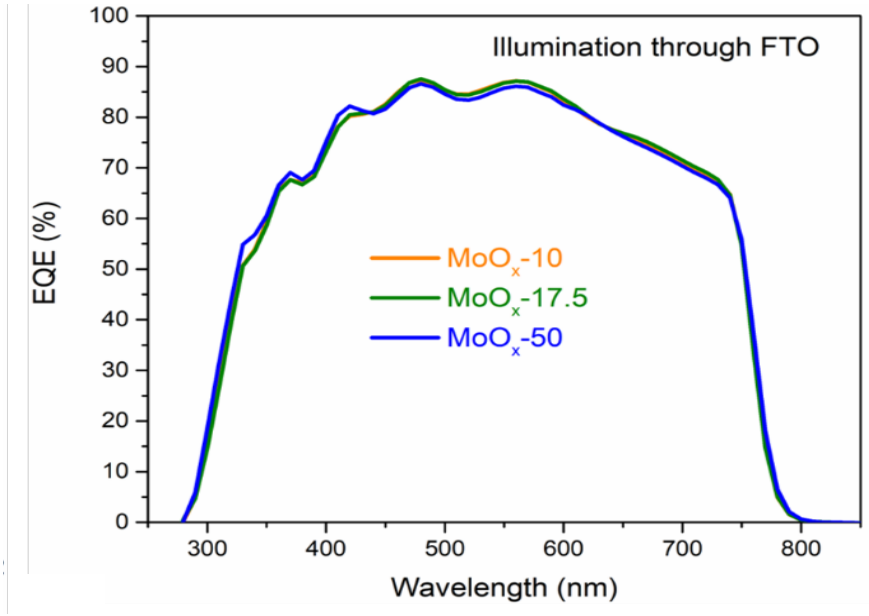

Figure 6.9: EQE curve of devices with illumination through the FTO side. The integrated J_{SC} from the EQE curves are 19.29 mA/cm^2 (MoOx-10), 19.32 mA/cm^2(MoOx-17.5) and 19.25 mA/cm^2(MoOx-50), respectively

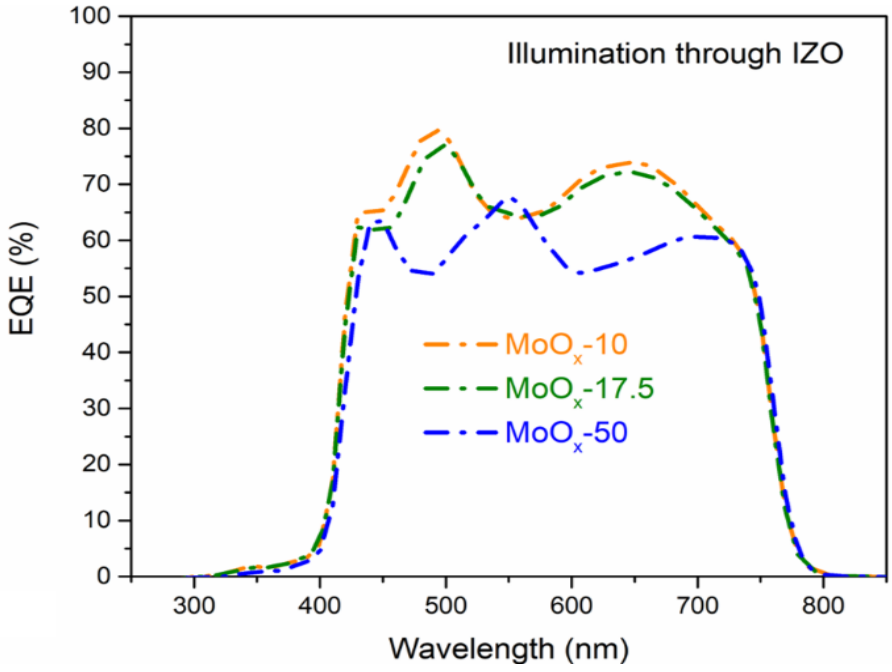

Figure 6.10: EQE curve of devices with illumination through the IZO side. The integrated J_{SC} from the EQE curves are 15.51 mA/cm^2 (MoOx-10), 15.18 mA/cm^2(MoOx-17.5) and 13.41mA/cm^2(MoOx-50), respectively.

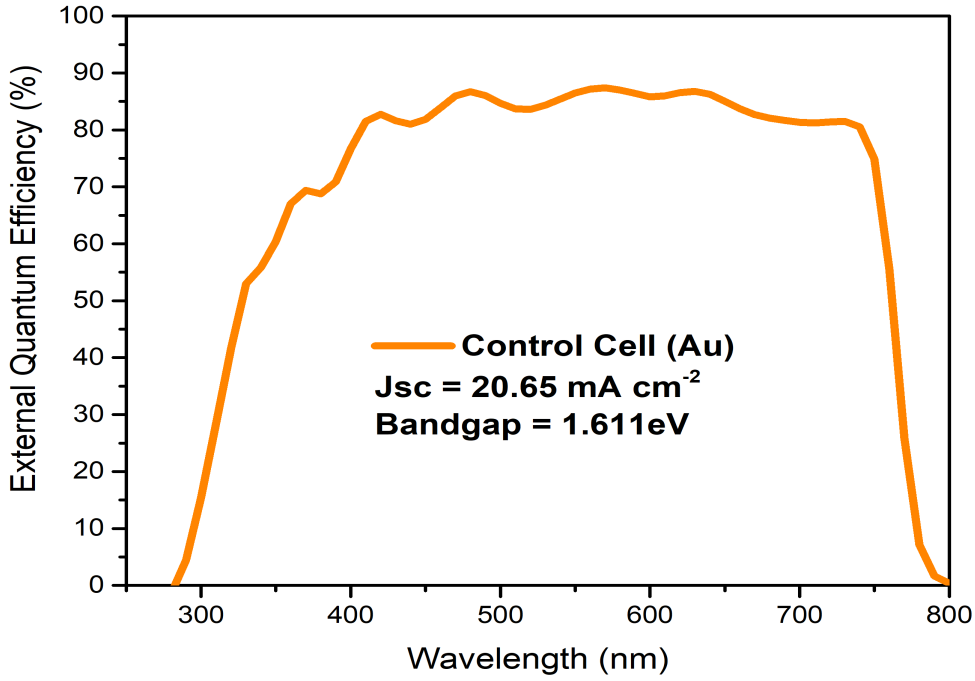

Figure 6.11: EQE curve of a control devices with illumination through the FTO side. The control device uses standard PVD deposited gold instead of the MoOx and IZO contact. The integrated J_{SC} from the EQE curves is 20.65 mA cm^{-2}.

As MoOx film thickness increased we noticed a small tailing off in V_{OC} that we attribute to a small increase in Schottky barriers associated with deep valence band of MoOx which inhibit charge extraction. There is a noticeable increase J_{SC} spread for all MoOx IZO films compared to the control cells. This can be partly attributed to problems lining up the sputtering mask to overlay the pixel area adequately, a faulty sample holder caused pixels to not be fully coated by IZO over the test area leading to regions with insufficient IZO coverings and unable to accumulate and contact charge. However, the effect wasn't catastrophic from the high PCE recorded. PCEs of all the devices illuminated through IZO drops significantly because of a reduction in J_{SC} as compared to those illuminated through FTO. These differences are also evident from EQE curves (Figure 6.9, 6.10 and 6.11). When illuminating through IZO, the low wavelength (250 -450 nm) UV photons are absorbed by high energy-band gap materials such as the IZO, MoOx and Spiro-OMeTAD, resulting in a higher cut-off of the EQE curve at 400 nm as opposed to 285 nm for cells illuminated through the FTO. Spiro has

previously been noted to screen UV light in the ranges of 200 nm to 400 nm when illuminated [23]. When we look at the refractive indexes of these materials we can see that the MoOx has a noticeable effect on the EQE drop off over 200-450nm with a refractive index over this region ranging from 2.6 to 3.1, whereas Spiro has a refractive index of below 2 for nearly the entire range (280 nm to 850 nm). The higher refractive index means less light is able to reach the perovskite absorber and a lower J_{SC} is recorded when illuminating through the IZO film as seen in table 6.1. This MoOx shielding component increases with thickness as more photons are absorbed by the thicker layers. The pronounced reduction in EQE in the visible regions (400 nm – 800 nm) could be due to higher reflectance of IZO compared to FTO (Figure 6.1).

The EQE curve of 50 nm of MoOx as seen in figure 6.10 correlates with the reduction in J_{SC} seen in table 6.2 once the MoOx passes a critical film thickness (between 25 and 50 nm). The reduced J_{SC} of devices employing the MoOx and IZO coating compared to that control cells that use PVD deposited opaque gold indicates there is little back reflection from the IZO of incident light and hence no boost to light absorption. This allows the IZO film to function as a dual-purpose window but with a trade off in reduced PCEs. This is also confirmed in the relatively low reflectance values measured for all devices employing the IZO contact when compared to evaporated solid contacts such as gold. The EQE of the control cell seen in figure 6.11 also highlights the decreased absorption of wavelengths from 600 to 750 nm when compared to figure 6.9 for cells measured through the FTO contact. A drop from around 85 % EQE to around 65 % is noted in the cells using the IZO contact over the region 600 to 750 nm whereas the control devices over the same spectral region drop by less than 5 % from 85 % EQE to just around 80 % at 750 nm. This again is further evidence of the back-reflection phenomena mentioned earlier.

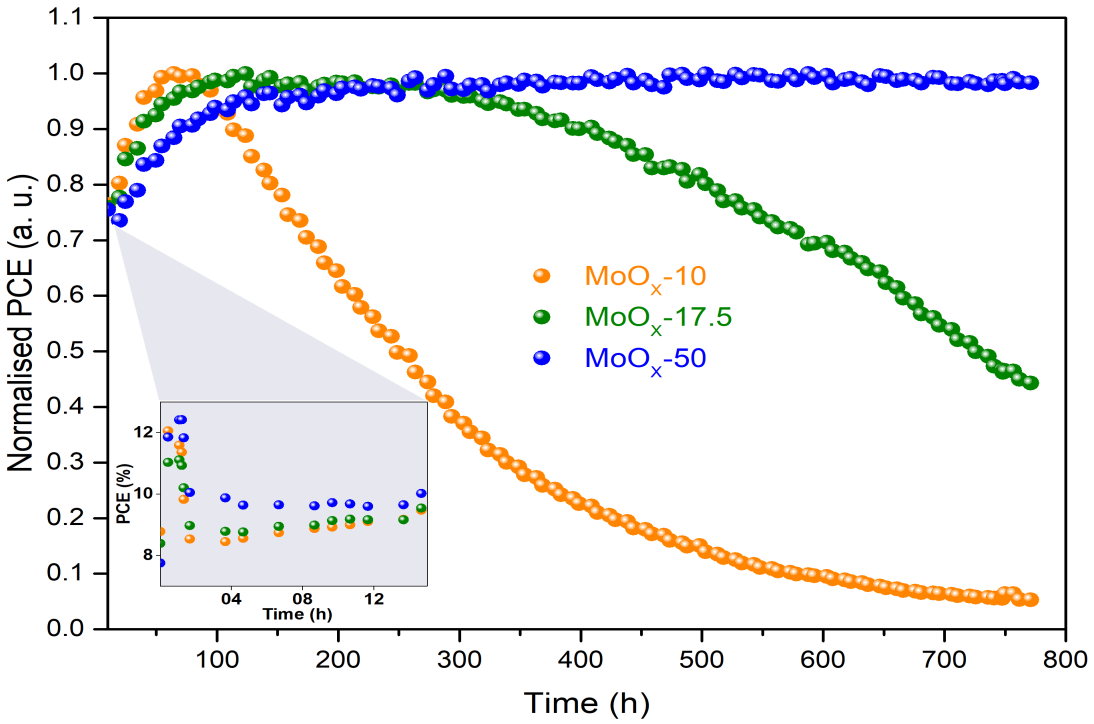

Figure 6.12: Stability comparison of representative semi-transparent perovskite solar cells with 10 nmc- (orange), 17.5 nm-thick (green) and 50 nm-thick (blue) MoOx layers under sulphur plasma lamp one sun equivalent illumination. The variation of normalised PCEs in first 15 hours for above three devices is shown in the inset. All the devices were illuminated through IZO.

Long term stability measurements were carried out in accordance with chapter 2.18. All devices were illuminated over the whole pixel area (0.24 cm^2) rather than the masked area (0.09 cm^2) through either IZO or FTO during the stability test as shown in Figure 6.13, meaning any effects from defects over the entire device and UV damage could be monitored [24][25][26].

Due to the IZO/MoOx/Spiro-OMeTAD layers acting as an effective UV filter, and hence improving stability, the normalised PCE degradation data for full devices with 10 nm, 17.5 nm thick and 50 nm thick MoOx layers illuminated through IZO are shown in Figure 6.12. For the device with a 50 nm thick MoOx, there is an impressive long-term stability of >770 h and >70% efficiency improvement in the end of the stability test compared to the at the beginning. Notably, the PCE of MoOx 50 nm sample increase dramatically (stage-I) to >12% in first 2 hours and

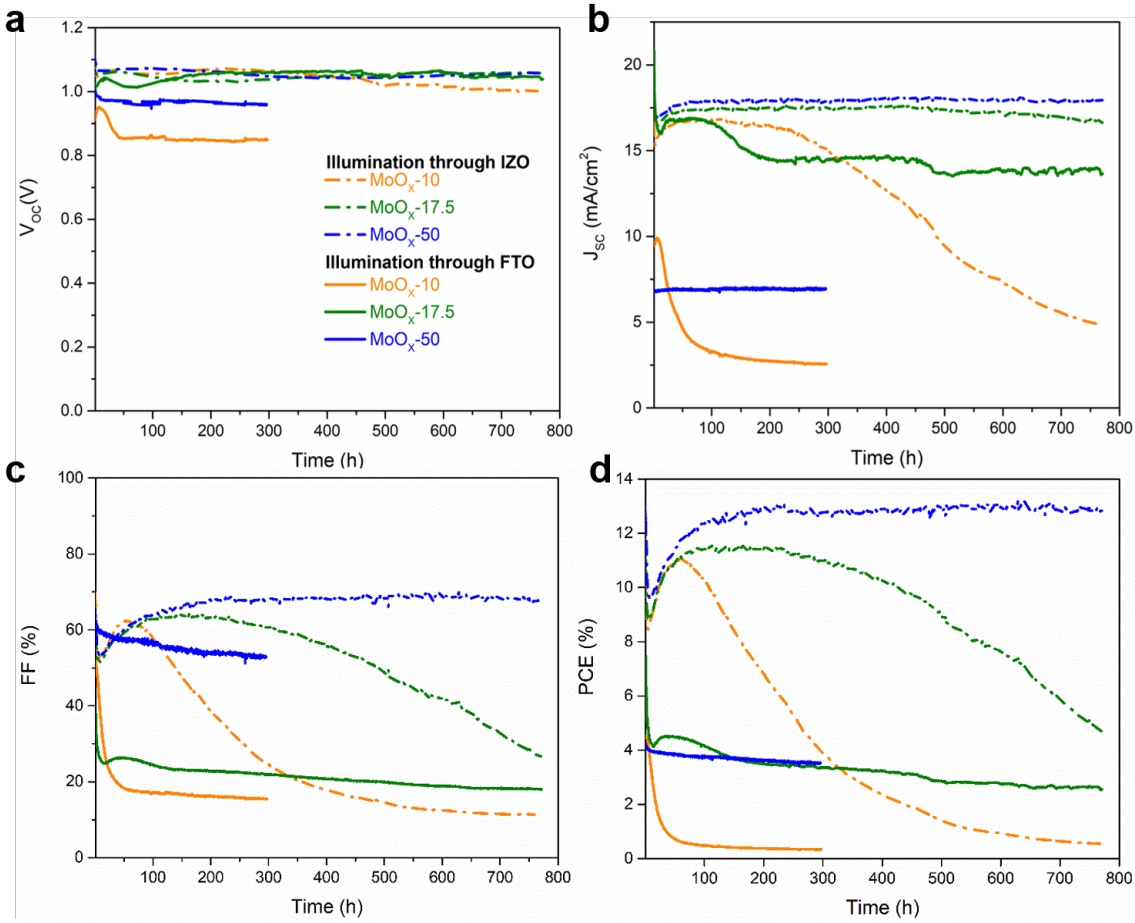

Figure 6.13. Stability studies of device parameters of representative semi-transparent perovskite solar cells with 10 nm (orange), 17.5 nm-thick (green) and 50 nm-thick (blue) MoOx. All devices illuminated through the FTO (solid line) and through IZO (dash dotted line) sides under sulphur plasma lamp one sun equivalent illumination.

drops to 10% in 4 hours as shown in the inset of Figure 6.12. There is then period of very steady increase (stage-II) to its stable PCE (~12.8%) at 150 h and maintains this until the end of the test in Figure 6.12. The stage-I PCE increase or single PCE increase has been reported previously for the perovskite solar cells incorporating SnO_2/ITO [13] and MoOx/IZO [27]. The initial light soaking period causes an increase in PCE over the first few hours (0-2 hours) before decreasing linearly over the next hour due to subsequent JV hysteresis during initial aging, caused by halide migration into the carrier selective layer under bias. This leaves additional vacancies in the perovskite layer or increased ionic conductivity from

moisture ingress. An initial increase in temperature in the first few hours, that likely initiates an increase in series resistance could also be a factor in the observed decrease in PCE from 1 to 3 hours. As temperature stabilises a second light soaking effect seems to take place as denoted by steady increase from 12 to 100 hours and hysteresis levels out. The thicker MoOx films (50 nm) remain steady for the next 800 hours whereas thinner films so a gradual tailing off in efficiency as the aforementioned hysteresis mechanism dominates and cells performances fall away [26].

However, the double-stage PCE increase for three samples with varied MoOx thickness was observed for the first time. With the highlight being a >70% increase in PCE with our 50 nm-thick-MoOx/IZO device. The stage-II PCE increase for all three selected MoOx thicknesses is predominately attributed to the significant increase of FF from 50% to over 65% (over 70% for 50 nm-thick-MoOx) that is linked to initial light soaking and optimal oxidation and increase in charge carrier mobility associated with the Spiro-OMeTAD and Li-TFSI . From figure 6.12. and 6.13 there appears to be a minor increase in J_{SC} while little change is observed at V_{OC}. This likely indicates that the stage-II PCE increase is because of an improved contact between the (MoOx/Spiro-OMeTAD) and/or optimised top contact/Spiro-OMeTAD interface. A similar effect was reported by Chan et al [28]where in an organic light emitting diode device, a combination of MoOx and NPB (N'-diphenyl-N,N'-bis(1-naphthyl)(1,1'-biphenyl)-4,4'diamine) formed a MoOx doped NPB interface that has the effect of increasing free carrier concentrations and hence improving the conductivity of the MoOx/NPB system. We postulate a similar doped interface between MoOx and Spiro-OMeTAD layers under continuous UV light illumination that reduces series resistance of the fabricated device that internally aids with charge transport and extraction at the IZO top contact. Figure 6.13 demonstrates that the cells illuminated through the FTO side (solid line) didn't survive for as long as those illuminated through the IZO, with the expectation of the 17.5 MoOx which managed to make it to 800 h with a <4 % PCE. We can attribute the degradation mechanism here as UV light instability on the part of the perovskite and Spiro, with the shielding effect from

the MoOx or IZO the cell was exposed to UV radiation which likely induced ion migration within the perovskite that would drastically reduce performance.

The rise of PCE accompanied with an increase in V_{OC} in stage-I is due to light or electrical field induced ion migration, increased perovskite crystallinity and improvement of the n-i-p interfaces [11][8][13][29][27]. V_{OC} of devices illuminated through both side retain their values until the end of the stability test except for a minor drop in samples with MoOx thickness of 10 nm as shown in Figure 6.13a. The decrease in PCE of devices with MoOx thicknesses of 10 nm and 17.5 nm (illuminated through IZO) occurs because of a fall in J_{SC} and FF over the course of 700 h testing (Figures 6.13b - 6.13d). There is a distinct difference between these two samples (10 nm and 17.5 nm), The devices with a MoOx of 17.5 nm exhibit a stable J_{SC} and decreasing FF. This is in contrast to devices with a 10 nm MoOx thickness where JSC and FF can both be seen to decrease over the course of the test. This indicates a clear correlation between the MoOx thickness and the device lifetime (as well as J_{SC} and FF) that relates to either a compositional change, with MoOx interacting with light-induced halogen diffusion species or its relative oxygen content [16], an interfacial effect between IZO/MoOx/Spiro-OMeTAD or a combination of the aforementioned issues. The thicker MoOx films will also help to filter high energy UV radiation, a factor known to induce ion migration and degradation of perovskite films, thus extending device lifetimes as ion migration is reduced.

The thinner the MoOx layer, the more UV light is able to reach the perovskite layer and consequently is able to excite more ions that can migrate over time. The ion migration towards carrier-selective layers under bias could trigger the diffusion of water into the hybrid perovskite materials [27]. Whereas device stability improves with an increase in thickness of MoOx, as seen in variations of early stage-I PCE improvement followed by a sharp-drop as shown in Figure 6.12. A MoOx/ITO/Ag/ITO top electrode system using a similar MoOx thickness demonstrated similar lifetime enhancement due to an increase in the distance required for Ag or halogen ions to travel before short circuit pathways or electrode corrosion can occur [1]. In addition, other elements could contribute to

the overall degradation of the PCE including the lack of an edge seal or pinholes in the IZO caused by dust or non-uniformity of underlying layers. This would in turn lead to degradation of the organic cation[13] and cause photo-induced oxidation of Spiro-OMeTAD[30]. All devices with illumination through the FTO side degrade much faster than illumination through the IZO side, we postulate that when illuminating through the FTO side, UV radiation is able to penetrate further into the perovskite absorber material because of a lack of UV filtering layers (such as IZO/MoOx/Spiro-MeOTAD when illuminating through the IZO side). This puts more stress on the perovskite and SnO_2, causing decomposition of the perovskite [31][32].

6.4 Conclusions

In conclusion we present a bifacial transparent conductive contact based on indium Zinc oxide and Molybdenum oxide for Window Applications. The MoOx is used a barrier to protect the soft HTMs used in fabricating most PSC from a 200 nm IZO top contact deposited by room temperature radio frequency magnetron sputtering. These vacuum processes help to produce a compact, conformal, uniform, highly transparent, conductive and UV filtering MoOx/IZO bilayer. The resulting solar cells with a 10 nm layer of MoOx demonstrated a very impressive power conversion efficiency of 16.03% when illuminated through the FTO contact and 13.8% when illuminated through the IZO contact. Increasing the thickness of MoOx layer to 50 nm had two notable effects, the first was a lowering of initial power conversion efficiency to 10.9 %, but the second effect was a to significantly improve the stability of devices. Impressively, these devices showed over 70% PCE increase after 150 h continues light soaking, achieving 12.8% PCE, which was retained over 700 h of operational lifetime. These results suggest MoOx/IZO electrodes can serve as an effective barrier to environmental stress factors such as UV light, oxygen and moisture. The added bonus of being able to tune a perovskite solar cells colour by varying the thickness of MoOx layer combined with impressive long-term stability and excellent optoelectronic

performance means perovskite solar cells have a real commercial potential for generating electricity in dual functional PV windows. The ability to colour tune the perovskite outward appearance via control of the MoOx thicknessis is also of great benefit to companies like NSG Pilkington who are trying to get a semi-transparent perovskite window to market. The next stages in the development of this work would be a systematic study of the optical MoOx thickness to give the best performance to optical properties compromise. Further down the line, non-vacuum, high volume deposition methods would be a significant development.

6.5 Bibliography

[1] Z. Wei, B. Smith, F. De Rossi, J. R. Searle, D. A. Worsley, and T. M. Watson, "Efficient and semi-transparent perovskite solar cells using a room-temperature processed MoO: X/ITO/Ag/ITO electrode," *J. Mater. Chem. C*, 2019.

[2] S. S. Shin *et al.*, "Colloidally prepared La-doped BaSnO3 electrodes for efficient, photostable perovskite solar cells.," *Science*, vol. 356, no. 6334, pp. 167–171, Apr. 2017.

[3] http://www.iec.ch>, "No Title."

[4] P. Holzhey and M. Saliba, "A full overview of international standards assessing the long-term stability of perovskite solar cells," *Journal of Materials Chemistry A*. 2018.

[5] K. A. Bush *et al.*, "Thermal and environmental stability of semi-transparent perovskite solar cells for tandems by a solution-processed nanoparticle buffer layer and sputtered ITO electrode," in *2017 IEEE 44th Photovoltaic Specialist Conference, PVSC 2017*, 2017.

[6] C. Hanmandlu, C.-Y. Chen, K. M. Boopathi, H.-W. Lin, C.-S. Lai, and C.-W. Chu, "Bifacial Perovskite Solar Cells Featuring Semitransparent Electrodes," *ACS*

Appl. Mater. Interfaces, vol. 9, no. 38, pp. 32635–32642, Sep. 2017.

[7] C. C. Boyd, R. Cheacharoen, T. Leijtens, and M. D. McGehee, "Understanding Degradation Mechanisms and Improving Stability of Perovskite Photovoltaics," *Chemical Reviews*. 2019.

[8] G. Grancini *et al.*, "One-Year stable perovskite solar cells by 2D/3D interface engineering," *Nat. Commun.*, vol. 8, no. 1, p. 15684, Aug. 2017.

[9] A. Mei *et al.*, "A hole-conductor-free, fully printable mesoscopic perovskite solar cell with high stability," *Science (80-.).*, 2014.

[10] J. Baker *et al.*, "High throughput fabrication of mesoporous carbon perovskite solar cells," *J. Mater. Chem. A*, 2017.

[11] K. A. Bush *et al.*, "Thermal and Environmental Stability of Semi-Transparent Perovskite Solar Cells for Tandems Enabled by a Solution-Processed Nanoparticle Buffer Layer and Sputtered ITO Electrode SI," *Adv. Mater.*, 2016.

[12] F. Fu *et al.*, "Low-temperature-processed efficient semi-transparent planar perovskite solar cells for bifacial and tandem applications," *Nat. Commun.*, vol. 6, no. 1, p. 8932, Dec. 2015.

[13] K. A. Bush *et al.*, "23.6%-efficient monolithic perovskite/silicon tandem solar cells with improved stability," *Nat. Energy*, 2017.

[14] J. Werner *et al.*, "Sputtered rear electrode with broadband transparency for perovskite solar cells," *Sol. Energy Mater. Sol. Cells*, vol. 141, pp. 407–413, Oct. 2015.

[15] H. Shen *et al.*, "Mechanically-stacked perovskite/CIGS tandem solar cells with efficiency of 23.9% and reduced oxygen sensitivity," *Energy Environ. Sci.*, 2018.

[16] E. M. Sanehira *et al.*, "Influence of Electrode Interfaces on the Stability of Perovskite Solar Cells: Reduced Degradation Using MoO x /Al for Hole Collection," *ACS Energy Lett.*, 2016.

[17] Q. Jiang, X. Zhang, and J. You, "SnO 2 : A Wonderful Electron Transport Layer for Perovskite Solar Cells," *Small*, vol. 14, no. 31, p. 1801154, Aug. 2018.

[18] G. Y. Kim, A. Senocrate, T. Y. Yang, G. Gregori, M. Grätzel, and J. Maier, "Large tunable photoeffect on ion conduction in halide perovskites and

implications for photodecomposition," *Nat. Mater.*, 2018.

[19] L. J. Phillips *et al.*, "Maximizing the optical performance of planar CH3NH3PbI3 hybrid perovskite heterojunction stacks," *Sol. Energy Mater. Sol. Cells*, 2016.

[20] Y. Jiang *et al.*, "Post-annealing of MAPbI3 perovskite films with methylamine for efficient perovskite solar cells†," *Mater. Horizons*, 2016.

[21] N. Marinova *et al.*, "Light harvesting and charge recombination in CH3NH3PbI3 perovskite solar cells studied by hole transport layer thickness variation," *ACS Nano*, 2015.

[22] Z. Hawash, L. K. Ono, and Y. Qi, "Recent Advances in Spiro-MeOTAD Hole Transport Material and Its Applications in Organic–Inorganic Halide Perovskite Solar Cells," *Advanced Materials Interfaces*. 2018.

[23] T. Krishnamoorthy *et al.*, "A swivel-cruciform thiophene based hole-transporting material for efficient perovskite solar cells," *J. Mater. Chem. A*, 2014.

[24] H. J. Snaith, "The perils of solar cell efficiency measurements," *Nature Photonics*. 2012.

[25] A. D. Sheikh, A. P. Patil, S. S. Mali, C. K. Hong, and P. S. Patil, "New insights into active-area-dependent performance of hybrid perovskite solar cells," *J. Mater. Sci.*, 2019.

[26] Y. Chen, L. Zhang, Y. Zhang, H. Gao, and H. Yan, "Large-area perovskite solar cells-a review of recent progress and issues," *RSC Advances*. 2018.

[27] F. Sahli *et al.*, "Fully textured monolithic perovskite/silicon tandem solar cells with 25.2% power conversion efficiency," *Nat. Mater.*, 2018.

[28] C. Y. H. Chan, C. M. Chow, and S. K. So, "Using transistor technique to study the effects of transition metal oxide dopants on organic charge transporters," *Org. Electron.*, 2011.

[29] T. Duong *et al.*, "Rubidium Multication Perovskite with Optimized Bandgap for Perovskite-Silicon Tandem with over 26% Efficiency," *Adv. Energy Mater.*, 2017.

[30] R. S. Sanchez and E. Mas-Marza, "Light-induced effects on Spiro-OMeTAD films and hybrid lead halide perovskite solar cells," *Sol. Energy Mater. Sol. Cells*, 2016.

[31] A. Farooq *et al.*, “Spectral Dependence of Degradation under Ultraviolet Light in Perovskite Solar Cells,” *ACS Appl. Mater. Interfaces*, 2018.

[32] B. Roose *et al.*, “Mesoporous SnO2 electron selective contact enables UV-stable perovskite solar cells,” *Nano Energy*, 2016.

Chapter 7

Conclusions and Future Work

In chapter 3 we presented an alternative technology to depositing compact TiO_2 via spray pyrolysis. EA originally designed for use as a solar control product, utilizes a thin, < 20 nm CVD TiO_2 compact layer and conductive FTO base layer to perform remarkably well in a mesoporous triple cation perovskite device with PCE exceeding 15%, this is higher than that produced via spray pyrolysis within our research group. The use of cyclic voltammetry indicated EA shows a strong blocking effect similar to that found in spray pyrolysis TiO_2 layers sintered at 550°C. TPV and CV analysis shows TiO_2 films on the EA substrate have fewer pinholes and stronger rectifying behaviours compared to conventionally processed c-TiO_2 layers prepared

via spray pyrolysis. EA doesn't suffer with the inconsistencies and technical difficulties associated with the scaling-up of spray pyrolysis (principally glass cracking and inhomogeneity of film coverage etc.) found when trying to replicate spray pyrolysis at scale. In summary EA proves superior to spray pyrolysis for the large-scale production of effective electron transport layers based on TiO_2. The body of work presented here provided a solid base from which to build a thesis, the concept of semi-transparent solar windows is of real value to a company like NSG Pilkington and from an environmental point of view. By incorporating an already existing product into a new PSC system we take an important first step to realising this goal. The next stages will involve the selection of appropriate materials and the development of transparent contacts for both sides of the solar cell. There is also potential for even better performances of EA by tuning the physical and optical TiO_2 parameters. The substrate has the potential to remove process bottlenecks such as the laborious spraying and sintering of blocking layers while at the same time streamlining the fabrication process to reduce total build times. Other future work in this area should be improving the long-term stability of PSC based on TiO_2, the application of UV filters that do not impede the visible spectrum will be of huge benefit in this area if TiO_2 based PSC are to be into production. By tuning the perovskite to absorb further into the infra-red region we could move away from the UV spectrum all together and TiO_2 based cells could flourish.

Chapter 4 built on and expanded the work done in chapter 3, again another mass manufactured ETL was investigated. By addressing the stability concerns of TiO_2 and proactively searching for a more stable material we diversify NSG Pilkington's product line to better take advantage of growing trends and new data with the perovskite community. SnO_2 is very highly regarded in the perovskite field as a material that could have real impact. Its excellent band alignment, high electron mobility, ease of manufacture and stability compared to other metal oxide ETL give real promise for the commercialisation of perovskite solar cells. The work here showed that even with very little optimisation (in part due to the limited supply of materials from NSG) a fantastic development was made to incorporate PCBM with

TEC15-D (a CVD SnO_2 FTO substrate) to solve the problem caused by the necessary laser ablation and a PCE of 18.4 % was record based on a SnO_2 based device. The progression in technology development from TiO_2 is clear and moving forward SnO_2 promises to further simplify the production process with its simple planar architecture. By building on the cyclic voltammetry work from chapter 3 we demonstrate that TEC15-D alone acts an effective hole blocking layer over the range -0.8 to +0.8 V and compares well with that achieved in chapter 3 with TiO_2. This is combined with impressive optical transmission, conductivity. While open circuit voltage verses sun intensity TPV suggests that an unoptimized TEC15-D compares well to optimised control cells and those with PCBM have a reduced rate of parasitic interfacial recombination. Chapters 3 and 4 helped to establish two existing NSG products as potential dual-purpose materials by re-engineering them and characterising them for use in perovskite solar cells as part of energy generating window. This base of knowledge could then be used to tackle the next challenge – developing transparent contacts for both sides of the solar cell. Future work here should be primarily focused on optimising the already impressive SnO_2 present in TEC15-D, SnO_2 can be combined with many different technologies to enhance performance so there are real possibilities here, combining them with a wider range of conjugated fullerenes other the PCBM is one such area of interest. But above all, more characterisation needs to done of Tec15-D to understand the beneficial properties of SnO_2 and their origins and working mechanisms. The first step would require securing an adequate supply of samples.

Chapter 5 began by taking the promising results in chapter 3 with an efficient TiO_2 based device and trying to further them by developing a transparent top contact composed of AgNW: CNT. There are various possible routes to go down when it comes to developing a transparent conductive and scalable contact and metal nanowires are one such way. However metal nanowires like Ag do have issues adhering to surfaces over prolonged period and when put under even the slight mechanical stress, this is where the novelty comes in, we combined AgNW with CNT that adhere well to most surfaces and couple together the beneficial properties of etc to produce a robust transparent contact material that can be simply deposited at room temperature via spray coating. The composite material based on AgNW and

single walled CNTs presented in this chapter display key advantages over conventional metal nanowire-based contacts. The issue of poor adhesion related to AgNWs has been alleviated by incorporating a longer length single walled CNT into a matrix design that adheres well even smooth substrates. While at the same time demonstrating sheet resistances comparable to that of evaporated metal contacts. Sheet and shunt resistances (RSH) were consistently lower than 10 Ωcm-2 across all samples. The processing technology used (spray coating) is relatively easy to upscale and simple to prepare, thus the issue of scale-up is also mitigated. The transparency of the contact allows a substantial portion of the electromagnetic spectrum to pass through unabated with excellent haze, clarity and optical (CIE colourimetry) performance. Full devices based on diluted MAPI perovskite absorbers demonstrated a stabilised PCE of over 7 % with an average transparency of 13 % over the visible spectrum. Future work for AgNW: CNT although easily scalable needs to focus on the stability of AgNW within the coating and what effect will prolonged illumination, moisture, excess heat and stress have on the nanowires. It should be understood what happens to the structure of these nanowires in severe environment as mentioned. If metal ion migration is an issue than research into effective barrier layers or proper interfacial engineering will be needed to overcome these challenges.

Chapter 6, the culmination of chapter 3,4 and 5 but more notable the latter 2. This time the focus looked at the one issue that constantly plagues perovskite solar cells: stability. And building on from the relatively stable SnO_2 work presented in chapter 4 a dual IZO/ MoOx bilayer was developed with exceptional optical properties and better than expected stability results. The MoOx is used a barrier to protect the soft HTMs used in fabricating most PSC from a 200 nm IZO top contact deposited by room temperature radio frequency magnetron sputtering. These vacuum processes help to produce a compact, conformal, uniform, highly transparent, conductive and UV filtering MoOx/IZO bilayer. The resulting solar cells with a 10 nm layer of MoOx demonstrated a very impressive power conversion efficiency of 16.03% when illuminated through the FTO contact and 13.8% when illuminated through the IZO contact. Increasing the thickness of MoOx layer to 50 nm had two notable effects, the first was a lowering of initial power conversion efficiency to 10.9 %, but the

second effect was a to significantly improve the stability of devices. Impressively, these devices showed over 70% PCE increase after 150 h continues light soaking, achieving 12.8% PCE, which was retained over 700 h of operational lifetime. These results suggest MoOx/IZO electrodes can serve as an effective barrier to environmental stress factors such as UV light, oxygen and moisture. The added bonus of being able to tune a perovskite solar cells colour by varying the thickness of MoOx layer combined with impressive long-term stability and excellent optoelectronic performance means perovskite solar cells have a real commercial potential for generating electricity in dual functional PV windows. Future work moving away from chapter 6 would be to look even more stable perovskite materials by moving away from soft organic molecules like Spiro-MeOTAD and towards more inorganic stable materials. In addition, the feasibility and scalability of sputtering as a deposition method should be effectively cost accessed to see if it can be commercially viable like thin film vacuum processes are in a lot of semiconductor technologies.

In conclusion of the thesis as a whole, this body of work identifies two potential existing products (Eclipse Advantage™ and TEC15-D) from the sponsoring company NSG Pilkington and reengineer them for use as dual purpose energy generating windows, solving key process bottlenecks along the way by developing two completely different transparent contact systems (AgNW: CNT composite for ease of manufacture and a bifacial bilayer IZO/ MoOx evaporated system for stability control) while also being aware of other critical properties such as haze, clarity and colourimetry, overall film transparency and need for continuous improvement and adaptability.